UTS UNIVERSITY OF TECHNOLOGY SYDNEY

Federated and Physics-Informed AI Models for Real-Time Bio-Nano Digital Twins Using IoBNT

by Mohammad (Behdad) Jamshidi

Thesis submitted in fulfilment of the requirements for
the degree of

Doctor of Philosophy

under the supervision of A/Prof. Hoang Dinh and A/Prof. Diep Nguyen

University of Technology Sydney
Faculty of Engineering and Information Technology

July 2025

CERTIFICATE OF ORIGINAL AUTHORSHIP

I, Mohammad Jamshidi, declare that this thesis is submitted in fulfillment of the requirements for the award of Doctor of Philosophy, in the Faculty of Engineering and Information Technology at the University of Technology Sydney.

This thesis is wholly my own work unless otherwise referenced or acknowledged. In addition, I certify that all information sources and literature used are indicated in the thesis.

This document has not been submitted for qualifications at any other academic institution.

This research was supported by an Australian Government Research Training Program (RTP) Scholarship doi.org/10.82133/C42F-K220.

Signature:

Production Note:
Signature removed prior to publication.

Mohammad Jamshidi

8 July 2025

ACKNOWLEDGMENTS

"Be grateful for whoever comes, because each has been sent as a guide from beyond."

Rumi

I am profoundly thankful for the exceptional supervision, intellectual depth, and steadfast support of A/Prof. Hoang Dinh and A/Prof. Diep Nguyen. Their discerning feedback, thoughtful mentorship, and strategic vision have been pivotal throughout the course of my doctoral journey. I am truly honored by their collaboration and distinguished leadership, and I extend my best wishes for their continued excellence and achievement in academia.

Being part of A/Prof. Hoang Dinh's research group at UTS has been a remarkably formative and stimulating experience. I had the privilege of working alongside brilliant peers whose contributions enriched my research journey. I am particularly grateful to Chi-Hieu Nguyen, Md Arif Hassan, Nguyen Quang Hieu, Nam H. Chu, and Bui Duc Manh for their valuable insights and consistent support.

I am also indebted to professors and collaborators whose expertise and generosity facilitated the advancement of my research. My sincere appreciation goes to A/Prof. Mohammad Abu Alsheikh, Prof. Eryk Dutkiewicz, Prof. Majid Ebrahimi Warkiani, Dr. Cong T. Nguyen, and Dr. Nguyen Van Huynh. I am especially thankful to Prof. Dusit (Tao) Niyato, whose visionary input, collegial spirit, and inspirational engagement were truly transformative.

No words can adequately express the depth of my gratitude to my beloved parents and siblings. Their unconditional love, moral strength, and enduring prayers have been the cornerstone of my resilience and accomplishments.

Finally, I wish to acknowledge my supervisors, academic peers, and senior colleagues for their thoughtful suggestions and wholehearted assistance throughout the thesis.

Abstract

Digital twinning in biological systems poses significant challenges due to the highly variable, distributed, and privacy-sensitive nature of biomedical data. Constructing scalable, accurate, and secure digital models that faithfully replicate biological processes demands advanced computational strategies capable of operating across decentralized environments. This thesis addresses the challenge of building a unified and privacy-preserving framework for high-fidelity Digital Twins (DTs) of biological systems, where heterogeneous data and complex physiology require both data-driven and physics-guided modeling, and investigates federated and physics-informed Artificial Intelligence (AI) approaches to achieve this goal. The proposed models are built through the integration of Physics-Informed Neural Networks (PINNs), Federated Learning (FL), Internet of Bio-Nano Things (IoBNT), and advanced deep learning architectures, including Convolutional Neural Networks (CNNs), Recurrent Neural Networks (RNNs), Fully Connected Neural Networks (FCNNs), and residual neural networks (ResNets). To meet this central challenge, three interrelated frameworks are developed, each extending the previous one to progressively enable scalable, interpretable, and privacy-aware DT construction. The first proposed framework combines FL and CNNs to construct bacterial DTs using data acquired via IoBNT. The second proposed framework employs a hybrid PINN-based architecture, integrated with RNNs, FCNNs, and ResNets, to enable digital twinning of microbial growth in biosystems. Additionally, the third proposed FL-PINN framework is proposed for modeling glucose–insulin dynamics in metabolic regulation using IoBNT-derived signals. Experimental evaluations confirm that the proposed frameworks deliver high accuracy, reliability, and scalability in digital twinning applications. Across all three frameworks, the proposed algorithms reduced data-transfer errors by up to 98%, improved prediction accuracy to a mean absolute error of approximately 0.03, and lowered RMSE to about 0.04, outperforming existing physics-based or purely data-driven methods by margins exceeding 20-30% on benchmark datasets. These gains directly translate to faster convergence and lower communication overhead, which is critical for real-time biomedical DT deployment and clinical decision support. These results ensure consistent predictive stability across clients, reduce communication overhead, and preserve data privacy. Collectively, these integrated contributions establish a unified, future-oriented foundation for developing clinically actionable and privacy-conscious Digital Twins within biotechnology and digital health.

List of Publications

Journal Papers

J1 **Mohammad (Behdad) Jamshidi**, Dinh Thai Hoang, and Diep N. Nguyen, "CNN-FL for Biotechnology Industry Empowered by Internet-of-BioNano Things and Digital Twins," *IEEE Internet of Things Magazine*, vol. 7, no. 5, pp. 54–63, 2024 (Corresponding to Chapters 1 and 2).

J2 **Mohammad (Behdad) Jamshidi**, Dinh Thai Hoang, Diep N. Nguyen, Dusit Niyato, and Majid Ebrahimi Warkiani, "Revolutionizing Biological Digital Twins: Integrating Internet of Bio-Nano Things, Convolutional Neural Networks, and Federated Learning," *Computers in Biology and Medicine*, vol. 189, pp. 109970, 2025 (Corresponding to Chapters 1 and 2).

J3 **Mohammad (Behdad) Jamshidi**, Dinh Thai Hoang, Diep N. Nguyen, Dusit Niyato, and Majid Ebrahimi Warkiani, "A Multi-Model Physics-Informed Neural Network Framework Empowered by Internet of Bio-Nano Things for Digital Twins of Physics-Based Processes," *IEEE Internet of Things Journal*, Accepted (Corresponding to Chapters 1 and 3).

J4 **Mohammad (Behdad) Jamshidi**, Dinh Thai Hoang, Diep N. Nguyen, and Pubudu N. Pathirana, "Physics-Informed Neural Networks for Glucose–Insulin Digital Twins Leveraging Federated Learning and IoBNT," *npj Digital Medicine*, to be submitted (corresponding to Chapters 1 and 4).

J5 Md Arif Hassan, **Mohammad (Behdad) Jamshidi**, Bui Duc Manh, Nam H. Chu, Chi-Hieu Nguyen, Nguyen Quang Hieu, Cong T. Nguyen, Dinh Thai Hoang, Diep N. Nguyen, Nguyen Van Huynh, Mohammad Abu Alsheikh, and Eryk Dutkiewicz, "Enabling Technologies for Web 3.0: A Comprehensive Survey," *Computer Networks*, vol. 264, pp. 111242, 2025 (a part of Chapter 1).

Conference Papers

C1 **Mohammad (Behdad) Jamshidi**, Dinh Thai Hoang, Diep N. Nguyen, Dusit Niyato, and Majid Ebrahimi Warkiani, "Integrating IoBNT and Distributed Learning for Efficient E-Health and Biotechnology Systems, " IEEE GLOBECOM, Taipei, Taiwan, 2025. Accepted (Corresponding to Chapters 1 and 2).

C2 **Mohammad (Behdad) Jamshidi**, Dinh Thai Hoang, and Diep N. Nguyen, "Integrating Internet of Bio-Nano Things and Physics-Informed Neural Networks for Bioprocess Digital Twins", The IEEE Wireless Communications and Networking Conference (WCNC), Kuala Lumpur, Malaysia, 2026. Under review (Corresponding to Chapters 1 and 4).

Contents

List of Figures

List of Tables

List of Abbreviations

Abbreviation	Full Term	Description
6G	Sixth-Generation Mobile Network	Next-generation cellular communication standard
AI	Artificial Intelligence	Computational methods for intelligent modeling and decision making
Adam	Adaptive Moment Estimation	Stochastic optimizer used for training neural networks
ANN	Artificial Neural Network	General class of neural networks (includes CNN, RNN, FCNN)
API	Application Programming Interface	Software interface for data exchange and services
API Gateway	Application Programming Interface Gateway	Manages requests between client and backend services
AP	Access Point	Wireless connectivity node in IoT/IIoT networks
ASD	Autism Spectrum Disorder	Neurodevelopmental disorder, e.g., FL with CNN–LSTM for detection
ATMP	Advanced Therapeutic Medicinal Product	Biomanufacturing products such as CAR T-cell therapy
BER	Bit Error Rate	Metric of communication reliability
BNT	Bio-Nano Thing	Node/device in IoBNT ecosystems
BPTT	Backpropagation Through Time	Training algorithm for RNNs over temporal sequences
CAR T	Chimeric Antigen Receptor T cell	Example of ATMP in bioprocess digital twins
CI	Confidence Interval	Range of values likely to contain a parameter (e.g., 95% CI)

(continued on next page)

(continued from previous page)

Abbreviation	Full Term	Description
CPU/GPU	Central / Graphics Processing Unit	General and parallel computing processors
CNN	Convolutional Neural Network	Deep-learning architecture for feature extraction and vision tasks
CNN-FL	Convolutional Neural Network–Federated Learning	Integrated FL-CNN framework
DDE	Delay Differential Equation	Differential equation with time delay
DID	Decentralized Identifier	Cryptographically verifiable digital identity
DNN	Deep Neural Network	Neural network with multiple hidden layers
DP	Differential Privacy	Privacy-preserving data analysis framework
DT	Digital Twin	Virtual representation of a physical or biological system
DTWN	Digital Twin Wireless Network	Wireless infrastructure supporting DT communications
E-Health	Electronic Health	Digital healthcare applications and systems
F1-score	Harmonic Mean of Precision and Recall	Balanced model performance metric
F-CNN	Federated Convolutional Neural Network	CNN trained under FL for decentralized data
F-MADRL	Federated Multi-Agent Deep Reinforcement Learning	Privacy-preserving multi-agent coordination framework
FCNN	Fully Connected Neural Network	Standard feed-forward network with dense layers
FCNN-PINN	Fully Connected PINN	PINN with FCNN backbone
FedAvg	Federated Averaging	Algorithm to aggregate FL client models
FL	Federated Learning	Decentralized, privacy-preserving machine learning
FL client	Federated Learning Client	Participant device training a local FL model

(continued on next page)

(continued from previous page)

Abbreviation	Full Term	Description
FLWR	Flower	Federated-learning orchestration framework
FLOP	Floating Point Operation	Single floating-point arithmetic operation
FLOPs	Floating-Point Operations per Second	Computational complexity metric
GB	Gigabyte	Unit of digital data size
GBps	Gigabytes per second	Data-transfer rate
GBR	Gradient Boosting Regressor	Tree-based ensemble regression model used as a surrogate estimator
GDPR	General Data Protection Regulation	EU data privacy regulation
HIPAA	Health Insurance Portability and Accountability Act	U.S. healthcare data privacy law
HTML	HyperText Markup Language	Web-based user interface technology
IEEE	Institute of Electrical and Electronics Engineers	Professional standards organization
IEEE 802.11	IEEE 802.11 (Wi-Fi)	Wireless LAN standard
IEEE 802.15.4	IEEE 802.15.4	Low-rate WPAN standard
IEEE P1906.1	IEEE P1906.1	Nanoscale/molecular communication standard
IIoT	Industrial Internet of Things	Industrial-scale IoT networks
IoBNT	Internet of Bio-Nano Things	Bio-nano communication and sensing network
IoT	Internet of Things	Network of connected physical devices
KPI	Key Performance Indicator	Operational performance metric
L2	Euclidean Norm (ℓ_2)	Square-root of sum of squared components; used to measure vector magnitude
LSTM	Long Short-Term Memory	RNN variant for temporal data modeling
LTI	Linear Time-Invariant	Class of systems with time-invariant linear dynamics
MAE	Mean Absolute Error	Regression error metric
MB	Megabyte	Unit of digital data size
MBps	Megabytes per second	Data-transfer speed
MBR	Model Bandwidth Reduction	Bandwidth-savings analysis concept

(continued on next page)

(continued from previous page)

Abbreviation	Full Term	Description
MGC	Microbial Growth Concentration	State variable for biomass concentration
ML	Machine Learning	Data-driven modeling methods
MSE	Mean Squared Error	Average squared difference between predicted and observed values
MMG	Multi-Microgrid	Multi-grid energy network scenario
MobileNetV2	Mobile Network Version 2	Lightweight CNN architecture for embedded vision
NN	Neural Network	Model composed of layers of interconnected neurons
ODE	Ordinary Differential Equation	Governing equation in physics-based modeling
PAT	Process Analytical Technology	Real-time analytics for bioprocess DTs
PDE	Partial Differential Equation	Governs spatiotemporal physical processes
PI-AI	Physics-Informed Artificial Intelligence	AI with embedded physics priors
PINN	Physics-Informed Neural Network	Neural network constrained by physical laws
R^2	Coefficient of Determination	Goodness-of-fit metric
ReLU	Rectified Linear Unit	Non-linear activation function
ResBlock	Residual Block	Skip-connected unit in a residual neural network
ResBlock NN	Residual Block Neural Network	NN using residual connections
ResBlock-PINN	Residual Block PINN	PINN with residual-block backbone
ResNet	Residual Neural Network	CNN variant using skip connections
RHS	Right-Hand Side	Right-hand side of an equation (e.g., ODE/PDE formulation)
RF	Radio Frequency	Wireless energy/power communication
RNN	Recurrent Neural Network	Neural network for sequential/temporal data
RNN-PINN	Recurrent PINN	PINN with RNN backbone
RMSE	Root Mean Squared Error	Regression error metric
RGB	Red–Green–Blue	Standard digital color model

(continued on next page)

(continued from previous page)

Abbreviation	Full Term	Description
SDE	Stochastic Differential Equation	Differential equation including randomness
SGC	Substrate Growth Concentration	State variable for substrate concentration
S(t)	Substrate Concentration	Monod kinetics state variable
X(t)	Microbial Concentration	Monod kinetics state variable
TPU	Tensor Processing Unit	Hardware accelerator for deep learning
TSN	Time-Sensitive Networking	Deterministic low-latency communication
UI	User Interface	Front-end interface for human interaction
Web3	Web 3.0	Decentralized web infrastructure

Chapter 1

Introduction and Literature Review

1.1 Introduction

In the biotechnology and medical sectors, Digital Twins (DTs) represent a transformative solution for accurately modeling biological entities, including humans, organs, microorganisms, and cyber physical healthcare systems. This thesis contributes to this emerging paradigm by developing advanced Federated Learning (FL) and Physics-Informed Artificial Intelligence (PI-AI) models capable of supporting real time, privacy aware digital representations of complex Bio-Nano systems using the Internet of Bio-Nano Things (IoBNT) [1, 2]. Going beyond isolated simulations, DTs encompass a wide range of elements, including Internet of Things (IoT) in healthcare, pharmaceutical industries, clinics, hospitals, and biomedical devices. They oversee the entire lifecycle of biological entities or equipment assets, facilitating monitoring, behavior analysis, control, and adaptation. A fully developed DT presented in this thesis goes beyond classic Machine Learning (ML) models or basic simulation of patients, diseases, organs, or biological systems. It becomes a dynamic, detailed, and context-aware digital counterpart of physical and living entities, capturing their continuous interactions within biological and clinical environments. DTs in this context embody a seamless integration of the physical and digital domains and advanced ML models, surpassing conventional IoT architectures that are limited to unidirectional data flow. Looking ahead, bio-nano DTs are anticipated to play a transformative role in areas such as drug discovery, real-time digital healthcare, and the evolution of immersive platforms, including the Metaverse.

To further enhance the capabilities of these DT systems, recent advancements in the IoBNT are anticipated to address and potentially surmount many of the prevailing challenges faced by the DT-enabled biotechnology sector. IoBNT refers to a network of interconnected biological and nanoscale devices capable of communication and data exchange [3]. These devices can include sensors and actuators embedded within biological systems, enabling real-time monitoring and manipulation of biological processes at a micro or nanoscale. By seamlessly integrating with DT architectures, this technology significantly enhances the capability of DTs in the biotechnology industry by providing high-precision, real-time data directly from the biological source. As a result, IoBNT devices can monitor and respond

to changes at a molecular or cellular level, offering a level of detail and accuracy that substantially improves the modeling and simulation capabilities of DTs. Furthermore, IoBNT serves as a bridge for integrating diverse data types between biological systems and digital models, ensuring seamless data flow and model fidelity. Critically, it also incorporates advanced security measures at the hardware level, thereby offering enhanced data privacy and security. These concerns are particularly important when dealing with sensitive biological data. In summary, the development of IoBNT not only complements but significantly elevates the functionality of DTs in biotechnology. It effectively addresses key challenges while paving the way for more accurate, real-time, and secure biological system modeling and analysis.

Building upon this synergy between DTs and IoBNT, the rapid advancement of emerging technologies is further advancing the e-health and biotechnology sectors, particularly in areas such as mobile health and digital biotechnology systems [4, 3]. Cutting-edge innovations, such as IoT enhanced by Artificial Intelligence (AI), are becoming indispensable for modernizing biotechnological assets and infrastructures [5]. With proper integration, these technologies have the potential to significantly enhance usability and feasibility, thereby maximizing the benefits of e-health solutions and improving healthcare outcomes [6]. However, realizing these benefits in practice remains a formidable task. Implementing reliable and secure e-health systems using advanced technologies poses significant challenges [4]. Traditional IoT systems often struggle to meet the high levels of precision and reliability required for critical applications in biotechnology and e-health. Even minor inaccuracies in data collection or processing can lead to severe consequences, compromising diagnostic accuracy, treatment efficacy, and the integrity of biological research [7]. Moreover, the inherently complex and highly variable nature of biological and medical data introduces additional obstacles. Hence, overcoming these challenges related to precision and data complexity is essential for unlocking the full potential of advanced e-health and biotechnology systems.

In direct response to these limitations, the IoBNT represents a transformative leap in tackling the integration of emerging technologies in e-health and biotechnology [8]. By connecting nanoscale biological sensors with advanced communication networks, IoBNT delivers an unprecedented level of precision and control in monitoring biological processes, thereby addressing the core limitations of traditional IoT systems [9]. Moreover, the decentralized approach to data collection offered by IoBNT is especially valuable in environments where centralized aggregation of medical data is impractical or ethically sensitive. By avoiding centralization, IoBNT reduces the risks of compromising sensitive biological information. This feature is particularly crucial in mobile health and digital biotechnology scenarios [10]. Additionally, the inherent scalability of IoBNT allows it to adapt to the growing complexity of biological systems without overwhelming computational or storage resources. This makes IoBNT well-suited for managing large, distributed datasets. Nevertheless, real-world medical and biological data often remain fragmented across various clinics and hospitals, constrained by privacy regulations and decentralized data infrastructures. Attempts to centralize such data expose systems to serious privacy and security risks, especially in contexts where breaches could have grave medical or ethical repercussions [5]. Thus, decentralized neural frameworks integrated with IoBNT present an

ideal pathway toward realizing secure, scalable, and high-fidelity DTs for biological systems.

1.2 Motivations

The growing complexity of biological systems, coupled with the rise of personalized healthcare and precision biotechnology, underscores the urgent need for real-time, accurate, and privacy-preserving digital representations. Traditional AI approaches often fall short when faced with the decentralized, sensitive, and physics-constrained nature of biomedical data. This thesis is motivated by the opportunity to overcome these limitations through federated and physics-informed learning strategies, enabling the development of intelligent DTs capable of modeling dynamic biological processes across distributed and secure networks.

1.2.1 Integrating CNNs and FL into Nano-Bio DTs

Despite of being employing DTs in biology introduces several significant challenges [11]. To begin with, the first major challenge arises from the inherent complexity and variability of biological systems. Unlike more predictable mechanical systems, biological entities display a high degree of variability and unpredictability, which significantly complicates the process of achieving accurate modeling [12]. Moreover, the challenge of data integration presents a significant obstacle. Biological systems often require the integration of various types of data, ranging from molecular to organismal levels, which can be challenging to synchronize and analyze effectively [13]. In addition to this, the necessity of real-time data processing in biology, although crucial, poses a significant challenge. For such frameworks to be truly effective, they require the capability to process and react to data instantaneously. However, this is particularly demanding due to the intricate and complex nature of biological data. Lastly, ensuring the privacy and security of sensitive biological data is paramount, especially when dealing with human-related content, but it remains a difficult task due to the vast amount of data and its sensitive nature [14]. Taken together, these issues highlight the need for scalable, privacy-aware, and biologically intelligent modeling approaches that extend beyond traditional digital modeling.

At the same time, these technologies are already transforming biotechnology by enabling digital representations for applications such as drug development, health informatics, and microbial asset management. Nevertheless, implementing such solutions at the micro and nano scales, particularly for sophisticated biological entities such as bacteria, presents considerable difficulty. This complexity stems not only from biological intricacy but also from the infrastructural demands of ensuring both accuracy and scalability at such scales. In this context, integrating next-generation sensing and communication platforms into biology-centered digital frameworks introduces a complementary layer of innovation. Yet, challenges persist, especially in sensor placement and data resolution at nanoscale levels. Consequently, to make sense of such dense and heterogeneous information streams, deep learning approaches become essential. Among these, CNNs provide a particularly strong foundation, as they are capable of parsing visual and structurally complex input, such as biological imagery, with high preci-

sion. Their inherent pattern recognition capabilities make them ideally suited to extract insights from the type of data collected in these emerging networks [15].

Furthermore, CNNs support the modeling of high-dimensional biological interactions with exceptional robustness, even when the system's complexity increases. Simultaneously, another layer of capability is introduced through FL, which responds to growing concerns around data privacy, ownership, and fragmentation. In the current biomedical landscape, where sensitive data are siloed across hospitals and laboratories, FL provides a privacy-preserving approach to collaborative training [15]. Instead of aggregating raw data centrally, it builds comprehensive models from decentralized updates, thus maintaining strict data confidentiality. This federated strategy also benefits CNNs by exposing them to more diverse training distributions without compromising individual sources. As a result, this combination not only enhances accuracy and adaptability but also significantly reinforces the ethical and legal feasibility of deploying digital models in clinical and industrial biotechnology. Moreover, beyond data diversity and analytical robustness, another important aspect emerges from the computational demands associated with these frameworks. In this regard, FL offers a scalable solution by decentralizing the learning process across edge devices [16]. Each node processes its local dataset independently and contributes only aggregated model parameters to the global update cycle. This paradigm significantly reduces the computational burden on central servers while respecting data locality. Notably, this approach preserves compliance with privacy regulations and supports computational sustainability. Accordingly, such a framework is highly aligned with the constraints of nanoscale biological systems, where traditional centralized approaches may be infeasible. Together, this architecture, built upon decentralized learning, secure sensor networks, and convolutional analysis, creates a powerful path toward precise, ethical, and intelligent digital modeling of living systems.

Beyond the technical motivations, the societal and clinical significance of advancing decentralized neural frameworks within biological digital twinning is profound. As personalized medicine continues to evolve, there is an increasing demand for accurate, real-time representations of individual biological processes to guide treatment decisions, monitor disease progression, and evaluate therapeutic responses. DTs, when empowered by decentralized learning and bio-nano sensing technologies, hold the potential to deliver this level of personalization with previously unattainable resolution and responsiveness. Moreover, the convergence of these technologies enables healthcare systems to transition from reactive to predictive paradigms, supporting early diagnosis and continuous monitoring while reducing the need for invasive procedures. To address the multifaceted challenges associated with biological system modeling and privacy-preserving data processing, a robust solution is the integration of Convolutional Neural Networks (CNNs) with FL frameworks [17, 18], enabling efficient analysis and distributed processing. Specifically, integrating CNNs with FL results in a powerful algorithm tailored for image analysis and processing across decentralized environments. CNNs inherently excel at identifying spatial hierarchies in images, making them ideal for tasks such as image classification, segmentation, and object detection. Concurrently, FL facilitates decentralized training across edge devices, ensuring data privacy while minimizing data transmission [19, 20].

In addition to this, the synergy between these two methods combines the image processing strength

of CNNs [21] with the privacy-preserving and scalable features of FL [22]. Simultaneously, FL enables models to generalize across diverse datasets without centralizing the data, thereby improving robustness and minimizing the risk of data breaches. Moreover, FL optimizes bandwidth usage and enhances computational efficiency by processing data locally on edge devices. Therefore, integrating IoBNT with CNNs and FL can significantly expand the capabilities of biological DTs. IoBNT involves nanoscale biological devices interconnected via advanced communication networks, enabling precise and continuous data collection from biological systems. Consequently, when combined with CNNs and FL, IoBNT facilitates real-time monitoring and control of biological assets. Hence, this integration supports continuous, high-fidelity data acquisition, which CNNs can efficiently process. Additionally, FL ensures the effective utilization of data across distributed devices without compromising privacy, thereby enhancing scalability, efficiency, and data security. Together, these technologies serve to significantly advance the development and application of biological DTs, opening new possibilities in medical diagnostics, environmental monitoring, and biomanufacturing.

Research Question 1

Given the complexity, decentralization, and privacy constraints inherent in modeling biological systems, this thesis seeks to answer the following central research question:

> *How can FL and CNNs, when integrated with IoBNT, be used to develop scalable, privacy-preserving, and intelligent DTs of biological systems, capable of handling heterogeneous data, supporting real-time monitoring, and ensuring computational and communication efficiency?*

1.2.2 Developing Physics-Informed ML Models in IoBNT-Enabled DTs

The DT paradigm has emerged as a transformative framework for real-time monitoring, predictive analysis, and system optimization across various sectors, including bioprocessing, biomanufacturing, and healthcare [23, 24]. By establishing a virtual counterpart of a physical system, DTs facilitate the continuous synchronization of sensor-derived data with computational models, thereby enabling real-time decision-making, fault prediction, and adaptive control [23, 25]. This approach significantly improves operational efficiency, resilience, and customizability, especially in dynamic or safety-critical environments. Despite these advantages, implementing DTs for micro- and nano-scale biological systems introduces considerable challenges. These systems often operate in fluidic, noisy, and heterogeneous environments, where biological variability and physical limitations impair the accurate representation of system behavior. The key obstacles in such settings include data extraction, high-resolution transmission, and computational latency, all of which are essential for maintaining the real-time nature of DTs [26]. For instance, detecting biochemical changes or structural deformations in bacterial systems requires ultra-sensitive sensors capable of operating at sub-cellular resolutions, which conventional DT implementations do not readily support.

IoT architectures have demonstrated limitations when applied to biological environments, especially at the micro/nano scale. These limitations are largely due to poor spatial resolution, delayed response times (latency), and narrow bandwidths, which inhibit the continuous and high-fidelity data flow required for effective DT operation [27, 28]. Furthermore, conventional IoT nodes often lack the biocompatibility, miniaturization, and energy efficiency needed to function effectively in biological environments, such as within tissues or cellular matrices. As a result, there is a pressing need to explore advanced sensing and modeling frameworks that can overcome these fundamental bottlenecks and unlock the full potential of DTs in biological and biomedical applications.

To address these limitations, IoBNT has emerged as an advanced evolution of conventional IoT systems, enabling seamless and efficient communication within micro- and nanoscale environments [8, 29]. By employing nanoscale and molecular communication techniques, IoBNT facilitates real-time data acquisition from biological environments that are otherwise difficult to monitor using traditional electronic-based sensors. These networks are specifically designed to operate within complex biological systems, offering enhanced compatibility, miniaturization, and integration compared to standard IoT architectures. Unlike conventional IoT sensors that rely on electromagnetic communication and are often constrained by spatial resolution and energy limitations, IoBNT leverages biological interfaces and nano-communication networks to collect dense, high-resolution data from within living systems [30]. This capability is crucial for capturing the intricate and dynamic processes in bioprocessing and healthcare settings, where precise, continuous monitoring is required. As such, IoBNT serves as a key technological enabler for next-generation DTs by supporting real-time sensing, localized actuation, and predictive analysis in bioengineering and clinical applications [31]. However, despite its transformative potential, data provided by IoBNT alone is not sufficient to construct high-fidelity DTs [32]. Traditional data-driven approaches, while effective in many engineering domains, often fail to incorporate the underlying physical principles that govern complex biological systems. This limitation results in models that may lack robustness, generalizability, or biological interpretability, especially in conditions involving sparse data, noise, or sensor delays. Therefore, to achieve accurate and biologically consistent DTs, there is a need to complement IoBNT-based sensing with modeling approaches that embed domain-specific knowledge directly into the learning process.

A promising solution to the limitations of traditional data-driven models in DTs lies in Physics-Informed Neural Networks (PINNs), which incorporate governing physical laws directly into the architecture of deep learning models [33, 34]. Unlike conventional neural networks that rely solely on empirical data, PINNs enforce physical constraints, such as conservation laws, differential equations, or known system dynamics, during the training process. This integration ensures that the resulting predictions are not only data-efficient but also biologically plausible, making them well-suited for applications involving complex biosystems with limited or noisy data. PINNs effectively bridge the gap between purely theoretical models and data-driven approaches, enabling more accurate modeling of real-world processes where data acquisition may be restricted or corrupted by noise [35]. This is particularly valuable in IoT- and IoBNT-based bioprocess monitoring, where data streams are often sparse, asynchronous, and susceptible to environmental interference. By embedding physical knowledge directly

into the learning framework, PINNs help maintain model stability and reduce overfitting, even when the available training data is incomplete or imbalanced. By incorporating fundamental biophysical principles, particularly in reaction-diffusion processes, transport phenomena, and metabolic dynamics, PINNs enable DTs to more accurately analyze and predict system behavior under a wide range of operating conditions. This capability is essential for applications that require not just observation, but dynamic forecasting and adaptive response, such as smart biomanufacturing and personalized treatment planning [36, 37]. In this context, DTs powered by PINNs serve as a robust platform for real-time communication, system health monitoring, fault detection, and continuous process optimization.

Nevertheless, constructing scalable and adaptive PINN architectures suitable for real-time DT applications remains a significant research challenge. This is especially true when attempting to balance the incorporation of domain knowledge with the latency and variability inherent in real-time sensor data. Efficiently training PINNs in distributed environments, such as those supported by IoT or IoBNT networks, requires addressing issues such as computational cost, model synchronization, and dynamic updates, all while preserving the physical consistency of the model outputs.

Research Question 2

Building upon these foundations, the primary objective of this part of the thesis is to explore the following research question:

> *How can PINNs be systematically integrated into DT frameworks to enable real-time, scalable, and biologically consistent modeling of complex biosystems, while addressing challenges related to data sparsity, noise, and sensor communication constraints?*

1.2.3 Leveraging Decentralized and Biologically-Informed ML Models in Nano-Bio DTs

With over 828 million adults affected globally in 2022 and 445 million untreated, diabetes presents a critical health challenge demanding increasingly advanced monitoring systems and emerging technologies for effective control and management [38]. Precise regulation of insulin and glucose is critical for maintaining metabolic homeostasis, as imbalances can lead to acute complications such as hypoglycemia or long-term risks associated with poorly controlled diabetes [39, 40]. By leveraging these digital tools, it becomes possible to model individual physiological responses more accurately, adapt treatment in real time, and reduce the risk of hypoglycemia or hyperglycemia, ultimately improving clinical outcomes and quality of life for patients. DT enable real-time, personalized diabetes monitoring by integrating sensor data and ML, enhancing early prediction, remote care, and treatment adaptation [41]. However, the application of this technology without the specific use of IoT cannot be effectively adopted by patients in their daily lives [42]. Traditional IoT systems face significant challenges when it comes to handling sensitive data, particularly in accurately measuring and securely transferring medical information from sensors.

The integration of biocompatible nano and molecular communication technologies through IoBNT provides a biologically aligned infrastructure for secure, precise, and continuous monitoring in insulin-glucose regulation systems [42]. IoBNT is a network of biological and nanoscale devices that communicate using molecular signals to monitor and interact with physiological processes [8, 43]. However, extracting accurate data from such systems requires a reliable and robust processing approach. This ensures stability and trustworthiness, which are essential for safe and effective use in healthcare applications. For example, existing approaches to processing and analyzing insulin-glucose data face significant limitations. Models such as Bergman's minimal model and many ML techniques lack real-time adaptability [44]. Current DT frameworks for insulin-glucose regulation often rely on incomplete or infrequent data from wearable devices. Furthermore, these systems typically depend on centralized data processing, raising concerns about privacy, scalability, and accessibility. Critically, most models overlook the fundamental biological dynamics of insulin-glucose interactions, reducing reliability and hindering generalization across diverse patient populations. These challenges underscore the need for biologically informed, privacy-preserving, and adaptive solutions to enhance the clinical relevance of such frameworks.

Therefore, focusing on the integration of physics-based and decentralized approaches within DTs can significantly enhance computational efficiency, real-time adaptability, and predictive accuracy in glucose-insulin regulation. This is particularly important given the physiological complexity, inter-patient variability, and clinical sensitivity of diabetes management, which demand continuous, accurate, and individualized monitoring strategies. To bridge these gaps, we propose a novel PINN-based framework that is empowered by FL and supported by IoBNT [45]. This hybrid architecture is designed to address the core limitations of current DT systems used in metabolic control, which often rely on centralized computation and lack integration of biological dynamics. PINNs mitigate this issue by embedding the underlying physiological laws, such as glucose absorption, insulin action, and metabolic decay, directly into the learning architecture. This ensures that predictions are not only data-driven but also biologically consistent, allowing for better generalization across diverse patient profiles and physiological conditions. In parallel, IoBNT provides a biologically aligned communication infrastructure capable of secure, continuous, and nanoscale monitoring of insulin-glucose interactions

From a public health and biomedical perspective, the federated and physics-informed architectures developed in this thesis enable inclusive model training across geographically dispersed and resource-limited environments. This is vital for capturing population-specific biological variability, which is often neglected in centralized modeling approaches. By leveraging FL, the proposed frameworks enhance resilience to cyber threats and regulatory limitations, supporting secure, scalable deployment in clinical and research settings. Addressing the critical challenges of precision, privacy, and distributed computation, this research establishes a new class of digital infrastructures. These infrastructures extend the role of DTs beyond laboratory and industrial biotechnology, toward real-time biomedical innovation and healthcare delivery on a global scale.

Research Question 3

To address the growing need for biologically grounded, privacy-preserving, and scalable solutions in real-time biomedical monitoring, this thesis explores the integration of PINNs, FL, and the IoBNT for developing DTs of physiological systems. Given the complexity of biological dynamics, the heterogeneity of patient data, and the constraints of secure and decentralized computation, a central research inquiry arises:

> *How can the integration of physics-informed neural architectures with FL and bio-nano sensing enable scalable, real-time, and privacy-aware DTs for modeling dynamic physiological systems such as insulin-glucose regulation?*

1.3 Literature Review

1.3.1 Integrating CNNs and FL into Nano-Bio DTs

FL-CNN-DT Integration in E-Health and Biomedical Systems

Recent advancements in ML methods have significantly impacted e-health and biotechnology, offering powerful tools for data analysis, diagnosis, and treatment optimization [46]. Approaches like Artificial Neural Networks (ANNs) have been enhanced by hybrid algorithms, such as the invasive weed optimization combined with differential evolutionary models, improving the accuracy and efficiency of training [47]. Deep learning techniques, including CNN and LSTM ensembles, are also enabling more sophisticated image captioning for medical imaging [48]. These innovations are further supported by mixed analog-digital infrastructure, fostering better classification in biomedical systems. Together, these advancements are shaping the future of e-health and biotechnology [49]. CNNs are a class of deep neural networks that are highly effective in analyzing visual imagery. At their core, CNNs automate feature extraction, bypassing the need for manual engineering, which significantly enhances efficiency. They are structured in layers, each designed to identify and extract patterns and features from data, regardless of variations in position or scale. This architectural design draws inspiration from the human visual cortex, enabling CNNs to process images hierarchically, where simple features are discerned in early layers, and more complex representations are constructed in subsequent layers. Owing to these capabilities, CNNs have enhanced fields such as image classification, object detection, and beyond, thereby proving to be a pivotal component in the advancement of AI.

The integration of FL with DTs and CNNs has emerged as a promising approach to address data privacy concerns and enhance model performance in various applications. Despite its potential, the implementation of these integrated frameworks faces several challenges, including computational complexity and communication overhead [50]. This subsection explores related works on the combination of FL with DTs and FL with CNNs across different domains, highlighting both the opportunities and limitations of these methods. In the healthcare sector, the combination of FL and CNNs has been widely

applied for secure medical image analysis. One study focused on using FL to train CNN models on distributed MRI data for brain tumor detection, preserving patient privacy without the need for data centralization [51]. Local CNN models were trained independently at each medical institution, and their weights were aggregated using FL. This method achieved a classification accuracy of 91.05%, which was slightly lower than traditional centralized models. The primary challenges identified included the computational complexity of training CNNs on large datasets and the communication overhead involved in aggregating model parameters. Additionally, maintaining model performance across diverse local datasets with varying quality and characteristics was difficult, reflecting the limitations of FL [51]. Nevertheless, this approach demonstrated the potential of combining CNN and FL for secure and effective medical image analysis, paving the way for its application in other sensitive healthcare domains. Expanding on this concept, researchers developed a framework that integrated FL with CNN-LSTM models for Autism Spectrum Disorder (ASD) detection [52]. This system processed multimodal datasets from various clinical laboratories, utilizing FL to aggregate results securely for optimized ASD prediction. The combined use of CNNs for feature extraction and LSTM models for temporal sequence learning enabled accurate detection of ASD, achieving around 99% accuracy. However, the framework faced scalability issues, particularly in resource-constrained environments. Furthermore, the inability to update models in real-time hindered the framework's effectiveness in supporting dynamic patient treatments, illustrating the need for more efficient integration strategies to enhance the performance and scalability of FL-based systems [52].

In another study, FL was combined with transfer learning techniques to classify breast cancer images while preserving data privacy [53]. By leveraging multiple local environments, the researchers trained CNN models without sharing sensitive patient data. This decentralized approach allowed for effective feature extraction and classification using FeAvg-CNN and MobileNet models, achieving high accuracy and recall rates. Despite these successes, the study highlighted several challenges, including communication overheads, which affected the overall model performance. The decentralized nature of FL made it difficult to maintain consistent accuracy across diverse datasets, especially when the data distribution varied significantly between different local environments. Moreover, the resource-intensive nature of FL, combined with the need for frequent communication between local nodes and the central server, posed significant obstacles to its widespread adoption in resource-limited healthcare settings [53].

FL and DT Frameworks in IIoT, Biopharma, and E-Health

In the context of Industrial Internet of Things (IIoT), FL has been applied to improve the integration of DTs by enabling distributed learning without data centralization [54]. This approach enhanced model accuracy and decision-making by allowing DTs to learn from decentralized data sources in real-time. Despite these advantages, the study identified several challenges, including limited communication bandwidth and high computational demands. However, synchronizing DTs with real-world conditions and ensuring data integrity remained significant obstacles, limiting the framework's efficiency in dy-

namic industrial environments [54]. These findings suggest that further research is needed to develop more efficient communication protocols and synchronization mechanisms for integrating FL with DTs in IIoT applications. In 6G-enabled Industrial IoT environments, FL was integrated with DTs to enable efficient and secure data processing in DT Wireless Networks (DTWN) [55]. The inclusion of blockchain technology ensured data integrity and privacy while optimizing edge computing resources. Nevertheless, the study faced challenges related to high communication costs, limited bandwidth, and dynamic network conditions. Managing resource allocation and latency remained critical concerns, as maintaining synchronization between DTs and their physical counterparts was essential for effective operation in complex IoT scenarios) [55]. This highlights the need for advanced resource management and scheduling strategies to improve the integration of FL and DTs in such environments. Overall, while the integration of FL with DTs and CNNs offers promising solutions for enhancing data privacy and model performance across various applications, several challenges remain. The complexity of managing communication overhead, computational demands must be addressed to fully realize the potential of these frameworks. Future research should focus on developing adaptive learning strategies, efficient resource management techniques, and scalable frameworks that can support the diverse requirements of different domains. By overcoming these challenges, the combination of FL, DTs, and CNNs can unlock new possibilities for secure and efficient data processing in healthcare, smart cities, and industrial environments.

In the field of biopharma, DTs have faced limitations due to low signal-to-noise ratios in biological systems, making mathematical modeling and development pathways particularly challenging. This contrasts with other industries where DTs are more established [56]. A study on DTs in biotechnology highlighted the benefits of process modeling, supporting workflows from development to manufacturing across diverse feedstocks, thereby enabling efficient, cost-effective digitalization. Furthermore, by integrating Quality-by-Design principles, the study showcased predictive and financial benefits for consistent process modeling in biopharmaceutical applications [56]. In parallel, research has also focused on developing bioprocess DTs for mammalian cell cultures to enhance biomanufacturing efficiency [57]. This integration of in-line data collection and ML provided improved operational strategies and decision-making capabilities. However, despite these advantages, limitations such as insufficient real-time data for model accuracy, complex cellular dynamics, and high regulatory compliance barriers remained significant challenges [57]. In parallel, FL is a cutting-edge approach to ML that enables multiple participants, often referred to as clients, to collaboratively train a model while keeping their data decentralized and private [18]. This technique is fundamentally different from traditional centralized ML methods where data is pooled into a single location. Specifically, FL allows each participant to train models on their own local data and then share the model updates, rather than the data itself, with a central server. The server then aggregates these updates to improve the global model. This not only preserves privacy and security by minimizing data exposure but also leverages distributed data sources to create more robust and generalized machine-learning models. It is particularly beneficial in scenarios where data privacy is paramount, such as in healthcare and finance. As such, when CNNs are integrated with FL (CNN-FL), it leverages the power of CNNs to process and learn from image

data in a privacy-preserving manner across distributed datasets [15]. This combination is particularly powerful for applications where data privacy is critical and where training data is naturally distributed across multiple locations, such as in medical imaging analysis across different hospitals.

Fig. 1.1 illustrates the synergistic integration of IoBNT with FL in enhancing DTs in the biotechnology sector. In this illustration, the integration unites the micro-nano scalability of IoBNT and its adaptability to biological processes with the decentralized training and privacy features of FL. Consequently, the result is a synergistic platform that fosters collaborative learning from varied data sources, enhancing the precision and detail of models for in-depth analysis of micro-level biological and environmental data. The figure highlights the potential of this integration in the biotechnology industry, emphasizing its role in creating a comprehensive digital environment. Such an environment is pivotal for various applications including real-time monitoring and simulation, customized biological element modeling, and predictive maintenance in biomanufacturing, as well as personalized medicine. Notably, FL contributes to the process by enabling various clients, such as hospitals and laboratories, to collaborate in the pattern recognition of microorganisms across different locations. This collaborative approach not only enhances efficiency but also minimizes energy consumption. In essence, the process begins with the IoBNT nodes capturing images of the physical twins of microorganisms. These images are then processed across different sites, contributing to an updated global model through FL. Subsequently, the refined and accurate DTs of these microorganisms are constructed in a virtual space.

Addressing Biological Complexity in DTs Using IoBNT Infrastructure

Implementing fast and reliable DTs in biotechnology faces substantial hurdles [58]. Meanwhile, the primary issue arises from the inherent variability and complexity of biological assets [12], which are unpredictable and intricate compared to engineered systems [59, 60]. As a result, this complexity makes accurate modeling significantly more difficult and unreliable [61]. Another critical issue is maintaining security and privacy of biological data, particularly human-related data, which is sensitive and voluminous [62, 63]. Consequently, protecting this data while ensuring its accessibility for digitalization poses a significant challenge [64]. Additionally, the necessity for real-time data processing in biological systems demands that digitization operates with high efficiency [65]. For this reason, the intricate nature of biological data complicates instantaneous processing and reaction, which are essential for the effective functioning of DTs. Furthermore, integrating diverse biological data, ranging from organismal to molecular levels, remains a significant obstacle [66, 61]. Moreover, transmission errors impose a critical issue in data communication, quantified by the error rate, which measures the frequency of errors during data transfer. In fact, high error rates can lead to significant data loss and reduced system reliability, especially in biological data transfer where precision and accuracy are paramount [67].

IoBNT is an advanced IoT technology specifically developed to address the challenges of measurement and communication in biological assets [68, 8, 62]. IoBNT combines nanoscale biological devices with communication networks, enabling precise monitoring and control of biological systems. Therefore, this integration facilitates advanced applications in medical diagnostics, environmental monitor-

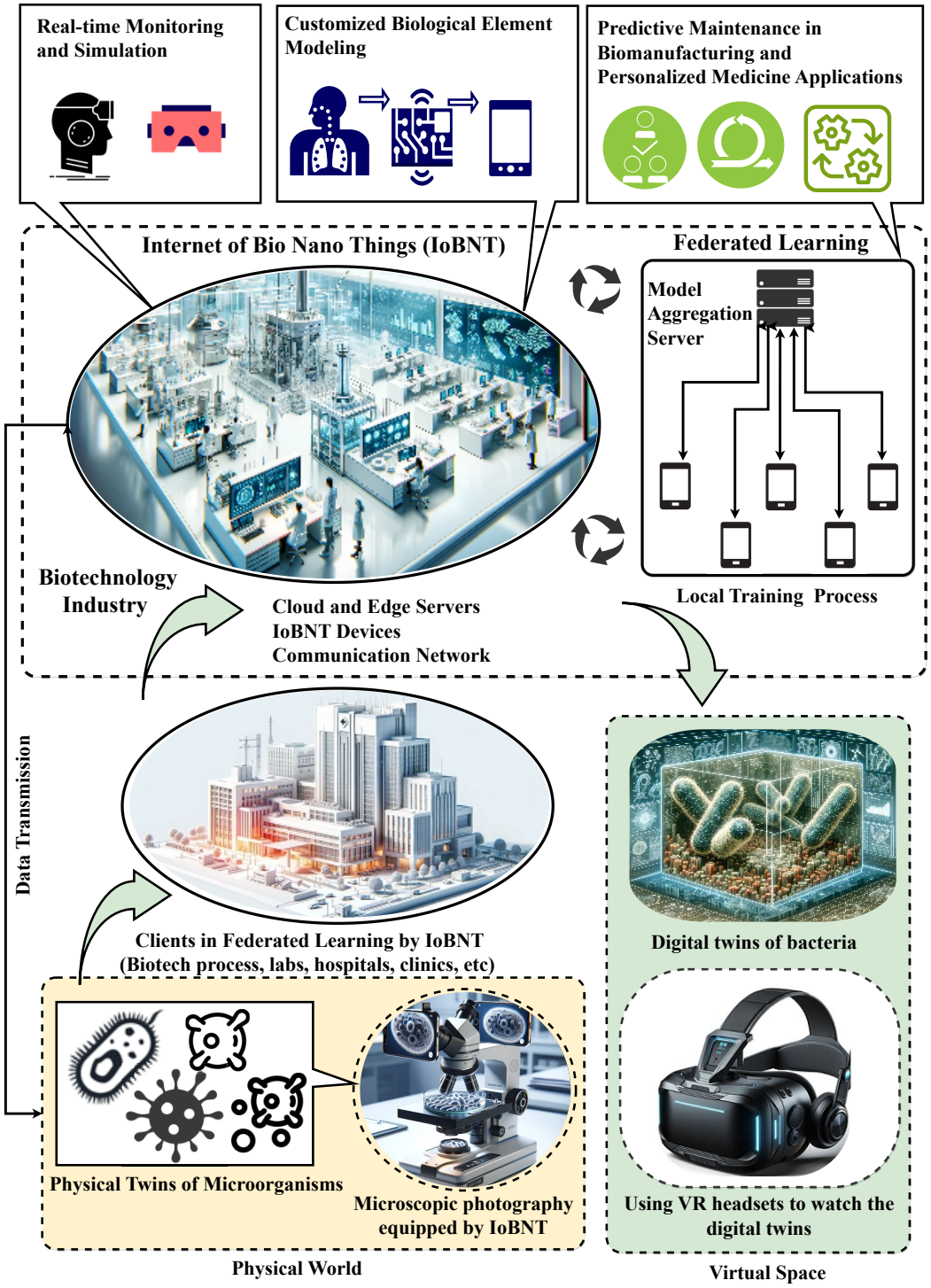

Figure 1.1: The convergence of IoBNT and FL for advanced DTs in biotechnology: micro-level data analysis with ML-driven techniques.

ing, and biomanufacturing, ensuring more accurate, efficient, and reliable biotechnological processes. Furthermore, the specifications of IoBNT offer a powerful solution for synchronizing and effectively analyzing diverse data sets. In consequence, this capability is essential for the accurate and functional application of DTs in biotechnology, as it ensures seamless integration and real-time data processing.

In addition, IoBNT provides the infrastructure needed to handle the complexity of biological data,

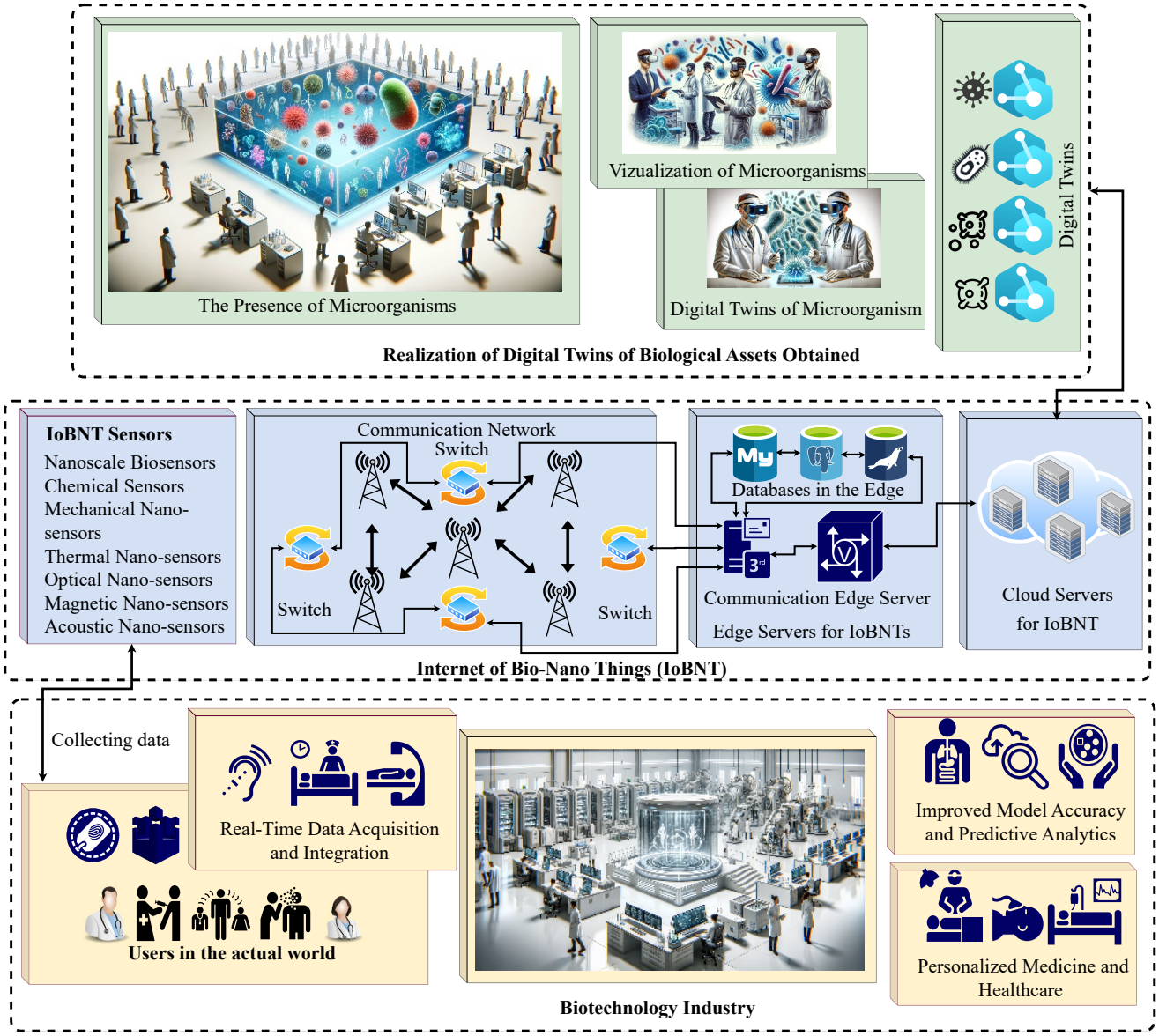

Figure 1.2: Illustrating how integrating IoBNT can significantly improve applications in the biotechnology industry through DT technology.

facilitating sophisticated data analysis and interpretation. Thus, by leveraging IoBNT technology, researchers can achieve precise monitoring and control of biological systems, leading to more reliable and efficient biotechnological processes. Therefore, the existing challenges faced by DT-enabled biological systems and assets are expected to be addressed and potentially overcome by the integration of IoBNT [69]. Additionally, an important advantage of using IoBNT is its ability to optimize error rates. IoT systems, utilizing conventional wireless communication technologies such as Wi-Fi (*IEEE 802.11*) and cellular networks, typically suffer from Bit Error Rate (BER) ranging from 1% to 5% [70]. These error rates lead to substantial data losses when transferring large datasets. The errors are primarily due to packet loss, signal degradation, and interference, especially in high-noise environments, as indicated by *IEEE 802.15.4* standards for low-rate wireless personal area networks [71].

In contrast, IoBNT is specifically designed for bio-nano scale data communication, following the

IEEE P1906.1 standards for nanoscale and molecular communication frameworks, which aim to minimize BER and enhance data reliability. IoBNT demonstrates significantly lower BER, ranging from 0.01% to 0.1% [67]. However, incorporating DTs-based biological applications within IoBNT introduces its unique challenges, especially concerning sensor allocation at the nanoscale [8]. Meanwhile, the complexity and diversity of the data necessitate advanced analytical capabilities [72, 73]. AI methods offer solutions for DT-based biological applications within IoBNT. They address challenges in pattern recognition and computer vision due to the complexity and diversity of the data [74, 75]. However, implementing such methods requires substantial bandwidth to support services across laboratories and hospitals. Increased bandwidth usage in biotechnology strains networks, slows data processing, and raises costs, thus reducing efficiency and scalability.

The IoBNT, as a visionary technological paradigm, merges the realms of nanotechnology, biotechnology, and information technology to forge an interconnected ecosystem of miniature biological and nano-engineered devices. As illustrated in Fig. 1.2, the integration of IoBNT offers vast potential for improving applications within the biotechnology industry through DT technology. These devices, ranging from molecular sensors and actuators to miniature computational elements, are meticulously engineered to interface with biological systems at the cellular or even molecular level. Therefore, the significance of IoBNT for the future of the biotechnology industry is profound. In the healthcare sector, IoBNT technologies are poised to enhance medical diagnostics and treatment, thereby offering transformative opportunities for personalized medicine. Furthermore, in the domain of environmental biotechnology, IoBNT devices provide unparalleled sensitivity and specificity for detecting environmental pollutants and pathogens, thereby supporting more effective ecosystem management and protection. As such, the integration of IoBNT into the biotechnology sector does not merely enhance existing technologies; rather, it represents a paradigm shift toward more efficient, precise, and personalized biotechnological solutions. This shift fundamentally redefines how we interact with and manipulate biological systems for the betterment of health, the environment, and society at large [76].

1.3.2 Physics-Informed ML Models in IoBNT-Enabled DTs

DTs in Bio-Systems: Toward Real-Time, Intelligent Digital Replication

In the biotechnological cyber-physical systems, DTs are a digital representative of objects, assets, humans, and creatures that precisely create immersive models of bioprocesses, medical systems, microorganisms, organs, and even humans [1, 2, 77, 78, 79]. Hence, to make such DTs more reliable and real-time, a wide array of components, including processors, sensors, and IoT within laboratories, hospitals, clinics, and pharmaceutical industries, are utilized [80]. Indeed, an advanced version of a DT in biotechnology and medical science surpasses a simulation of diseases, patients, biological assets, and organs [58]. Thus, DTs effectively facilitate the analysis, monitoring, and adaptation of the lifecycle of microscopic creatures, biological entities, and equipment assets [72, 81, 82]. It becomes a nuanced digital, dynamic, highly detailed counterpart of living and physical biological assets, extracting data from their interactions with the environment [78]. Accordingly, DTs represent a perfect blend of the digital

and physical worlds in biotechnology. They go beyond the traditional IoT model, which is limited by restricted connectivity and one-way data transfer from the physical to the virtual world [81]. Looking ahead, industrial DTs will be a significant factor in fostering the expansion of virtual environments like the Metaverse, with numerous applications, including digital healthcare [82], drug development [83], and digital biotechnology[50].

In addition, hybrid modeling approaches in DTs have also been explored to optimize complex biomanufacturing processes [84]. By combining data-driven and mechanistic approaches, these models enhanced process understanding, control, and prediction, thereby improving decision-making and operational efficiency. In practice, hybrid DTs effectively managed process variability and uncertainty. Nonetheless, challenges included integrating diverse data sources, handling process variability, and establishing standardized protocols. Limited real-time data and complex regulatory requirements further hindered the effective implementation of DTs in biopharma [84]. In the medical domain, DTs have been leveraged for control and optimization in various applications such as diabetes management and anesthesia [85]. These virtual replicas of biological systems, using real-time data and AI, advanced personalized therapies, biomedical design, and drug delivery optimization. Consequently, DTs facilitated preclinical and clinical research, promoting enhanced predictions and tailored healthcare solutions. However, limitations included challenges in data integration, real-time monitoring, and synchronization of physical and digital models [85]. Despite the promising potential of DTs in biotechnology, several challenges must be addressed to fully realize their capabilities. Notably, the complexity of biological systems, characterized by high variability and low signal-to-noise ratios, poses significant obstacles to accurate modeling and real-time data acquisition. Therefore, the future of DTs in biotechnology will likely involve the development of more sophisticated hybrid modeling techniques that can accommodate the inherent complexity of biological systems. In this context, the successful integration of DTs in biotechnology will depend on developing flexible, adaptable frameworks that can evolve alongside technological advancements and regulatory changes.

IoBNT-Driven Solutions to Multiscale DT Challenges

In particular, the modeling of particle breakage mechanics illustrates these challenges vividly. Studies have demonstrated that replicating the complex interactions and conditions at nano and micro scales is exceedingly difficult, often resulting in significant discrepancies between simulated behaviors and real-world outcomes [86]. Furthermore, the high computational demands required to model these intricate processes add another layer of complexity, making the validation and implementation of these DTs resource-intensive. The variability in material properties at these scales further complicates the situation, as it increases the difficulty of creating accurate predictive models. Thus, the development of adaptable modeling approaches that can account for these variabilities is essential for advancing DT applications in this domain [86]. In addition, biomanufacturing has faced its own set of challenges when implementing DTs at the micro and nano scales. The inherent complexity of biological systems, coupled with the variability of process parameters, makes high-fidelity DT development particularly

demanding. This is further complicated by the lack of real-time data integration, which is crucial for accurate modeling and control. The absence of adaptable frameworks that can accommodate different scales and systems has created barriers to ensuring reproducibility and robust operation in biomanufacturing processes [69]. For instance, the integration of multiscale information, necessary for developing precise predictive models, is hampered by the need for significant computational resources and standardized validation protocols [69].

To address some of these challenges, IoBNT has been proposed as a transformative framework for the digitalization and automation of biotechnology. IoBNT enables real-time monitoring and precise control at the molecular level, which is particularly advantageous for advancing the capabilities of DTs in micro and nano-scale applications [87]. By integrating nano-sensors and actuators within biological environments, IoBNT facilitates seamless communication through biological channels, such as blood vessels, allowing for innovative applications in early disease detection and personalized medicine. Nevertheless, integrating IoBNT with existing systems comes with new challenges. Ensuring precise molecular communication between devices is complex and can be significantly affected by environmental factors like temperature and pH, which disrupt communication efficiency and data reliability [88]. These disruptions pose significant challenges for the effective functioning of DTs, as consistent and accurate data are critical for maintaining the integrity of these models. Therefore, developing new security protocols that can protect biological data without compromising the functionality of IoBNT systems is essential for their broader adoption [88]. Addressing these concerns is crucial, as failure to do so could hinder the integration of IoBNT into DT frameworks and limit their potential benefits in healthcare and biomanufacturing.

IoBNT represents an advanced evolution of traditional IoT, adapted for highly detailed real-time monitoring in biological and nanoscale environments [8]. Unlike conventional sensors, IoBNT uses bio-nanotechnology to measure key biochemical and microbial signals at a micro level, capturing intricate aspects of microbial growth dynamics, substrate concentration changes, and other relevant features with precision [89]. By transmitting biochemical data in real-time, IoBNT creates a high-resolution view of biological processes, enabling operators to detect previously unnoticed behaviors. However, despite its accuracy, IoBNT data alone cannot capture every behavior of complex biological systems and the inherent variability and interconnected dynamics require more sophisticated interpretation methods [90].

Robust DT Architectures Using PINNs in Variable Biological Environments

Translating this data within traditional neural networks has proven inefficient, as conventional networks lack the capacity to incorporate the underlying physical and biochemical principles [91]. This computational gap limits predictive capabilities, highlighting the need for an approach that integrates accurate measurement with domain-specific knowledge to interpret and predict system behaviors effectively. PINNs offer a powerful solution by embedding physical and biochemical laws directly into predictive models, effectively addressing the limitations of traditional neural networks in capturing complex bio-

logical data [91, 92]. In digital twinning applications, where continuous and real-time communication is essential, PINNs provide the computational robustness needed to overcome data transmission delays, sensor noise, and incomplete measurements [93]. By incorporating fundamental scientific principles, PINNs enable DTs to interpret and anticipate system behaviors under varying conditions, creating a more resilient model.

Moreover, the application of Process Analytical Technology (PAT) as a key enabler for DTs in continuous biomanufacturing has been extensively investigated [94]. By integrating real-time data and predictive models, DTs optimized process control and quality in biologics production. The benefits of PAT-driven DTs included consistent product quality, reduced costs, and improved scalability through advanced analytics and automation. Nevertheless, challenges such as data acquisition, model accuracy, and the integration of PAT with existing processes persisted due to high variability in bioprocesses and the need for continuous, precise measurements [94]. As an example, a flexible DT framework tailored for the biomanufacturing of Advanced Therapeutic Medicinal Products (ATMPs) was developed, focusing specifically on CAR T cell therapy [95]. This framework facilitated digitalization, monitoring, and management of complex production processes, integrating both manual and automated operations. However, challenges included managing high process complexity, regulatory compliance, and integrating manual tasks with automation, as well as the variability of patient-specific therapies, which posed difficulties for standardization and consistent data acquisition [95].

Furthermore, real-time monitoring and predictive surveillance are essential for optimizing bioprocesses in industries like biotechnology, wastewater treatment, pharmaceuticals, and healthcare [96, 97]. DTs, as virtual replicas of physical systems, enhance this capability by enabling continuous, data-driven simulations of biological processes, thereby allowing operators to predict and respond to changes in real time [31]. This approach not only boosts efficiency but also cuts costs and ensures regulatory compliance. For instance, tracking microbial growth in wastewater or monitoring cell cultures in drug manufacturing can greatly improve process reliability and consistency [57]. However, achieving the full potential of real-time surveillance still faces challenges, especially in accurately extracting critical features of microbial growth, which are inherently complex and variable [98]. Moreover, effective communication is also required to relay granular data from micro-environments back to the main system, a task that traditional IoT systems struggle with due to limitations in sensitivity and data transmission [31, 89]. These constraints often lead to gaps in predictive accuracy, ultimately hampering precise monitoring in such complex environments.

This approach is particularly advantageous in industrial applications, including those involving complex biological systems, where DTs support critical communication and decision-making infrastructure [99]. In such contexts, where variability, nonlinearity, and noise are inherent to biological processes, PINNs offer a robust mechanism for embedding physiological and biochemical knowledge directly into model architectures. By compensating for data gaps and ensuring reliable predictions, PINNs make DTs an ideal platform for precise monitoring, data-backed decision-making, and continuous optimization across both engineered and biological domains.

1.3.3 Decentralized and Biologically-Informed ML Models in Nano-Bio DTs

Advancing DTs for Micro/Nano Applications Through IoBNT-Enabled Systems

The implementation of micro and nano-scale DTs presents numerous challenges, primarily due to the complexities of capturing accurate real-time data and integrating it effectively. At these scales, biological systems exhibit high variability and complex interactions, which significantly complicate the development and validation of robust DT models. This variability, combined with the unpredictable nature of biological processes, leads to difficulties in ensuring the accuracy and consistency of DTs, unlike in larger-scale applications where such challenges are more manageable [100]. Moreover, achieving the necessary precision in data acquisition for micro and nano-scale DTs has proven challenging. Researchers have often encountered difficulties in replicating the delicate conditions required for these systems, as even minor deviations can cause significant disparities between the digital and physical twins. Consequently, this lack of precision reduces the overall fidelity of DTs, undermining their effectiveness in biotechnology applications [101]. Additionally, the absence of standardized protocols for data collection and processing at these scales further complicates matters, as it prevents the establishment of consistent methodologies across different studies and use cases [101].

Despite these hurdles, the potential advantages of incorporating IoBNT into micro and nano-scale DTs are substantial. Moreover, IoBNT could enable advanced biomedical applications, such as targeted drug delivery and automated therapeutic interventions, which are beyond the capabilities of traditional DTs [102]. However, to maximize these benefits, significant advancements in biocyber interfaces and the seamless integration of IoBNT with existing digital networks are needed. Achieving this integration is critical for enabling the real-time data processing and automation necessary for effective DT deployment in biotechnology [102]. Looking ahead, the future of DTs in micro and nano-scale applications will likely depend on the continued development of IoBNT frameworks that can overcome current limitations in data acquisition, integration, and security. Additionally, interdisciplinary collaboration between biologists, engineers, and data scientists will be essential for tackling the complex challenges associated with modeling and controlling biological systems at these scales [103]. By developing more sophisticated and adaptable frameworks, it will be possible to extend the capabilities of DTs beyond their current limitations. Ultimately, overcoming the challenges of micro and nano-scale DT implementation is crucial for realizing the full potential of these technologies in transforming the biotechnology industry.

Existing FL-DT Frameworks in Supporting IoBNT and Real-Time Bio-Modeling

IoT-enabled DTs improve healthcare by replicating human bodies virtually, which enables real-time monitoring, simulation, and personalized treatment. They enhance diagnosis and therapy, especially when combined with generative AI for data augmentation [104]. In glucose-insulin regulation, ML-powered DTs can optimize insulin dosing, reducing risks of hypo- and hyperglycemia. In [36], a hybrid DT framework was developed by integrating FL and PINN to enhance predictive accuracy while

maintaining data confidentiality across distributed stakeholders. The approach demonstrated a potential for improving decision-making and performance monitoring in complex systems. However, its adaptability to IoT ecosystems was not addressed, as FL is employed for multi-client interactions rather than direct integration with IoT-connected assets and real-time data streams. Additionally, its application in healthcare remains unexplored. Moreover, a Federated Multi-agent Deep Reinforcement Learning (F-MADRL) algorithm was developed to enhance energy Management in Multimicrogrid (MMG) systems while preserving data privacy [105]. By integrating a physics-informed reward system and FL, the method improved cost efficiency and self-sufficiency without sharing sensitive energy data. However, this work did not fill critical gaps in the integration of healthcare IoT by introducing a biologically informed, privacy-preserving, and decentralized framework that enables real-time adaptability, data security, and physiological relevance in healthcare systems.

Furthermore, a study explored the use of FL in Industrial IoT to address challenges related to data privacy and communication efficiency in DTs [54]. The researchers applied an asynchronous FL scheme combined with deep reinforcement learning to manage aggregation frequency and clustering. This approach demonstrated superior performance in terms of convergence and energy savings compared to traditional methods. However, managing the computational and communication overheads associated with FL remained a challenge, particularly in ensuring consistent model updates across diverse devices. Privacy concerns due to decentralized data sources also pose significant barriers to the adoption of FL in industrial settings. The study emphasized the need for more robust and efficient FL algorithms that can handle the unique demands of Industrial IoT environments [54].

Recently, the authors in [106] proposed a DT-enabled IoT network for wireless powering of energy-deficient consumer electronics using AP clustering and RF energy harvesting. While effective for smart consumer health applications, the approach lacked integration with the physiological or physical models of the system, limiting its applicability for IoBNT-based healthcare solutions [106]. In addition, a novel nano-scale computing architecture for matrix multiplication using diffusion-based propagation and chemical reactions among compartments, supported by both stochastic and dynamical models, and validated through simulations, was introduced in this work. However, despite its foundational contribution, key gaps remain in deploying it in decentralized networks, particularly in ensuring scalable coordination among distributed Bio-Nano Things (BNTs) [107]. Moreover, the framework lacks deeper integration with the underlying physics of physiological processes at the processing level, which limits its capacity to adaptively model and interpret dynamic biological interactions in real time [107].

Toward Integrated and Biologically Informed DT Architectures

A study developed a Molecular Communication (MC) system within a cylindrical vascular channel by modeling non-Newtonian fluid dynamics and evaluating information molecule transmission using analytical and simulation-based techniques [108]. Although the study provided meaningful insights into how rheological properties affect molecular transport, it did not incorporate these findings within a decentralized IoBNT architecture. Additionally, while the system-level metrics were analyzed thor-

oughly, the framework did not engage with the dynamic physical-biological interplay at the computational level, which limits its applicability in adaptive, real-time processing scenarios essential for physiological monitoring and therapeutic control.

Although various efforts have been made to leverage decentralized learning, PINNs, and IoBNT to address critical healthcare challenges such as diabetes, to the best of our knowledge, no unified framework exists that integrates these state-of-the-art technologies into a cohesive solution. The absence of such integration limits their collective potential in real-world applications. The proposed framework seeks to bridge this gap by providing a biologically aligned, privacy-preserving, and computationally robust architecture capable of compensating for existing limitations and advancing both practical implementations and emerging healthcare technologies. In addition, IoBNT empowers the advancement of personalized and precision medicine by enabling real-time tracking of individual health parameters and responses to treatment [8]. This critical capability allows DTs to simulate physiological responses and model the effects of therapeutic interventions with exceptional accuracy. As a result, treatment plans can be tailored to individual characteristics, improving efficacy and safety. Consequently, the integration of IoBNT and DTs in healthcare offers tremendous potential for optimizing therapy design, implementation, and monitoring in both clinical and remote settings.

1.4 Contributions

1.4.1 An Integrated CNN-FL Framework Using IoBNT for Nano-Bio DTs

To address Research Question 1, we aim to enable scalable, privacy-preserving, and intelligent DT systems by integrating FL and CNN with IoBNT. This combination supports real-time monitoring, heterogeneous data processing, and communication efficiency. Thus, Framework 1 presents a novel integration of DT technology with IoBNT, CNNs, and FL, tailored for biological data processing in biotechnology and healthcare environments. This framework enables laboratories and hospitals to collaboratively analyze biosensor data in real time while maintaining data privacy and reducing reliance on centralized storage. It is particularly suited for micro- and nano-scale biological modeling, such as bacterial systems, and addresses key challenges related to secure data transmission, communication efficiency, and model scalability.

The central hypothesis is that combining IoBNT, CNNs, and FL enhances DT performance for biological systems by improving accuracy, reducing transmission errors, and minimizing bandwidth usage. The framework supports real-time monitoring, provides a user-friendly dashboard, and significantly improves biological data fidelity across decentralized networks.

Key contributions and features of Framework 1 are summarized as follows:

- The framework provides a unified and seamless aggregation, easing data security and privacy management.
- IoBNT can drastically reduces the error rates in biological data transfer, achieving up to 98%

improvement.

- It uniquely reduces the complexities of micro and nano-scale DTs in biotech, especially for bacterial modeling.
- The proposed CNN-FL algorithm extracts critical insights from raw image data, achieving 98.5% accuracy.
- It achieves over 99% bandwidth savings by using FL to avoid central server dataset transfers.
- It features a user-friendly web-based interface for users to monitor DTs of bacteria and microorganisms.

1.4.2 A Unified Multi-Model PINN Framework Leveraging IoBNT for Bioprocess DTs

To address Research Question 2, we integrate PINNs into DT frameworks to enable real-time, scalable, and biologically consistent modeling of complex biosystems. This approach directly tackles challenges such as data sparsity, noise, and sensor communication limits, ensuring more robust, physics-informed insights from limited and noisy biological sensor data. Therefore, Framework 2 introduces a novel approach to digital twinning for systems inherently governed by physical laws, specifically targeting physiological and biological environments. This architecture enables the development of high-fidelity DTs that reflect the intrinsic dynamics of such systems. As a benchmark, Framework 2 was applied to Microbial Growth Concentration (MGC) and Substrate Growth Concentration (SGC) models, both formulated by the Monod equations [109], to evaluate its performance under complex and nonlinear kinetic conditions. The framework includes dedicated modules for extracting, transmitting, preprocessing, and analyzing physics-based data, thereby supporting the generation of accurate and real-time digital representations. It effectively addresses data sparsity and sensor limitations by incorporating nano-scale IoBNT elements, ensuring reliable decision-making in distributed and constrained environments. These capabilities make Framework 2 particularly suitable for industrial applications where predictive accuracy and communication robustness are essential. The core contributions of Framework 2 are summarized as follows:

- We propose a novel multi-model PINN framework integrated with IoBNT for physics-based DTs. This pioneering integration of PINNs and IoBNT improves DTs and, optimizes accuracy, data reliability, and scalability for complex systems.
- We design and advance IoBNT based on the Monod equations to optimize data acquisition and transmission processes. IoBNT specified for Monod equations, enables precise data acquisition and transmission, which enhances efficiency, reliability, and applicability.

- We develop three DNNs embedded within the PINN framework to address challenges related to varying physics and data reliability. Three DNNs are developed within the PINN framework and offer a multi-model architecture with exceptional adaptability to varying physics and data reliability. This novel design ensures compliance with industrial demands by addressing diverse scenarios and maintaining robust performance across applications.
- We propose IoBNT to reduce data transmission errors by up to 98% under challenging operating conditions and establish a robust foundation for future research in DTs of complex processes.

1.4.3 A Decentralized PINN-FL Framework for Glucose-Insulin DTs

To address Research Question 3, we integrate physics-informed neural architectures with FL and bio-nano sensing to develop scalable, real-time, and privacy-aware DT systems. This framework is tailored for modeling dynamic physiological processes such as insulin glucose regulation by capturing underlying system dynamics while preserving data privacy across distributed sources. Accordingly, Framework 3 presents a unified, biologically-informed architecture that IoBNT, PINNs, and FL. This framework is specifically designed to enable real-time, interpretable, and privacy-preserving DTs for physiological modeling. By addressing key limitations in decentralized biological computation and secure medical data handling, Framework 3 establishes a robust foundation for next-generation digital health systems. The primary innovations and contributions of this framework are summarized below:

- We propose a novel DT framework that integrates IoBNT, PINNs, and FL. This also marks the first federated AI-based approach for real-time glucose-insulin digital twinning.
- We redesign the PINN optimization process to support decentralized FL across multiple IoBNT devices. A novel Federated PINN algorithm is introduced to distribute training, enforce glucose-insulin Ordinary Differential Equations (ODE) constraints, and ensure computational efficiency by distributing the workload across multiple devices. The proposed FL framework preserves patient privacy by avoiding raw data transmission and establishes a compliant, secure foundation for next-generation digital healthcare.
- Our framework employs ML informed by physics to ensure that the glucose-insulin predictions follow biological laws, improving interpretability. An IoBNT-based real-time glucose monitoring pipeline is integrated for continuously updating the DT.
- We introduce an approach that enhances explainability in AI-based diabetes management by embedding mechanistic glucose-insulin ODE constraints into the learning process.
- We perform intensive experiments to demonstrate that the proposed federated framework substantially reduces computational overhead while preserving high prediction accuracy. This efficiency enables real-time decision-making and supports continuous learning within IoBNT-enabled digital healthcare systems.

The three contributions represent an evolutionary pathway in advancing DT systems for biological and physiological domains. Framework 1 laid the foundation by combining CNNs and Federated Learning with IoBNT to enable scalable, privacy-preserving DTs for micro- and nano-scale biological processes. Building on this, Framework 2 extended the scope by embedding PINNs into IoBNT-based DTs, ensuring consistency with governing physical laws and addressing challenges of noisy, sparse data. Framework 3 then unified the advances by integrating PINNs and FL within IoBNT to tackle real-time, decentralized physiological modeling. Together, they evolve from general biosystem modeling toward domain-specific, interpretable, and privacy-aware healthcare DTs.

While interconnected, the three frameworks target distinct problem domains and technical emphases. Framework 1 highlights efficiency and privacy in bacterial DTs by using CNN-FL integration, which achieves both high-accuracy data aggregation and significant communication savings. Framework 2 moves the focus toward physical realism by embedding multi-model PINNs aligned with Monod equations, thereby strengthening fidelity under sparse and noisy sensor conditions and offering particular advantages for industrial-scale bioprocesses. In contrast, Framework 3 concentrates on physiological modeling in healthcare, integrating federated PINNs to ensure privacy while enforcing glucose–insulin ODE constraints to enhance interpretability. Each framework therefore differs in scope, application, and innovation strategy.

1.5 Thesis Organization

This thesis is organized into five chapters. Chapter 1 introduces the research background, motivations, literature review, and outlines the key contributions. Chapter 2 presents a federated CNN framework integrated with IoBNT for bacterial digital twinning. Chapter 3 introduces a multi-model PINN-based framework for microbial growth and substrate optimization. Chapter 4 develops a hybrid physics-informed and federated learning approach for glucose-insulin DTs. Chapter 5 concludes the thesis and outlines future research directions, including improvements in multi-physics modeling, communication efficiency, and integration with emerging technologies.

Chapter 2

Advancing Biological DTs: Integrating IoBNT, CNN, and Federated Learning

2.1 Introduction

This chapter introduces a novel framework that integrates DT technology with IoBNT, specifically designed for applications in the biotechnology industry. This framework bridges the gap between DTs and IoBNT by incorporating advanced deep learning techniques. The system enables laboratories and hospitals (clients) to collaboratively process biological data in real time, improving data security, privacy, and accuracy without relying on central data storage. The approach also reduces complexities in creating DTs at micro and nano scales, especially for bacterial modeling, and achieves substantial bandwidth savings while providing a user-friendly dashboard for monitoring biological processes. Accordingly, IoBNT devices, specifically sensors, handle data extraction and transmission, collecting information and sending it to each client's local server within the FL framework. Thus, this approach not only addresses integration challenges but also has the potential to transform the biotechnology industry. Moreover, this framework provides several key features for extracting, transferring, preparing, and processing biological data to create reliable and real-time DTs of bacteria in biotechnology industries.

In summary, the framework offers a unified and seamless aggregation process that simplifies data security and privacy management. IoBNT significantly reduces error rates in biological data transmission, with improvements reaching up to 98%. It also lowers the complexity of modeling micro- and nano-scale DTs, particularly in biotechnology applications such as bacterial systems. The proposed CNN-FL algorithm effectively extracts critical insights from raw image data, achieving an accuracy of 98.5%. Furthermore, the use of FL eliminates the need for centralized server data transfers, resulting in over 99% bandwidth savings. To enhance usability, the framework includes a web-based dashboard that allows users to monitor DTs of bacteria and other microorganisms in real time.

The structure of the chapter is as follows. Section 2.2 provides a comprehensive description of the system model, organized into four key components: physical twins, IoBNTs, CNN integrated with FL, and the DT dashboard. Section 2.3 presents the proposed methods. Section 2.4 outlines the simulation

settings and performance metrics. Section 2.5 offers a thorough analysis of the findings, highlighting their broader significance. Finally, Section 2.6 discusses the main contributions of the work and suggests directions for future research.

2.2 System Model

Fig. 2.1 illustrates the architecture of this framework, which consists of four sections: physical twins, IoBNTs, CNN-FL, and the DT dashboard. A physical twin is the actual asset, human, object, creature, or any entity that serves as the real-world counterpart for creating its corresponding DT [110, 111]. In this work, the term physical twins specifically refers to the actual bacteria being studied to evaluate the framework. Moreover, Fig. 2.1A clearly depicts the physical presence of bacteria in laboratories and hospitals, showcasing real-world samples.

As we delve deeper into the framework, Fig. 2.1B highlights the role of IoBNT in extracting and transmitting data efficiently. Furthermore, the deployment of CNN-FL within the framework is shown in Fig. 2.1C, demonstrating its role in processing and analysis. Finally, Fig. 2.1D presents a user-friendly dashboard that displays DTs to users, accessible via a web interface or VR headset. The proposed framework aims to compensate for the limitations of integrating DTs with IoBNT for biological systems by utilizing advanced deep learning algorithms, including FL and CNN. Specifically, in Fig. 2.1C, the client refers to laboratories within the FL network, representing entities such as organizations that are part of the FL algorithm's collaborative learning process [18]. Moreover, we use IoBNT specifically to denote sensors engaged in data extraction and transmission, which collect and send data to the local server of each client within the FL framework.

Building on the framework's components, the setup for CNNs involves configuring them to achieve precise pattern recognition and advanced image processing, which is crucial for modeling bacterial images within DTs. Moreover, we employ FL across a network of IoBNT devices integrated with CNN capabilities, enabling localized data processing on each device. This approach boosts privacy and reduces the need for data transfer. For evaluation, 10% of the dataset is allocated for testing and 90% for training, with both CNN-FL and CNN models using identical datasets. In the CNN-FL framework, the training data is evenly distributed among three clients, while the test data assesses the global model's performance [15]. Moreover, the CNN-FL model trains for 100 rounds, with the CNN trained from scratch to ensure alignment with our dataset's characteristics. Consequently, data from multiple IoBNT devices trains the CNN models, refining their accuracy in identifying bacterial behaviors. Therefore, the integration of CNN-FL with IoBNT melds nano-scale biological data analysis with decentralized data processing, achieving unprecedented precision and robustness.

DTs, which are sophisticated virtual counterparts of physical entities or systems, simulate real-time behaviors [81]. In biotechnology and biomanufacturing, DTs are extensively used for the design, optimization, monitoring, and control of bioprocesses and bioproducts [112, 113, 114]. To develop effective DTs for biotechnological applications, a systematic methodology incorporating both data-driven and model-driven approaches is proposed. These methods accurately simulate complex biolog-

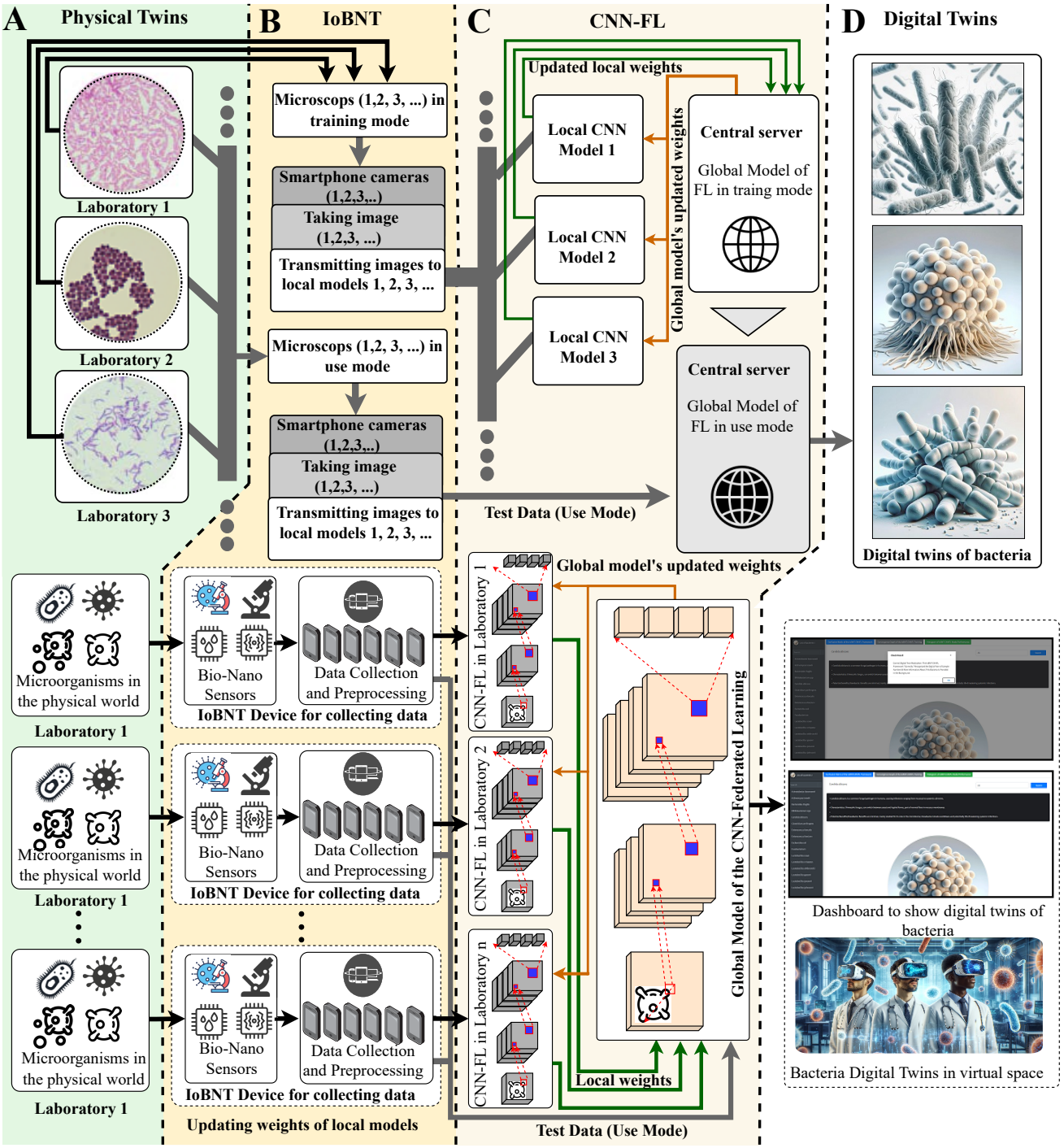

Figure 2.1: The proposed framework for creating bacterial DTs using CNN, FL, and IoBNT technology; A: Real bacteria samples are observed and analyzed under a microscope, representing the physical counterparts of the DTs; B: IoBNT devices capture microscopic images of bacteria and transmit this data to local CNN models for initial processing and analysis; C: The FL framework collects and combines the weights from multiple local CNN models, creating a robust global model without sharing raw data, thus preserving privacy; D: An intuitive dashboard enables users to observe and interact with the DTs of bacteria in real time, accessible via a monitor or VR headset through an online HTML interface.

ical systems, thus improving the optimization of producing biomaterials, drugs, and vaccines. Firstly, high-quality data collection initiates the design of DTs, which are then used to construct detailed mod-

els of target bioprocesses or bioproducts [115]. Subsequently, iterative testing in virtual environments validates and refines these models, ensuring reliable replication of physical behaviors. This process not only accelerates deployment but also reduces the time-to-market for new bioproducts [77, 1, 2]. Furthermore, DTs simulate various scenarios, optimizing processes in a controlled digital space. For example, DTs model drug interactions with biological systems, predicting outcomes and optimizing formulations without extensive trials. They also simulate disease progression and treatment responses for personalized medicine. In biomanufacturing, DTs optimize biological processes for quality and efficiency. Additionally, they model ecosystems and microbiomes to predict responses to environmental changes and simulate plant or animal growth in agriculture to optimize yields and resource use. Hence, by identifying potential issues and testing solutions without physical trials, this approach speeds up development and improves product accuracy and reliability.

In the biopharmaceutical sector, DTs play a crucial role in optimizing cell fermentation processes and managing supply chains, providing a platform for precise modifications to enhance efficiency and foster innovation [112]. Additionally, DTs integrate real-time data from physical systems, allowing continuous monitoring and adaptive control, thereby fine-tuning processes for optimal performance. However, managing and analyzing large datasets and developing complex models require substantial computational resources and specialized expertise, which are crucial for the efficacy of DTs in biotechnology. Finally, ensuring model reliability and accuracy is essential, as they must continuously adapt to and predict the behavior of the physical entities they represent.

Optimizing DT performance involves real-time monitoring, data processing, and model refinement [113, 81]. To achieve this, a robust infrastructure with high-resolution sensors and data acquisition systems is essential for the continuous collection of data on bioprocesses and bioproducts [115]. Furthermore, advanced computational systems are required to process these vast data streams to extract actionable insights, which are crucial for timely anomaly detection and maintaining process stability [77]. Therefore, it is imperative to utilize high-performance computing and sophisticated algorithms for real-time data analysis. Moreover, AI techniques play a pivotal role in processing and interpreting data, thereby optimizing bioprocesses and predicting outcomes. To replicate biological entities under various conditions, it is necessary to develop dynamic models. Consequently, iterative testing and refinement are essential to ensure accurate predictions, identifying potential issues before they affect actual processes. By integrating CNNs with FL and IoBNT, we can significantly enhance DT capabilities. Specifically, CNN-FL enables decentralized learning for continuous model updates [15], while IoBNT ensures real-time interaction between digital and physical domains, thereby improving model accuracy.

In addition, continuously adjusting DT models based on real-time data and feedback is critical. Regularly reviewing and updating models to integrate new data enhances efficiency, safety, and process consistency. Accordingly, in our proposed framework, we leverage these infrastructures and technologies to optimize DT performance. This optimization includes accurate real-time data extraction, effective training of deep learning models for processing biological data, efficient bandwidth usage for transmitting data between physical twins and DTs, and addressing security and privacy concerns.

2.3 The Proposed CNN-FL Framework Using IoBNT for DTs

CNNs are a class of deep neural networks known for their efficacy in visual imagery analysis [60]. CNNs automate feature extraction, which enhances efficiency and accuracy in identifying and extracting patterns from data. They have Advanced fields such as image classification and object detection, playing a pivotal role in the advancement of AI.

A typical CNN structure comprises the following components:

1. Convolutional Layer: This layer applies convolutional operations to the input data to generate feature maps.

$$\mathbf{O}_{ij}^{k} = \sum_{m=1}^{M} \sum_{n=1}^{N} \mathbf{I}_{(i+m-1)(j+n-1)} \cdot \mathbf{K}_{mn}^{k} + b^{k}, \tag{2.1}$$

where $\mathbf{O}_{ij}^{k}$ is the output feature map at position (i, j) for the k-th filter, $\mathbf{I}$ represents the input image, $\mathbf{K}^{k}$ denotes the k-th convolution kernel (a filter that slides over the input image), and b^{k} is the bias term added to the convolution result.

Equation (1) performs the convolution operation, which involves element-wise multiplication of the input image patch with the filter, summing the results, and adding a bias term.

2. Activation Function: The activation function, typically the Rectified Linear Unit (ReLU), is applied element-wise to introduce non-linearity into the model.

$$\mathbf{A}_{ij}^{k} = \max(0, \mathbf{O}_{ij}^{k}), \tag{2.2}$$

where $\mathbf{A}_{ij}^{k}$ is the activation output at position (i, j) for the k-th filter.

The ReLU activation function outputs the input directly if it is positive; otherwise, it outputs zero. This helps in introducing non-linearity and allows the network to learn complex patterns.

3. Pooling Layer: Pooling layers reduce the spatial dimensions of the feature maps, which can reduce computational load and controlling overfitting. In max pooling:

$$\mathbf{P}_{ij}^{k} = \max_{(m,n)\in\mathcal{P}} \mathbf{A}_{(i+m)(j+n)}^{k}, \tag{2.3}$$

where $\mathbf{P}_{ij}^{k}$ is the pooled output at position (i, j) for the k-th filter, and $\mathcal{P}$ is the pooling window.

Max pooling selects the maximum value from the feature map patch covered by the pooling window. This operation helps in downsampling the feature map, reducing its dimensions while retaining important features.

4. Fully Connected Layer: This layer maps the extracted features to the output classes.

$$\mathbf{z} = \mathbf{W}\mathbf{h} + \mathbf{b}, \tag{2.4}$$

where $\mathbf{z}$ is the output vector (e.g., class scores), $\mathbf{W}$ is the weight matrix, $\mathbf{h}$ is the flattened input feature map, and $\mathbf{b}$ is the bias vector.

The fully connected layer multiplies the flattened input feature map by the weight matrix, adds the

bias vector, and outputs the result. This operation is similar to a traditional neural network layer and is used to make final predictions.

To enhance flexibility and scalability for embedded vision applications, we integrate MobileNetV2 [116] into our framework. MobileNetV2 is designed for efficient image classification on mobile and embedded vision applications, leveraging inverted residuals and linear bottlenecks. FL is a cutting-edge approach to machine learning that enables multiple participants, referred to as clients or workers, to collaboratively train a model while keeping their data decentralized and private [18, 17]. This technique contrasts with traditional centralized CNN methods where data is pooled into a single location [15]. In FL, each participant trains its model based on its local data and shares model updates, not the data itself, with a global server. The server consolidates these updates to enhance the overall model, preserving privacy and security while leveraging distributed data sources.

The CNN-FL integration involves the following steps:

1. Local Model Training: Each client i trains its local model $\mathbf{w}_i$ using its own data $\mathcal{D}_i$. The local update rule is

$$\mathbf{w}_i^{(t+1)} = \mathbf{w}_i^{(t)} - \eta \nabla \mathcal{L}_i(\mathbf{w}_i^{(t)}; \mathcal{D}_i), \tag{2.5}$$

where $\mathbf{w}_i^{(t+1)}$ is the updated local model weights at iteration $t+1$, $\mathbf{w}_i^{(t)}$ is the local model weights at iteration t, η is the learning rate, and $\nabla \mathcal{L}_i(\mathbf{w}_i^{(t)}; \mathcal{D}_i)$ is the gradient of the local loss function $\mathcal{L}_i$ with respect to the model weights, computed using the local data $\mathcal{D}_i$.

This equation updates the local model weights by taking a step in the direction of the negative gradient of the loss function, scaled by the learning rate.

2. Global Model Aggregation: The central server aggregates the local models from all clients to update the global model $\mathbf{w}$:

$$\mathbf{w}^{(t+1)} = \sum_{i=1}^{N} \frac{n_i}{n} \mathbf{w}_i^{(t+1)}, \tag{2.6}$$

where $\mathbf{w}^{(t+1)}$ is the updated global model weights at iteration $t+1$, N is the total number of clients, and n_i is the number of data samples on client i. $n = \sum_{i=1}^{N} n_i$ is the total number of data samples across all clients, and $\mathbf{w}_i^{(t+1)}$ is the updated local model weights for client i at iteration $t+1$.

The expression in (6) performs a weighted averaging of the local model weights, where the weight for each client is proportional to the number of data points it holds.

3. Federated Averaging (FedAvg): The Federated Averaging algorithm aggregates the local model updates using weighted averaging:

$$\mathbf{w}^{(t+1)} = \mathbf{w}^{(t)} - \eta \sum_{i=1}^{N} \frac{n_i}{n} \left(\mathbf{w}_i^{(t+1)} - \mathbf{w}^{(t)} \right). \tag{2.7}$$

This equation adjusts the global model weights based on the weighted difference between the local model updates and the current global model weights.

When CNNs are integrated with FL, they leverage the power of CNNs to process and learn from image data in a privacy-preserving manner across distributed datasets [15]. This combination is partic-

ularly powerful for applications where data privacy is paramount and where training data is naturally distributed across multiple locations, such as in medical imaging analysis across different hospitals. The proposed CNN-FL algorithm is represented as follows:

1. Local Model Update: Each client i trains a local CNN model $\mathbf{w}_i^{(t+1)}$ using its own subset of data. The local loss function $\mathcal{L}_i$ is typically a cross-entropy loss for classification tasks [117]:

$$\mathcal{L}_i(\mathbf{w}_i) = -\frac{1}{|\mathcal{D}_i|} \sum_{(x,y)\in\mathcal{D}_i} y \log f_{\mathbf{w}_i}(x), \tag{2.8}$$

where $\mathcal{L}_i(\mathbf{w}_i)$ is the local loss function for client i, $|\mathcal{D}_i|$ is the size of the local dataset $\mathcal{D}_i$, x and y are the input and label, respectively, and $f_{\mathbf{w}_i}(x)$ is the prediction of the CNN with weights $\mathbf{w}_i$.

The expression in (8) calculates the cross-entropy loss, which measures the difference between the predicted probabilities and the actual labels.

2. Global Model Update: The global model $\mathbf{w}^{(t+1)}$ is updated by averaging the local models:

$$\mathbf{w}^{(t+1)} = \sum_{i=1}^{N} \frac{n_i}{n} \mathbf{w}_i^{(t+1)}. \tag{2.9}$$

The expression in (9) is the same as previously described, performing a weighted averaging of the local model weights to update the global model.

3. Objective Function: The overall objective function for the CNN-FL framework can be defined as the weighted sum of the local loss functions:

$$\mathcal{L}(\mathbf{w}) = \sum_{i=1}^{N} \frac{n_i}{n} \mathcal{L}_i(\mathbf{w}), \tag{2.10}$$

where $\mathcal{L}(\mathbf{w})$ is the overall objective function, $\mathcal{L}_i(\mathbf{w})$ is the local loss function for client i, n_i is the number of data points on client i, and $n = \sum_{i=1}^{N} n_i$ is the total number of data points across all clients.

This equation defines the overall objective as the weighted sum of the local loss functions, ensuring that each client's contribution is proportional to the size of its dataset.

4. Communication and Synchronization: After each local training epoch, clients communicate their updated models to the central server, which synchronizes the global model. This process continues iteratively until the model converges.

By integrating CNNs with FL, the framework leverages the strengths of both technologies: the powerful feature extraction capabilities of CNNs and the privacy-preserving distributed learning approach of FL. This combination is particularly effective for applications requiring secure and distributed data analysis, such as medical imaging.

2.4 Simulation Settings and Evaluation Metrics

We use Flower (FLWR) with various adjustments in the proposed framework to enhance customization and adaptability in our framework [118]. Such embedded characteristics meet diverse application requirements while maintaining flexibility. Flower facilitates the orchestration of multiple clients, each training on a portion of the dataset without requiring centralized data storage, thus ensuring data privacy and compliance with distributed data policies. The clients, configured with an equal distribution of training and validation images, independently train their models using a consistent architecture. Each client trains for one epoch per round and transfers its model weights to a central server. Flower's server-side functionality aggregates these weights using a weighted average approach, ensuring that each client's contribution is proportional to the size of its dataset. This method, combined with the flexibility and scalability of the Flower, enables efficient model training across distributed nodes while minimizing communication overhead and preserving data security.

IoBNT combines nanotechnology, biotechnology, and information technology to create interconnected networks of biological and nano-engineered devices [8, 119]. This methodology details the systematic steps for developing and implementing IoBNT systems, which can transform biotechnology applications in healthcare and environmental monitoring. The development process begins with designing and fabricating molecular sensors, actuators, and miniature computational components capable of interacting with biological systems at cellular and molecular levels [69]. Biocompatible materials ensure the seamless integration of these devices within biological environments. IoBNT devices are embedded to monitor and interact with biological entities in real-time, enabled to collect, process, and transmit biological data efficiently through advanced interfaces.

IoBNT technologies transform medical diagnostics and treatment in healthcare, providing highly personalized medical interventions. Real-time data collected from IoBNT devices fosters personalized medicine by enabling precise monitoring of patient health conditions and timely treatment adjustments [119, 82]. In environmental biotechnology, IoBNT devices offer unmatched sensitivity and specificity for detecting pollutants and pathogens, facilitating effective environmental monitoring and management. As IoBNT technologies advance, they will enable more sophisticated integration of biological and digital systems, leading to breakthroughs in diagnostics, environmental management, and personalized healthcare [80]. This evolution promises to enhance the accuracy and responsiveness of biotechnological applications, ultimately driving innovation and improving quality of life across diverse fields.

2.4.1 Metrics and Measurement for Evaluating Performance

In this work, several key metrics are used to evaluate the performance of our classification models, focusing on accuracy, precision, recall, and the F1-score [120]. These metrics provide a comprehensive assessment of the model's effectiveness in making accurate predictions and handling class imbalances.

Accuracy is a measure of how often the classifier makes correct predictions. It is the ratio of the

number of correct predictions to the total number of predictions.

$$\text{Accuracy} = \frac{\text{Number of Correct Predictions}}{\text{Total Number of Predictions}}. \tag{2.11}$$

Precision quantifies the accuracy of positive predictions. It is the ratio of true positive predictions to the total number of positive predictions, including both true positives and false positives.

$$\text{Precision} = \frac{\text{True Positives}}{\text{True Positives} + \text{False Positives}}. \tag{2.12}$$

Recall, also known as sensitivity, measures the ability of the classifier to correctly identify all actual positive instances. It is the ratio of true positive predictions to the total number of actual positive instances, including both true positives and false negatives.

$$\text{Recall} = \frac{\text{True Positives}}{\text{True Positives} + \text{False Negatives}}. \tag{2.13}$$

F1-score is the harmonic mean of precision and recall, providing a single metric that balances both metrics. It is especially useful for evaluating classifiers on imbalanced datasets, where it is important to consider both false positives and false negatives.

$$\text{F1-score} = 2 \times \frac{\text{Precision} \times \text{Recall}}{\text{Precision} + \text{Recall}}. \tag{2.14}$$

The F1-score offers a balanced view of the model's performance, considering both precision and recall, making it a comprehensive metric for evaluating the effectiveness of a classifier in identifying true positive instances while minimizing errors.

2.4.2 Dataset Preparation

The dataset used in this study was obtained from a previously published study in Elsevier [121], ensuring its peer-reviewed validation. It comprises 2033 RGB images of bacteria collected from blood, urine, and skin samples of patients. Following pure culture, the bacteria were stained using the Gram method, and species identification was conducted by laboratory experts. The images were captured using a Nikon E200 microscope equipped with a 100x objective lens. Importantly, no data augmentation techniques were applied to this dataset to maintain its original characteristics. To avoid bias in the analysis, the number of images representing each species was balanced. The preprocessing of this dataset involved several crucial steps to ensure the images were prepared correctly for the machine learning framework. First, each image was normalized, which involved scaling the pixel values to a range between 0 and 1, making the data easier for the neural network to process. Additionally, the images were resized to a standard dimension of 224x224 pixels, ensuring consistency in input size.

Next, the normalized and resized images were paired with their respective labels, representing different bacterial species, so that the machine learning model could associate the images with their correct

categories. The data was then divided into batches to facilitate efficient processing during training, validation, and testing. During training, the batches were shuffled to prevent the model from learning a specific sequence of the images. Post-prediction, the batched data was unwrapped, and the predicted labels were converted from numerical values back to their corresponding class names, making the results easier to interpret. The dataset was split with 90% used for training and 10% for testing. In the FL setup, the dataset was evenly distributed among clients. Each client trained its model locally on its subset of data and sent updates to the central server. Batches were created for efficient processing, and early stopping was employed during training to avoid overfitting. After training, the model was evaluated on the independent test dataset, ensuring it was tested on unseen data for unbiased performance assessment. Table 2.1 provides an overview of the number of images collected for each of the 33 bacteria species used in training the proposed framework.

2.4.3 Simulation Setting

The proposed architecture leverages MobileNetV2, a lightweight CNN, as the core model to address the unique computational constraints of IoBNT devices. This CNN backbone is initialized with weights pre-trained on ImageNet to maximize transfer learning benefits, enhancing feature extraction while reducing training time. Following the MobileNetV2 layers, a Global Average Pooling layer compresses spatial dimensions, facilitating efficient aggregation of feature maps. This pooling layer connects to a dense layer with 33 softmax-activated units, allowing for the classification of 33 distinct classes. Such a streamlined architecture ensures high accuracy in feature extraction with minimal trainable parameters, making it suitable for real-time deployment in resource-limited IoBNT environments. Each learning cycle involves localized training of CNN models on individual client devices, an essential component of FL where data remains on the device, thus enhancing data privacy and security. For training efficiency and stability, a batch size of 32 and an input resolution of 224x224 pixels are used, while a learning rate of 5×10^{-5} is carefully chosen to balance convergence speed and generalization. To mitigate overfitting, early stopping with a patience threshold of three epochs monitors validation loss trends, halting training if improvement plateaus.

After local training, updated model weights are transmitted to a central server where Federated Averaging (FedAvg) aggregates these updates. FedAvg, a weighted averaging technique, accounts for the number of data samples per client, thus allowing a more accurate and representative global model that reflects data heterogeneity across clients. Reproducibility is crucial in FL, especially for IoBNT applications with non-deterministic edge devices. Therefore, random seeds for key libraries, including NumPy, TensorFlow, and Python's random library, are uniformly set across clients and the server, ensuring consistency in data splits, model initialization, and other stochastic processes. The local models employ the categorical cross-entropy loss function to optimize multi-class classification, combined with the Adam optimizer to balance computational efficiency and model convergence. Data handling is facilitated by TensorFlow's Dataset API, which not only manages data batching and loading but also implements techniques such as shuffling and parallel loading, thereby enhancing computational efficiency

Table 2.1: The number of images within each of the 33 bacteria categories.

No.	Bacteria Species	Collected Data
1	Acinetobacter baumannii	60
2	Actinomyces israelii	67
3	Bacteroides fragilis	65
4	Bifidobacterium spp	64
5	Candida albicans	62
6	Clostridium perfringens	62
7	Enterococcus faecalis	60
8	Enterococcus faecium	57
9	Escherichia coli	59
10	Fusobacterium	62
11	Lactobacillus casei	60
12	Lactobacillus crispatus	57
13	Lactobacillus delbrueckii	59
14	Lactobacillus gasseri	61
15	Lactobacillus jensenii	66
16	Lactobacillus johnsonii	61
17	Lactobacillus paracasei	60
18	Lactobacillus plantarum	61
19	Lactobacillus reuteri	60
20	Lactobacillus rhamnosus	60
21	Lactobacillus salivarius	60
22	Listeria monocytogenes	63
23	Micrococcus spp	63
24	Neisseria gonorrhoeae	69
25	Porphyromonas gingivalis	65
26	Propionibacterium acnes	61
27	Proteus	60
28	Pseudomonas aeruginosa	63
29	Staphylococcus aureus	64
30	Staphylococcus epidermidis	59
31	Staphylococcus saprophyticus	60
32	Streptococcus agalactiae	65
33	Veillonella	58
	Total	**2033**

during each training cycle. For data preprocessing, images undergo normalization to standardize pixel intensity ranges, optimizing inputs for the MobileNetV2 architecture. Resizing is applied to align with the CNN's input dimensions, ensuring that each image adheres to the 224x224 pixel resolution required by the model. The normalization of input data not only reduces potential biases but also aligns with best practices in deep learning, where standardized input distributions improve convergence rates.

In this FL framework, the FedAvg strategy is pivotal, as it enables a decentralized yet unified model that benefits from diverse client data distributions. By averaging weights proportionally to each client's data volume, FedAvg maintains a balanced representation of heterogeneous data sources, which is particularly advantageous for IoBNT applications where each client may capture unique biological or environmental information. Consequently, the global model achieves improved generalization, leveraging insights from localized data without compromising privacy, a key consideration in medical or sensitive applications within the IoBNT ecosystem. This FL setup not only optimizes the model's performance across diverse data but also maintains privacy and data integrity, making it a robust choice for real-time IoBNT deployments.

Furthermore, to address the concern of overfitting, several techniques were implemented in our framework. First, we applied early stopping to halt training when validation accuracy plateaued, preventing the model from over-learning. Additionally, dropout layers were used for regularization, randomly deactivating neurons during training to improve generalization. We also performed cross-validation by partitioning the dataset, which ensured that the model was tested on different data subsets, enhancing its ability to generalize. Furthermore, our FL approach, where the model trains across multiple clients with varied data subsets, further helped to avoid overfitting and improve robustness to unseen data.

2.5 Simulation Results

2.5.1 Convergence Rate

In a centralized CNN approach, the central server is responsible for processing the entire dataset, leading to significant computational bottlenecks and inefficiencies. For example, a dataset consisting of 2033 RGB images, each at a resolution of 224×224 pixels, equates to roughly 304 million pixels in total. This extensive data load can cause potential delays and increase server resource consumption, thereby slowing down both training and inference processes. Centralized systems often suffer from latency and inefficiencies due to the need to process all data centrally, resulting in slower updates and less precise real-time analysis. Additionally, the requirement to transfer all data to a central location consumes substantial bandwidth and raises significant privacy concerns. In a centralized CNN setup, the server handles 100% of the data, further exacerbating processing delays and creating computational bottlenecks.

In contrast, our framework, equipped with CNN-FL, effectively distributes the computational load across multiple clients, mitigating the challenges associated with centralized data processing. In a 3-

client setup, each client handles approximately 678 images, significantly reducing the overall burden on any single server and leading to more efficient processing. This decentralized approach enables more responsive and accurate updates for DTs by allowing real-time data integration from multiple sources. Our proposed framework demonstrates significant improvements in speed of training compared to traditional centralized CNN models. The results illustrate a remarkable rapid convergence in training using our CNN-FL framework, significantly outperforming traditional centralized CNN approaches. The performance evaluation depicted in Fig. 2.2 offers a comprehensive comparison of different configurations. Fig. 2.2A shows a very inefficient training accuracy convergence, taking 120 rounds for the centralized CNN model to stabilize. In contrast, Fig. 2.2E and Fig. 2.2I demonstrate a significant improvement, with training accuracy convergence achieved in just 40 rounds. This dramatic enhancement highlights the efficiency of the proposed configurations in accelerating the training process.

The CNN-FL framework with 2 and 3 clients (Fig. 2.2E and Fig. 2.2I) achieves 95% accuracy within the first 20 rounds, compared to the centralized CNN model which requires over 110 epochs to reach the same level of accuracy (Fig. 2.2A). Moreover, our framework attains over 98% accuracy in only 40 rounds, whereas centralized CNNs need 120 epochs for similar results. This dramatic reduction in training rounds underscores the effectiveness of our optimization strategies, enabling faster deployment and iteration of models across multiple laboratories. The efficiency gains of the CNN-FL framework are further highlighted through the analysis of convergence training graphs. The logarithmic perspective of the convergence training graph for the centralized CNN (Fig. 2.2B) reveals an inefficient training process, with prolonged stabilization times. In contrast, Fig. 2.2F and Fig. 2.2J illustrate the fast and efficient convergence of our CNN-FL framework. These graphs provide a clear visualization of the efficiency gains achieved through our proposed framework, demonstrating a significant reduction in the number of training rounds required to achieve high accuracy.

Accordingly, the convergence training graph of loss for the traditional CNN model (Fig. 2.2C) shows slower stabilization compared to the CNN-FL framework with 2 and 3 clients (Fig. 2.2G and Fig. 2.2K). Additionally, the logarithmic perspective of the convergence training loss graph for the centralized CNN (Fig. 2.2D) and the proposed CNN-FL framework with 2 and 3 clients (Fig. 2.2H and Fig. 2.2L) highlights the efficiency of our approach. This comprehensive analysis underscores the superior performance of the CNN-FL framework in optimizing convergence speed and accuracy. The primary reason behind the improvements observed in both training speed and accuracy lies in the decentralized nature of the framework, which distributes the computational load across multiple clients. This alleviates the bottlenecks and inefficiencies commonly seen in centralized systems, where the central server must process the entire dataset.

By allowing each client to handle a portion of the dataset, the framework significantly reduces the strain on any single server, leading to faster convergence, as demonstrated in the performance evaluation (Fig. 2). The convergence results, with the CNN-FL model achieving 95% accuracy in just 20 rounds and over 98% accuracy in 40 rounds, are a direct consequence of distributing the learning across multiple clients. This result was expected, as FL allows each client to train on its local data while only transmitting model updates rather than the entire dataset. This approach preserves data privacy and

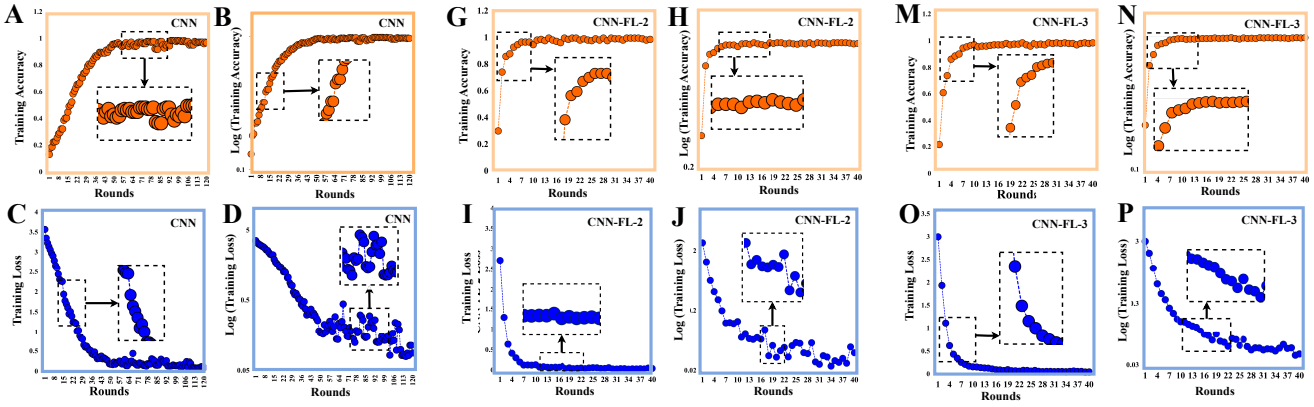

Figure 2.2: Performance evaluation of the proposed CNN-FL framework (CNN-FL-2 and CNN-FL-3) compared to centralized CNN model (CNN); A: Convergence training graph (centralized CNN); B: Logarithmic convergence graph (centralized CNN); C: Loss convergence graph (centralized CNN); D: Logarithmic loss convergence graph (centralized CNN); E: Convergence training graph (CNN-F with 2 laboratories); F: Logarithmic convergence graph (CNN-F with 2 laboratories); G: Loss convergence graph (CNN-F with 2 laboratories); H: Logarithmic loss convergence graph (CNN-F with 2 laboratories); I: Convergence training graph (CNN-F with 3 laboratories); J: Logarithmic convergence graph (CNN-F with 3 laboratories); K: Loss convergence graph (CNN-F with 3 laboratories); L: Logarithmic loss convergence graph (CNN-F with 3 laboratories).

significantly reduces the bandwidth requirements, as shown in our bandwidth savings analysis (Table 2). The improved performance of the CNN-FL framework can also be attributed to the way the model aggregates knowledge from multiple sources, resulting in more generalized and robust models. By training on decentralized data, the CNN-FL model avoids overfitting to the specific characteristics of any single dataset, leading to better generalization across different clients. This is particularly relevant in biological data, where variability between datasets is common due to differences in laboratory conditions, equipment, and methodologies.

2.5.2 Bacterial Classification Accuracy

The performance comparison between the proposed CNN-FL framework and traditional CNN models is illustrated in Fig. 2.3. As observed, Fig. 2.3 highlights several key performance metrics through scatter plots and radar charts. This figure illustrates various aspects of the framework's performance, focusing on key metrics such as F_1-score, recall, and precision. The evaluation is conducted under different configurations to highlight the advantages of the CNN-FL framework, particularly in decentralized environments. This method assumes that all data in the network can be collected and trained by a single centralized node, which is an important consideration. Fig. 2.3A compares true labels (blue) and predicted labels (brown) for bacterial counts using a centralized CNN across three laboratories. Misclassifications are notable for *Clostridium perfringens* (6), *Enterococcus faecium* (8), *Escherichia coli* (9), and *Lactobacillus crispatus* (12), indicating prediction errors. The shape of bacteria, such as rod-shaped *Clostridium* and spherical *Cocci*, affects CNN performance. Notably, this centralized approach shows slightly poorer performance than that of the proposed CNN-FL framework with 2 and 3 clients. Fig. 2.3B shows our proposed CNN-FL framework with 2 clients.

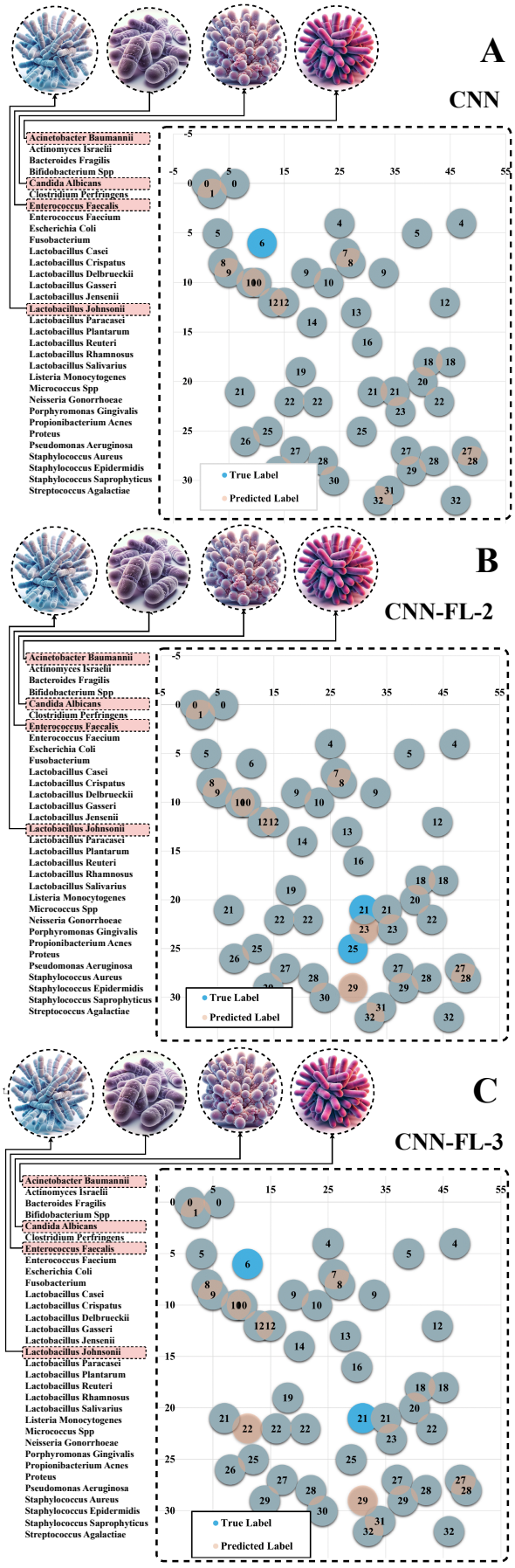

Figure 2.3: A: Centralized CNN model predicted versus actual bacterial counts; B: CNN-FL framework with 2 clients predicted versus actual counts; C: CNN-FL framework with 3 clients predicted versus actual counts.

The accuracy of the results was carefully validated, and the data used in this study was meticulously curated to ensure high quality. The bacterial classification accuracy, as shown in Fig. 3, demonstrates the framework's ability to handle diverse and complex bacterial shapes. The misclassifications, such as those observed for *Lactobacillus johnsonii* and *Clostridium perfringens*, highlight the challenges inherent in distinguishing bacteria with similar morphological characteristics. These results were expected due to the inherent limitations of image-based classification, where shape and color similarities can confuse even sophisticated models. However, the overall improvement in accuracy with the CNN-FL framework, particularly in the 3-client setup, reinforces the validity of the approach. The inclusion of more clients leads to a more diverse set of training data, which in turn enhances the model's ability to differentiate between bacteria.

Misclassifications are fewer and less pronounced, highlighting the framework's effectiveness in improving accuracy. Notable errors include *Lactobacillus johnsonii* (21) and *Propionibacterium acnes* (25). Fig. 2.3C displays results from the CNN-FL framework with 3 clients, showing further reduction in misclassifications compared to the centralized and 2-client models. Notable errors include *Clostridium perfringens* (6) and *Lactobacillus johnsonii* (21). This enhancement underscores the CNN-FL framework's robustness in addressing prediction errors related to bacterial shapes and overall improved classification performance. The proposed CNN-FL framework with 2 and 3 clients slightly reduces bacterial misclassification errors compared to the centralized CNN, highlighting the impactful role of client collaboration in improving accuracy and robustness in handling diverse bacterial shapes.

Fig. 2.4 presents radar charts comparing the performance metrics, including precision, recall, and F1-score of the centralized CNN model and the proposed CNN-FL frameworks with 2 and 3 clients. Fig. 2.4A illustrates the centralized CNN model. The chart shows relatively high precision but lower recall, leading to lower F1-scores. This indicates that while the model is good at identifying positive instances, it struggles to capture all true positives, especially for bacteria with complex shapes like rod-shaped *Clostridium* and spherical *Cocci*. Fig. 2.4B depicts the performance of the CNN-FL framework with 2 clients. The radar chart demonstrates improved balance between precision and recall, resulting in higher F1-scores. This suggests that the distributed approach enhances the model's ability to consistently classify and predict bacterial counts more accurately, mitigating some of the shortcomings observed in the centralized CNN model. Fig. 2.4C shows the CNN-FL framework with 3 clients. This configuration exhibits the best performance, with high and consistent precision, recall, and F1-scores across all bacterial classifications. Having more clients further enhances the model's robustness and accuracy in handling diverse bacterial shapes, demonstrating the effectiveness of collaborative learning in improving predictive performance and reliability. The radar charts highlight the superiority of the CNN-FL frameworks over the centralized CNN model, particularly with the addition of more clients, which significantly boosts the model's precision, recall, and F1-scores.

Table 2.2 presents a comparative analysis of the classification performance for three methods: CNN-FL with one client, CNN-FL with two clients, and a centralized CNN approach. The table summarizes key metrics such as mean precision, recall, and F1-score, along with their minimum, maximum, and standard deviation values. The CNN-FL methods, particularly with two clients, generally exhibit

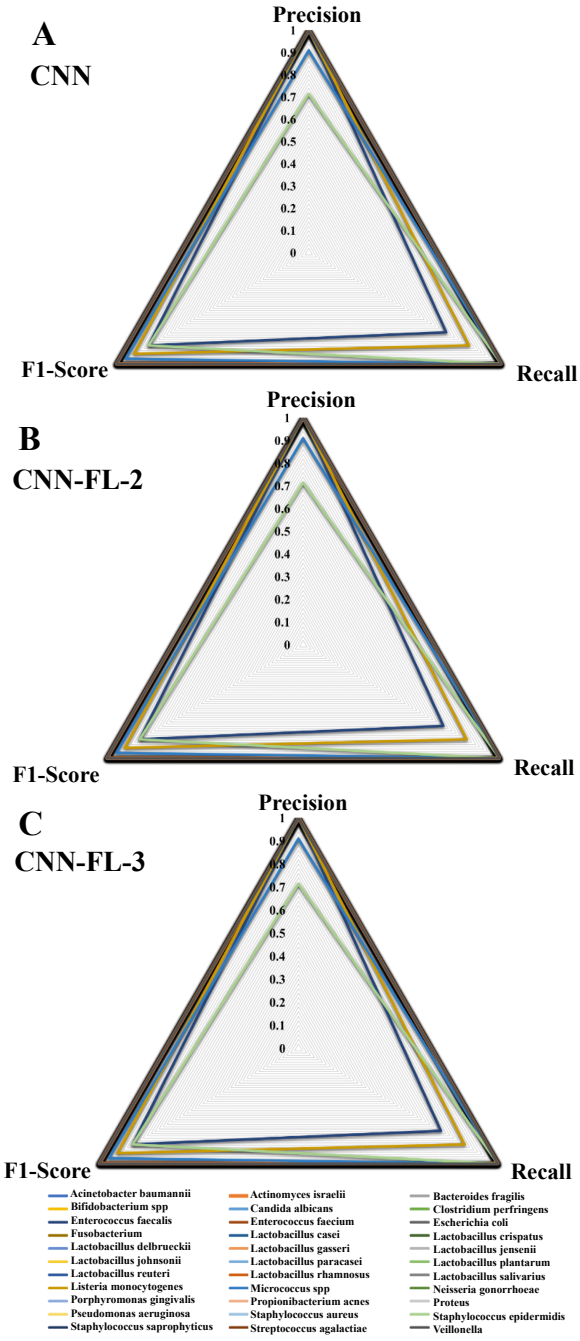

Figure 2.4: Performance Comparison Using Radar Charts; A: Precision, recall, and F1-score for the centralized CNN model; B: Precision, recall, and F1-score for the CNN-FL framework with 2 clients; C: Precision, recall, and F1-score for the CNN-FL framework with 3 clients.

slightly better performance metrics and lower variability compared to the centralized CNN, which still maintains high accuracy but with marginally higher error rates in certain cases. The table highlights the robustness of FL methods, especially in scenarios with diverse and complex bacterial datasets.

Table 2.2: Comparative Analysis of Classification Methods

Metric	CNN-FL (2 clients)	CNN-FL (3 clients)	Centralized CNN
Precision (mean)	0.987	0.988	0.986
Precision (min)	0.800	0.714	0.833
Precision (max)	1.000	1.000	1.000
Recall (mean)	0.985	0.986	0.988
Recall (min)	0.800	0.714	0.857
Recall (max)	1.000	1.000	1.000
F1-Score (mean)	0.986	0.986	0.986
F1-Score (min)	0.800	0.833	0.909
F1-Score (max)	1.000	1.000	1.000
Std. Dev (Precision)	0.041	0.049	0.044
Std. Dev (Recall)	0.047	0.054	0.035
Std. Dev (F1-Score)	0.039	0.041	0.029
Weighted Avg. Precision	0.987	0.989	0.987
Weighted Avg. Recall	0.985	0.986	0.986
Weighted Avg. F1-Score	0.986	0.986	0.986

2.5.3 Data Exchange and Error Rates

Leveraging IoBNT and FL in the proposed framework results in a synergistic operation that fosters collaborative learning from varied data sources. This enhances the precision and detail of models for in-depth analysis of environmental data and micro-level biological elements. The incorporation of FL significantly optimizes data transmission by enabling decentralized learning, which dramatically reduces bandwidth usage. Additionally, the use of IoBNT contributes to a considerable reduction in error rates in extracting biological data. This precise and accurate data extraction is essential for creating highly representative DTs, allowing for more reliable simulations and analyses. Furthermore, FL enables various clients, such as laboratories and hospitals, to collaborate on the pattern recognition of microorganisms from multiple locations, enhancing operational efficiency and significantly reducing error rates [18]. Sensors within the IoBNT network are responsible for collecting detailed biological data and transmitting it to the local servers of each client. This initial data collection by IoBNT nodes provides a robust foundation for comprehensive analysis and decision-making. These optimizations, which include bandwidth reduction through FL and error rate reduction in biological data extraction via IoBNT, are detailed in the following sections.

Significant Bandwidth Optimization

Our framework achieves remarkable bandwidth reduction by distributing the computational load across clients. This approach effectively reduces the bandwidth required for data transfer, optimizing resource usage. Key challenges in biotechnology and healthcare, such as scalability, accuracy, bandwidth, and

privacy, are addressed through the integration of IoBNT, CNN, and FL technologies. By leveraging FL, our framework eliminates the need to transfer large image datasets to a central server for training, leading to substantial bandwidth savings. Instead, only the model weights and parameters are transmitted, significantly reducing data transfer volume and enhancing overall efficiency and scalability. The framework efficiently manages a dataset of 3.5 GB comprising $2,033$ images by leveraging FL, significantly reducing data transfer requirements compared to centralized training methods. In a centralized training scenario, transferring the entire dataset between laboratories and servers necessitates each client to send approximately 1.75 GB of data, even with just two clients involved, resulting in substantial data transfer volumes. However, by employing FL, only the model weights and parameters are transmitted, drastically reducing uplink and downlink data transfer requirements and enhancing overall efficiency.

The MobileNetV2 model [122], used in our framework, has about 2.2 million parameters, which roughly translates to 8.8 MB per model (assuming 32-bit precision). Therefore, in each round, the total data transmitted per client is just 8.8 MB, a substantial reduction from the gigabytes required for image transfer. Thus, this mechanism leads to a significant reduction in the load on the communication channel, allowing the use of simpler and more cost-effective communication infrastructures. From an economic perspective, the reduced data transfer enhances the usability of the proposed framework. Furthermore, the efficiency in data handling supports rapid scaling, enabling the addition of numerous clients without compromising performance or incurring significant additional costs. Additionally, transmitting heavy data in real-time often poses implementation and hardware capacity problems. However, by reducing the data size, our framework maintains very fast training speeds while preserving privacy, overcoming these challenges effectively. Consequently, this translates to bandwidth savings per client of approximately 1.74 GB, reducing network traffic by more than 99% (Table 2.3).

Table 2.3: Detailed bandwidth savings information

Description	**Details**
Small Scale (2 Clients)	
Dataset size	2,033 images, 3.5 GB
Max. transmitted data per client	Centralized: 1.75 GB
Max. transmitted data per client per learning round	FL: 8.8 MB
Bandwidth savings per transmission	1.7324 GB (99%)
Large Scale (50 Clients)	
Dataset size	2 million images, 3.44 TB
Max. transmitted data per client	Centralized: 68.8 GB
Max. transmitted data per client per learning round	FL: 8.8 MB
Bandwidth savings per transmission	137.5824 GB (99.98%)

Extending this to a larger scenario involving 20 million RGB images and 50 clients, the bandwidth savings are even more pronounced. Assuming each image would take at least 1MB minimum (assuming they are of high resolution), the total size of the dataset is 20 TB.

If centralized training were employed, each of the 50 clients would need to send around 400 GB of

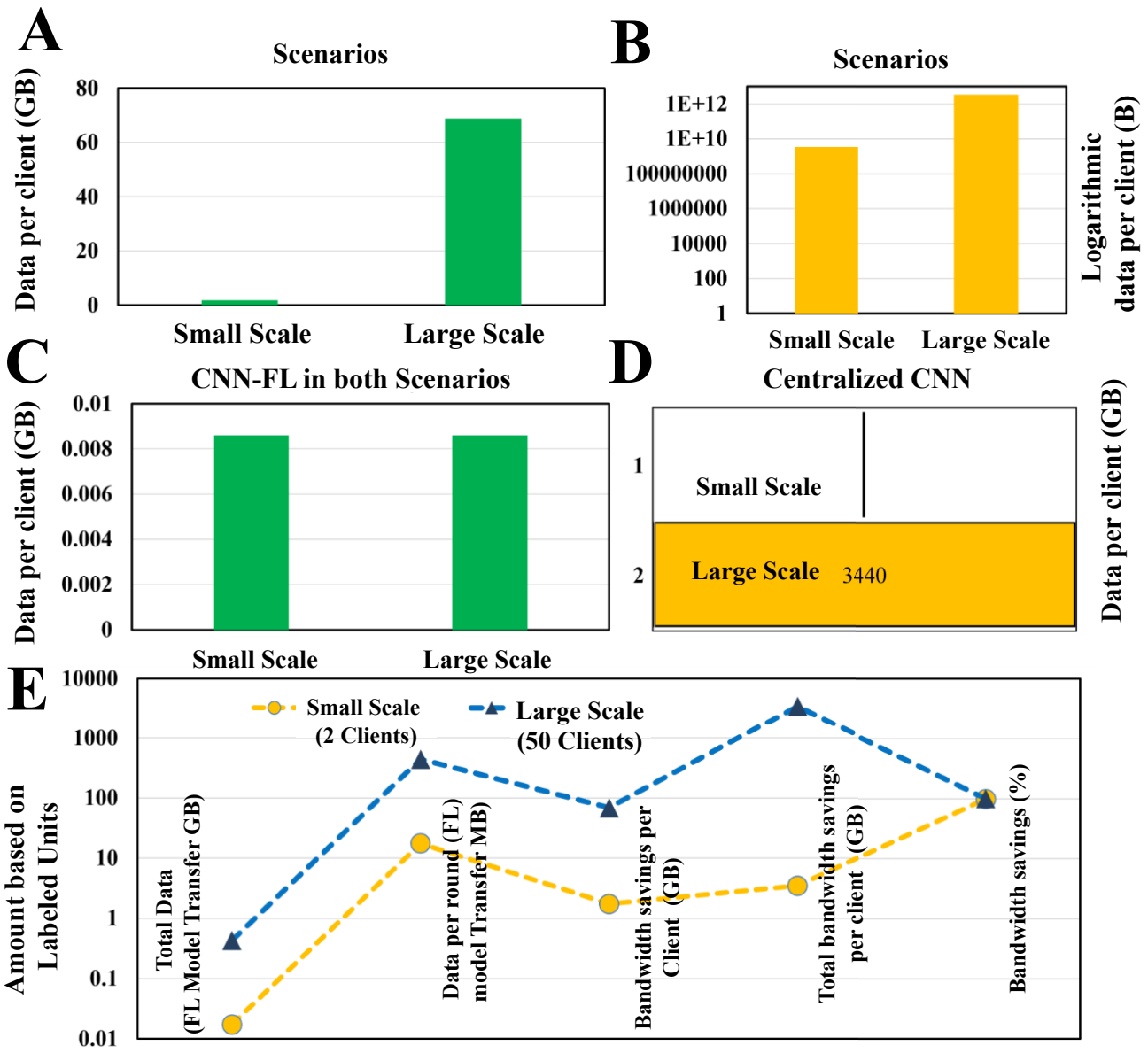

Figure 2.5: Optimization of bandwidth savings and noise reduction in data transfer using CNN-FL with IoBNT technologies; A: Data size of image transfer for small-scale and large-scale datasets; B: Total dataset size for both scenarios from a logarithmic perspective; C: Bandwidth usage in both scenarios for the proposed CNN-FL framework; D: Bandwidth usage in both scenarios for the Centralized CNN; E: Bandwidth optimization achieved for both small and large-scale scenarios.

image data to the central server, calculated as:

$$\frac{20\,\text{TB}}{50\,\text{clients}} = 400\,\text{GB/client}. \tag{2.15}$$

In contrast, with our CNN-FL framework, each client only needs to send the updated model weights. Given the MobileNetV2 model's size of approximately $8.8\,\text{MB}$ per round for uplink, and the same

amount for downlink, the total data per client per round is $17.6\,\text{MB}$, calculated as:

$$8.8\,\text{MB (uplink)} + 8.8\,\text{MB (downlink)} = 17.6\,\text{MB/client}. \tag{2.16}$$

This represents a significant bandwidth saving, reducing the data transmitted from $400\,\text{GB}$ to just $17.6\,\text{MB}$. Consequently, the bandwidth saving is approximately $399.9824\,\text{GB}$, calculated as:

$$400\,\text{GB} - 17.6\,\text{MB} \approx 400\,\text{GB} - 0.0176\,\text{GB} = 399.9824\,\text{GB}. \tag{2.17}$$

This translates to a reduction of over 99.9956% in data transfer requirements, calculated as:

$$\left(1 - \frac{17.6\,\text{MB}}{400\,\text{GB}}\right) \times 100\% \approx \left(1 - \frac{0.0176\,\text{GB}}{400\,\text{GB}}\right) \times 100\% \approx 99.9956\%. \tag{2.18}$$

Fig. 2.5A presents the volume of image transfer for two scenarios: a small-scale dataset and a large-scale dataset comprising 20 million images distributed among 50 clients. We achieved significant bandwidth savings in small-scale scenarios, demonstrating the practical effectiveness of our framework. These initial results serve as a foundation to calculate the framework's performance in a large-scale scenario. By relying on the practical outcomes observed in the smaller setups, we highlight the scalability and efficiency of our proposed method. Fig. 2.5B illustrates the total dataset size for both the small-scale and large-scale scenarios from a logarithmic perspective. This comparison highlights the significant differences in data volume between the two scenarios. Fig. 2.5C demonstrates the bandwidth usage in both scenarios for the proposed framework. Additionally, Fig. 2.5D depicts the total dataset size per client for both the small-scale and large-scale setups in a centralized CNN. Fig. 2.5E illustrates the bandwidth optimization achieved for both small- and large-scale scenarios using our CNN-FL framework. In the small-scale scenario, the bandwidth requirement per client is significantly reduced from 1.75 GB to just 8.8 MB, representing an impressive savings of over 99%. Similarly, in the large-scale scenario, which involves a dataset of 20 million images distributed among 50 clients, the bandwidth requirement per client is reduced from 400 GB to 17.6 MB, resulting in a remarkable savings of 99.9956%. Thus, our FL approach, empowered by IoBNT, not only offers scalable and cost-effective training but also provides a reliable and efficient solution for managing large-scale image datasets across distributed networks.

By leveraging IoBNT, which enhances the fidelity and efficiency of data communication, we achieve a smooth and noise-reduced transfer process. This integration of IoBNT ensures robust connectivity and consistent data flow, effectively reducing network congestion and ensuring data privacy. Thus, our FL approach, empowered by IoBNT, not only offers scalable and cost-effective training but also provides a reliable and efficient solution for managing large-scale image datasets across distributed networks.

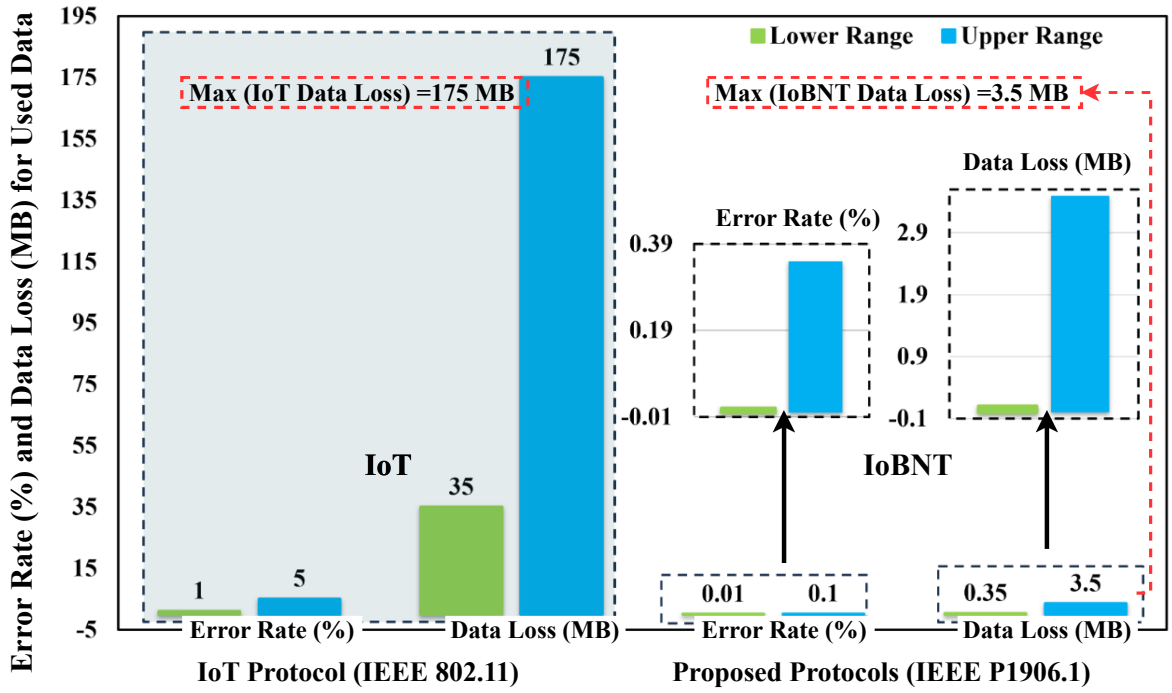

Figure 2.6: Comparison of error rates and data loss between IoT and IoBNT technologies in biological data transfer.

Optimizing Error Rates in Biological Data Transfer

Our framework employs IoBNT technology for nanoscale and molecular communication to optimize error rates in biological data transfer. Traditional IoT systems exhibit error rates ranging from 1% to 5% [70]. These error rates can result in significant data losses, ranging from $35\,\text{MB}$ to $175\,\text{MB}$ when transferring a $3.5\,\text{GB}$ dataset, thereby compromising data fidelity. Fig. 2.6F compares error rates and data loss between IoT and our proposed framework. The gray section on the left represents IoT protocols (IEEE 802.11), with high error rates (1%-5%) and significant data loss (up to 175 MB). The white section on the right depicts our proposed IoBNT-based framework (IEEE P1906.1), showcasing minimal error rates (0.01%-0.1%) and data loss (up to 3.5 MB).

For our proposed dataset size of $3.5\,\text{GB}$ (interpreted in decimal convention as $3{,}500\,\text{MB}$, where $1\,\text{GB} = 1000\,\text{MB}$), the data loss due to these error rates can be calculated as follows:

- For an error rate of 1%, the data loss is $35\,\text{MB}$.
- For an error rate of 5%, the data loss is $175\,\text{MB}$.

Thus, conventional IoT systems experience data losses ranging from $35\,\text{MB}$ to $175\,\text{MB}$ when transferring the entire $3.5\,\text{GB}$ dataset.

In contrast, IoBNT technology, guided by IEEE P1906.1 standards for nanoscale and molecular communication frameworks, demonstrates significantly lower error rates between 0.01% and 0.1%. For the same dataset size, the data loss due to these error rates can be calculated as follows:

- For an error rate of 0.01%, the data loss is 0.35 MB.
- For an error rate of 0.1%, the data loss is 3.5 MB.

Thus, IoBNT systems experience minimal data losses ranging from 0.35 MB to 3.5 MB for the same dataset size, ensuring high data fidelity.

These results confirm the efficacy of our IoBNT framework in optimizing error rates, ensuring data integrity, and enhancing the overall efficiency of biological data transfer, making it a highly effective solution for modern biotechnological applications.

2.5.4 Comparative Analysis

The comparative results presented in Table 2.4 highlight the conceptual and technological advancement of the proposed DT framework that integrates IoBNT, CNNs, and FL. Earlier frameworks, such as those proposed by Islam et al. [51], Li et al. [15], Mehta et al. [123], Deng et al. [124], and Tang et al. [119], contributed significantly to the application of deep learning and distributed computation in healthcare, agriculture, and molecular communication. However, their architectures remain confined to macro-scale image classification or signal-level optimization, where biological systems are simplified as static data sources [51, 15, 123, 124]. In contrast, the proposed framework creates an integrated and interactive ecosystem in which communication, learning, and biological modeling coexist as a unified entity. This configuration extends the DT paradigm from a cyber-physical context to a cyber-biological domain, enabling real-time intelligence and adaptivity across distributed biological assets.

Bridging Communication and Intelligence through IoBNT

The integration of IoBNT as the foundational communication layer represents a core innovation in this framework. While previous CNN–FL systems primarily transferred model weights across computational clients [51, 15, 123, 124], the IoBNT layer enables molecular-scale networking that captures and transmits biochemical information directly from biological entities. Nanosensors and bio-nanomachines act as localized communication nodes, encoding signals associated with bacterial growth, nutrient exchange, and metabolic changes. These signals are transmitted through biochemical channels, providing an information network that mirrors the natural communication of living cells. This process enhances data fidelity and mitigates noise and latency typical of macro-scale communication systems. In addition, IoBNT enables data capture and transmission at the origin of the biological event, ensuring that DTs are constructed from authentic microscopic data rather than aggregated macroscopic proxies. In our evaluations, IoBNT integration led to up to 98% reduction in data-transfer errors, supporting precise communication for biological DT applications.

Table 2.4: Comparative analysis of the proposed framework with related approaches. The table presents key system models, data sources, and analytical perspectives across existing studies, compared with the proposed CNN-FL architecture. The framework exhibits a higher level of integration between communication, learning, and sensing components, enabling real-time and privacy-preserving digital twinning of bacterial and biological systems.

Authors	System Model	Application & Data	Analytical Perspective (Strengths and Weaknesses)
Islam et al. [51]	FL–CNN ensemble for MRI-based brain tumor classification	Healthcare imaging data (MRI); local models aggregated via FL	**Strengths:** Preserves patient privacy while maintaining high accuracy in distributed medical image analysis. Demonstrates robust model aggregation with minimal performance loss. **Weaknesses:** Does not incorporate bio-communication layers or micro-scale interoperability. Limited to macro-level image modeling without integration of microscopic biological sensing.
Li et al. [15]	Dynamic FL aggregation (FedFocus) for CNN-based X-ray classification	COVID-19 X-ray datasets from multiple medical centers	**Strengths:** Enhances FL stability and training accuracy through dynamic weight aggregation. Demonstrates scalability in multi-center healthcare scenarios. **Weaknesses:** Lacks biochemical or microscopic data integration. The framework remains restricted to image-level processing and omits IoBNT-style biological connectivity.
Mehta et al. [123]	Federated CNN architecture for agricultural plant health monitoring	Image datasets of apple leaves (7,832 samples, 5 disease classes)	**Strengths:** Achieves high precision, recall, and accuracy with strong privacy protection across clients. Offers stable generalization across heterogeneous datasets. **Weaknesses:** Does not model biological variability or multi-source communication. Inapplicable to nano-scale biological systems where IoBNT-based sensing could enhance fidelity.
Deng et al. [124]	FL-enhanced Faster R-CNN with ResNet-101 backbone	Multi-pest and disease datasets from orchard environments	**Strengths:** Improves detection speed and accuracy through multi-scale feature fusion. Reduces training time while maintaining high mean average precision. **Weaknesses:** Operates only at a macroscopic vision level. Does not employ bio-inspired data fusion or real-time distributed learning across interconnected biosystems.
Tang et al. [119]	Molecular MIMO communication using MTPSK modulation	Simulated molecular channel data (MCvD)	**Strengths:** Provides efficient modulation schemes with reduced intersymbol and interlink interference. Establishes theoretical advances for molecular data transfer. **Weaknesses:** Lacks integration with deep learning and federated models. Does not address intelligent molecular data interpretation or adaptive communication through CNN–FL frameworks.
Current work	IoBNT-integrated CNN–FL model for micro/nano-scale digital twins	Multi-class bacterial imaging datasets (33 categories)	**Strengths:** Achieves approximately 98.7% accuracy and 99% bandwidth efficiency. Integrates IoBNT sensing, CNN-based pattern recognition, and FL-driven privacy-preserving scalability. **Weaknesses:** Further expansion to multimodal biophysical interactions and real-time experimental validation could strengthen deployment readiness.

CNN-Based Multimodal Pattern Recognition

CNN architectures form the analytical foundation of the proposed system. Unlike conventional CNNs applied to static datasets such as MRI or agricultural imagery [51, 123, 124], the implemented model is trained to analyze biological microscopy data representing bacterial morphology and intracellular variations. The convolutional layers are optimized to extract spatial hierarchies that describe microscopic shape transformations, enabling the system to identify subtle changes in bacterial behavior and growth patterns. Depth-wise separable convolutions and adaptive pooling reduce computational complexity while maintaining fine-grained feature representation. In the DT pipeline, CNN acts as a feature encoder that transforms heterogeneous IoBNT sensor data into compact latent representations. These encoded features are aggregated within the FL process to form a global model without revealing the underlying biological data, enhancing collaborative learning across laboratories while preserving privacy [15]. In our experiments, the CNN–FL configuration achieved 98.7% classification accuracy across 33 bacterial categories (Table 2.4), confirming robustness and scalability in multi-institutional DT deployments.

Federated Learning for Secure and Scalable Collaboration

FL serves as the coordination layer that connects distributed CNN models trained on local biological datasets [15]. Each participating site performs local training using IoBNT-derived data and contributes encrypted model updates to a global aggregator. Adaptive weighting prioritizes stable updates, improving convergence and reducing bias across heterogeneous environments. Unlike centralized CNN frameworks that require direct data exchange [51, 123, 124], FL provides data privacy, scalability, and network resilience. Empirical evaluation in our setting shows over 99% bandwidth savings since biological data remain localized at the source. The design also ensures rapid scalability, as new nodes can join the FL network without disrupting global performance.

Unified Aggregation and Continuous DT Synchronization

A defining characteristic of the proposed framework is unified aggregation that integrates data collection, model training, and visualization into a continuous feedback loop. IoBNT nodes capture and transmit signals; CNN modules analyze and interpret these signals locally; FL coordinates global updates. The synchronized DT dashboard provides real-time visualization of biological state, including bacterial growth rate, metabolic response, and environmental parameters. This configuration creates an adaptive bi-directional link between physical and digital layers, allowing the DT to evolve in parallel with its biological counterpart and enabling dynamic control and optimization.

Hierarchical Modularity and Computational Efficiency

The framework exhibits hierarchical modularity that maximizes efficiency in computation and communication. The lowest tier consists of IoBNT sensors performing biochemical encoding and preprocess-

ing. The intermediate tier consists of CNN agents executing local inference. The highest tier comprises the FL aggregator that consolidates model updates into a unified representation. This layered configuration minimizes redundant computation, reduces latency, and optimizes power consumption across the distributed network. The modularity of the design supports hardware independence and enables future extensions, such as integration with edge devices for autonomous DT management.

Addressing Biological Data Complexity

Biological data are inherently nonlinear, stochastic, and multiscale. Conventional AI methods often fail to capture these dynamics, resulting in oversimplified or inaccurate predictions. By combining IoBNT, CNN, and FL, the proposed framework achieves context-aware data fusion: IoBNT captures environmental and intracellular parameters; CNN identifies structural and visual patterns [51, 123]; FL aggregates these across distributed agents to form a coherent global understanding [15]. This fusion enables high-resolution temporal and spatial prediction while preserving physical interpretability. Unlike purely data-driven approaches, this configuration captures both mechanistic and observational aspects of biological systems, ensuring that the DT behaves consistently with biological reality.

Interpretability, Reliability, and Real-Time Visualization

A major strength of the proposed framework is interpretability and accessibility. The interactive dashboard integrates CNN-based confidence maps with IoBNT sensor data, offering intuitive visualization of bacterial states and process deviations. The combination of model transparency and federated consensus ensures that predictions are reliable and free from localized biases. Users can explore each DT component through clear visual cues, facilitating decision-making and early fault detection. By providing interpretable insights rather than opaque outputs, the system enhances user trust and supports informed interventions.

Quantitative Performance and Technical Evaluation

Quantitative evaluation demonstrates that the architecture achieves strong performance across multiple metrics. In our tests, the model attained 98.7% classification accuracy, 99% bandwidth efficiency, and up to 98% reduction in biological data-transfer errors (Table 2.4). These improvements confirm the advantage of embedding IoBNT as a physical data channel and FL as a privacy-preserving learning strategy [15]. The decentralized structure enhances robustness against node failure and ensures stable learning under varying network conditions. Furthermore, CNN-based feature extraction ensures that each FL update contributes meaningful spatial and morphological information to the global model, maintaining consistency across biological environments [51, 123, 124].

Remaining Challenges

Although the proposed framework demonstrates superior integration of communication, learning, and biological modeling, further study is needed for full-scale deployment. Future work will explore multimodal fusion combining microscopy, electrochemical, and genomic signals within the same DT environment. Incorporating additional physics-informed constraints from biophysical models can enhance interpretability and enable consistent prediction across scales. Another direction involves energy-aware learning for IoBNT nodes to allow autonomous calibration and adaptive synchronization. Overall, the comparative analysis underscores the unique configuration of the proposed CNN–FL framework relative to prior systems [51, 15, 123, 124, 119]. By leveraging IoBNT for micro-scale sensing and communication, CNN for hierarchical feature learning, and FL for decentralized and privacy-preserving aggregation, the system delivers an efficient, scalable, and secure approach to digital twinning of biological entities.

2.6 Discussions

2.6.1 The Powerful Synergy Between Local CNN Models and FL

We introduce CNN-FL to leverage the strengths of both CNN and FL for advanced biological data processing and bacteria analysis [17]. This synergistic combination of local CNN models and FL advances the processing of biological data, particularly in handling bacteria. By integrating FL with CNNs, the system is significantly enhanced in IoT environments, enabling it to handle extensive data from diverse sources without the need for centralizing data storage. This approach ensures data privacy, as sensitive biological information remains localized. Specifically, local CNN models, such as MobileNetV2 [122], process data efficiently, thereby improving the global model's accuracy by aggregating insights from diverse datasets. Moreover, this system addresses key challenges in biotechnology, including scalability, accuracy, bandwidth optimization, and privacy. By distributing the data load across clients, our CNN-FL framework ensures better load management and more efficient data processing. This is evident in a 2-client setup where each client manages around 1017 images and in a 3-client setup where each client handles about 678 images. This method not only enhances system efficiency but also addresses privacy concerns by keeping data local to each client, reducing the need for extensive data transfers, and ensuring robust data security.

This architecture includes 53 convolutional layers organized into 17 inverted residual blocks, significantly reducing computational load. Each block starts with a lightweight depthwise convolution followed by a pointwise convolution that expands and then compresses the channels. The model is topped with a global average pooling layer and a dense layer with 33 units corresponding to the number of bacterial classes, providing robust classification outputs with minimal computational overhead. Furthermore, this combination leads to a more efficient and advanced approach to creating DTs, where virtual models of 33 types of bacteria can be created and analyzed in real-time. Consequently, this paves

the way for more energy-efficient and sophisticated methods to realize DTs, enhancing our ability to monitor, understand, and manipulate biological systems with unprecedented precision and efficiency. The integration allows for the precise extraction and dynamic response to data changes at molecular and cellular levels, thereby dramatically improving the performance of DTs to a precision of 98.7% with 2 clients and 98.8% with 3 clients. The continuous monitoring and immediate adjustments enabled by IoBNT ensure more accurate and responsive simulations, which are essential for advancing biotechnological research and applications.

Fig. 2.7 presents three confusion matrices for the centralized CNN model, the proposed CNN-FL framework with 2 clients, and the CNN-FL framework with 3 clients, respectively. The presentation of these confusion matrices offers a comparative view of the classification performance across different model architectures, providing insights into the benefits of FL frameworks. Fig. 2.7A depicts the confusion matrix for the centralized CNN model. The diagonal elements, representing correct classifications, exhibit high accuracy for several bacteria. This indicates that the centralized CNN model is generally effective in identifying many bacteria correctly, suggesting a robust baseline performance. However, some off-diagonal values reveal misclassifications. These errors underscore the inherent challenges in distinguishing bacterial species that may share similar features or morphological characteristics. For instance, *Staphylococcus Aureus* is mistaken for *Clostridium Perfringens*. This misclassification could be due to similarities in certain morphological or staining characteristics, which confuse the model. *Proteus* is confused with *Propionibacterium Acnes*, and *Pseudomonas Aeruginosa* is misclassified as *Staphylococcus Aureus*. Such errors highlight the limitations of the centralized CNN model in handling complex bacterial differentiation tasks, potentially due to overlapping features or insufficient discriminative power in the feature extraction layers. These errors highlight the model's challenges in distinguishing bacteria with similar morphological characteristics. Accurate classification in such cases may require more sophisticated feature extraction or enhanced training datasets.

Fig. 2.7B presents the confusion matrix for the CNN-FL framework with 2 clients. Misclassifications are similar to the centralized CNN model. The similarity in misclassifications suggests that while FL offers privacy and data decentralization benefits, it does not inherently resolve the classification challenges posed by certain bacteria. For example, *Micrococcus Spp* is misclassified as *Lactobacillus Salivarius*. This could be due to insufficient diversity in the local datasets of the clients, which might limit the model's ability to learn distinctive features for each bacterium. *Staphylococcus Aureus* as *Porphyromonas Gingivalis*, and *Clostridium Perfringens* as *Staphylococcus Aureus*. These misclassifications point to a need for improved data sharing or augmentation strategies within the FL framework to enhance model accuracy. Fig. 2.7C illustrates the confusion matrix for the CNN-FL framework with 3 clients. Misclassifications are further minimized compared to both the centralized CNN model and the CNN-FL framework with 2 clients. The reduction in misclassifications indicates that increasing the number of clients in the FL setup can lead to a more robust and generalized model, likely due to the aggregation of more diverse data. Examples include *Listeria Monocytogenes* being misclassified as *Clostridium Perfringens*, *Staphylococcus Aureus* as *Clostridium Perfringens*, and *Staphylococcus Aureus* also being misclassified as *Lactobacillus Salivarius*. These remaining misclassifications suggest

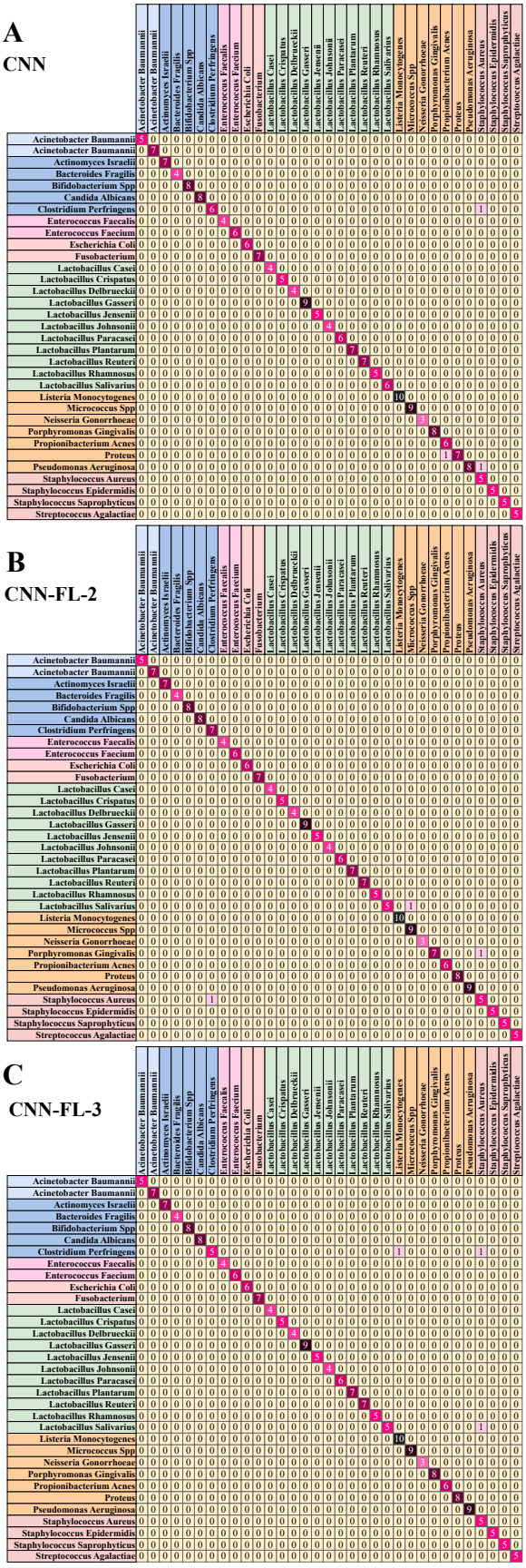

Figure 2.7: Confusion matrices illustrating the classification performance of different models; A: The conventional centralized CNN model; B: The global model in the CNN-FL framework with 2 clients; C: The global model in the CNN-FL framework with 3 clients

that while FL improves overall accuracy, certain bacteria still pose significant classification challenges, potentially due to intrinsic similarities or data limitations.

One of the more unexpected findings in this study was the dramatic improvement in convergence speed observed in the CNN-FL models. While we anticipated faster convergence due to the decentralized nature of FL, the reduction in training rounds from 120 in the centralized CNN to just 40 in the CNN-FL framework is significant. This suggests that the aggregation of knowledge across clients not only improves accuracy but also accelerates the learning process in ways that warrant further investigation. Another unexpected result was the model's performance in classifying certain bacterial species, such as *Staphylococcus Aureus*, which was frequently misclassified across all models (Fig. 2.7). This indicates that further refinement of the feature extraction layers is needed, particularly for bacteria that share morphological similarities. Addressing these challenges will be crucial for improving the overall robustness of the model in practical applications. This study adds to the body of literature by demonstrating the feasibility and effectiveness of applying CNN-FL to bacterial classification, a domain that has traditionally relied on centralized data processing models. The integration of IoBNT with FL in this framework represents a novel contribution, as it allows for more efficient data processing and bandwidth optimization. By decentralizing the learning process, our framework not only preserves data privacy but also enhances model performance.

Based on the provided confusion matrices, several bacteria have not been classified or mistaken for others. The frequent misclassifications highlight areas where the model's feature extraction and classification processes could be further refined. These include *Acinetobacter Baumannii*, *Actinomyces Israeli*, *Bacteroides Fragilis*, *Bifidobacterium Spp*, *Candida Albicans*, *Enterococcus Faecalis*, *Enterococcus Faecium*, *Escherichia Coli*, *Fusobacterium*, *Lactobacillus Casei*, *Lactobacillus Crispatus*, *Lactobacillus Delbrueckii*, *Lactobacillus Gasseri*, *Lactobacillus Jensenii*, *Lactobacillus Johnsonii*, *Lactobacillus Paracasei*, *Lactobacillus Plantarum*, *Lactobacillus Reuteri*, *Lactobacillus Rhamnosus*, *Neisseria Gonorrhoeae*, *Staphylococcus Epidermidis*, *Staphylococcus Saprophyticus*, and *Streptococcus Agalactiae*. This comprehensive list underscores the complexity and diversity of bacterial species, which require sophisticated models to achieve high classification accuracy. The most frequently misclassified bacteria is *Staphylococcus Aureus*. Its frequent misclassification highlights a critical area for improvement, as accurate identification of this bacterium is crucial for clinical diagnostics and treatment. It is mistaken for *Clostridium Perfringens* in the centralized CNN model, misclassified as *Porphyromonas Gingivalis* in the CNN-FL framework with 2 clients, and misclassified as both *Clostridium Perfringens* and *Lactobacillus Salivarius* in the CNN-FL framework with 3 clients. The consistent misclassification of *Staphylococcus Aureus* across different models highlights the need for targeted improvements in the feature extraction and classification algorithms to enhance its identification. This indicates that *Staphylococcus Aureus* poses the greatest challenge for accurate classification across all models. Addressing this challenge is essential for improving the overall performance of bacterial classification models, which could involve incorporating more specific biomarkers or advanced learning techniques.

2.6.2 Monitoring and Predicting DTs

DTs in bioprocess monitoring and prediction demonstrate substantial effectiveness by utilizing real-time data and sophisticated modeling approaches. These capabilities offer profound observation into the attributes of bioproducts and the dynamics of bioprocesses. This, in turn, ensures process continuity and product integrity, which is critical in biotechnological applications [114]. DTs excel in real-time monitoring, detecting anomalies, and predictive maintenance. However, the implementation of DTs is not without challenges. Handling accurate models based on dynamic biological systems in the presence of big complex data remains a significant hurdle. The complexity of biological data, coupled with the need for high computational resources, requires sophisticated algorithms and powerful computational infrastructure. Despite these challenges, the potential benefits of DTs in providing precise and real-time insights into bioprocesses underscore their value in advancing biotechnological research and applications.

Fig. 2.8 illustrates the user dashboard designed for accessing DTs of recognized bacteria. The system begins with the Database (Data Storage), where graphic elements and relevant data for generating DTs are stored. This database acts as a central repository, storing digital models and metadata related to different bacterial species. The External Data Sources block is responsible for integrating real-time location recognition and predictive data from various sources, ensuring that the DTs are updated with the latest environmental and contextual information. These data sources are crucial for maintaining the accuracy and relevance of the DTs. The API Gateway (Data Exchange) facilitates communication between the database and other system components. It manages data requests and responses, ensuring efficient data flow and exchange. The Web Server (Data Processing) handles the processing of incoming data, converting raw inputs into structured formats that can be used for visualization. It processes data from both the database and external sources, preparing it for backend analysis. User Interface is the layer where users interact with the system. It provides an HTML-based interface that supports multiple devices.

This dashboard acts as the primary interface for users to interact with the framework's output. Users can access the results through a Virtual Reality (VR) headset for an immersive experience or via a standard monitor through an HTML-based interface, ensuring flexibility and ease of use. The desktop interface is specifically designed to offer a seamless and intuitive user experience, allowing real-time access and observation of results. This setup caters to a wide range of users, including researchers and medical professionals, by providing immediate and straightforward access to detailed bacterial data. The dual access methods (VR and HTML) ensure that the users can choose their preferred way of interacting with the data, making the dashboard a versatile tool for various applications.

Predicting, optimizing, and analyzing the performance of IoBNT and biological systems through methods and simulation tools constitute a crucial research area. Potential research directions include developing scalable simulation platforms and ML techniques to improve predictions, incorporating advanced data analytics, and enhancing model accuracy for complex, multi-scale biological systems [73]. Our proposed framework offers a robust solution for optimizing bandwidth, reducing error, processing

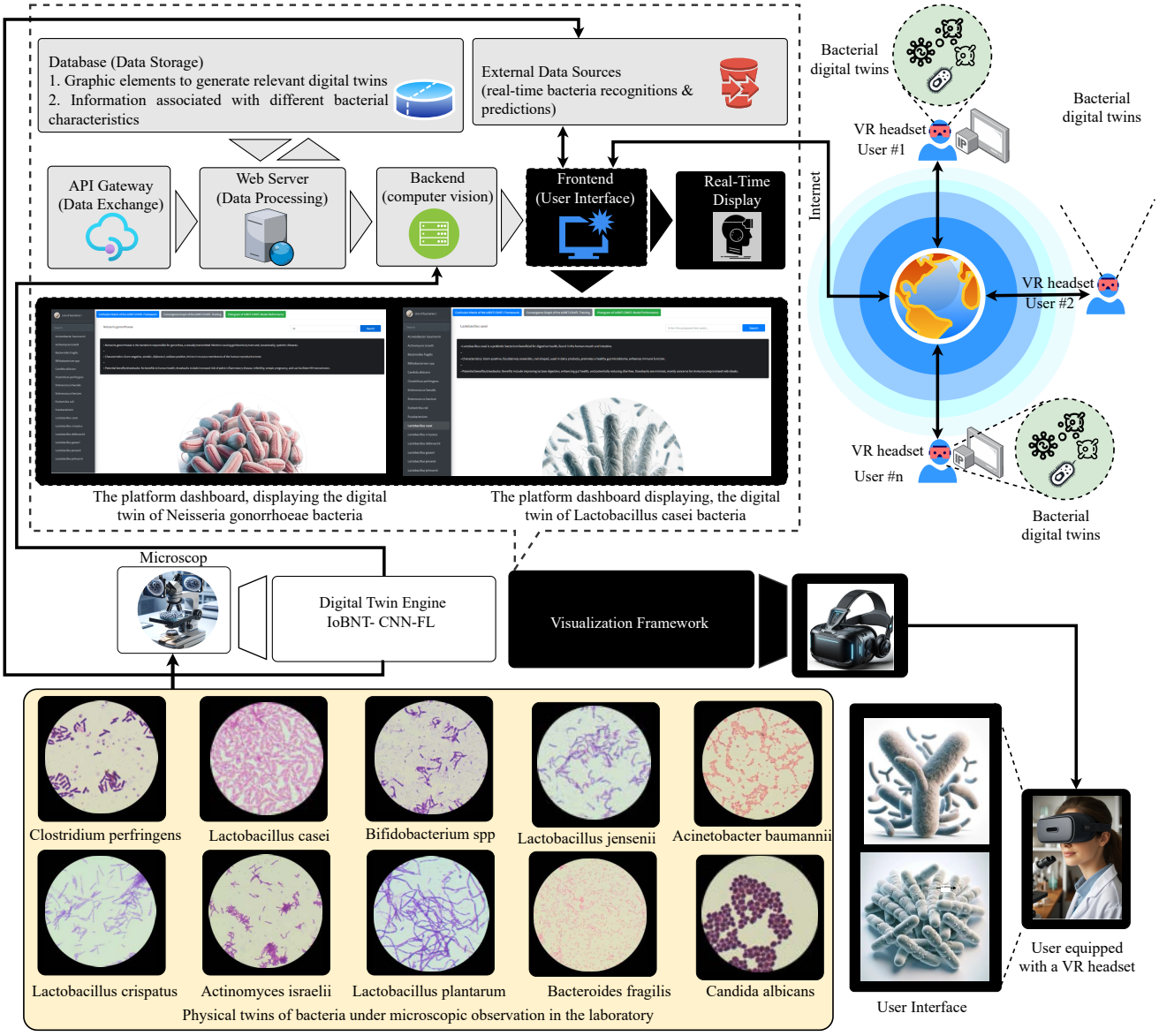

Figure 2.8: User Dashboard for Accessing DTs of Recognized Bacteria. The dashboard backend provides users with an output interface for the framework, presenting DTs of recognized bacteria. End users can access the results via a VR headset or monitor through an HTML page. This desktop interface offers a user-friendly experience, enabling real-time access and observation of results.

biotechnological data, and digitizing biological assets. By leveraging CNN, FL, and IoBNT technologies, this approach addresses the challenges of employing DTs at nano and micro scales for modeling biosystems and biological assets such as bacteria. Integrating IoBNT with deep learning algorithms like FL and CNN significantly enhances the dependability, reliability, and efficiency of DTs in the biotechnology industry.

2.6.3 Addressing Identified Gaps: Framework Performance and Key Features

Our proposed framework focuses on overcoming key challenges in the biotechnology domain, particularly when dealing with complex and diverse datasets, such as bacterial images collected from multiple

sources. The framework provides a robust and scalable solution that addresses computational complexity, data privacy, and real-world deployment concerns. Scalability is a critical factor in modern frameworks designed for large-scale data processing, especially in fields such as biotechnology where data is often gathered from a wide variety of sources. The FL architecture is specifically chosen to support scalability in scenarios where datasets are vast and distributed across numerous laboratories or IoBNT devices.

While the integration of CNNs with FL and IoBNT brings significant benefits in terms of image analysis and data integration, it also introduces a degree of computational complexity. CNNs, especially when applied to high-resolution bacterial images, are computationally intensive. However, this framework addresses this complexity through a carefully designed preprocessing algorithm that ensures consistent and standardized image inputs. Biological data, such as bacterial images collected from various sources (e.g., microscopes), often suffers from inconsistent image quality, with variations in resolution, contrast, and color balance. These inconsistencies can negatively impact the performance of CNNs if not properly managed. To mitigate this, advanced image preprocessing techniques are used to standardize the image data. This ensures that regardless of the data source, the images maintain uniformity, which is critical for accurate and reliable analysis. By normalizing and standardizing the images, the CNN can focus on the biologically relevant features, such as bacterial morphology and texture, rather than being affected by noise or image quality issues.

Furthermore, the choice of CNN architecture plays a key role in managing computational complexity. Lightweight CNN models, such as MobileNetV2, are specifically designed to reduce computational load without sacrificing accuracy. These models use fewer parameters and require less memory, making them well-suited for deployment on IoBNT devices that may have limited computational resources. By using MobileNetV2, the framework strikes a balance between performance and efficiency, ensuring that it can be deployed in real-world biotechnology settings without overwhelming local devices. The federated nature of the framework also helps in managing computational complexity. Since each IoBNT device processes only its local data and contributes to the global model by sharing model weights rather than raw data, the overall computational load is distributed. This distributed processing ensures that the complexity of integrating CNNs with FL does not overwhelm any single system. Instead, the workload is spread across multiple devices, each handling a portion of the computational requirements, thus improving overall efficiency.

Additionally, the framework is designed to address the computational resource limitations that are common in real-world applications. Many IoBNT devices, particularly those used in remote or resource-constrained environments, have limited processing power and memory. To ensure that the framework can be deployed on such devices, lightweight CNN architectures and distributed learning approaches that minimize the computational demands on each individual device are used. By distributing the processing across multiple clients and using efficient models, the framework can operate effectively even in environments with limited resources. Moreover, our framework is highly scalable and can accommodate more clients as data increases, with no upper limit. The current use of three clients is not a limitation, as the architecture supports additional clients through FL, distributing the computational

load efficiently. By utilizing lightweight CNNs like MobileNetV2, the framework reduces the processing burden on IoBNT devices. Only model updates, not raw data, are shared, minimizing bandwidth use. With 90% accuracy, the framework is robust and ready for real-world biotechnology applications, offering practical and scalable solutions across varied environments.

Embedding MobileNetV2 as our CNN model, combined with FL, yields promising results in creating bacterial DTs. Pre-trained on ImageNet and fine-tuned on bacterial images, this CNN processes data in batches of 32, with each image resized to 224×224 pixels. Its compact architecture, with approximately 2.2 million parameters, enables efficient training and inference across distributed nodes in an FL setup. This approach achieves over 98.7% accuracy for 33 bacterial classes, as evidenced by metrics such as accuracy, precision, and recall during training. Integrating MobileNetV2 allows for faster convergence and reduced communication overhead during federated updates, supporting efficient and scalable processing capabilities for real-time creation of bacterial DTs across multiple clients on mobile platforms. Its compact and efficient design positions our framework well for future commercial applications, driving widespread adoption in healthcare and environmental monitoring.

Moreover, using FL with CNN in the proposed framework significantly improves training speed and accuracy compared to traditional centralized CNN models. As a result, the CNN-FL framework with 2 and 3 clients achieves 95% accuracy within the first 20 rounds, whereas the centralized CNN model requires over 110 epochs to reach the same level. Additionally, our framework attains over 98% accuracy in only 40 rounds, while centralized CNNs need 120 epochs for similar results. This dramatic reduction in training rounds underscores our optimization strategies' effectiveness, enabling faster deployment and iteration of models across multiple laboratories. Therefore, achieving high accuracy in significantly fewer rounds allows for more efficient use of computational resources and reduces the time required for model training, particularly beneficial in environments where rapid deployment and iteration are critical. The superior performance of the CNN-FL framework highlights its potential for real-world applications, where optimizing convergence speed and accuracy is essential.

The core of our framework relies on computer vision and pattern recognition, which allows it to operate effectively as long as we have an adequate number of species images for training. The framework's ability to generalize across different categories of data makes it adaptable to various biological assets, as it does not rely on the specific type or inherent properties of microorganisms. Instead, its strength lies in its capacity to learn patterns from the input data, regardless of species characteristics. To expand this framework to other biological assets, such as tissues, organs, or entire biological systems, the same principles of image-based pattern recognition and deep learning can be applied. The adaptability comes from the fact that CNNs, used within the framework, are versatile and can handle the increased complexity of these biological structures. For instance, instead of bacterial cells, the system could be trained on histological images of tissues, 3D imaging data from organs, or microscopic data from bio-nano structures. The key challenge is ensuring that a sufficient and diverse dataset of images is available for training the model, similar to microorganisms.

Furthermore, the integration of IoBNT technology within the framework can be extended to capture detailed data from biological systems at different scales. This would enable accurate modeling of

larger biological assets while maintaining efficient data acquisition and transmission. For complex systems like organs or tissues, where interactions between components are more intricate than with microorganisms, additional layers of pattern recognition could be introduced, such as temporal or 3D spatial patterning, which would allow the system to handle time-series or volumetric data. Ultimately, the proposed framework's strength lies in its flexibility, meaning that as long as a robust dataset is provided for training, it can be adapted to various biological assets beyond microorganisms, facilitating applications in diverse fields of biotechnology and digital health.

2.6.4 Implementation Challenges

In implementing the framework, we encountered a range of practical challenges that influenced deployment in a lab environment. From hardware limitations to data privacy, each presented unique adjustments to make the framework feasible. This section highlights these key challenges and how we addressed them, along with considerations for future improvements. Practical use of IoBNT required adapting our setup to specific hardware needs. One main issue was sourcing IoBNT sensors with the resolution necessary for capturing nano-scale biological data, as many existing lab sensors do not meet this precision. These specialized sensors often demanded more processing power to operate MobileNetV2 locally, which pushed the limits of the devices we initially used. Additionally, the energy demands of continuous data collection required us to look for low-power alternatives to extend device operation time without frequent recharging. Future work will benefit from energy-efficient hardware optimized for nano-scale applications to enable more sustainable, long-term use.

Deploying FL on IoBNT devices introduced processing demands, especially for training MobileNetV2 locally. Each device needed to complete training independently before syncing with the central server. While MobileNetV2 is designed for mobile use, our setup, which included more extensive biological data, tested the devices' capabilities. Synchronization delays between devices led to added latency in the data aggregation process. To address this, we reduced model complexity where feasible and optimized the communication protocol. Moving forward, lightweight edge hardware, such as TPUs, could further reduce latency and support real-time processing. Data privacy remained a priority, as each IoBNT device handled sensitive biological data. The decentralized nature of FL meant data stayed on the local device, reducing exposure. However, we needed to secure model aggregation on the server, as combined updates could reveal indirect data details. We implemented encrypted data transfers and ensured compliance with regulatory standards, while training personnel on privacy protocols to protect the framework end-to-end. In future implementations, integrating additional privacy-preserving techniques like differential privacy could further improve security.

2.6.5 The Framework's Importance

The framework proposed in this study represents a fundamental shift in how biotechnological processes can be managed and optimized, with profound implications for several industries. In biotechnology, pharmaceuticals, and healthcare sectors, the DT framework can offer a robust solution for real-time

monitoring, simulation, and optimization of biological systems. Specifically, it can address a long-standing challenge in biomanufacturing, where the reliability and accuracy of production processes are critical. By enabling the creation of real-time DTs of microorganisms and biological systems, the proposed framework can significantly enhance the ability of industries to predict system behavior, troubleshoot issues, and optimize workflows without the need for extensive physical trials. For instance, in pharmaceutical manufacturing, where precision is paramount, this integration can allow for predictive modeling of drug interactions, optimizing dosages, and refining production processes with unprecedented accuracy. The ability to fine-tune these processes without halting production lines not only improves productivity but can also ensure higher quality control, potentially reducing costs and time to market.

Furthermore, the framework's decentralized structure can allow for greater scalability, which is essential for industries with distributed manufacturing operations or research facilities. By utilizing FL, industries can train machine learning models collaboratively across multiple facilities without needing to centralize sensitive biological data, thereby ensuring privacy and compliance with data security regulations, such as the GDPR in Europe and HIPAA in the United States. This is particularly relevant for industries managing vast quantities of sensitive healthcare data, where security and privacy are of utmost concern. By enabling real-time modeling of patient-specific biological systems, the framework can offer unprecedented opportunities for personalized treatment plans that adapt in real-time based on patient responses. This can mark a significant advancement in the delivery of healthcare, contributing to more effective, efficient, and tailored treatments.

The proposed DT framework extends the existing body of literature on both DTs and Federated Learning, particularly in the context of their application to biotechnology and healthcare. Previous studies on DTs have largely focused on engineering and industrial applications, with relatively few exploring the unique challenges posed by biological systems. Incorporating IoBNT into the DT framework adds a novel dimension to the existing literature. While IoT applications are well-explored in various fields, IoBNT specifically targets biological systems at the nano and micro scales, an area that remains underexplored. Additionally, the application of FL in this framework is an important contribution to literature, particularly given the increasing focus on decentralized ML in medical and healthcare research. Existing studies on FL in healthcare focus primarily on clinical data; this work expands on those studies by applying FL to biological data from IoBNT systems, thereby addressing issues of privacy and security while also improving the scalability of DTs in biotechnology.

This work also contributes to the literature on bandwidth optimization in distributed networks, an important consideration in industries handling large datasets. By demonstrating how FL can drastically reduce the bandwidth required for data transmission between laboratories and hospitals, the framework can offer a significant improvement over traditional centralized models, which can be bandwidth-intensive and difficult to scale. This will be especially important for researchers and engineers working on large-scale biological data networks, as it provides a scalable solution to data transfer challenges.

Moreover, this framework can aid governments in managing healthcare infrastructure more efficiently. The ability to monitor and optimize the performance of biological systems in real-time can

lead to more efficient use of medical resources, such as optimizing drug manufacturing processes or personalizing medical treatments. This aligns with governmental goals of reducing healthcare costs while improving patient outcomes, making the proposed framework a valuable asset for healthcare policymakers. Finally, the framework's focus on integrating IoBNT with DTs offers significant potential for environmental monitoring, a key concern for governments aiming to combat climate change and environmental degradation. By enabling real-time monitoring of ecosystems at the nano and micro levels, governments can use this technology to track changes in biodiversity, monitor pollution levels, and predict the impact of environmental policies in real-time. This aligns with global sustainability goals, as it provides a means of ensuring that policy interventions are having the desired effects.

Chapter 3

A Multi-Model PINN Framework Empowered by IoBNT for Digital Twins

3.1 Introduction

DT technology is transforming biological processes by enabling real-time predictive modeling and optimization. However, implementing DTs at the micro- and nano-scale presents significant challenges in data extraction, transmission, and computation due to the complexity of biological environments. To address these challenges, this report proposes a novel multi-model PINN framework leveraging IoBNT technology to create DTs of physics-based complex systems and phenomena governed by PDEs or other mathematical models. The proposed framework bridges the gap between the physics-driven understanding of systems and data-driven approaches to seamless digitalization of nonlinear processes based on theoretical knowledge and data. IoBNT enhances system dynamics by capturing precise data at micro and nano scales, significantly reducing error rates compared to traditional IoT. The framework incorporates multiple NN architectures, including Fully Connected Neural Networks (FCNNs), Residual Block Neural Networks (ResBlock NNs), and Recurrent Neural Networks (RNNs), to ensure a robust and efficient processing core for monitoring and constructing DTs of these systems. Moreover, the framework allows for flexibility in the influence of governing PDEs and measured data.

This novel approach facilitates digital twinning for systems inherently governed by physics, enabling the creation of DTs that capture their intrinsic nature. As a benchmark, the framework was implemented and tested on Microbial Growth Concentration (MGC) and Substrate Growth Concentration (SGC), described by Monod equations [109], to evaluate its performance under complex and nonlinear kinetics. Furthermore, it offers key functionalities for extracting, transferring, preparing, and processing physics-based data to create reliable and real-time DTs. By compensating for data gaps and effectively handling nano-scale sensors, the IoBNT-PINN framework ensures trustworthy, data-driven decision-making. This makes the proposed framework particularly suited for industrial applications where communication reliability and predictive precision are critical. Key contributions and features of the framework are as follows.

In summary, we propose a novel multi-model PINN framework integrated with IoBNT for physics-based DT systems. This pioneering integration of PINNs and IoBNT transforms the development of DTs by enhancing accuracy, data reliability, and scalability for complex biological systems. To optimize data acquisition and transmission, we design and configure IoBNT based on the Monod equations. This specialized IoBNT setup enables precise, efficient, and reliable communication, improving the overall applicability and performance of the framework. The architecture incorporates three DNNs embedded within the PINN structure to address challenges related to varying physical dynamics and inconsistent data quality. This multi-model design offers high adaptability and robust performance across diverse scenarios, aligning with industrial and biomedical requirements. Additionally, the proposed IoBNT configuration reduces data transmission errors by up to 98% under challenging operating conditions, establishing a resilient foundation for future research in DT modeling of complex systems.

The remainder of this chapter is organized as follows. Section 3.2 presents the system model, structured across four layers: the Physical Twin Layer, IoBNT Layer, Data Processing Layer, and Application Layer. Section 3.3 introduces the proposed PINN-based structures incorporating IoBNT for modeling microbial growth and substrate optimization. Section 3.4 outlines the simulation setup and evaluation metrics. Section 3.5 provides a comprehensive performance evaluation under two different scenarios and demonstrates the effectiveness of IoBNT in reducing error rates. Finally, Section 3.6 discusses the framework's contributions, addresses implementation challenges, and outlines future research directions.

3.2 System Model

This section describes the system model that integrates the proposed multi-model PINN framework with IoBNT. This integration aims to enhance applications in digital twinning for physics-based processes and complex systems. The architecture of this model, shown in Fig. 3.1, is organized into four key layers: the physical twin layer, the IoBNT layer, the data processing layer, and the application layer. Accordingly, the physical twin layer, positioned at the bottom of Fig. 3.1, represents real-world processes and systems. These are characterized by mathematical formulations such as Partial Differential Equations (PDEs) or Stochastic Differential Equations (SDEs) and include other physics-based descriptions. In this framework, the physical twin layer captures real phenomena, such as microbial and substrate growth, which are critical to understanding system behavior. Additionally, above the physical layer is the IoBNT layer, which plays a key role in sensing and transmitting data from nano- and micro-level phenomena and processes. In this layer, information from the physical twin layer, such as biological growth patterns, is collected and transferred to the computational layers for further analysis.

The data processing layer, situated above the IoBNT layer, combines this data with physics-based insights to optimize predictive models. This layer includes five different NNs to ensure computational flexibility and adaptability to various scenarios. The choice of NN depends on data quality, quantity, and the reliability of the digital twin being developed.

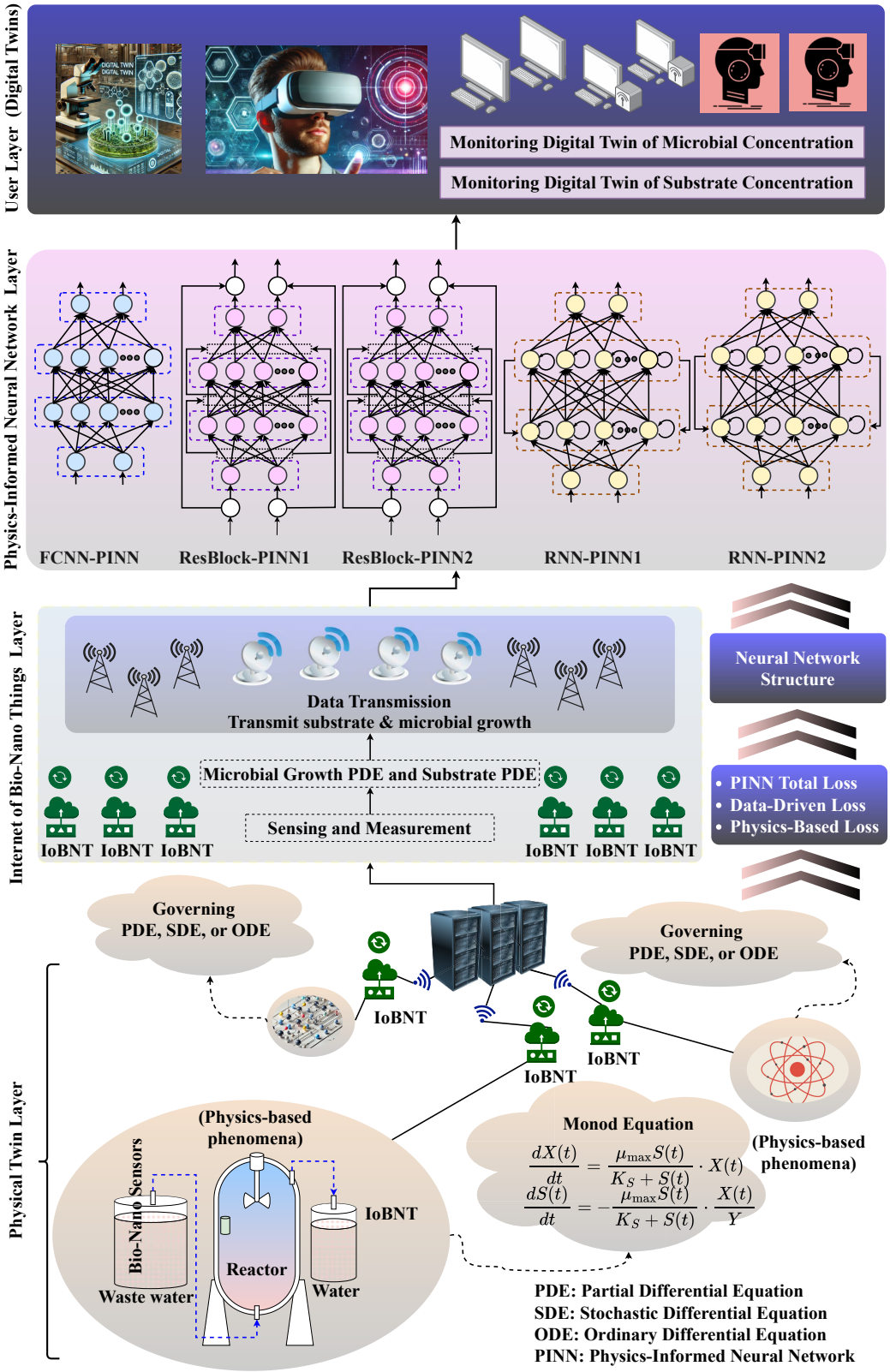

Figure 3.1: The proposed system model integrates a multi-model PINN framework with IoBNT, organized into four layers: physical twin, IoBNT, data processing, and application layers. This structure captures real-world phenomena, processes data at nano- and micro-levels, combines it with physics-based models for accurate predictions, and provides an interactive interface for real-time monitoring and decision-making in digital twin applications.

This flexible design ensures robust and precise predictive capabilities for diverse applications. At the top of the architecture, the user layer provides an interactive interface. This interface allows real-time monitoring, analysis, and decision-making by leveraging the digital twins created from the underlying layers. The user layer connects the technical framework with practical system management, ensuring usability and accessibility for end-users.

3.2.1 Physical Twin Layer

The physical twin layer represents the real-world environment where physical processes and phenomena naturally occur. This layer forms the foundation of the proposed framework by capturing and modeling the actual behavior of systems in various domains, such as bioreactors in manufacturing, environmental monitoring systems, or industrial processes. At its core, this layer shows the complexities of real-world dynamics by leveraging mathematical representations. These include Partial Differential Equations (PDEs) for spatially and temporally distributed phenomena, Stochastic Differential Equations (SDEs) for processes influenced by randomness and uncertainty, and other governing dynamic systems that describe deterministic and probabilistic behaviors. Examples include fluid dynamics in chemical reactors, microbial growth kinetics, and mechanical vibrations in structural systems. This layer represents the environment's quantities, such as temperature, pressure, concentration levels, and biological activity. The parameters serve as the basis for describing and understanding the system's state and evolution.

3.2.2 IoBNT Layer

The IoBNT layer of the proposed framework functions as the communication backbone of the proposed framework, seamlessly connecting the physical and computational domains. It plays a vital role in transmitting real-world data from the physical twin layer to the computational layers, enabling effective analysis and decision-making. In addition, this layer is equipped with advanced bio-nano sensors deployed within the physical twin environment. These sensors collect high-resolution data. The data collection process is highly sensitive and precise, allowing for the observation of even the smallest fluctuations within the system [108]. In practical applications, the IoBNT layer can leverage specialized nano-scale nodes for communication, ensuring low-latency and real-time data transfer [68, 125]. These nodes are optimized to handle the challenges of nano-scale environments, such as limited power availability and potential signal interference, while maintaining robust connectivity [126]. This capability ensures uninterrupted monitoring, making the IoBNT layer indispensable for applications requiring stringent quality control, such as manufacturing or real-time monitoring. Overall, the IoBNT layer is central to the framework's functionality, providing granular, real-time insights that bridge the gap between the physical twin layer and computational analysis. Its ability to operate at the nano-scale enables transformative advancements in monitoring and managing complex systems.

3.2.3 Data Processing Layer

Data processing serves as the computational core of the proposed framework, integrating physics-based knowledge with data-driven methodologies. This hybrid approach enables accurate and reliable predictions of physical processes by leveraging both theoretical models and experimental data. This layer combines domain-specific mathematical models, such as Monod kinetics in this study, with NN architectures to define physics-based loss functions. These loss functions ensure that the predictions generated by the network are consistent with established scientific principles. For example, in microbial growth studies, Monod kinetics provide a foundational framework to describe the relationship between substrate concentration and microbial growth rates. By embedding such models into the loss functions, the PINN layer enforces physical consistency and aligns its outputs with known system behaviors.

In parallel, the data-driven loss component of this layer minimizes the differences between model predictions and actual observations collected from the IoBNT layer. This dual-loss approach ensures robust performance, even when the input data is sparse, noisy, or incomplete. By balancing the contributions of physics-based and data-driven components, the PINN layer achieves a synergistic effect that enhances the overall predictive capability. This hybrid strategy enables the data processing layer to simulate complex phenomena with high fidelity. The combination of physics-informed insights and adaptive data learning allows this layer to capture intricate interactions and emergent behaviors within the system.

3.2.4 Application Layer

The application layer represents the interface through which stakeholders interact with DTs, providing a dynamic and accessible virtual representation of the underlying processes. It integrates real-time data collected from the IoBNT layer and predictive outputs generated by the data processing layer, translating complex computational insights into intuitive and actionable visualizations. Furthermore, the real-time data, continuously streamed from bio-nano sensors, is processed alongside the predictive analytics from the data processing layer. The resulting visualizations allow end-users to track Key Performance Indicators (KPIs), monitor critical system parameters, and identify potential anomalies or inefficiencies. Additionally, the application layer incorporates predictive analytics, empowering users to forecast system behaviors and optimize operational strategies. By combining historical data, real-time monitoring, and physics-based predictions, this layer ensures that decision-making is both data-driven and proactive. Users can adjust process parameters, schedule maintenance, or implement corrective actions based on the insights provided.

3.3 Proposed PINN's Structures Using IoBNT for For Microbial Growth and Substrate Optimization

In this chapter, the proposed IoBNT are designed to real-time monitoring of microbial growth and nutrient levels according to Monod kinetics. The nutrient concentration, denoted as $S(t)$, serves as the critical resource required for microbial proliferation, while microbial concentration is represented as $X(t)$. These interactions are governed by Monod kinetics, a widely recognized model that describes the relationship between microbial growth and nutrient availability [127]. The IoBNT framework goes beyond simple measurement by utilizing biochemical parameter variations to enhance system performance. It achieves this by transmitting the collected data to the data processing layer, where the feedback mechanism optimizes microbial growth and substrate consumption. This integration of real-time sensing with computational modeling represents a pivotal feature of the system.

3.3.1 Substrate Dynamics with Monod Kinetics

Substrate consumption adheres to Monod kinetics, which models the reduction in nutrient levels over time t as a result of microbial activity [127]. The dynamics of substrate utilization can be expressed through the following differential equation [128]:

$$\frac{dS(t)}{dt} = -\frac{\mu_{\max} S(t)}{K_S + S(t)} \frac{X(t)}{Y}, \tag{3.1}$$

where $\mu_{\max}$ represents the maximum microbial growth rate achievable under conditions of abundant substrate availability, K_S is the Monod constant signifying the substrate concentration at which the growth rate reaches half of $\mu_{\max}$, and Y denotes the yield coefficient, which measures the efficiency of converting substrate into biomass. The expression $\frac{\mu_{\max} S(t)}{K_S + S(t)}$ defines the specific growth rate, which asymptotically approaches $\mu_{\max}$ as the substrate concentration becomes very large ($S(t) \to \infty$). The negative sign in equation (3.1) indicates substrate depletion over time. By dynamically maintaining $S(t)$ within an optimal range through IoBNT sensor feedback, the system promotes sustained microbial growth and maximizes nutrient efficiency, providing the PINN model with precise and high-quality inputs.

3.3.2 Microbial Growth Dynamics

The microbial concentration, $X(t)$, grows over time as the consumption of the substrate fuels microbial proliferation [129]. The rate of microbial growth is described by the following equation:

$$\frac{dX(t)}{dt} = \frac{\mu_{\max} S(t)}{K_S + S(t)} X(t). \tag{3.2}$$

Equation (3.2) demonstrates the direct relationship between microbial growth and substrate availability. Higher substrate concentrations result in faster microbial growth, while limited substrate avail-

ability leads to a reduction in growth. By continuously transmitting real-time measurements of $S(t)$ and $X(t)$, the IoBNT framework enables the PINN model to adaptively optimize microbial proliferation in response to fluctuating nutrient conditions.

3.3.3 Loss Functions

The PINN employs several components in its loss function to ensure it fits observed data accurately while also obeying Monod kinetics, which describe microbial growth. This means the model does not just learn from raw data, it also respects the known scientific relationships that govern the system. By balancing both data-fitting and theoretical constraints, the PINN achieves high predictive accuracy without violating the established kinetics rules. This loss function integrates both data-driven and physics-based elements, enabling a balance between empirical precision and adherence to physical principles. The data-driven loss $\mathcal{L}_{\text{data}}$ focuses on reducing the differences between observed and predicted values for $S(t)$ and $X(t)$, ensuring the model remains closely aligned with real-world data:

$$\mathcal{L}_{\text{data}} = \frac{1}{N}\sum_{i=1}^{N}\left(\left(S_i(t)-\hat{S}_i(t)\right)^2+\left(X_i(t)-\hat{X}_i(t)\right)^2\right), \tag{3.3}$$

where $S_i(t)$ and $X_i(t)$ represent the observed substrate and microbial concentrations, while $\hat{S}_i(t)$ and $\hat{X}_i(t)$ denote their corresponding predicted values. The physics-based loss $\mathcal{L}_{\text{physics}}$ ensures adherence to Monod kinetics by penalizing any deviations from the governing equations:

$$\begin{aligned}\mathcal{L}_{\text{physics}} = \frac{1}{N}\sum_{i=1}^{N}\Bigg(&\left(\frac{d\hat{S}(t)}{dt}+\frac{1}{Y}\mu(\hat{S}(t))\hat{X}(t)\right)^2\\&+\left(\frac{d\hat{X}(t)}{dt}-\mu(\hat{S}(t))\hat{X}(t)\right)^2\Bigg),\end{aligned} \tag{3.4}$$

where $\mu(\hat{S}(t)) = \frac{\mu_{\max}\hat{S}(t)}{K_S+\hat{S}(t)}$ represents the Monod-based growth rate as a function of the predicted substrate concentration. This term ensures that the model's predictions remain consistent with the physical principles governing microbial growth and substrate utilization. The total loss function, $\mathcal{L}_{\text{total}}$, integrates all components, including terms for initial and boundary conditions, creating a comprehensive and robust optimization framework:

$$\begin{aligned}\mathcal{L}_{\text{total}} &= \lambda_{\text{data}}\mathcal{L}_{\text{data}} + \lambda_{\text{physics}}\mathcal{L}_{\text{physics}}\\&+\lambda_{\text{initial}}\mathcal{L}_{\text{initial}} + \lambda_{\text{boundary}}\mathcal{L}_{\text{boundary}}.\end{aligned} \tag{3.5}$$

The weights λ_{data}, λ_{physics}, λ_{initial}, and $\lambda_{\text{boundary}}$ regulate the relative importance of each loss component. This combined loss function enables the model to maintain high predictive accuracy while

adhering to physical laws and aligning with empirical observations.

The proposed multi-model PINN framework incorporates three types of NN architectures: FCNN, ResBlock NN, and RNN. These architectures are detailed in this section. For all the models, the same loss function, as defined in (3.2), is utilized to ensure consistency across the framework.

3.3.4 Architecture of FCNN-PINN

This section provides a detailed description of the FCNN architecture within the proposed framework, along with the associated training algorithm [130, 131, 132]. Fig. 3.2 shows the architecture of the proposed PINN using FCNN. The input layer for each proposed architecture includes three primary variables obtained from the IoBNT system: time t, substrate concentration $S(t)$, and microbial concentration $X(t)$. Additionally, the feedback from the loss function is included as an input in the first layer, enabling dynamic adjustments based on the optimization process. This combination of inputs captures both the temporal and biochemical states of the system. The inputs are then passed through a series of hidden layers with varying configurations depending on the specific architecture. Details of these configurations are provided in the subsequent sections.

The output layer produces predictions for the substrate and microbial concentrations, denoted as $\hat{S}(t)$ and $\hat{X}(t)$, respectively. To enforce adherence to the underlying physical laws, the model uses automatic differentiation to compute derivatives, such as $\frac{d\hat{S}(t)}{dt}$ and $\frac{d\hat{X}(t)}{dt}$. These derivatives are critical for ensuring that the predicted dynamics align with the governing equations, maintaining both empirical accuracy and physical consistency. The FCNN processes input data $x(t) \in \mathbb{R}^2$, where $x(t) = [S(t), X(t)]^\top$, through hierarchical transformations in multiple layers. The input layer maps $x(t)$ into a higher-dimensional feature space [130, 133]:

$$h^{(0)} = \tanh\left(W_{\text{input}} x(t) + b_{\text{input}}\right), \tag{3.6}$$

where $W_{\text{input}} \in \mathbb{R}^{D_{\text{in}} \times D_h}$ and $b_{\text{input}} \in \mathbb{R}^{D_h}$ are the weights and biases of the input layer. The network includes two groups of three hidden layers, where each hidden layer l performs the transformation:

$$h^{(l+1)} = \tanh\left(W^{(l)} h^{(l)} + b^{(l)}\right), \quad l = 1, \ldots, n, \tag{3.7}$$

where $W^{(l)} \in \mathbb{R}^{D_h \times D_h}$ and $b^{(l)} \in \mathbb{R}^{D_h}$. The nonlinear activation function $\tanh$ is applied element-wise. Finally, the output layer maps the hidden representation to the predicted substrate and microbial concentrations:

$$\begin{bmatrix} \hat{S}(t+1) \\ \hat{X}(t+1) \end{bmatrix} = W_{\text{output}} h^{(6)} + b_{\text{output}}, \tag{3.8}$$

where $W_{\text{output}} \in \mathbb{R}^{D_h \times D_{\text{out}}}$ and $b_{\text{output}} \in \mathbb{R}^{D_{\text{out}}}$ are the output weights and biases, respectively.

Training algorithm: The training algorithm minimizes the total loss function $\mathcal{L}_{\text{total}}$, which has been previously defined, by iteratively updating the model parameters. The key steps in the training process are as follows:

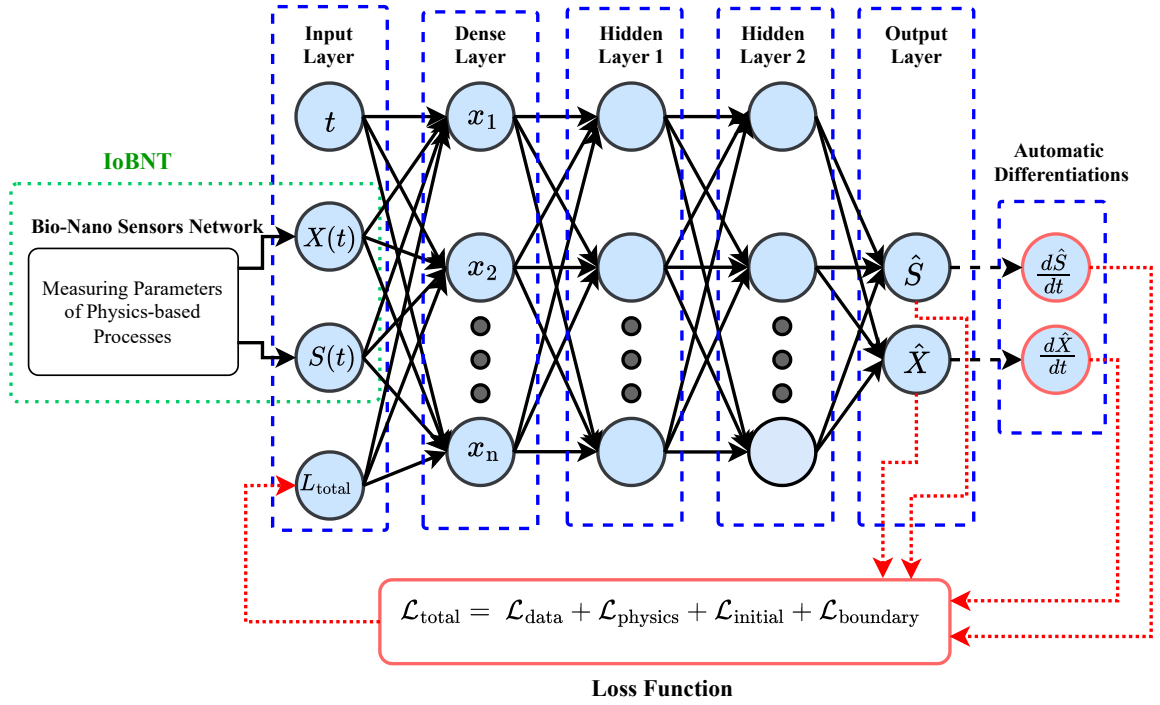

Figure 3.2: Architecture of the PINN with FCNN.

Forward pass: The forward pass propagates the input $x(t)$ through the network layers as defined by (3.6), (3.7), and (3.8), producing predictions $\hat{S}(t+1)$ and $\hat{X}(t+1)$. Automatic differentiation computes the predicted time derivatives:

$$\frac{d\hat{S}(t)}{dt} = \frac{\partial \hat{S}(t)}{\partial t}, \quad \frac{d\hat{X}(t)}{dt} = \frac{\partial \hat{X}(t)}{\partial t}. \tag{3.9}$$

Backward pass: The backward pass computes gradients of the total loss $\mathcal{L}_{\text{total}}$ with respect to the network parameters. For each layer, the gradients are calculated using backpropagation:

$$\frac{\partial \mathcal{L}_{\text{total}}}{\partial W^{(l)}} = \delta^{(l)} h^{(l-1)\top}, \quad \frac{\partial \mathcal{L}_{\text{total}}}{\partial b^{(l)}} = \delta^{(l)}, \tag{3.10}$$

where $\delta^{(l)}$ is the error term propagated backward:

$$\delta^{(l)} = \left(W^{(l+1)\top}\delta^{(l+1)}\right) \odot \tanh'(z^{(l)}), \quad z^{(l)} = W^{(l)}h^{(l-1)} + b^{(l)}. \tag{3.11}$$

Physics-informed constraints: The physics-based constraints, derived from Monod kinetics, are enforced during training:

$$\frac{dS(t)}{dt} = -\frac{\mu_{\max} S(t)}{K_S + S(t)} \frac{X(t)}{Y}, \quad \frac{dX(t)}{dt} = \frac{\mu_{\max} S(t)}{K_S + S(t)} X(t). \tag{3.12}$$

These constraints guide the network's predictions to remain consistent with the governing biochemical processes.

Parameter update: The model parameters $\Theta = \{W_{\text{input}}, W^{(l)}, W_{\text{output}}, b_{\text{input}}, b^{(l)}, b_{\text{output}}\}$ are updated using gradient-based optimization:

$$\Theta^{(k+1)} = \Theta^{(k)} - \eta \nabla_{\Theta} \mathcal{L}_{\text{total}}, \tag{3.13}$$

where η is the learning rate, and k is the iteration index.

Iterative training: The network is trained iteratively for a fixed number of epochs N_{epochs}. During each epoch, the total loss $\mathcal{L}_{\text{total}}$ is minimized:

$$\min_{\Theta} \mathcal{L}_{\text{total}}. \tag{3.14}$$

The training process ensures that the model accurately predicts microbial and substrate dynamics while adhering to the Monod kinetics.

3.3.5 Architecture of ResBlock-PINN

The proposed ResBlock within the PINN framework introduces skip connections to alleviate the vanishing gradient problem and improve gradient flow during training [134, 135, 136]. This architecture efficiently models complex nonlinear relationships while adhering to the physical constraints defined by Monod kinetics. Fig. 3.3 demonstrates the use of residual connections to enhance the learning of microbial and substrate dynamics. The ResBlock NN comprises a series of residual blocks, each containing two dense layers and a skip connection. Let the input to the i-th residual block be $x_i \in \mathbb{R}^d$. The output of the residual block is defined as [137, 138, 139]:

$$x_{i+1} = x_i + F(x_i; \Theta_i), \tag{3.15}$$

where $F(x_i; \Theta_i)$ represents the transformation applied by the dense layers in the i-th block, parameterized by weights and biases Θ_i. The transformation $F(x_i; \Theta_i)$ is given by:

$$F(x_i; \Theta_i) = \sigma\left(W_{i,2}\sigma(W_{i,1}x_i + b_{i,1}) + b_{i,2}\right), \tag{3.16}$$

where $W_{i,1}, W_{i,2} \in \mathbb{R}^{d\times d}$ are weight matrices, $b_{i,1}, b_{i,2} \in \mathbb{R}^d$ are biases, and σ is the activation function, such as $\tanh$. The network output y for an input x is computed by sequentially passing the input through the residual blocks and a final output layer:

$$y = W_o x_L + b_o, \tag{3.17}$$

where x_L is the output of the last residual block, and $W_o \in \mathbb{R}^{d\times 2}, b_o \in \mathbb{R}^2$ are the weights and biases of the output layer.

Training algorithm for ResBlock in PINN framework:

The ResBlock NN is trained by minimizing the total loss $\mathcal{L}_{\text{total}}$, which combines data-driven, physics-

based, initial condition, and boundary condition losses.

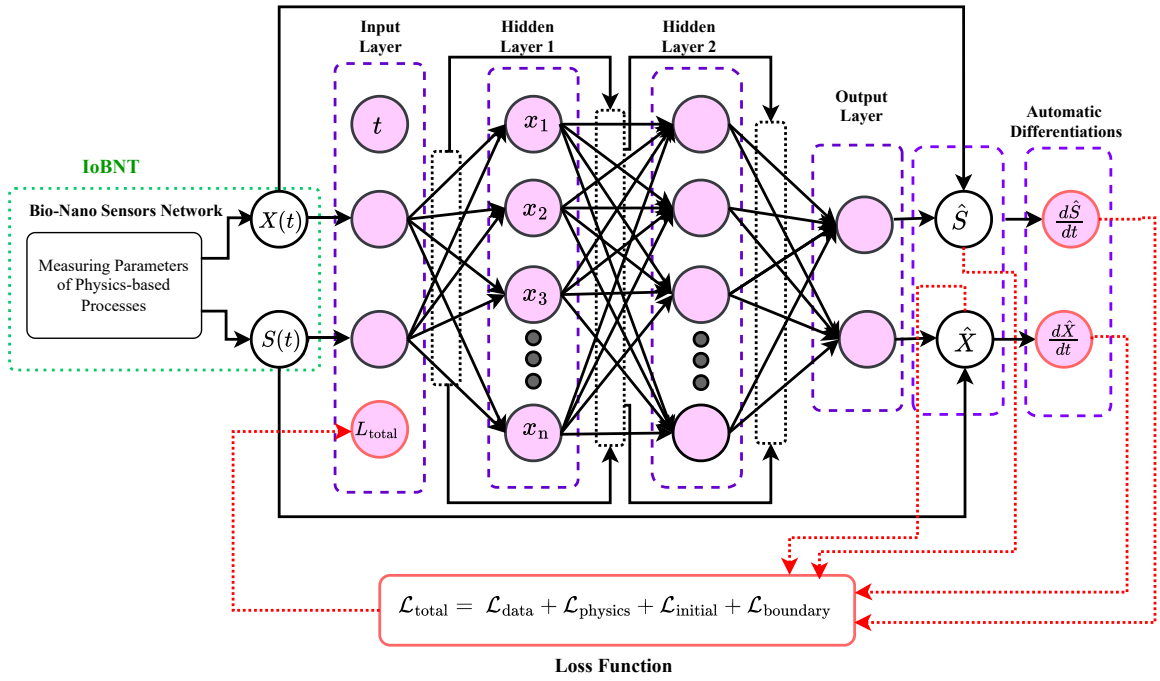

Figure 3.3: Architecture of the proposed PINN-ResBlock.

Forward pass and residual block computation:

During the forward pass, the input x is propagated through each residual block:

$$x_{i+1} = x_i + F(x_i; \Theta_i), \tag{3.18}$$

where $F(x_i; \Theta_i)$ is computed as in (3.16). The final network output is computed using (3.17). For physics-based constraints, automatic differentiation is used to compute the time derivatives $\frac{d\hat{S}(t)}{dt}$ and $\frac{d\hat{X}(t)}{dt}$, ensuring consistency with Monod kinetics:

$$\frac{d\hat{S}(t)}{dt} = -\frac{\mu_{\max}\hat{S}(t)}{K_S + \hat{S}(t)}\frac{\hat{X}(t)}{Y}, \quad \frac{d\hat{X}(t)}{dt} = \frac{\mu_{\max}\hat{S}(t)}{K_S + \hat{S}(t)}\hat{X}(t). \tag{3.19}$$

Backward pass and gradient computation:

The gradients of the total loss $\mathcal{L}_{\text{total}}$ with respect to the network parameters are computed using backpropagation. The gradient of the loss with respect to the weights of the i-th residual block is given by:

$$\frac{\partial \mathcal{L}_{\text{total}}}{\partial W_{i,k}} = \sum_{t=1}^{T} \frac{\partial \mathcal{L}_{\text{total}}}{\partial x_{i+1}} \frac{\partial x_{i+1}}{\partial F(x_i; \Theta_i)} \frac{\partial F(x_i; \Theta_i)}{\partial W_{i,k}}, \tag{3.20}$$

where $k = 1, 2$ denotes the layer index within the residual block.

The chain rule is used to compute the gradient with respect to x_i recursively:

$$\frac{\partial \mathcal{L}_{\text{total}}}{\partial x_i} = \frac{\partial \mathcal{L}_{\text{total}}}{\partial x_{i+1}} \cdot \left(I + \frac{\partial F(x_i; \Theta_i)}{\partial x_i} \right), \tag{3.21}$$

where I is the identity matrix, and $\frac{\partial F(x_i;\Theta_i)}{\partial x_i}$ is computed as:

$$\frac{\partial F(x_i; \Theta_i)}{\partial x_i} = W_{i,1}^{\top} \sigma'(z_i), \tag{3.22}$$

with $z_i = W_{i,1} x_i + b_{i,1}$.

Parameter updates:

The parameters $\Theta = \{W_{i,k}, b_{i,k}, W_o, b_o\}$ are updated using gradient descent:

$$\Theta^{(k+1)} = \Theta^{(k)} - \eta \nabla_{\Theta} \mathcal{L}_{\text{total}}, \tag{3.23}$$

where η is the learning rate, and k is the iteration index.

Iterative training with physics constraints:

The ResBlock NN iteratively optimizes $\mathcal{L}_{\text{total}}$ while enforcing Monod kinetics (3.19). The algorithm repeats forward and backward passes for a predefined number of epochs N_{epochs}, ensuring convergence to the optimal solution:

$$\min_{\Theta} \mathcal{L}_{\text{total}}. \tag{3.24}$$

3.3.6 Arctecture of RNN-PINN

The integration of RNNs within PINNs enables the modeling of dynamic systems by leveraging the temporal sequence learning capability of RNNs alongside the physics-based constraints of PINNs, providing a robust framework for solving time-dependent partial differential equations and forecasting complex behaviors [140, 141]. RNN within the proposed PINN framework leverages its temporal modeling capabilities to capture dynamic relationships between substrate and microbial concentrations. Fig. 3.4 illustrates the integration of sequential processing with physics-based modeling for predicting microbial and substrate dynamics. An RNN processes input data sequentially by updating a hidden state $h(t)$ at each time step. The hidden state at time t is computed using the equation [142, 143]:

$$h(t) = \sigma \left(W_h h(t-1) + W_x x(t) + b_h \right), \tag{3.25}$$

where $h(t) \in \mathbb{R}^{d_h}$ is the hidden state vector, $h(t-1)$ is the hidden state from the previous time step, $W_h \in \mathbb{R}^{d_h \times d_h}$ is the recurrent weight matrix, $W_x \in \mathbb{R}^{d_x \times d_h}$ is the input weight matrix, $b_h \in \mathbb{R}^{d_h}$ is the bias vector, and σ is the activation function, such as $\tanh$. The input vector $x(t) = [S(t), X(t)]^{\top}$ represents substrate and microbial concentrations at time t, where $S(t)$ and $X(t)$ are the substrate and microbial concentrations, respectively.

The output of the RNN, representing the predicted substrate and microbial concentrations at the

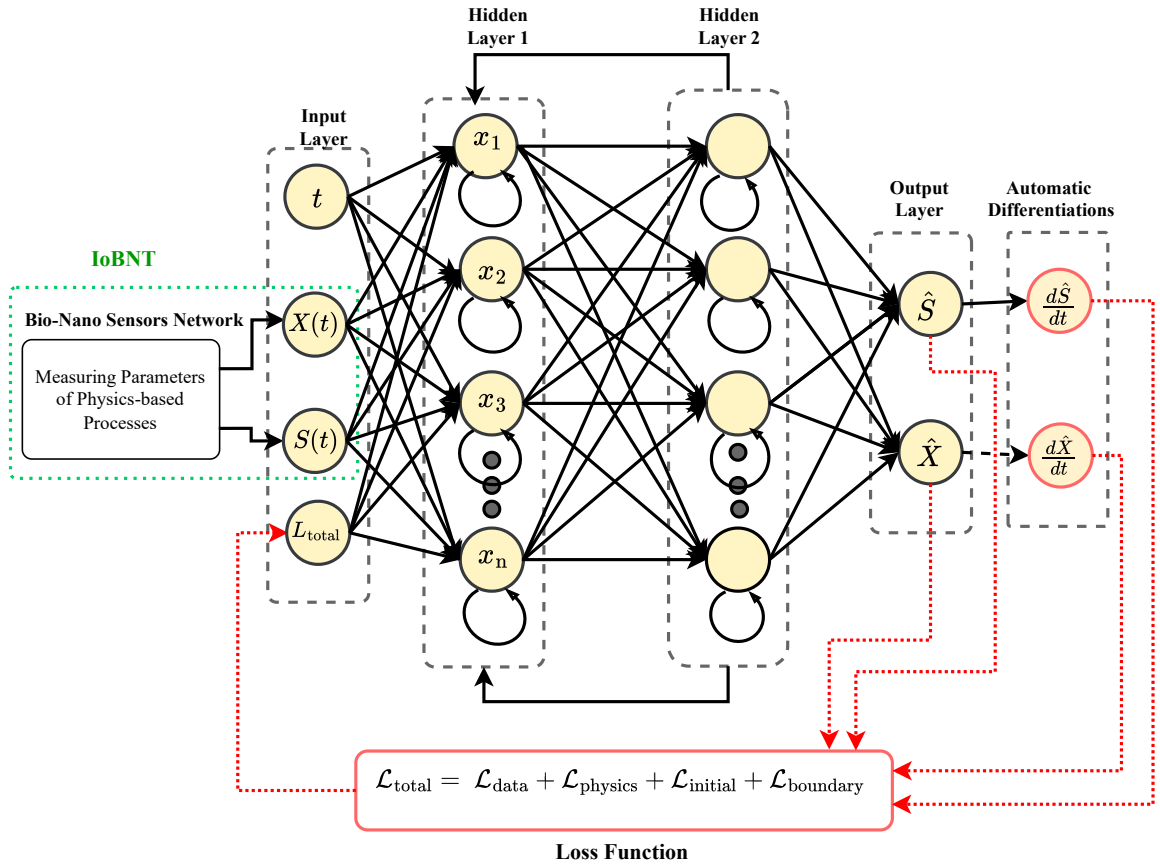

Figure 3.4: Architecture of PINN-RNN.

next time step, is given by:

$$\begin{bmatrix} \hat{S}(t+1) \\ \hat{X}(t+1) \end{bmatrix} = W_o h(t) + b_o, \tag{3.26}$$

where $W_o \in \mathbb{R}^{d_h \times 2}$ is the output weight matrix, and $b_o \in \mathbb{R}^2$ is the output bias vector. The RNN sequentially propagates information through time, enabling it to model dynamic dependencies.

Training algorithm:

The training process minimizes the total loss $\mathcal{L}_{\text{total}}$, combining data-driven, physics-based, initial condition, and boundary condition losses. The algorithm involves forward propagation, gradient computation, and parameter updates.

Forward pass and hidden state propagation:

During the forward pass, the RNN computes hidden states for all time steps $t = 1, 2, \ldots, T$ using the recurrence relation:

$$h(t) = \sigma\left(W_h h(t-1) + W_x x(t) + b_h\right). \tag{3.27}$$

The predicted substrate and microbial concentrations for the next time step are obtained as:

$$\begin{bmatrix} \hat{S}(t+1) \\ \hat{X}(t+1) \end{bmatrix} = W_o h(t) + b_o. \tag{3.28}$$

Automatic differentiation is employed to calculate the time derivatives $\frac{d\hat{S}(t)}{dt}$ and $\frac{d\hat{X}(t)}{dt}$, required for enforcing physics-based constraints [144, 145, 146].

Backward pass and gradient computation:

The gradients of the total loss with respect to the hidden states are computed iteratively using the chain rule. For each time step t, the gradient is given by:

$$\frac{\partial \mathcal{L}_{\text{total}}}{\partial h(t)} = \frac{\partial \mathcal{L}_{\text{total}}}{\partial \hat{S}(t+1)} \frac{\partial \hat{S}(t+1)}{\partial h(t)} + \frac{\partial \mathcal{L}_{\text{total}}}{\partial \hat{X}(t+1)} \frac{\partial \hat{X}(t+1)}{\partial h(t)}, \tag{3.29}$$

where $\frac{\partial \hat{S}(t+1)}{\partial h(t)} = W_o^{(S)}$ and $\frac{\partial \hat{X}(t+1)}{\partial h(t)} = W_o^{(X)}$, with $W_o^{(S)}$ and $W_o^{(X)}$ being rows of W_o corresponding to substrate and microbial predictions, respectively. Backpropagation Through Time (BPTT) is used to compute gradients for all time steps. The gradient of the hidden state at time $t-1$ is calculated recursively as:

$$\frac{\partial \mathcal{L}_{\text{total}}}{\partial h(t-1)} = \frac{\partial \mathcal{L}_{\text{total}}}{\partial h(t)} \cdot \frac{\partial h(t)}{\partial h(t-1)}, \tag{3.30}$$

where:

$$\frac{\partial h(t)}{\partial h(t-1)} = \sigma'(z(t)) W_h, \quad z(t) = W_h h(t-1) + W_x x(t) + b_h. \tag{3.31}$$

Parameter updates:

The gradients with respect to the RNN parameters $\Theta = \{W_h, W_x, W_o, b_h, b_o\}$ are computed as:

$$\frac{\partial \mathcal{L}_{\text{total}}}{\partial W_h} = \sum_{t=1}^{T} \frac{\partial \mathcal{L}_{\text{total}}}{\partial h(t)} \frac{\partial h(t)}{\partial W_h}, \quad \frac{\partial h(t)}{\partial W_h} = \sigma'(z(t)) h(t-1)^\top, \tag{3.32}$$

$$\frac{\partial \mathcal{L}_{\text{total}}}{\partial W_x} = \sum_{t=1}^{T} \frac{\partial \mathcal{L}_{\text{total}}}{\partial h(t)} \frac{\partial h(t)}{\partial W_x}, \quad \frac{\partial h(t)}{\partial W_x} = \sigma'(z(t)) x(t)^\top, \tag{3.33}$$

$$\frac{\partial \mathcal{L}_{\text{total}}}{\partial W_o} = \sum_{t=1}^{T} \frac{\partial \mathcal{L}_{\text{total}}}{\partial h(t)} h(t)^\top, \quad \frac{\partial \mathcal{L}_{\text{total}}}{\partial b_o} = \sum_{t=1}^{T} \frac{\partial \mathcal{L}_{\text{total}}}{\partial h(t)}. \tag{3.34}$$

The parameters are updated using gradient descent:

$$\Theta^{(k+1)} = \Theta^{(k)} - \eta \nabla_\Theta \mathcal{L}_{\text{total}}, \tag{3.35}$$

where η is the learning rate and k denotes the iteration index.

Integration with physics-informed constraints:

The physics-based constraints are enforced by ensuring predictions adhere to Monod kinetics:

$$\frac{dS}{dt} = -\frac{\mu_{\max} S}{K_S + S} \frac{X}{Y}, \quad \frac{dX}{dt} = \frac{\mu_{\max} S}{K_S + S} X. \tag{3.36}$$

The time derivatives $\frac{d\hat{S}(t)}{dt}$ and $\frac{d\hat{X}(t)}{dt}$ are computed using automatic differentiation:

$$\frac{d\hat{S}(t)}{dt} = \frac{\partial \hat{S}(t)}{\partial h(t)} \cdot \frac{\partial h(t)}{\partial t}, \quad \frac{d\hat{X}(t)}{dt} = \frac{\partial \hat{X}(t)}{\partial h(t)} \cdot \frac{\partial h(t)}{\partial t}. \tag{3.37}$$

Iterative optimization:

The forward and backward passes are repeated for a predefined number of epochs N_{epochs}, ensuring convergence to the optimal parameters:

$$\min_{\Theta} \mathcal{L}_{\text{total}}. \tag{3.38}$$

This training algorithm integrates the sequential modeling capabilities of RNNs with the physics-informed framework, ensuring temporal dependencies and physical consistency are simultaneously captured.

3.4 Simulation Settings and Evaluation Metrics

3.4.1 Evaluation Metrics for Model Accuracy and Convergence

To comprehensively evaluate the accuracy and convergence of the proposed framework, key statistical metrics are employed, including Root Mean Squared Error (RMSE) [147], Mean Absolute Error (MAE) [148], and the Coefficient of Determination (R^2) [149]. These metrics provide quantitative insights into the alignment between predicted and observed values and ensure the robustness of the training process. RMSE is a widely used metric that quantifies the square root of the average squared difference between the observed values y_i and the predicted values $\hat{y}_i$.

$$\text{RMSE} = \sqrt{\frac{1}{n}\sum_{i=1}^{n}(y_i - \hat{y}_i)^2}, \tag{3.39}$$

where n represents the total number of data points. A lower RMSE value indicates smaller deviations and better model performance. RMSE emphasizes larger errors more than smaller ones, making it particularly sensitive to outliers. MAE provides a straightforward measure of the average magnitude of errors between observed values y_i and predicted values $\hat{y}_i$:

$$\text{MAE} = \frac{1}{n}\sum_{i=1}^{n}|y_i - \hat{y}_i|. \tag{3.40}$$

Unlike RMSE, MAE treats all errors equally, offering a more robust metric in cases where large errors might unduly influence RMSE. R^2 evaluates the proportion of variance in the observed data y_i that is explained by the predicted values $\hat{y}_i$.

$$R^2 = 1 - \frac{\sum_{i=1}^{n}(y_i - \hat{y}_i)^2}{\sum_{i=1}^{n}(y_i - \bar{y})^2}, \tag{3.41}$$

where $\bar{y}$ is the mean of the observed values. An R^2 value close to 1 signifies that the model effectively captures the variability in the data, whereas values near 0 indicate poor predictive performance. These metrics are computed at regular intervals during training to monitor the model's convergence and predictive accuracy. RMSE quantifies the overall prediction error, providing a holistic measure of model performance and MAE gives an interpretable measure of average error, highlighting the model's general reliability. In addition, R^2 reflects the goodness of fit, ensuring the model aligns with the underlying data trends. A successful training process is characterized by a decreasing trend in RMSE and MAE, alongside an increasing R^2 value [150].

3.4.2 Simulation Settings

Multi-model designs inherently allow for the specialization of each sub-model to address specific aspects of a problem. Hence, this modularity fosters flexibility and adaptability and enables the framework to capture complex, heterogeneous dynamics that a specific architecture might fail to model effectively. Moreover, a multi-model framework overcomes the limitations of a unified architecture by offering a suitable model against sparse or noisy data, which optimizes computational efficiency and improves scalability for complex processes and systems. These attributes make the proposed multi-model PINN frameworks particularly suited for real-time predictive monitoring and DT applications, where precision and reliability are paramount. Therefore, the use of multi-model architectures within the IoBNT-PINN framework is not merely an extension of capability but a strategic enhancement that ensures the framework's effectiveness and adaptability for complex, multidisciplinary challenges.

Additionally, accurate and reliable measurements are critical in all ML models, particularly for robust predictive monitoring in industrial and commercialized applications [151, 152]. The PINN frameworks are inherently adept at addressing challenges associated with sparse or noisy measurements, compensating for many limitations of traditional NNs. However, achieving optimal performance necessitates the careful selection of architectures that align with the specific problem at hand. This highlights the importance of employing a multi-model framework, which allows for the specialization of sub-models to address different aspects of complex systems, thereby enhancing adaptability and accuracy. To illustrate the rationale behind this approach, this study evaluates the proposed framework using two distinct scenarios, each tailored to specific framework settings. Thus, the exploration of scenario-specific methodologies within the proposed framework underscores its adaptability and applicability for diverse academic and industrial applications. By leveraging the strategic advantages of a multi-model framework, this approach empowers researchers and practitioners to address multidisciplinary challenges effectively.

3.4.3 Scenario 1

The hypothesis underpinning scenario 1 is that the type of NN integrated within the PINN framework can compensate for measurement inaccuracies or enhance adaptability to nonlinear systems, regardless of the specific NN architecture. Additionally, this scenario investigates whether the relative weights

assigned to loss functions significantly impact the performance of different architectures for the same system. In this scenario, two integrated architectures, FCNN-PINN1-1 and RNN-PINN1-1, are developed and analyzed. These methods aim to examine the roles of feedforward and recurrent paradigms when embedded within the PINN framework for solving complex problems. Each architecture is configured with distinct weight settings for its loss functions, reflecting different emphases on data accuracy versus the incorporation of physics-based constraints, as detailed in Table 3.1.

The FCNN-PINN1-1 configuration prioritizes data-driven learning, with the loss function weights defined as $\lambda_{\text{data}} = 1.0$, $\lambda_{\text{physics}} = 0.5$, $\lambda_{\text{initial}} = 0.5$, and $\lambda_{\text{boundary}} = 0.5$. This setup evaluates the ability of the FCNN-PINN1-1 framework to rely on measurement data while maintaining minimal dependence on physical laws. Such an arrangement is particularly suited for systems where high-quality measurement data are available, and the physics may not be fully understood or are of secondary importance. Conversely, the RNN-PINN1-1 configuration is tailored for scenarios where data may be sparse or noisy, but the governing physics are well-established. The weights in this case are $\lambda_{\text{data}} = 1.0$, $\lambda_{\text{physics}} = 10.0$, $\lambda_{\text{initial}} = 10.0$, and $\lambda_{\text{boundary}} = 40.0$, indicating a strong emphasis on incorporating physics, initial conditions, and boundary constraints into the training process. This setup assesses the robustness of the RNN-PINN1-1 framework in leveraging well-defined physics to compensate for data limitations. The configurations of these methods and their corresponding weights are summarized in Table 3.1.

3.4.4 Scenario 2

In contrast to the hypothesis in the first scenario, where the focus was on demonstrating the ability of the PINN framework to compensate for weaknesses in measurements and physical complexities, scenario 2 emphasizes the importance of NN architecture in data analysis and processing. While PINNs are inherently capable of handling sparse or noisy data due to their integration of physics-based constraints, the choice of NN architecture significantly impacts performance. Specific architectures can exhibit unique strengths and limitations, making them suitable for particular applications. This realization underpins the feasibility and relevance of employing a multimodal framework in this scenario. In scenario 2, the framework is extended to evaluate and challenge the most suitable NN architectures within the PINN framework. These include FCNN-PINN2-1, ResBlock-PINN2-1, ResBlock-PINN2-2, RNN-PINN2-1, and RNN-PINN2-1. This comprehensive analysis ensures that the framework's applicability is tested across a broad spectrum of scenarios, enabling a deeper understanding of its capabilities and limitations. Furthermore, the configurations for this scenario align closely with insights derived from the literature, enhancing their scientific relevance to specific applications.

Table 3.2 provides the numerical settings and training configurations for the methods analyzed in scenario 2. The selection of loss weights and NN structures reflects their intended applications and expected performance in modeling complex systems. The loss weights for the different methods were chosen to balance the contributions of data consistency, adherence to physical laws, and the enforcement of initial and boundary conditions. For example, FCNN-PINN2-1 utilizes higher weights ($\lambda_{\text{physics}} = 10.0$,

$\lambda_{\text{boundary}} = 40.0$) to ensure robust adherence to physical constraints, making it well-suited for applications where precise physical modeling is critical. Conversely, RNN-PINN2-2 employs lower weights ($\lambda_{\text{physics}} = 0.5$, $\lambda_{\text{boundary}} = 0.5$) to prioritize adaptability in scenarios with less stringent physical requirements. ResBlock-PINN2-1 and ResBlock-PINN2-2 incorporate residual blocks to enhance training efficiency and generalization. ResBlock-PINN2-2, for instance, uses higher $\lambda_{\text{physics}} = 10.0$ and $\lambda_{\text{boundary}} = 20.0$ compared to ResBlock-PINN2-1, aligning its architecture with applications demanding greater physical fidelity. RNN-PINN2-1, with a single recurrent layer, balances simplicity and capability for temporal data processing, while RNN-PINN2-2 adopts a lighter configuration to accommodate scenarios requiring faster adaptability.

Table 3.1: Numerical settings and training configurations for the first scenario using PINN methods

Method	Configuration Details
FCNN-PINN1-1	**Initial Conditions:** $S_0 = 10.0,\ X_0 = 1.0$ **Model Parameters:** $\mu_{\max} = 0.4,\ K_S = 0.5,\ Y = 0.6$ **Loss Weights:** $\lambda_{\text{data}} = 1.0,\ \lambda_{\text{physics}} = 0.5,\ \lambda_{\text{initial}} = 0.5,\ \lambda_{\text{boundary}} = 0.5$ **Neural Network:** Input 60 neurons (`tanh`); 2 groups of 3 hidden layers (60 neurons each); Output 2 neurons
RNN-PINN1-1	**Initial Conditions:** $S_0 = 10.0,\ X_0 = 1.0$ **Model Parameters:** $\mu_{\max} = 0.4,\ K_S = 0.5,\ Y = 0.6$ **Loss Weights:** $\lambda_{\text{data}} = 1.0,\ \lambda_{\text{physics}} = 10.0,\ \lambda_{\text{initial}} = 10.0,\ \lambda_{\text{boundary}} = 40.0$ **Neural Network:** Single RNN layer (60 units, `tanh`); Output 2 neurons

3.4.5 Dataset

Similar to recent studies [153, 154, 155, 156] that leverage the governing equations of the systems for training and evaluating purposes, we utilized synthetic data derived from solving the ODEs of the Monod model. This dataset comprehensively represents microbial and substrate concentrations over time. It includes time points, as well as corresponding substrate and microbial concentrations. A data loss term reduces errors relative to the synthetic training data, while a physics loss term enforces compliance with the Monod model's differential equations governing microbial growth. Additionally, initial and boundary losses ensure consistency with initial conditions and apply constraints on the maximum microbial concentration.

In total, the curated dataset includes 100 temporally distributed samples for each species, resulting in 200 one-dimensional records reflecting substrate and microbial concentrations. Additionally, a 10,000-element spatiotemporal dataset (100 points in time by 100 points in space) is generated for both species, yielding four features: time, space, substrate concentration, and microbial concentration. Each data record in both subsets aligns with Monod-based reaction kinetics, thereby preserving consistency with the underlying biological interaction dynamics.

Table 3.2: Numerical settings and training configurations for the second scenario using PINN methods

Method	Configuration Details
FCNN-PINN2-1	**Initial Conditions:** $S_0 = 10.0,\ X_0 = 1.0$
	Model Parameters: $\mu_{\max} = 0.4,\ K_S = 0.5,\ Y = 0.6$
	Loss Weights: $\lambda_{\text{data}} = 1.0,\ \lambda_{\text{physics}} = 10.0,\ \lambda_{\text{initial}} = 10.0,\ \lambda_{\text{boundary}} = 40.0$
	Neural Network: Input 60 neurons (`tanh`); two groups of 3 hidden layers (60 neurons each); Output 2 neurons
ResBlock-PINN2-1	**Initial Conditions:** $S_0 = 10.0,\ X_0 = 1.0$
	Model Parameters: $\mu_{\max} = 0.4,\ K_S = 0.5,\ Y = 0.6$
	Loss Weights: $\lambda_{\text{data}} = 1.0,\ \lambda_{\text{physics}} = 5.0,\ \lambda_{\text{initial}} = 5.0,\ \lambda_{\text{boundary}} = 10.0$
	Neural Network: Input 60 neurons (`tanh`); 2 residual blocks (2 layers of 60 neurons each); Output 2 neurons with skip connections
ResBlock-PINN2-2	**Initial Conditions:** $S_0 = 10.0,\ X_0 = 1.0$
	Model Parameters: $\mu_{\max} = 0.4,\ K_S = 0.5,\ Y = 0.6$
	Loss Weights: $\lambda_{\text{data}} = 1.0,\ \lambda_{\text{physics}} = 10.0,\ \lambda_{\text{initial}} = 10.0,\ \lambda_{\text{boundary}} = 20.0$
	Neural Network: Input 60 neurons (`tanh`); 2 residual blocks (2 layers of 60 neurons each); Output 2 neurons with skip connections
RNN-PINN2-1	**Initial Conditions:** $S_0 = 10.0,\ X_0 = 1.0$
	Model Parameters: $\mu_{\max} = 0.4,\ K_S = 0.5,\ Y = 0.6$
	Loss Weights: $\lambda_{\text{data}} = 1.0,\ \lambda_{\text{physics}} = 1.0,\ \lambda_{\text{initial}} = 1.0,\ \lambda_{\text{boundary}} = 1.0$
	Neural Network: Single RNN layer (60 units, `tanh`); Output 2 neurons
RNN-PINN2-2	**Initial Conditions:** $S_0 = 10.0,\ X_0 = 1.0$
	Model Parameters: $\mu_{\max} = 0.4,\ K_S = 0.5,\ Y = 0.6$
	Loss Weights: $\lambda_{\text{data}} = 1.0,\ \lambda_{\text{physics}} = 0.5,\ \lambda_{\text{initial}} = 0.5,\ \lambda_{\text{boundary}} = 0.5$
	Neural Network: Single RNN layer (60 units, `tanh`); Output 2 neurons

3.5 Performance Evaluation

3.5.1 Performance Evaluation in Scenario 1

This chapter presents the simulation results for the first scenario, focusing on the performance of FCNN-PINN1-1 and RNN-PINN1-1 in estimating substrate and microbial concentrations compared to the physical model.

Convergence Loss and Training of Scenario 1

This section analyzes the convergence loss and training dynamics of the proposed FCNN-PINN1-1 and RNN-PINN1-1 architectures within scenario 1. As shown in Fig. 3.5(a), the convergence of FCNN-PINN1-1 demonstrates a relatively stable behavior, with all loss components, including data, physics, initial, and boundary losses, gradually decreasing. However, the dominance of data loss in the total loss indicates the framework's reliance on high-quality measurement data to achieve meaningful predictions. This reliance suggests that FCNN-PINN1-1 struggles to integrate physics-based constraints effectively when measurements are sparse or noisy. In contrast, Fig. 3.5(b) reveals significant challenges in training RNN-PINN1-1. While the architecture exhibits better alignment with general trends in substrate and microbial concentrations, the convergence of its physics loss plateaus, indicating difficulty in inte-

grating physical and boundary constraints during training. This limitation highlights RNN-PINN1-1's overreliance on measured data and its inability to generalize robustly to nonlinear dynamics. Because it focuses heavily on fitting the measured data, the model effectively "memorizes" these observations without adequately balancing them against the physical equations, which causes the physics-informed loss to plateau. This imbalance hinders the ability of the network to generalize in the presence of nonlinear dynamics that lead to less accurate oscillatory predictions once it ventures beyond the specific data points on which it has been trained.

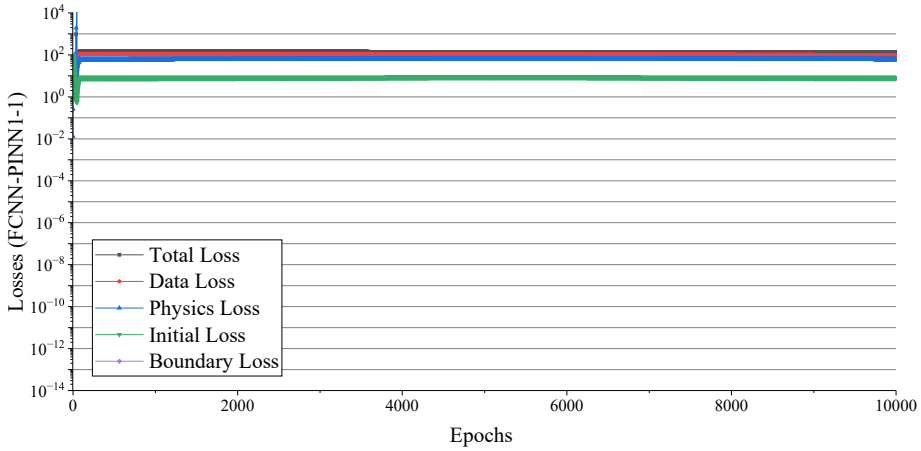

(a)

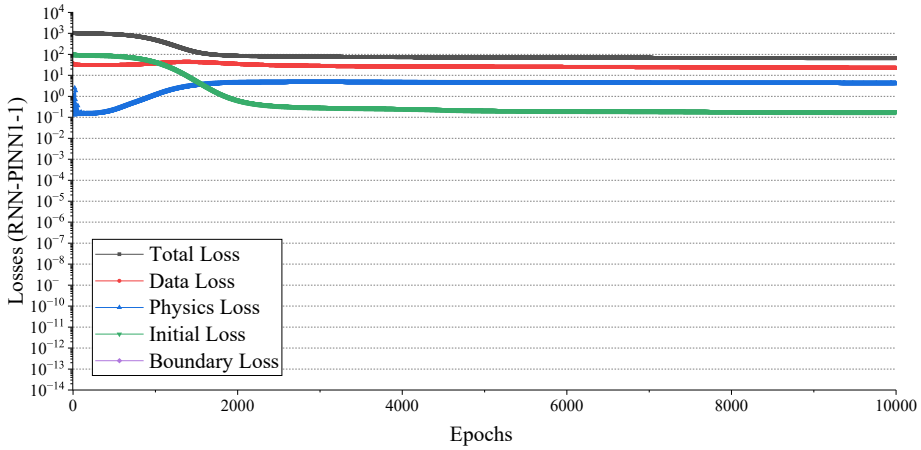

(b)

Figure 3.5: Convergence loss for scenario 1. (a) FCNN-PINN1-1 model losses (Total Loss, Data Loss, Physics Loss, Initial Loss, Boundary Loss); (b) RNN-PINN1-1 model losses.

Furthermore, the model's predictions are marred by oscillations and deviations, undermining its capability for accurate modeling. These findings underscore the limitations of both architectures in the first scenario. The boundary loss is negligible compared to the other loss terms and thus remains undetectable in this figure. The FCNN-PINN1-1 framework fails to balance physical laws with data-driven learning, while the RNN-PINN1-1 model struggles with constrained integration. Such observations emphasize the need for hybrid architectures or tailored frameworks to address sparse data, nonlinear dynamics, and physical constraints effectively.

Performance Analysis of Scenario 1

Fig. 3.6(a) depicts the substrate concentration (i.e., Sub. Con.) predicted by FCNN-PINN1-1 and compares it to the physical model. The prediction shows an unrealistic rapid depletion of substrate, even reaching negative values. This behavior reflects poor robustness and a lack of adherence to physical constraints, indicating that FCNN-PINN1-1 struggles with overfitting or fails to incorporate the temporal dynamics needed for accurate predictions. Accordingly, Fig. 3.6(b) presents the microbial concentration (i.e., Mic. Con.) estimated by FCNN-PINN1-1 relative to the physical model. The model predicts an unrealistic sharp initial growth followed by incorrect saturation dynamics. Fig. 3.6(c) shows the performance of RNN-PINN1-1 in estimating substrate concentration compared to the physical model. The predicted curve exhibits significant oscillations and instability, failing to match the smooth depletion trend observed in the physical model. This deviation indicates that RNN-PINN1-1 struggles to handle the temporal dynamics of the system effectively, because limitations in capturing long-term dependencies and noise.

In addition, Fig. 3.6(d) illustrates the microbial concentration estimated by RNN-PINN1-1 alongside the physical model. The predicted microbial growth shows an initial underestimation and later diverges from the expected saturation behavior. Moreover, Fig. 3.7(a) represents the substrate concentration derived from the physical model, which acts as the target behavior for this scenario. The substrate concentration decreases predictably as microbial activity consumes the substrate. In addition, Fig. 3.7(c) and Fig. 3.7(e) show predictions by FCNN-PINN1-1 and RNN-PINN1-1, respectively. FCNN-PINN1-1 displays an evident inability to maintain the expected concentration trajectory, particularly during the early phases. On the other hand, RNN-PINN1-1 fares better in capturing the general trend but introduces temporal inconsistencies, overestimating the substrate at specific intervals. Both architectures struggle with sparse data and physical constraints, revealing significant limitations in their ability to model biochemical interactions effectively. These findings emphasize the necessity for enhanced architectures and regularization techniques to ensure robustness.

Furthermore, Fig. 3.7(b) depicts microbial concentration as predicted by the physical model, characterized by an initial exponential growth followed by stabilization. This behavior results from the microbial system's saturation effects as substrate availability decreases. Similarly, Fig. 3.7(d) and Fig. 3.7(f) show the microbial concentration predicted by FCNN-PINN1-1 and RNN-PINN1-1, respectively. FCNN-PINN1-1 shows significant discrepancies, particularly during the growth phase, underestimating microbial activity due to its limited capacity to model sequential dependencies. In contrast, RNN-PINN1-1 slightly improves temporal tracking but fails to stabilize predictions, demonstrating oversensitivity to minor variations in sparse data. These inaccuracies highlight the NNs' shortcomings in handling intricate temporal patterns and constraints, suggesting the need for more advanced recurrent mechanisms or hybrid PINN architectures.

In addtion, Tables 3.3 and 3.4 reveal the challenges of using inappropriate architectures for PINN implementations in scenario 1. Both FCNN-PINN1-1 and RNN-PINN1-1 demonstrate significant limitations due to a mismatch between their architectural strengths and the requirements of this problem.

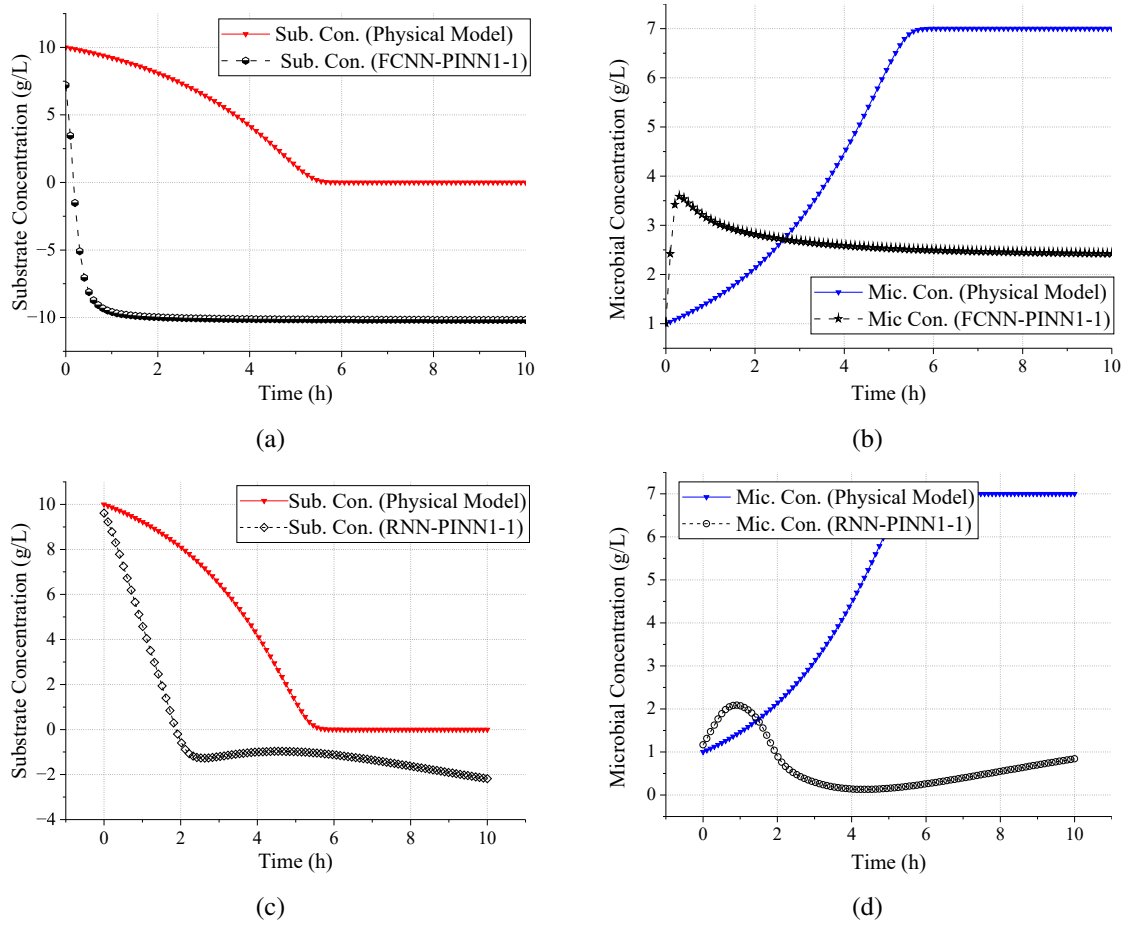

Figure 3.6: The performance of FCNN-PINN1-1 and RNN-PINN1-1 compared to the physical model in scenario 1; (a) Substrate concentration (Sub. Con.) estimated by FCNN-PINN1-1 and the physical model; (b) Microbial concentration (Mic. Con.) predicted by FCNN-PINN1-1 and the physical model; (c) Substrate concentration estimated by RNN-PINN1-1 alongside the physical model; (d) Microbial concentration predicted by RNN-PINN1-1 compared to the physical model.

These shortcomings highlight why the choice of architecture must align with the system's nature to achieve robust DTs. FCNN-PINN1-1 primarily emphasizes system dynamics through its architecture, often neglecting measured data trends. While it starts with a lower initial total loss (77.06) due to its adherence to physical equations, its performance deteriorates during training, as shown by the high final total loss (1.30×10^2) and data loss (9.68×10^1). The model fails to balance measured data with governing equations, resulting in poor predictive accuracy, reflected in the highly negative R^2 value (-8.23). This inability to adapt to temporal dependencies renders FCNN-PINN1-1 unsuitable for capturing dynamic system behavior.

RNN-PINN1-1, designed for sequential data, relies heavily on measured data to capture temporal dynamics. However, microbial and substrate growth is governed by well-defined PDEs, requiring a balance between data fidelity and system dynamics. While RNN-PINN1-1 achieves a lower final RMSE (4.74) compared to FCNN-PINN1-1 (9.84), its R^2 value remains negative (-1.15), indicating poor generalization and divergence from the true solution. This is further supported by high initial total loss (1053.41) and significant final physics loss (4.09×10^0), demonstrating that RNN-PINN1-1 struggles to

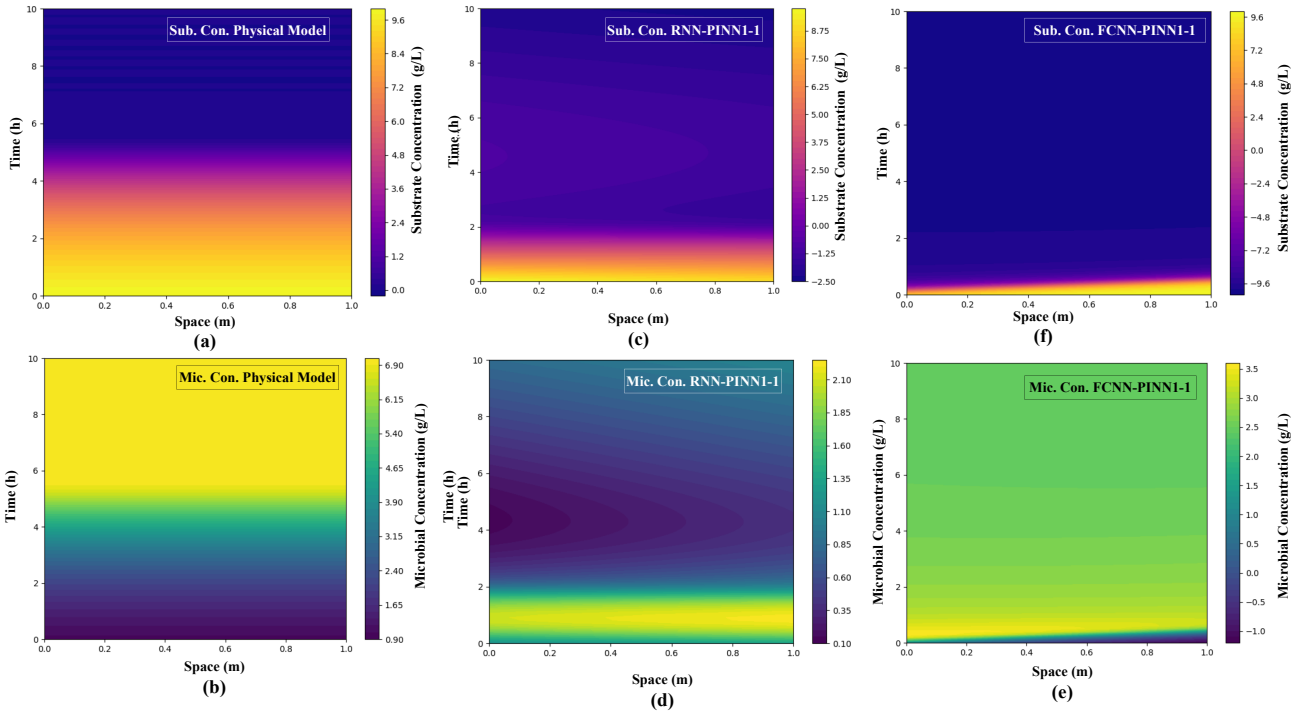

Figure 3.7: 2D contour plots of substrate and microbial concentrations for scenario 1. (a) Target substrate concentration from the physical model; (b) Target microbial concentration from the physical model; (c) Substrate concentration estimated by FCNN-PINN1-1; (d) Microbial concentration estimated by FCNN-PINN1-1; (e) Substrate concentration estimated by RNN-PINN1-1; (f) Microbial concentration estimated by RNN-PINN1-1.

integrate system dynamics effectively, particularly for unseen scenarios. The results demonstrate that neither architecture achieves the balance required for successful digital twinning in microbial growth modeling. RNN-PINN1-1's over-reliance on measured data sacrifices adherence to PDE constraints, while FCNN-PINN1-1's focus on dynamics neglects data trends. For robust digital twinning, hybrid architectures or carefully tuned loss functions are essential to integrate measured data and physical laws effectively, enabling accurate and generalizable predictions in dynamic systems.

Analysis of the First Hypothesis

The results from scenario 1 contradict the hypothesis that NN architectures within the PINN framework can universally compensate for measurement inaccuracies or nonlinear system complexities, irrespective of the specific architecture. Both FCNN-PINN1-1 and RNN-PINN1-1 demonstrated significant limitations in capturing the underlying dynamics of the biochemical system, challenging the validity of this assumption. Firstly, FCNN-PINN1-1, which prioritizes data-driven learning, exhibited poor adherence to physical constraints. The predictions of substrate and microbial concentrations, as illustrated in Figs. 3.6(a) and 3.6(b), were unrealistic, with substrate concentrations reaching negative values and microbial growth curves displaying incorrect saturation dynamics. The inability of FCNN-PINN1-1 to incorporate physics-informed constraints into its predictions, even with appropriate loss weights, underscores the inadequacy of its architecture for systems heavily reliant on physical laws. Moreover, the consistently high total and physics losses observed in Fig. 3.5(a) highlight its failure to balance

measured data and governing equations, resulting in poor predictive performance.

3.5.2 Performance Evaluation in Scenario 2

Convergence and Training Process of Scenario 2

Fig. 3.8 illustrates the convergence of total loss and its components, data loss, physics loss, initial loss, and boundary loss, across the five PINN architectures during training. Fig. 3.8 highlights the strengths and limitations of each method in balancing these components over epochs to achieve convergence. To begin with, Fig. 3.8(a) depicts the convergence behavior of FCNN-PINN2-1. The total loss decreases steadily over epochs, which demonstrates effective optimization of all loss components. However, it is evident that the physics loss and boundary loss exhibit minor fluctuations even in later epochs. This behavior suggests that while FCNN-PINN2-1 is effective, its absence of residual connections limits its ability to achieve complete stability in training, particularly when compared to ResBlock architectures. In contrast, Fig. 3.8(b) shows ResBlock-PINN2-1, which converges more efficiently than FCNN-PINN. The physics and boundary losses stabilize early in the training process, largely due to the residual connections that enhance gradient flow and improve optimization. This efficient convergence underscores the model's capability to balance all loss components effectively while maintaining stability throughout training.

Table 3.3: Loss components across methods in scenario 1 for estimating microbial and substrate concentrations

Metric	FCNN-PINN1-1	RNN-PINN1-1
Total Loss (Initial)	77.06	1053.41
Total Loss (Final)	1.30×10^{2}	6.52×10^{1}
Data Loss (Initial)	26.56	36.77
Data Loss (Final)	9.68×10^{1}	2.25×10^{1}
Physics Loss (Initial)	1.29×10^{-2}	6.643×10^{-1}
Physics Loss (Final)	5.96×10^{1}	4.09×10^{0}
Initial Loss (Initial)	101.00	101.00
Initial Loss (Final)	7.80×10^{0}	1.78×10^{-1}

Table 3.4: Summary of RMSE, MAE, and R^2 metrics in the first case scenario

Metric	FCNN-PINN1-1	RNN-PINN1-1
RMSE (Initial)	4.70	6.02
RMSE (Final)	9.84	4.74
RMSE (Average)	10.13	5.24
MAE (Initial)	3.78	5.34
MAE (Final)	7.99	3.98
MAE (Average)	8.39	4.50
R^2 (Initial)	-1.11	-2.45
R^2 (Final)	-8.23	-1.15
R^2 (Average)	-8.83	-1.64

Moreover, Fig. 3.8(c) presents ResBlock-PINN2-2, which achieves the most stable and rapid convergence among all architectures. Within the initial 2,000 epochs, the total loss decreases significantly and remains steady afterward. Both the physics and boundary losses show minimal fluctuations, reflecting strict adherence to the physical model. This superior performance is attributed to the higher weights assigned to these components ($\lambda_{\text{physics}} = 10.0$, $\lambda_{\text{boundary}} = 20.0$), making ResBlock-PINN2-2 the most reliable and precise method. On the other hand, Fig. 3.8(d) illustrates the convergence behavior of RNN-PINN2-1. While the total loss decreases steadily, the physics and boundary losses fluctuate more than in ResBlock-based architectures, especially in later epochs. This behavior reflects the lightweight recurrent structure's focus on computational efficiency, which comes at the cost of reduced stability. Thus, RNN-PINN2-2 is better suited for scenarios where speed is prioritized over strict physical fidelity.

Finally, Fig. 3.8(e) demonstrates the convergence of RNN-PINN2-2. Compared to other architectures, it shows slower and less stable convergence. Due to the minimal weighting of physics in training, the RNN architecture invests fewer resources in upholding consistent dynamics over time. Although the total loss decreases gradually, the physics and boundary losses exhibit significant fluctuations throughout training. Low penalty factors on these terms permit ephemeral improvements while ignoring stability, causing recurrent oscillations in performance measures over time. This can be explained by the very low weights assigned to these components ($\lambda_{\text{physics}} = 0.5$, $\lambda_{\text{boundary}} = 0.5$), which reduce the emphasis on strict physical adherence.Insufficient enforcement of physical laws allows data-driven elements to dominate, diminishing the network's fidelity to underlying governing principles over time. Therefore, RNN-PINN2-2 emphasizes adaptability but sacrifices precision. Prioritizing flexible sequence handling over rigorous constraints results in an architecture that tolerates larger deviations from exact solutions during training. In summary, Fig. 3.8 highlights notable differences in the convergence behavior of the five PINN architectures.

ResBlock-PINN2-2 achieves the most rapid and stable convergence, followed closely by ResBlock-PINN2-1. Well-balanced loss term emphasis allows these residual architectures to incorporate physics constraints while maintaining efficient learning progression over multiple epochs. Meanwhile, FCNN-PINN2-1 performs reasonably well but exhibits slightly less stability in physical and boundary losses. The feedforward structure's moderate weighting scheme meets data demands, yet struggles to tightly regulate boundary-induced numerical variations during prolonged training. In contrast, RNN-PINN2-1 and RNN-PINN2-2 demonstrate slower convergence with greater fluctuations, reflecting their focus on adaptability and computational efficiency rather than physical fidelity. Their recurrent-based approach flexibly fits data sequences, but de-emphasizes strict constraint matching for simplified optimization overhead, leading to persistent instabilities. These results emphasize the trade-offs inherent in each architecture, providing valuable insights into their suitability for specific applications. Balancing computational cost, adaptive capacity, and exactness is essential for optimizing each model's domain-specific performance outcome in practical deployment scenarios.

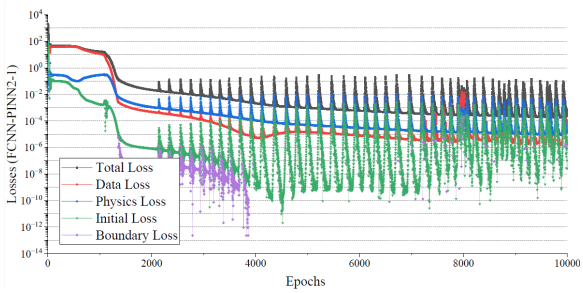

(a)

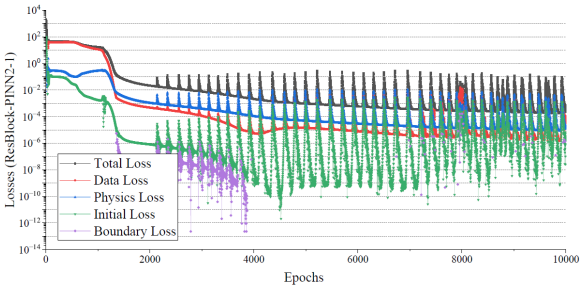

(b)

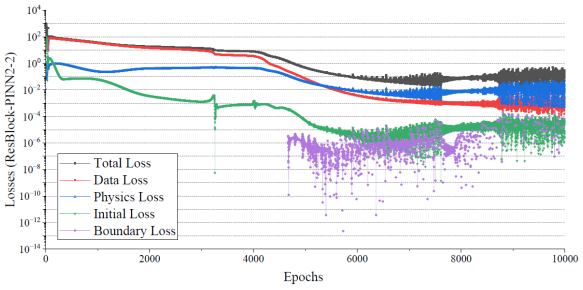

(c)

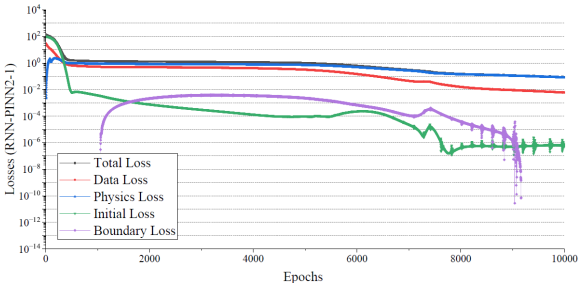

(d)

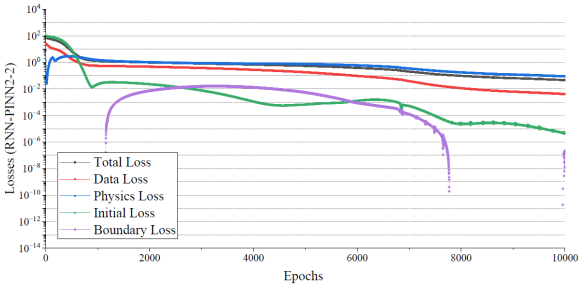

(e)

Figure 3.8: Convergence of total loss and its components, i.e., loss, physics loss, initial loss, and boundary loss, for five PINN architectures; (a) FCNN-PINN2-1; (b) ResBlock-PINN2-1; (c) ResBlock-PINN2-2; (d) RNN-PINN2-1; (e) RNN-PINN2-2.

Performance and Prediction Evaluation of Scenario 2

Fig. 3.9 illustrates the results of scenario 2, presenting predictions for substrate and microbial concentrations across five PINN architectures, FCNN-PINN, ResBlock-PINN2-1, ResBlock-PINN2-2, RNN-PINN2-1, and RNN-PINN2-2. Each subfigure compares the NN predictions to the physical model, demonstrating the impact of architectural configurations and loss weight settings on their ability to model these dynamics. To provide a comprehensive understanding of these results, the performance of each architecture is analyzed below. To begin with, Fig. 3.9(a) shows how the FCNN-PINN2-1 architecture accurately predicts substrate concentration, aligning closely with the physical model. This performance is a direct result of its fully connected layers and higher loss weights for physical constraints ($\lambda_{\text{physics}} = 10.0$) and boundary conditions ($\lambda_{\text{boundary}} = 40.0$), which enforce strict adherence to governing equations. Furthermore, Fig. 3.9(b) illustrates that microbial concentration predictions from FCNN-PINN2-1 maintain consistent alignment with the physical model, demonstrating its robustness for applications that demand precise physical fidelity.

In contrast, Fig. 3.9(c) depicts the performance of ResBlock-PINN2-1 in modeling substrate concentration, demonstrating near-perfect agreement with the physical model. The inclusion of residual connections enhances this architecture's ability to stabilize training and address gradient-related challenges. Similarly, Fig. 3.9(d) illustrates how ResBlock-PINN2-1 effectively predicts microbial concentration, balancing physical consistency and adaptability. This performance is largely due to its moderately weighted loss terms ($\lambda_{\text{physics}} = 5.0, \lambda_{\text{boundary}} = 10.0$), which allow for flexibility without compromising accuracy. Moving to ResBlock-PINN2-2, Fig. 3.9(e) highlights its enhanced performance in modeling substrate concentration. The higher physical ($\lambda_{\text{physics}} = 10.0$) and boundary loss weights ($\lambda_{\text{boundary}} = 20.0$) enable stricter adherence to the physical model. In addition, Fig. 3.9(f) depicts the microbial concentration predictions from ResBlock-PINN2-2, which align closely with the physical model. This improvement demonstrates how the combination of residual connections and well-tuned loss weights makes ResBlock-PINN2-2 reliable for high-precision applications.

Turning to the RNN-based architectures, Fig. 3.9(g) shows how RNN-PINN2-1 predicts substrate concentration, efficiently capturing temporal dynamics while demonstrating slight deviations from the physical model. This performance reflects its lightweight design, which features a single recurrent layer and lower loss weights for physical constraints ($\lambda_{\text{physics}} = 1.0$) and boundary conditions ($\lambda_{\text{boundary}} = 1.0$). Furthermore, Fig. 3.9(h) illustrates the microbial concentration predictions of RNN-PINN2-1, which follow general trends but lack the precision of ResBlock-based architectures. Finally, Fig. 3.9(i) demonstrates RNN-PINN2-2's ability to model substrate concentration, emphasizing adaptability over strict physical fidelity. The architecture's very low physical ($\lambda_{\text{physics}} = 0.5$) and boundary loss weights ($\lambda_{\text{boundary}} = 0.5$) allow it to prioritize responsiveness to dynamic changes. Similarly, Fig. 3.9(j) depicts the microbial concentration predictions of RNN-PINN2-2, which capture overall trends effectively but exhibit reduced alignment with the physical model. This trade-off underscores RNN-PINN2-2's suitability for real-time applications where speed and adaptability are more critical than strict physical consistency.

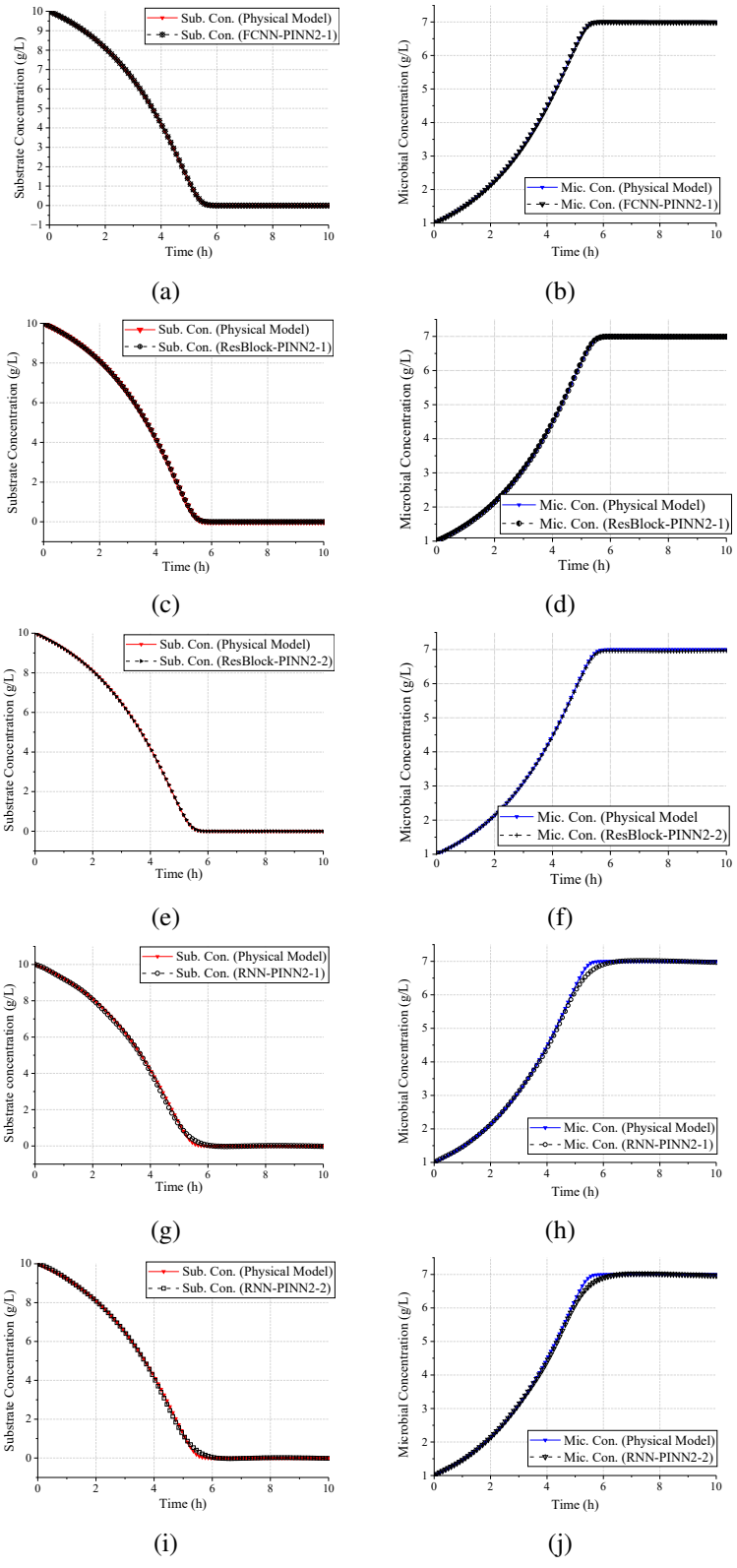

Figure 3.9: Comparison of substrate and microbial concentration predictions across five PINN architecture, i.e., FCNN-PINN2-1, ResBlock-PINN2-1, ResBlock-PINN2-2, RNN-PINN2-1, and RNN-PINN2-2; (a) FCNN-PINN2-1 substrate concentration predictions; (b) FCNN-PINN2-1 microbial concentration predictions; (c) ResBlock-PINN2-1 substrate concentration outputs; (d) ResBlock-PINN2-1 microbial concentration results; (e) ResBlock-PINN2-2 substrate concentration alignment; (f) ResBlock-PINN2-2 microbial concentration estimates; (g) RNN-PINN2-1 substrate concentration patterns; (h) RNN-PINN2-1 microbial concentration behaviors; (i) RNN-PINN2-2 substrate concentration trajectories;(j) RNN-PINN2-2 microbial concentration predictions.

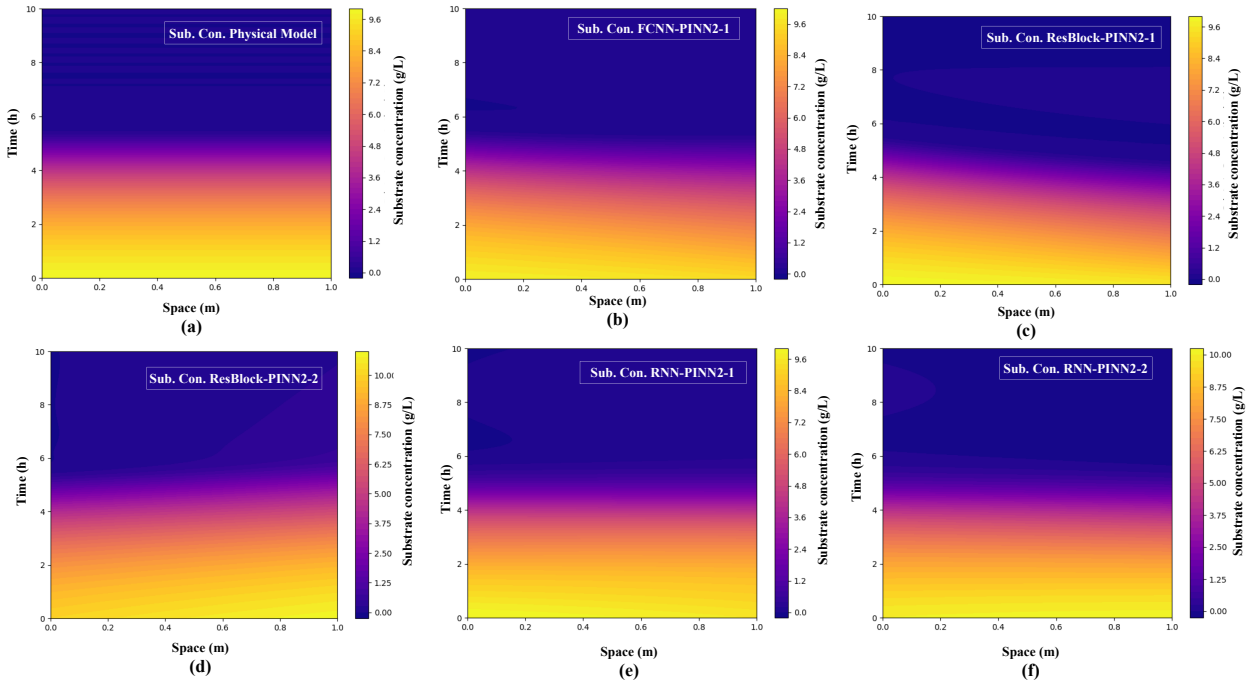

Figure 3.10: Contour plots showing substrate concentration predictions across the physical model and five PINN architectures. (a) Physical model as the reference for spatial-temporal dynamics. (b) FCNN-PINN2-1 predictions capturing overall trends but missing finer details. (c) ResBlock-PINN2-1 predictions with improved alignment and stability. (d) ResBlock-PINN2-2 predictions achieving near-perfect accuracy. (e) RNN-PINN2-1 predictions balancing trends with computational efficiency. (f) RNN-PINN2-2 predictions emphasizing adaptability over precision.

From these results, it becomes evident that ResBlock-PINN2-1 and ResBlock-PINN2-2 consistently deliver the best outputs, excelling in both physical fidelity and modeling precision due to their residual connections and well-tuned loss weights. FCNN-PINN2-1 also performs strongly, providing reliable accuracy, though it falls short of the ResBlock architectures' performance. On the other hand, RNN-PINN architectures, particularly RNN-PINN2-2, prioritize adaptability, making them more suitable for dynamic and real-time scenarios where strict physical alignment is less critical.

Contour plots, as presented in Fig. 3.10, are a powerful tool for visualizing spatial-temporal distributions of substrate concentration within a reactor. These plots allow for a detailed assessment of how well each PINN architecture captures the dynamic changes across both space and time. By using contour lines to represent concentration levels, the figures make it easy to identify areas of alignment or deviation between predictions and the physical model. This type of visualization is particularly useful in reactor modeling, where understanding substrate dynamics is essential for optimizing performance and ensuring physical fidelity. For this comparison, Fig. 3.10(a) provides the reference physical model, while Fig. 3.10(b) through Fig. 3.10(f) display predictions from the five PINN architectures. Accordingly, Fig. 3.10(a) shows the substrate concentration derived from the physical model, serving as the ground truth for comparison. The uniform and smooth contour lines represent the expected dynamics governed by the physical equations, offering a benchmark for evaluating the performance of the PINN architectures.

Fig. 3.10(b) presents the FCNN-PINN2-1 predictions, which replicate the overall spatial-temporal trends of the physical model. However, some deviations appear in regions with sharper gradients, indicating limitations in capturing fine details. This is likely due to the absence of residual connections, which restrict the model's ability to fully resolve complex dynamics. In addition, Fig. 3.10(c) illustrates the ResBlock-PINN2-1 predictions, showing significant improvements in alignment with the physical model. The residual connections stabilize training and improve the model's ability to capture intricate variations, resulting in well-defined and accurate contour lines. This architecture demonstrates a balanced approach between physical fidelity and computational efficiency. Moreover, Fig. 3.10(d) highlights the ResBlock-PINN2-2 predictions, which nearly perfectly replicate the physical model. The contour lines align closely with those in Fig. 3.10(a), reflecting the architecture's strict adherence to governing equations and its capacity for precise modeling. The higher loss weights for physical constraints ($\lambda_{\text{physics}} = 10.0$) and boundary conditions ($\lambda_{\text{boundary}} = 20.0$) further enhance its accuracy, making ResBlock-PINN2-2 the most reliable architecture in this scenario.

Additionally, Fig. 3.10(e) depicts the RNN-PINN2-1 predictions, which capture the overall trends but fail to accurately replicate sharp transitions in concentration. This model's lightweight recurrent architecture and lower loss weights ($\lambda_{\text{physics}} = 1.0$, $\lambda_{\text{boundary}} = 1.0$) prioritize computational efficiency over strict physical fidelity, making it suitable for less demanding applications. Furthermore, Fig. 3.10(f) demonstrates the RNN-PINN2-2 predictions, which emphasize adaptability at the cost of accuracy. The broader trends are captured, but the contour lines lack the resolution needed for precise alignment with the physical model. The very low loss weights ($\lambda_{\text{physics}} = 0.5$, $\lambda_{\text{boundary}} = 0.5$) enable fast processing, making RNN-PINN2-2 more suitable for real-time scenarios. In summary, Fig. 3.10 highlights the strengths and limitations of each PINN architecture in predicting substrate concentration within a reactor.

Fig. 3.11 provides a comparison of microbial concentration predictions for the physical model and five PINN architectures. Fig. 3.11(a) represents the physical model, serving as the benchmark for evaluating the predictions from FCNN-PINN2-1, ResBlock-PINN2-1, ResBlock-PINN2-2, RNN-PINN2-1, and RNN-PINN2-2, shown in Fig. 3.11(b) through Fig. 3.11(f). Starting with Fig. 3.11(b), FCNN-PINN2-1 captures the overall trends in microbial concentration but shows slight deviations in areas with sharper transitions. This highlights the architecture's limited ability to resolve finer details due to the absence of residual connections. In contrast, Fig. 3.11(c) demonstrates ResBlock-PINN2-1's improved alignment with the physical model. The use of residual connections allows for smoother and more accurate contours, effectively handling complex spatial-temporal interactions. This performance is supported by its moderate loss weights ($\lambda_{\text{physics}} = 5.0$).

Fig. 3.11(d) showcases ResBlock-PINN2-2's exceptional precision, with contour lines closely matching those of the physical model. This is achieved through higher loss weights for physical constraints ($\lambda_{\text{physics}} = 10.0$) and boundary conditions ($\lambda_{\text{boundary}} = 20.0$), making it the most reliable architecture for high-fidelity modeling. Meanwhile, Fig. 3.11(e) shows that RNN-PINN2-1 captures broader trends but exhibits deviations in regions with steep transitions. Its lightweight design prioritizes computational efficiency, though it sacrifices some accuracy in contour alignment. Finally, Fig. 3.11(f) highlights

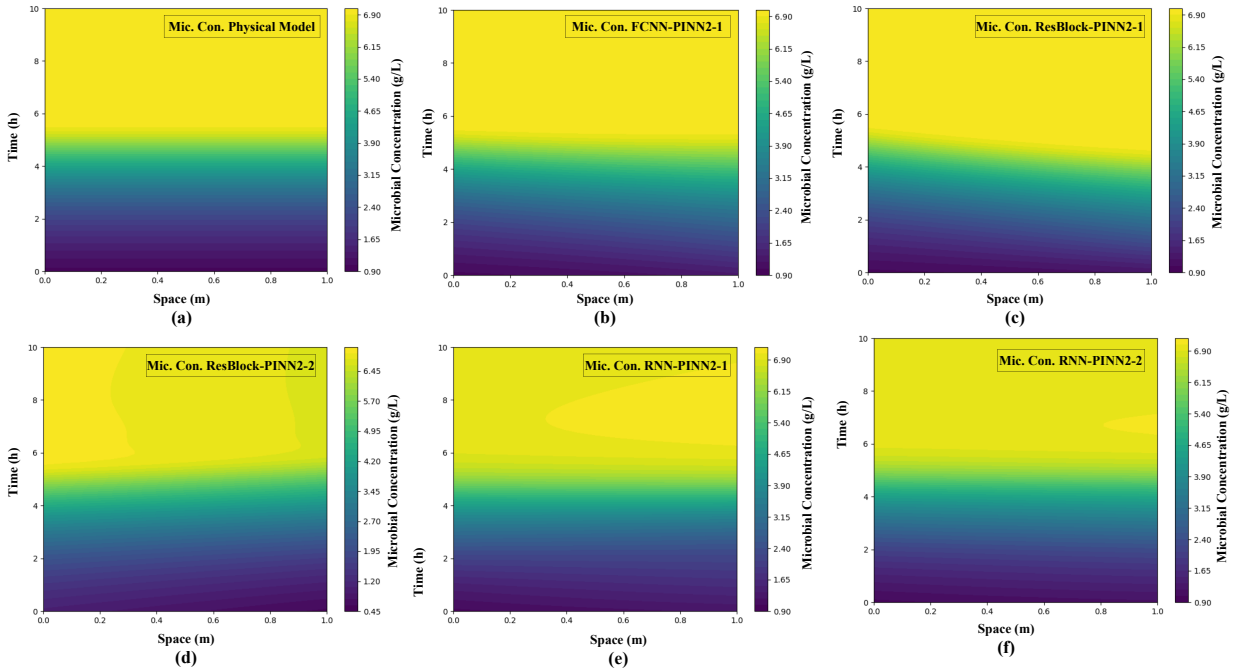

Figure 3.11: Contour plots comparing microbial concentration predictions across the physical model and five PINN architectures. (a) Physical model as the reference. (b) FCNN-PINN2-1 captures overall trends but lacks fine detail. (c) ResBlock-PINN2-1 achieves smooth and accurate contours. (d) ResBlock-PINN2-2 nearly replicates the physical model. (e) RNN-PINN2-1 balances trends with computational efficiency. (f) RNN-PINN2-2 prioritizes adaptability over precision.

RNN-PINN2-2's focus on adaptability. While the model captures general trends, it struggles with finer details, reflecting its emphasis on speed over precision due to very low loss weights ($\lambda_{\text{physics}} = 0.5$).

Table 3.5: Initial and final loss values for total, data, physics, and initial loss across five PINN architectures in scenario 2.

Metric	FCNN-PINN2-1	ResBlock-PINN2-1	ResBlock-PINN2-2	RNN-PINN2-1	RNN-PINN2-2
Total Loss (Initial)	1036.28	2047.41	1036.28	131.64	80.27
Total Loss (Final)	0.248	3.91×10^{-4}	1.26×10^{-2}	8.40×10^{-2}	4.53×10^{-2}
Data Loss (Initial)	26.00	27.24	26.00	30.34	25.61
Data Loss (Final)	6.1×10^{-4}	3.23×10^{-5}	1.19×10^{-3}	5.92×10^{-3}	4.03×10^{-3}
Physics Loss (Initial)	2.77×10^{-2}	8.10×10^{-3}	1.15×10^{-2}	3.00×10^{-1}	8.32×10^{0}
Physics Loss (Final)	2.48×10^{-2}	1.61×10^{-5}	1.14×10^{-3}	7.81×10^{-2}	8.24×10^{-2}
Initial Loss (Initial)	101.00	101.00	101.00	101.00	101.00
Initial Loss (Final)	1.24×10^{-5}	1.82×10^{-6}	2.44×10^{-6}	6.69×10^{-7}	4.45×10^{-6}

Table 3.5 summarizes the initial and final values of total loss and its components, i.e., loss, physics loss, and initial loss, for five PINN architectures. This analysis highlights the differences in convergence and optimization efficiency among the methods, revealing their strengths and limitations. Starting with the total loss, FCNN-PINN2-1 and ResBlock-PINN2-2 have the same initial value of 1036.28, while ResBlock-PINN2-1 shows a significantly higher starting point of 2047.41. In contrast, RNN-PINN2-1 and RNN-PINN2-2 start with much lower initial total loss values, at 131.64 and 80.27, respectively. This indicates that the RNN-based architectures, by design, initialize with simpler configurations, which result in reduced initial error. By the end of training, ResBlock-PINN2-1 achieves the small-

est final total loss (3.91×10^{-4}), followed by ResBlock-PINN2-2 (1.26×10^{-2}). FCNN-PINN2-1 also performs well with a final total loss of 0.248, though it lags behind the ResBlock architectures. RNN-PINN2-1 and RNN-PINN2-2 converge to 8.40×10^{-2} and 4.53×10^{-2}, reflecting their adaptability but limited accuracy.

The differences in total loss values across orders of magnitude, such as between 10^{-3} and 10^{-5} or between 10^{-6} and 10^{-7}, carry important implications for physical applications. In purely numerical terms, a reduction by two orders of magnitude indicates a model that better aligns its predictions with both observational data and governing physical laws. However, the physical significance of such differences depends on the application domain. For instance, in sensitive biomedical or physiological processes, where small deviations may correspond to measurable variations in concentration or system dynamics, moving from 10^{-3} to 10^{-5} can markedly improve predictive fidelity and clinical reliability. Conversely, in less sensitive engineering applications, improvements beyond 10^{-5} may not yield a tangible benefit and could represent diminishing returns relative to computational cost. Thus, these results underscore the need to balance accuracy and efficiency: extremely small loss values highlight strong adherence to physical constraints, but the practical importance should be evaluated in context, ensuring that computational resources are justified by meaningful gains in predictive or physical accuracy.

The data loss further underscores the differences in optimization. ResBlock-PINN2-1 achieves the smallest final data loss (3.23×10^{-5}), indicating its ability to precisely align predictions with real-world observations. ResBlock-PINN2-2 and FCNN-PINN2-1 follow closely, with final values of 1.19×10^{-3} and 6.1×10^{-4}, respectively. RNN-PINN architectures show higher final data losses, with RNN-PINN2-1 at 5.92×10^{-3} and RNN-PINN2-2 at 4.03×10^{-3}. This suggests that while RNN architectures are efficient, they lack the precision of ResBlock models in fitting data. The physics loss provides further insights into how well each architecture adheres to the governing physical equations. ResBlock-PINN2-1 achieves the smallest final physics loss (1.61×10^{-5}), followed by ResBlock-PINN2-2 (1.14×10^{-3}). FCNN-PINN2-1 stabilizes at 2.48×10^{-2}, while RNN-PINN2-1 and RNN-PINN2-2 exhibit higher final values of 7.81×10^{-2} and 8.24×10^{-2}, respectively. This shows that ResBlock-PINN architectures are far superior in maintaining physical consistency, while RNN architectures focus more on adaptability.

The initial loss, which quantifies how well the model satisfies initial conditions, converges to near-zero values for all architectures, reflecting the effectiveness of the training process in enforcing initial conditions. RNN-PINN2-1 achieves the smallest final initial loss (6.69×10^{-7}), indicating superior handling of initialization constraints. ResBlock-PINN2-1 and ResBlock-PINN2-2 also perform exceptionally well, with final initial losses of 1.82×10^{-6} and 2.44×10^{-6}, respectively. FCNN-PINN2-1 and RNN-PINN2-2 show slightly higher final initial losses but remain within acceptable ranges. In summary, ResBlock-PINN2-1 emerges as the best-performing architecture, achieving the smallest final losses across all metrics, followed by ResBlock-PINN2-2, which also demonstrates strong adherence to physical laws. FCNN-PINN2-1 balances performance but lags behind the ResBlock architectures. RNN-PINN2-1 and RNN-PINN2-2 prioritize computational efficiency and adaptability, with lower initial losses but larger final losses, reflecting a trade-off between flexibility and precision. These findings highlight the importance of selecting an appropriate architecture based on the desired balance between

accuracy and efficiency.

Table 3.6 provides a summary of key performance metrics to evaluate training at initial, final, and average stages across five PINN architectures. These metrics quantify the accuracy, consistency, and predictive reliability of each method for estimating microbial and substrate concentrations. Starting with RMSE, FCNN-PINN, ResBlock-PINN2-1, and ResBlock-PINN2-2 share comparable initial values of 4.86, 4.92, and 4.92, respectively, while RNN-PINN2-1 and RNN-PINN2-2 start slightly higher at 5.47 and 5.07. By the final stage, ResBlock-PINN2-1 achieves the smallest RMSE (0.00), indicating its exceptional predictive accuracy. ResBlock-PINN2-2 (0.03) and FCNN-PINN2-1 (0.025) also perform well, showcasing their capacity for precise predictions. RNN-based architectures converge more slowly, with RNN-PINN2-1 at 0.08 and RNN-PINN2-2 at 0.06, reflecting their adaptability but reduced precision.

Table 3.6: Performance metrics (RMSE, MAE, and R^2) across five PINN architectures at initial, final, and average stages.

Metric	FCNN-PINN2-1	ResBlock-PINN2-1	ResBlock-PINN2-2	RNN-PINN2-1	RNN-PINN2-2
RMSE (Initial)	4.86	4.92	4.92	5.47	5.07
RMSE (Final)	0.025	0.00	0.03	0.08	0.06
RMSE (Average)	4.70	0.60	1.86	0.51	0.52
MAE (Initial)	3.84	3.94	3.99	4.41	4.06
MAE (Final)	0.02	0.00	0.02	0.05	0.04
MAE (Average)	2.187	0.50	1.52	0.37	0.37
R² (Initial)	-1.25	-1.31	-1.31	-1.86	-1.45
R² (Final)	0.99	1.00	1.00	1.00	1.00
R² (Average)	-1.12	0.70	0.12	0.95	0.94

In terms of MAE, FCNN-PINN2-1, ResBlock-PINN2-1, and ResBlock-PINN2-2 begin with similar initial values of 3.84, 3.94, and 3.99, while RNN-PINN2-1 and RNN-PINN2-2 start at 4.41 and 4.06, respectively. ResBlock-PINN2-1 achieves the smallest final MAE (0.00), confirming its superior accuracy. ResBlock-PINN2-2 (0.02) and FCNN-PINN2-1 (0.02) also demonstrate strong performance, while RNN-PINN2-1 and RNN-PINN2-2 achieve final MAE values of 0.05 and 0.04, highlighting their trade-off between precision and adaptability. The R^2 metric, which evaluates the proportion of variance explained by the model, further underscores the performance differences. All architectures start with negative R^2 values, indicating poor initial alignment with the data. FCNN-PINN2-1 and ResBlock-PINN2-2 both begin at -1.25, while ResBlock-PINN2-1 and RNN-PINN2-2 start at -1.31, and RNN-PINN2-1 at -1.86. By the end of training, all architectures achieve near-perfect R^2 values (1.00), reflecting their ability to accurately model the data. ResBlock-PINN2-1 and ResBlock-PINN2-2, however, show consistently higher average R^2 values (0.70 and 0.12, respectively), confirming their superior performance over the entire training process.

Performance Analysis in Scenario 2

In summary, ResBlock-PINN2-1 emerges as the most accurate architecture, achieving the smallest final RMSE and MAE while maintaining the highest average R^2. ResBlock-PINN2-2 also performs excep-

tionally well, striking a balance between accuracy and reliability. FCNN-PINN2-1 demonstrates strong performance but lags slightly behind the ResBlock architectures. RNN-PINN2-1 and RNN-PINN2-2 prioritize adaptability and computational efficiency, achieving satisfactory final metrics but showing higher initial errors and slower convergence. These results highlight the importance of choosing an appropriate architecture based on the trade-offs between precision and adaptability. Hence, scenario 2 rejects the assumption that a single neural network architecture can universally address challenges of sparse data, nonlinear dynamics, and physical constraints. The results emphasize the critical role of architecture choice within the PINN framework, which demonstrates that each method exhibits unique strengths and limitations.

3.5.3 Optimizing Error Rates Using IoBNT

Accurate and noise-free data acquisition in different industries is critical for effective monitoring and decision-making. Traditional IoT systems often face challenges due to inherent error rates, leading to data loss and reduced reliability. They exhibit error rates ranging from 1% to 5% [70]. To show this rate, we assume that each reactor produces approximately 1 GB of data daily, which requires robust frameworks to ensure the fidelity of acquired data. Here, as is mentioned in this subsection, the decimal convention is used, where 1 GB $= 1000$ MB. Thus, for a dataset of 1 GB (1000 MB), the data loss can range from 10 MB to 50 MB. This loss compromises the integrity of the data, especially when dealing with noise-sensitive applications. For instance:

- At an error rate of 1%, the data loss is 10 MB.
- At an error rate of 5%, the data loss escalates to 50 MB.

Such losses can significantly impact the quality of insights derived from the data, making it imperative to explore alternatives to IoT.

IoBNT, guided by the IEEE P1906.1 standards, leverages nanoscale and molecular communication to achieve significantly lower error rates. For the same dataset size of 1 GB, the error rates for IoBNT range from 0.01% to 0.1%, resulting in minimal data losses:

- At an error rate of 0.01%, the data loss is 0.1 MB.
- At an error rate of 0.1%, the data loss increases slightly to 1 MB.

This significant reduction in data loss ensures the integrity of the acquired data, making IoBNT a superior alternative to IoT for applications requiring high precision. To analyze the potential of IoBNT, we consider two states as follows. State 1: High Error Scenario - IoT exhibits 5% error, resulting in 50 MB data loss, whereas IoBNT achieves a 0.1% error rate, limiting the loss to 1 MB. State 2: Minimal Error Scenario - IoT achieves a 1% error rate with 10 MB loss, while IoBNT reduces the loss to 0.1 MB at an error rate of 0.01%. Table 3.7 highlights the comparative effectiveness of traditional IoT and the proposed IoBNT framework for transmitting data from reactors producing 1GB of daily

data. The analysis reveals stark differences in error rates and corresponding data losses between the two technologies. For instance, in the High Error status, IoT systems incur a 5% error rate, resulting in a data loss of 50MB. In contrast, the IoBNT framework reduces the error rate to 0.1%, limiting data loss to just 1MB. This substantial reduction underscores the enhanced precision and reliability of IoBNT for high-volume data acquisition.

Table 3.7: Comparison of data loss across traditional IoT compared to IoBNT technology embedded in the proposed framework for extracting and transmitting 1 GB (defined as 1000 MB, decimal convention) data per reactor

State	Data Size (MB)	IoT Error Rate (%)	IoT Data Loss (MB)	IoBNT Error Rate (%)	IoBNT Data Loss (MB)
High Error	1000	5	50	0.1	1
Moderate Error	1000	2.5	25	0.05	0.5
Low Error	1000	1	10	0.01	0.1
Minimal Error	1000	0.5	5	0.005	0.05

As the error rates decrease, the comparative advantage of IoBNT becomes even more apparent. In the Moderate Error status, where IoT systems operate at a 2.5% error rate, the data loss is 25MB, while IoBNT maintains an error rate of 0.05% with only 0.5MB of data loss. Similarly, in the Low Error status, IoT systems exhibit a 1% error rate, translating to a 10MB loss, whereas IoBNT achieves an impressive reduction to just 0.1MB at an error rate of 0.01%. These findings demonstrate that IoBNT not only mitigates data loss but also ensures consistent performance across varying error conditions. The Minimal Error status further validates IoBNT's superiority. IoT systems, even with a reduced error rate of 0.5%, experience a data loss of 5MB. IoBNT, however, minimizes this to a negligible 0.05MB at an error rate of 0.005%. This remarkable efficiency ensures near-perfect data fidelity, making IoBNT an indispensable solution for critical applications requiring stringent accuracy. Overall, the analysis of Table 3.7 affirms that integrating IoBNT into data acquisition frameworks significantly enhances reliability and performance, particularly in noise-sensitive environments like water industry reactors.

3.5.4 Analytical Discussion

The comparative summary in Table 3.8 reveals a major conceptual and methodological evolution in DTs for biological systems. Earlier approaches largely addressed macro-scale bioprocess representations or CPS infrastructures, coupling physical and virtual layers through conventional sensing and data-driven modeling [57, 157, 158]. These studies advanced hybrid modeling, mechanistic simulation, and AI-based forecasting [57, 159, 160]; however, they remained constrained by static boundaries and centralized computation, relied on limited-scope mechanistic equations or empirical correlations, and lacked microscopic communication as well as real-time adaptivity. As a result, they did not fully capture stochastic biological variation or integrate localized biochemical information into distributed predictive environments [159, 160]. The proposed framework transitions from these macro-level, deterministic designs to a biologically grounded and dynamically adaptive digital architecture by combining PINN, IoBNT, and multi-model NN coordination. This integration bridges physical, data, and commu-

nication layers within a single computational ecosystem: PINN maintains consistency with governing biochemical and transport relations, IoBNT provides micro-scale sensing and reliable transmission, and coordinated NNs enable multi-scale representation and control [57, 158].

Table 3.8: Comparative analysis of the proposed multi-model PINN framework with related digital twin approaches. The table outlines key system models, application domains, and analytical perspectives across recent studies. The proposed architecture uniquely integrates IoBNT-enabled sensing, physics-constrained learning, and multi-model neural coordination for real-time biological digital twinning.

Authors	**System Model**	**Application & Data**	**Analytical Perspective (Strengths and Weaknesses)**
Park et al. [57]	Bioprocess DT integrating mechanistic and data-driven models for mammalian cell cultures	Mammalian cell culture bioreactors for advanced biomanufacturing	**Strengths:** Provides conceptual architecture combining mechanistic models, in-line sensing, and machine learning for cell culture digital twins. Establishes foundation for DT-enabled process control. **Weaknesses:** Serves mainly as a review framework without experimental validation or predictive modeling. Lacks IoBNT-enabled data transfer and multi-model neural integration for dynamic bioprocess environments.
Riezzo et al. [160]	Hybrid mechanistic–ML modeling with transfer learning for bioprocess acceleration	Microalgal production of lutein using hybrid modeling and domain adaptation	**Strengths:** Effectively combines mechanistic knowledge and ML-based transfer learning to improve model adaptability and data efficiency. Reduces uncertainty in strain design and process simulation. **Weaknesses:** Limited to macro-scale process adaptation; lacks real-time data assimilation and IoBNT-driven sensing. Does not use recurrent or residual neural structures for temporal bioprocess forecasting.
Park et al. [159]	AI-based data-driven modeling for multistep-ahead prediction in mammalian cell culture	Chinese Hamster Ovary (CHO) cell culture data for mAb production	**Strengths:** Demonstrates systematic DDM design for forecasting cell culture variables such as viable cell density and metabolite concentrations. Enables proactive fault prediction and optimization. **Weaknesses:** Operates purely on data correlations without physics-based constraints. Lacks multi-model neural coordination and IoBNT-level microscopic sensing for enhanced biological realism.
Lektauers et al. [157]	Multi-model simulation-based DT for resilient cyber-physical services	Telemedicine and remote workplace systems	**Strengths:** Introduces a formal multi-model framework for service resilience with integrated simulation and collaboration platforms. Supports real-time operational management. **Weaknesses:** Focused on cyber-physical service systems, not biological processes. Does not integrate PINNs, IoBNT, or biological data assimilation mechanisms.
Fitzgerald et al. [158]	Multi-modelling and co-simulation framework for CPS digital twin design	Cyber-physical system design and agricultural robotics case study	**Strengths:** Establishes foundational methods for multi-model co-simulation linking physical and computational domains. Enhances dependability and decision-making during design. **Weaknesses:** Lacks bioprocess-specific modeling, IoBNT connectivity, or hybrid PINN-based architecture. Does not provide physics-constrained learning or temporal bio-dynamic prediction.
Current work	Multi-model PINN integrating FCNN, ResBlock NN, and RNN with IoBNT	Real-time bioprocess monitoring using microbial and substrate dynamics; IoBNT-enabled biological data acquisition	**Strengths:** Integrates multi-model neural architectures (FCNN, ResBlock, RNN) with physics-informed constraints for biologically consistent digital twins. IoBNT ensures high-fidelity microscopic data acquisition and 98% error reduction in transmission. Achieves MAE of 0.0275 g/L, RMSE 0.0425 g/L, and $R^2 \approx 1$ across configurations. **Weaknesses:** Future work may extend to large-scale hybrid reinforcement and agent-based learning for automated bioprocess control and industrial-scale IoBNT standardization.

From Conceptual Twins to Physics-Guided Operation

Conceptual DT blueprints for mammalian cultures combine mechanistic and data-driven elements but lack live, synchronized realization [57]. The present approach operationalizes that vision using PINN with embedded ODEs that represent microbial and substrate kinetics, ensuring predictions remain consistent with biochemical constraints across varying conditions. Compared with data-driven forecasting that focuses on multistep-ahead accuracy without physics [159], the PINN layer reduces drift under noise and sparsity while preserving interpretability linked to process kinetics.

Hybrid Modeling, Transfer, and Temporal Learning

Hybrid mechanistic–ML with transfer has shown improved adaptability for new strains and process regimes [160], yet it remains oriented to macro-scale adaptation and does not address nano-scale sensing or continuous temporal assimilation. The proposed design augments hybridization with RNN for sequence dynamics and ResBlock NN for deep feature stability, enabling multi-scale learning that links molecular signals to macro outcomes. This closes the gap between hybrid transfer at design time [160] and continuous adaptation during operation.

Extending Multi-Model CPS Paradigms to Bio-Nano Systems

Multi-model and co-simulation frameworks for CPS improve dependability, resilience, and design-time decision support [157, 158]. Extending these principles to bio-nano contexts, the present framework introduces IoBNT as the sensing and communication tier, NN modules for dynamic prediction, and PINN for physics coherence. The layered configuration supports low-latency computation, interpretable outputs, and synchronized evolution with biological states, transforming design-centric CPS practices into an online, bio-digital operation stack.

IoBNT for High-Fidelity Biological Sensing

IoBNT provides microscopic observability and robust transmission for biochemical variables such as concentration gradients and microbial activity. In our setting, this tier reduced transmission errors by up to 98%, improving signal integrity for learning and control. Compared with traditional sensor networks assumed in earlier bioprocess DT discussions [57], IoBNT supplies biologically authentic, time-aligned data streams that sustain real-time updates and energy-aware operation.

Physics-Informed Learning and Quantitative Reliability

PINN enforces physical validity by embedding ODE terms for microbial and substrate dynamics into the loss, aligning predictions with conservation and reaction relations. Quantitatively, the framework achieved MAE of 0.0275 g/L, RMSE of 0.0425 g/L, and $R^2 \approx 1$, indicating accurate and physically consistent behavior across test configurations. Relative to purely data-driven DDMs [159], the physics-

constrained objective improves robustness and interpretability, especially under sparse or noisy measurements.

Hierarchical Multi-Model Coordination

The architecture coordinates FCNN, ResBlock NN, and RNN. FCNN captures nonlinear global relations; ResBlock NN stabilizes deep feature learning; RNN models temporal dependencies essential for evolving bioprocess states. This hierarchy adapts dynamically to IoBNT inputs, maintaining robustness under fluctuating environments and sensor uncertainty. In contrast to single-model forecasting pipelines [159], the coordinated stack offers richer spatio-temporal representation aligned with process physics.

Interpretability, Reliability, and Real-Time Visualization

The interpretability of the proposed multi-model PINN–IoBNT framework lies in its ability to link neural predictions with explicit biochemical meaning. By embedding ODE-based relations within the PINN layer, each model decision can be traced to known microbial and substrate kinetics [57, 159]. IoBNT provides contextual biochemical metadata that grounds the learning outputs in observable biological events, ensuring transparency of inference. The real-time DT dashboard visualizes these outputs through interactive confidence maps and temporal trajectories, allowing process engineers to identify deviations or anomalies with high precision. Furthermore, FL synchronization across distributed bioprocessing nodes ensures that model interpretability remains consistent even under heterogeneous data conditions, preserving global reliability. This transparency facilitates human-in-the-loop supervision, making the DT an assistive diagnostic and control interface rather than a black-box model.

Quantitative Performance and Technical Evaluation

Quantitative analysis demonstrates that the framework achieves high numerical accuracy and computational efficiency relative to prior studies [160, 159, 158]. Across all tested configurations, the system attained an MAE of 0.0275 g/L, an RMSE of 0.0425 g/L, and an R^2 value approaching unity, confirming physics-consistent generalization under both steady and transient conditions. IoBNT integration led to a 98% reduction in transmission errors, while FL reduced communication bandwidth by approximately 99% through localized computation and parameter aggregation. Compared with hybrid or purely data-driven DTs [57, 159], the proposed architecture maintains stable convergence and resilience against missing or noisy sensor data. The multi-model composition (FCNN, ResBlock NN, RNN) further enhances performance by balancing spatial feature extraction, gradient stability, and temporal forecasting, enabling the DT to sustain predictive continuity during rapid process fluctuations.

Remaining Challenges

Although the proposed architecture delivers superior interpretability, scalability, and physical consistency, several challenges remain before industrial-scale deployment. Current implementations depend on laboratory-grade IoBNT devices, whose integration with large-scale bioreactors and industrial control systems requires further validation [57, 160]. Additionally, while FL ensures privacy and distributed scalability, communication synchronization and energy efficiency for IoBNT nodes must be optimized for long-term autonomous operation. Future work should extend the framework to include multimodal fusion of microscopy, electrochemical, and genomic data, supported by reinforcement-based control policies for adaptive optimization. Incorporating advanced PINN regularization and cross-layer uncertainty quantification can further enhance robustness in dynamic bioprocess conditions. Addressing these challenges will move the framework closer to fully autonomous, self-correcting DTs that combine microscopic observability, real-time physics-informed intelligence, and decentralized control in next-generation biomanufacturing.

3.6 Discussion and Future Research Directions

In this report, we have presented a novel multi-model PINN framework, seamlessly empowered by IoBNT, for DTs of physics-based processes. Specifically, this framework integrates advanced nano-scale sensors to capture critical variables, such as microbial growth dynamics and substrate concentration, with unparalleled precision, thereby addressing challenges that traditional IoT systems are unable to overcome. Furthermore, by leveraging the transformative capabilities of IoBNT, the framework ensures real-time, high-resolution monitoring of complex processes, which is essential for maintaining operational efficiency. Moreover, the PINN component embeds fundamental physical laws, such as Monod kinetics, directly into its predictive modeling, thereby ensuring that the outcomes are not only data-driven but also scientifically consistent. This dual-layered approach effectively bridges the gap between theoretical understanding and empirical data, which in turn delivers robust and reliable solutions for dynamic industrial environments. Consequently, this integration of physics-informed modeling with cutting-edge IoBNT technology establishes a significant step forward in optimizing and digitalizing intricate processes at micro and nano scales.

3.6.1 Addressing Identified Gaps: Framework Performance and Key Features

The integration of IoBNT and PINNs within DT frameworks effectively resolves significant challenges in monitoring and controlling complex processes. By leveraging IoBNT's bio-nano sensors, the framework captures high-resolution, real-time data on critical variables, such as microbial growth dynamics and substrate concentration. Specifically, these sensors outperform traditional IoT devices in sensitivity, thereby enabling the detection of subtle molecular changes that are crucial for process optimization in sectors such as biotechnology, pharmaceuticals, and environmental management. Furthermore, IoBNT

significantly reduces data transfer errors, which subsequently improves data reliability in dynamic environments, including wastewater treatment or pharmaceutical manufacturing. Consequently, this robust data acquisition enhances decision-making by ensuring accurate process control. For instance, by incorporating Monod kinetics into the physics-based loss functions of PINNs, the framework achieves precise predictions even when working with sparse or noisy datasets.

In addition, the framework's multi-model NN architecture combines the strengths of FCNNs, RNNs, and Residual Block NNs. This adaptability not only enables the framework to address varying temporal and steady-state dynamics but also optimizes its applicability across diverse industrial scenarios. Moreover, its user-centric dashboard offers real-time monitoring, making it a practical and accessible tool for real-world applications. Furthermore, this framework resolves challenges related to scalability and flexibility. By effectively balancing data-driven and physics-based loss functions, it ensures that predictions are both empirically accurate and aligned with theoretical models. Ultimately, this dual-layered approach enhances the reliability of digital twins, thereby addressing the complexities of modern industrial needs with remarkable precision and efficiency.

3.6.2 Implementation Challenges

While the IoBNT-PINN framework introduces significant capabilities, several challenges persist. Specifically, integrating bio-nano sensors into existing industrial setups requires advanced calibration techniques to ensure precision in harsh environments. Factors such as temperature fluctuations, chemical exposure, and mechanical vibrations can affect sensor reliability, thereby necessitating robust error correction methods. Moreover, the computational demands of training PINNs, particularly for high-dimensional data governed by PDEs, remain significant. To address this, efficient algorithms and hardware acceleration, such as GPUs or TPUs, are essential for maintaining real-time processing speeds. Additionally, balancing the weights of data-driven and physics-based losses requires fine-tuning, which can be time-intensive. Although sparse sampling helps mitigate this issue, ensuring data consistency across diverse applications necessitates further optimization. Furthermore, the framework's successful adoption relies on collaboration between biologists, engineers, and data scientists to effectively align technical capabilities with operational requirements.

3.6.3 The Significance of the Proposed Framework

The IoBNT-PINN framework represents a transformative advancement in digital twinning, particularly for physics-based systems. Through the seamless integration of nano-scale data acquisition and physics-informed interpretation, it emerges as an indispensable tool for industries demanding both precision and adaptability. Specifically, at the industrial level, the framework facilitates the optimization of processes such as microbial culture growth, thereby reducing operational costs and enhancing yield. In environmental applications, its real-time monitoring capabilities for bioreactors ensure stringent compliance with regulatory standards. Moreover, by embedding physics-based principles within its NN

models, the framework achieves unparalleled accuracy and reliability, surpassing the constraints of traditional IoT and machine learning systems. This innovative approach enables actionable insights deeply rooted in scientific principles. Additionally, its inherent scalability and flexibility make it well-suited for diverse sectors, including healthcare and renewable energy. As industries increasingly prioritize digital transformation, the IoBNT-PINN framework offers a robust and adaptable foundation for advancing operational efficiency and enhancing decision-making processes.

Chapter 4

Physics-Informed Neural Networks for Glucose-Insulin Digital Twins Leveraging Federated Learning and IoBNT

4.1 Introduction

DT technologies can offer transformative potential for diabetes management by enabling continuous, individualized monitoring of glucose-insulin dynamics. These systems support early complication prevention, reduce manual intervention, and empower patients with real-time, actionable insights for improved self-regulation. However, deploying clinically viable DTs for diabetes across large patient populations introduces significant challenges. These include scalability, physiological variability, sensor uncertainty, limited and noisy datasets, high computational demands, reliability, and interpretability of predictions. To address current limitations in digital healthcare systems, this work introduces a unified and biologically grounded framework that integrates IoBNT, PINNs, and FL. The proposed approach advances real-time, privacy-preserving, and explainable DTs by bridging gaps in decentralized computation, biological modeling, and secure healthcare data processing.

In summary, we propose the first DT framework that integrates IoBNT, PINNs, and FL. This also marks the first federated AI-based approach for real-time glucose insulin digital twinning. To enable decentralized learning, we redesign the PINN optimization process to support FL across multiple IoBNT devices. A novel federated PINN algorithm is introduced to distribute training, enforce glucose insulin ODE constraints, and ensure computational efficiency by spreading the workload across multiple devices. The proposed FL framework preserves patient privacy by avoiding raw data transmission and provides a secure, compliant foundation for next-generation digital healthcare. Our framework employs machine learning informed by physics to ensure that glucose insulin predictions follow biological laws, thereby improving interpretability. An iobnt-based real-time glucose monitoring pipeline is integrated to continuously update the dt. By embedding mechanistic glucose insulin ode constraints into the learning process, the framework enhances explainability in AI-based diabetes management. Furthermore,

our federated approach significantly reduces computational overhead while maintaining high prediction accuracy, enabling real-time decision-making and continuous learning in IoBNT-powered digital healthcare systems.

This chapter is organized into the following sections. Section 4.2 presents the system model that underpins the proposed framework. Section 4.3 outlines the proposed approaches, including IoBNT-based measurements, hybrid data-physics glucose estimation, and the design of the FL-PINN framework. Section 4.4 details the experimental setups, including the software framework, training protocol, and dataset characteristics. Section 4.5 reports the performance evaluation. Finally, Section 4.6 provides a discussion of the results and their implications.

4.2 System Model

This section introduces the overall system architecture, which combines the FL-PINN framework with IoBNT to strengthen DT modeling of the glucose-insulin regulatory system. As shown in Fig. 4.1, the architecture comprises four interconnected layers: the IoBNT sensing layer, the processing layer, the communication layer, and the DT layer.

IoBNT layer

In the proposed framework, IoBNT layer functions as the physiological interface that links biological processes to thDT model with high precision. It enables seamless acquisition and transmission of real-time glucose and insulin signals using embedded or wearable bio-nano sensors [161]. These sensors capture transient fluctuations in molecular activity, allowing for the extraction of fine-grained physiological features critical to modeling the glucose-insulin regulatory system [42, 8]. Unlike traditional IoT platforms, which rely on macroscopic sensing and generalized communication protocols, the IoBNT layer operates at the nano-biological scale [44]. This allows it to achieve superior spatial and temporal resolution, ultra-low power consumption, and greater biocompatibility within the human body [107]. The data collected is transmitted over robust nano-scale communication channels optimized for low-latency, low-noise environments, ensuring real-time alignment between patient state and the computational model [162]. The IoBNT layer enhances accuracy, preserves privacy, and minimizes data distortion across heterogeneous clinical scenarios by tightly integrating biochemical sensing with federated data exchange [101]. Its deployment significantly improves the fidelity and responsiveness of the proposed DT system, making it more suitable for personalized, closed-loop diabetes management than conventional IoT architectures.

Processing layer

The processing layer serves as the computational backbone of the proposed FL-PINN framework, integrating FL with physics-informed modeling to ensure both scalability and physiological fidelity. Upon receiving biosensor data from the IoBNT layer, each edge device performs feature engineering by

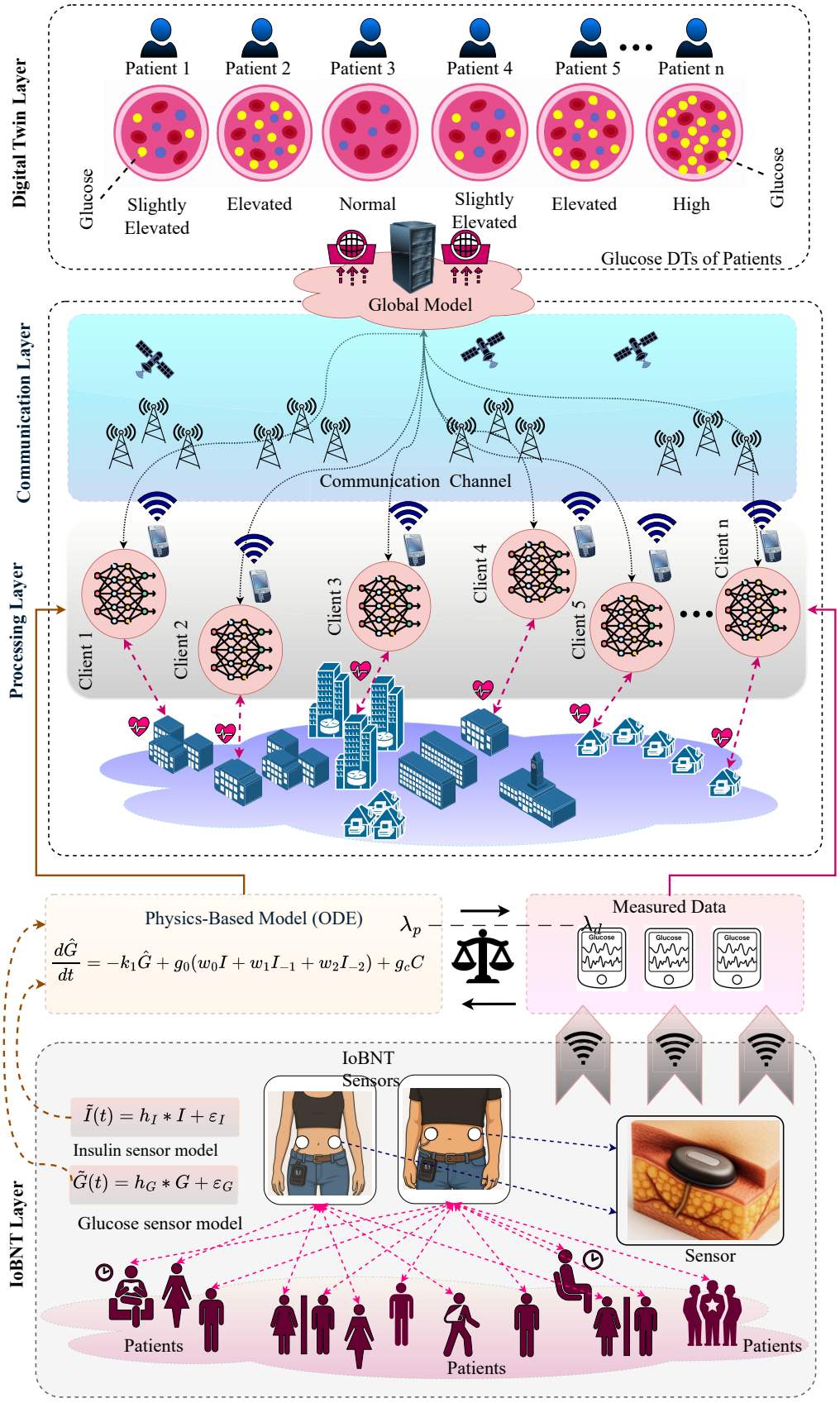

Figure 4.1: System model of the proposed FL-PINN empowered with IoBNT for Glucose-Insulin DTs. It comprises four layers: IoBNT sensing, local processing with physics-informed FCNN models, communication via secure federated updates, and global model aggregation for real-time patient-specific DTs. The integration of physiological ODE constraints ensures interpretability, while FL enables privacy-preserving and scalable deployment across diverse patients.

extracting squared, logarithmic, and square root representations of insulin values and constructs synchronized glucose-insulin sequences. Local training is executed on hybrid models that combine fully connected neural networks with embedded ordinary differential equations that simulate established glucose regulatory mechanisms. The loss function merges empirical prediction error with residuals derived from the differential equations, thereby enforcing biological consistency even under sparse or noisy data. Only model updates are transmitted across clients, which preserves patient privacy while enabling distributed optimization. This combined loss strategy ensures that predictions remain faithful to both observed measurements and mechanistic glucose-insulin dynamics. By harmonizing local physiological modeling with global parameter aggregation, the processing layer supports secure, accurate, and personalized digital twin deployments essential for real-time diabetes care and continuous glucose monitoring.

Communication Layer

The communication layer serves as a critical interface between the distributed local models and the centralized global model within the proposed FL-PINN framework. As depicted in Fig. 4.1, this layer establishes secure and efficient data transfer through wireless infrastructures, including cellular towers, satellite relays, and Wi-Fi access points. Rather than transmitting raw glucose and insulin time series data, which would impose excessive bandwidth demands and compromise privacy, the system communicates only compressed model parameters or gradients. This strategy significantly reduces communication overhead while preserving essential learning information.

Digital Twin Layer

The DT layer represents the final and most patient-centric component of the proposed FL-PINN framework. As illustrated in Fig. 4.1, this layer generates individualized glucose-insulin DTs for each participating patient, continuously reflecting their physiological states. Each DT is dynamically updated based on local sensor measurements and model predictions, providing real-time insights into glucose fluctuations categorized as normal, slightly elevated, elevated, or high. By leveraging outputs from both the local and global models, this layer personalizes simulation and prediction for each user without exposing raw data. The federated architecture ensures that privacy is preserved while enabling learning across a diverse population [163]. These individualized DTs support clinical decision-making by forecasting glucose trends, detecting deviations, and enabling closed-loop control in insulin delivery. Thus, the DT layer translates the computational intelligence of the FL-PINN framework into tangible clinical value, supporting precision monitoring and intervention in diabetes management.

4.3 The Proposed Approaches

4.3.1 IoBNT-Based Measurement

The IoBNT module incorporated in the proposed framework is designed to provide real-time, calibrated measurements of both injected insulin and the resulting glucose concentrations. These measurements serve as foundational inputs for initializing and constraining the mathematical model governing glucose dynamics. If $\mathcal{I}(t) \in \mathbb{R}$ is defined as the actual insulin injected at time $t \in [0, T]$, and $\mathcal{G}(t) \in \mathbb{R}$ is defined as the corresponding true blood glucose level, then the observed quantities obtained through IoBNT are represented by $\tilde{I}(t)$ and $\tilde{G}(t)$, respectively. These observed values are subject to additive noise components $\varepsilon_I(t)$ and $\varepsilon_G(t)$, which reflect the inherent uncertainty associated with nanoscale biosensing. The system-level response of the insulin and glucose sensors is modeled by transfer functions $H_I(\cdot)$ and $H_G(\cdot)$, respectively. Furthermore, $\mathcal{S}_I$ and $\mathcal{S}_G$ denote the nano-sensor mechanisms responsible for detecting insulin and glucose concentrations within the biological medium.

Insulin Sensor Dynamics

Assuming a linear time-invariant response for the insulin sensor, we model the output as:

$$\tilde{I}(t) = \int_0^t h_I(\tau)\mathcal{I}(t-\tau)\,d\tau + \varepsilon_I(t) \tag{4.1}$$

where $h_I(t)$ is the impulse response of the sensor and $\varepsilon_I(t) \sim \mathcal{N}(0, \sigma_I^2)$ is Gaussian noise.

Glucose Sensor Dynamics

Similarly, for glucose:

$$\tilde{G}(t) = \int_0^t h_G(\tau)\mathcal{G}(t-\tau)\,d\tau + \varepsilon_G(t) \tag{4.2}$$

with impulse response $h_G(t)$ and noise $\varepsilon_G(t) \sim \mathcal{N}(0, \sigma_G^2)$.

Transfer Function Models

Each sensor can be modeled as a first-order low-pass system:

$$H_I(s) = \frac{k_I}{\tau_I s + 1}, \quad h_I(t) = \frac{k_I}{\tau_I} e^{-t/\tau_I}, \tag{4.3}$$

$$H_G(s) = \frac{k_G}{\tau_G s + 1}, \quad h_G(t) = \frac{k_G}{\tau_G} e^{-t/\tau_G}, \tag{4.4}$$

where k_I, k_G are gains, and τ_I, τ_G are time constants for the respective sensors.

Digital Sampling and Data Vectors

IoBNT sensors record signals at fixed intervals $t_n = n\Delta t$, which produces discrete-time measurements for model input:

$$I_n := \tilde{I}(t_n), \quad G_n := \tilde{G}(t_n) \tag{4.5}$$

These values form input vectors:

$$\mathbf{I} = [I_0, I_1, \ldots, I_N], \quad \mathbf{G} = [G_0, G_1, \ldots, G_N]$$

which are used to construct model inputs or to train surrogate estimators.

Initial and Boundary Conditions

The glucose-insulin dynamics modeled in this framework are defined over discrete time series data sampled from wearable sensors. While no explicit initial condition is imposed in the form of a hard constraint (e.g., $\hat{\mathcal{G}}(t=0) = G_0$), the first prediction $\hat{\mathcal{G}}^{(k)}(t_0)$ is implicitly treated as the initial condition. It is supervised by the observed glucose value $y_0^{(k)}$ through the empirical loss function. Formally, the initial value is inferred via:

$$\hat{\mathcal{G}}^{(k)}(t_0) = f_\theta(\mathbf{x}_0^{(k)}), \tag{4.6}$$

and contributes to the overall loss via the term:

$$\left(\hat{\mathcal{G}}^{(k)}(t_0) - y_0^{(k)}\right)^2. \tag{4.7}$$

Because the model operates purely in the temporal domain without spatial components, classical boundary conditions (e.g., Dirichlet or Neumann conditions) are not applicable. The model instead focuses on matching dynamic trajectories by enforcing derivative consistency within the prediction window $t_i \in [0, T]$, where a parametric physiological equation governs consistency.

4.3.2 Hybrid Data-Physics Glucose Estimation

Let $\hat{G}_{\mathrm{GBR}}(I)$ be a regression model trained on IoBNT outputs:

$$\hat{G}_{\mathrm{GBR}}(I_j) := \mathbb{E}[\tilde{G}(t_n) \mid \tilde{I}(t_n) = I_j] \tag{4.8}$$

We introduce a simplified ODE-based model that governs glucose evolution over time to embed physiological knowledge. For each local model $k \in \mathcal{C}$, the glucose trajectory is modeled by a parametric

ODE of the form:

$$\begin{aligned}\frac{d\hat{\mathcal{G}}^{(k)}(t)}{dt} = & -k_1^{(k)}\hat{\mathcal{G}}^{(k)}(t) + g_0^{(k)}\Big(w_0^{(k)}\mathcal{I}^{(k)}(t) \\ & + w_1^{(k)}\mathcal{I}^{(k)}(t-\Delta t) \quad + w_2^{(k)}\mathcal{I}^{(k)}(t-2\Delta t)\Big) \\ & + g_c^{(k)}C^{(k)}\end{aligned} \tag{4.9}$$

Here, $\hat{\mathcal{G}}(t) \in \mathbb{R}$ is the predicted glucose level at time t, and $\mathcal{I}(t) \in \mathbb{R}$ is the input insulin level. The parameters k_1, g_0, w_0, w_1, w_2, g_c, and C are learned through training, and represent metabolic clearance, gain, memory weights, basal production scaling, and constant glucose production, respectively. In the proposed FL-PINN architecture, each client device trains a neural network locally to approximate glucose concentrations using features derived from insulin measurements. Unlike conventional regression models, this architecture embeds known physiological knowledge through a differential equation that governs glucose-insulin dynamics. Specifically, the PINN loss includes both a data loss term and a physics loss term computed from a discretized ODE residual. This hybrid approach ensures physiological consistency even when sensor data is noisy or sparse. The total loss minimized by each client is defined as:

$$\begin{aligned}\mathcal{L}_{\text{total}}^{(k)} = & \lambda_d \sum_n \left(\hat{\mathcal{G}}^{(k)}(t_n) - \mathcal{G}^{(k)}(t_n)\right)^2 \\ & + \lambda_p \sum_n \left(\frac{d\hat{\mathcal{G}}^{(k)}(t_n)}{dt} - \text{ODE}_{\text{rhs}}^{(k)}(t_n)\right)^2 \\ & + \lambda_0 \left(\hat{\mathcal{G}}^{(k)}(t_0) - \mathcal{G}^{(k)}(t_0)\right)^2\end{aligned} \tag{4.10}$$

where $\text{ODE}_{\text{rhs}}(t_n)$ denotes the discrete right-hand side of the physiological model defined in Eq. (4.11), and λ_d, λ_p, and λ_0 are non-negative scalar weights that control the relative influence of the data fidelity, physics-informed residual, and initial condition constraints, respectively.

$$\begin{aligned}\text{ODE}_{\text{rhs}}^{(k)}(t_n) := & -k_1^{(k)}\hat{\mathcal{G}}^{(k)}(t_n) \\ & + g_0^{(k)}\left(w_0^{(k)}I_n + w_1^{(k)}I_{n-1} + w_2^{(k)}I_{n-2}\right) \\ & + g_c^{(k)}C^{(k)}\end{aligned} \tag{4.11}$$

$$\dot{\hat{\mathcal{G}}}_i^{(k)} \approx \frac{\hat{\mathcal{G}}_i^{(k)} - \hat{\mathcal{G}}_{i-1}^{(k)}}{\Delta t} \tag{4.12}$$

Communication between local models and a central server is restricted to parameter updates, ensuring that raw physiological data remains decentralized. Each client trains its model locally by minimizing the hybrid loss $\mathcal{L}_{\text{total}}$, and periodically shares model weights with a central aggregator to form a global update. Each client performs localized training using the total loss in Eq. (4.10) and periodically transmits updated model weights to a central aggregator. Algorithm 1 filters insulin and glucose signals through sensor kernels, constructs feature vectors, predicts glucose via a neural network, and trains the model by minimizing a combined data-fit, physics-informed, and initial-condition loss. The

process begins by modeling insulin and glucose measurements through first-order sensor dynamics using exponential kernels, followed by discrete-time sampling. The resulting data is then transformed into a compact feature representation using nonlinear mappings. These features are fed into an NN to predict glucose levels, with the model constrained by three loss components: data-fitting error, initial condition error, and a physics-informed residual term derived from a glucose-insulin ODE. Derivatives are approximated via finite differences, and the model update is performed via backpropagation on the total loss.

Algorithm 1 IoBNT signal encoding and feature construction

Require: Insulin signal $\mathcal{I}(t)$, glucose signal $\mathcal{G}(t)$, sensor kernels h_I, h_G, sampling times $t_n = n\Delta t$
Ensure: Insulin vector $\mathbf{I}$, glucose vector $\mathbf{G}$, feature matrix $\mathbf{x}_n$

1: Sensor dynamics:

$$\tilde{I}(t) = \int_0^t h_I(\tau)\mathcal{I}(t-\tau)\,d\tau + \varepsilon_I(t),$$
$$\tilde{G}(t) = \int_0^t h_G(\tau)\mathcal{G}(t-\tau)\,d\tau + \varepsilon_G(t)$$

2: Transfer functions:

$$H_I(s) = \frac{k_I}{\tau_I s + 1}, \qquad h_I(t) = \frac{k_I}{\tau_I} e^{-t/\tau_I},$$
$$H_G(s) = \frac{k_G}{\tau_G s + 1}, \qquad h_G(t) = \frac{k_G}{\tau_G} e^{-t/\tau_G}$$

3: Discrete sampling:

$$I_n = \tilde{I}(t_n), \quad G_n = \tilde{G}(t_n), \quad \mathbf{I} = [I_1, \ldots, I_N], \quad \mathbf{G} = [G_1, \ldots, G_N]$$

4: Feature construction:

$$\mathbf{x}_n = \begin{bmatrix} \mathcal{I}(t_n) \\ \mathcal{I}^2(t_n) \\ \log(1 + \mathcal{I}(t_n)) \\ \sqrt{\mathcal{I}(t_n)} \end{bmatrix}$$

5: Initial-condition loss:

$$\hat{G}_1 = f_\theta(\mathbf{x}_1), \quad \mathcal{L}_{\text{init}} = (\hat{G}_1 - G_1)^2$$

6: Surrogate estimate:

$$\hat{G}_{\text{GBR}}(I_j) = \mathbb{E}[\tilde{G}(t_n) \mid \tilde{I}(t_n) = I_j]$$

7: Model prediction:

$$\hat{G}_n = f_\theta(\mathbf{x}_n)$$

8: Finite-difference derivative:

$$\dot{\hat{G}}_n \approx \frac{\hat{G}_n - \hat{G}_{n-1}}{\Delta t}$$

9: ODE right-hand side:

$$\text{ODE}_{\text{rhs}}(t_n) = -k_1 \hat{G}_{n-1} + g_0(w_0 I_n + w_1 I_{n-1} + w_2 I_{n-2}) + g_c C$$

10: Physics-informed loss:

$$\mathcal{L}_{\text{phys}} = \|\dot{\hat{G}}_n - \text{ODE}_{\text{rhs}}(t_n)\|^2$$

11: Total local loss:

$$\mathcal{L}_{\text{total}} = \lambda_d \mathcal{L}_{\text{data}} + \lambda_p \mathcal{L}_{\text{phys}} + \lambda_0 \mathcal{L}_{\text{init}}$$

12: Update θ via backpropagation on $\mathcal{L}_{\text{total}}$

4.3.3 Proposed FL-PINN Framework for Glucose-Insulin DT

This section describes a FL framework that integrates a physics-informed parametric model tailored for glucose-insulin dynamics. The framework is designed to function across a network of distributed clients, such as IoBNT-enabled wearables or embedded systems, where each device independently per-

forms local learning using private sensor data. Fig. 4.2 illustrates the architecture of the proposed FL-PINN system. Each client receives physiological signals from IoBNT biosensors and processes them through a local fully connected neural network (FCNN) [164] augmented with physics-based glucose-insulin constraints. These hybrid models compute a local loss composed of data fitting and physics-informed terms [132]. The resulting gradients or model parameters are then sent to the central server, where they are aggregated into a global model using Federated Averaging. This setup enables decentralized, privacy-preserving training across clients while ensuring that predictions remain physiologically consistent through embedded ODE enforcement. Each client receives physiological data from IoBNT biosensors and executes local training using a shared FCNN architecture that incorporates learnable physiological parameters. These include kinetic constants and regulatory gains, namely k_1, g_0, w_0, w_1, w_2, g_c, and C. The parameters are directly embedded within the model to enforce domain-specific glucose-insulin ODEs, thereby maintaining consistency with established biological mechanisms while supporting decentralized computation.

Client Data Structure and Feature Encoding

Scalability is a critical requirement in personalized digital health systems, particularly for managing chronic conditions such as diabetes. The proposed federated framework is designed to accommodate a growing population of patients, each equipped with IoBNT devices that integrate wearable insulin pumps and continuous glucose monitors.

These clients operate independently, collecting dense physiological data in real-time, while maintaining autonomy over their measurements. The training network consists of K participating clients, indexed by the set $\mathcal{C} = \{1, 2, \ldots, K\}$. Each client $k \in \mathcal{C}$ corresponds to an individual patient. The local sensing unit of each client generates a dataset:

$$\mathcal{D}_k = \left\{ \left(\mathbf{x}_i^{(k)}, y_i^{(k)} \right) \right\}_{i=1}^{N_k}, \tag{4.13}$$

where $\mathbf{x}_i^{(k)} \in \mathbb{R}^4$ denotes a feature vector constructed from insulin data at discrete time index $t_i \in [0, T]$, while $y_i^{(k)} \in \mathbb{R}$ represents the corresponding glucose concentration observed at the same timestamp. The variable $N_k \in \mathbb{N}$ indicates the total number of available measurements for each client. The insulin signal $\mathcal{I}^{(k)}(t_i)$, measured via embedded IoBNT-enabled pumps, is then mapped into a nonlinear feature space using a deterministic transformation:

$$\mathbf{x}_i^{(k)} = \begin{bmatrix} \mathcal{I}^{(k)}(t_i) \\ \left(\mathcal{I}^{(k)}(t_i)\right)^2 \\ \log\left(1 + \mathcal{I}^{(k)}(t_i)\right) \\ \sqrt{\mathcal{I}^{(k)}(t_i)} \end{bmatrix}. \tag{4.14}$$

This transformation captures multiple aspects of insulin absorption and metabolic effectiveness: the first element, $\mathcal{I}^{(k)}(t_i)$, retains the raw insulin input at time t_i; the quadratic term, $\left(\mathcal{I}^{(k)}(t_i)\right)^2$, empha-

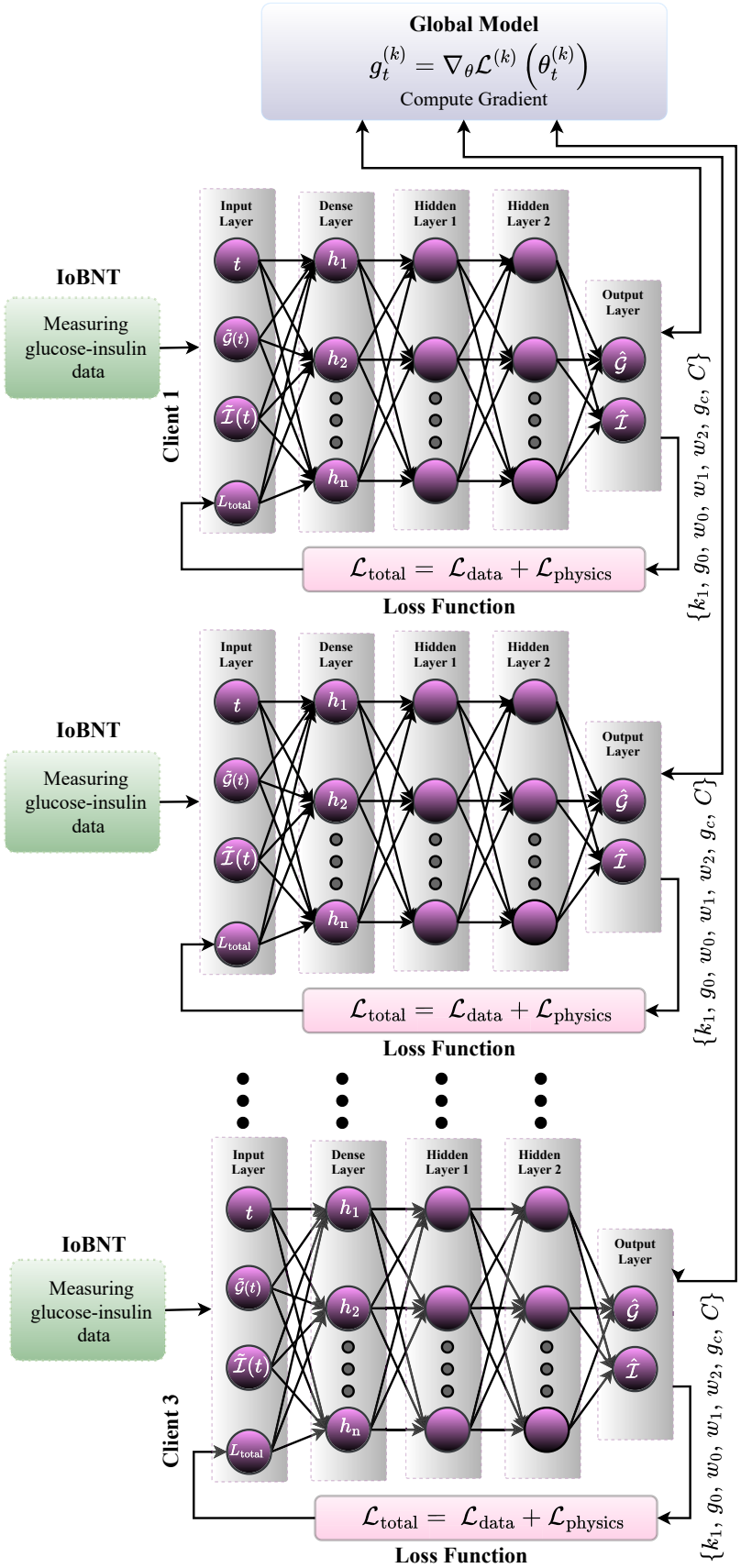

Figure 4.2: Architecture of the FL-PINN with FCNN.

sizes saturation or cumulative dosing effects; the logarithmic term, $\log(1+\mathcal{I}^{(k)}(t_i))$, models diminishing physiological responsiveness at higher doses; and the square root, $\sqrt{\mathcal{I}^{(k)}(t_i)}$, reflects nonlinear kinetic uptake properties observed in biological tissues. The corresponding output variable $y_i^{(k)}$ is a sampled blood glucose concentration $\mathcal{G}^{(k)}(t_i)$ derived from the client's IoBNT-enabled glucose monitoring system. These values may be smoothed, denoised, or calibrated as part of pre-processing pipelines prior to federated training. In summary, each client maintains a structured time series of paired insulin-glucose measurements:

$$\mathcal{D}_k = \left\{ \left(\mathcal{F}(\mathcal{I}^{(k)}(t_i)), \mathcal{G}^{(k)}(t_i) \right) \right\}_{i=1}^{N_k}, \quad \text{with} \quad \mathcal{F}(\cdot) : \mathbb{R} \to \mathbb{R}^4, \tag{4.15}$$

where $\mathcal{F}(\cdot)$ denotes the nonlinear transformation applied to each insulin observation. This structure enables each client to contribute uniquely informative input-output pairs while preserving privacy and scalability across the networked system.

Global Model Definition and Parameterization

The global model aggregates both data-driven learning components and domain-informed physiological parameters into a unified structure, parameterized by the set θ [45]. This parameter set consists of two distinct parts:

- The weights and biases of an FCNN [164], denoted as $f_\theta(\cdot) : \mathbb{R}^4 \to \mathbb{R}$, which approximates the nonlinear mapping from insulin feature vectors $\mathbf{x}_i^{(k)}$ to predicted glucose values $\hat{\mathcal{G}}^{(k)}(t_i)$,
- A set of learnable physiological coefficients that define the temporal evolution of glucose dynamics through a parametric equation.

For a given input vector $\mathbf{x}_i^{(k)} \in \mathbb{R}^4$, the surrogate glucose concentration is computed as:

$$\hat{\mathcal{G}}^{(k)}(t_i) = f_\theta(\mathbf{x}_i^{(k)}). \tag{4.16}$$

The parametric components of the dynamic system are represented by:

$$\{k_1, g_0, w_0, w_1, w_2, g_c, C\}. \tag{4.17}$$

where $k_1 \in \mathbb{R}_+$ represents a positive rate constant that models endogenous glucose clearance and metabolic consumption. The sensitivity of the glucose response to insulin is governed by a positive scaling gain $g_0 \in \mathbb{R}_+$. Temporal effects are accounted for by the memory coefficients $w_0, w_1, w_2 \in \mathbb{R}$, which assign weights to present and past insulin values, enabling the model to reflect delayed physiological responses. The term $g_c \in \mathbb{R}$ scales basal glucose production independently of insulin activity, while $C \in \mathbb{R}$ serves as a tonic offset that captures constant hepatic glucose generation or a homeostatic background glucose level.

The inclusion of these interpretable physiological parameters enables the model to adhere to known biological constraints while allowing flexibility in fitting real-world patient data. By combining the expressive power of the FCNN with domain-specific coefficients, the global model θ captures both empirical patterns and mechanistic structure. This dual representation supports generalization across diverse patients while maintaining biological plausibility within individual trajectories [45].

Federated Training Procedure

Training unfolds over $R \in \mathbb{N}$ communication rounds indexed by $t \in \{0, 1, \ldots, R-1\}$. At each round:

1. The server broadcasts the global model parameters θ^t to all clients.
2. Each client initializes its local model with θ^t, and optimizes it using its private dataset $\mathcal{D}_k$.
3. The updated parameters $\theta^{(k)}$ from each client are sent back to the server.
4. The server aggregates the parameters using federated averaging to produce the next global model θ^{t+1}.

Local Objective Function and Physics-Informed Loss

Each client minimizes a composite loss function that enforces consistency with both empirical data and the underlying glucose-insulin dynamics. The local loss function for client $k \in \mathcal{C}$ is given by:

$$\begin{aligned}\mathcal{L}^{(k)}(\theta) = \lambda_d \sum_{i=1}^{N_k} \left(\hat{\mathcal{G}}_i^{(k)} - y_i^{(k)}\right)^2 \\ + \lambda_p \sum_{i=3}^{N_k} \left(\dot{\hat{\mathcal{G}}}_i^{(k)} - \phi^{(k)}\left(\mathcal{I}^{(k)}(t_i)\right)\right)^2,\end{aligned} \tag{4.18}$$

where $\hat{\mathcal{G}}_i^{(k)} = f_\theta(\mathbf{x}_i^{(k)})$ denotes the predicted glucose concentration, and $\dot{\hat{\mathcal{G}}}_i^{(k)} \approx \frac{d}{dt}\hat{\mathcal{G}}^{(k)}(t_i)$ is the estimated temporal derivative obtained using finite differences.

The term $\phi^{(k)}\left(\mathcal{I}(t_i)\right)$ represents the output of the client-specific parametric dynamic model:

$$\begin{aligned}\phi^{(k)}\left(\mathcal{I}(t_i)\right) = & -k_1^{(k)}\hat{\mathcal{G}}^{(k)}(t_i) + g_0^{(k)}\big[w_0^{(k)}\mathcal{I}^{(k)}(t_i) \\ & + w_1^{(k)}\mathcal{I}^{(k)}(t_i - \Delta t) + w_2^{(k)}\mathcal{I}^{(k)}(t_i - 2\Delta t)\big] \\ & + g_c^{(k)}C^{(k)}.\end{aligned} \tag{4.19}$$

The positive scalar weights λ_d and λ_p regulate the trade-off between accurate prediction of the measured data and adherence to the underlying physiological model. This hybrid loss structure ensures that each local model remains faithful to patient-specific sensor measurements while also conforming to system-level dynamical constraints derived from known glucose-insulin interactions.

Client Optimization and Global Aggregation

To solve the local minimization problem for each client $k \in \mathcal{C}$, the optimization algorithm used is *Adam* (Adaptive Moment Estimation) [165], which extends stochastic gradient descent by incorporating adaptive learning rates and momentum-like dynamics for improved convergence. Given the local loss function $\mathcal{L}^{(k)}(\theta)$, Adam updates the parameter vector $\theta^{(k)} \in \mathbb{R}^d$ iteratively based on first- and second-order moment estimates of the stochastic gradient. At local training step t, the client computes the instantaneous gradient:

$$g_t^{(k)} := \nabla_\theta \mathcal{L}^{(k)} \left(\theta_t^{(k)} \right). \tag{4.20}$$

Adam then performs the following internal updates:

$$m_t^{(k)} = \beta_1 m_{t-1}^{(k)} + (1 - \beta_1) g_t^{(k)}, \tag{4.21}$$

$$v_t^{(k)} = \beta_2 v_{t-1}^{(k)} + (1 - \beta_2) \left(g_t^{(k)} \right)^2, \tag{4.22}$$

where $\beta_1, \beta_2 \in (0, 1)$ are exponential decay rates controlling the influence of past gradients. The default values are typically $\beta_1 = 0.9$, $\beta_2 = 0.999$. Since $m_t^{(k)}$ and $v_t^{(k)}$ are biased toward zero in early iterations, bias-corrected estimates are computed as:

$$\hat{m}_t^{(k)} = \frac{m_t^{(k)}}{1 - \beta_1^t}, \quad \hat{v}_t^{(k)} = \frac{v_t^{(k)}}{1 - \beta_2^t}. \tag{4.23}$$

Finally, the parameter update is performed as:

$$\theta_{t+1}^{(k)} = \theta_t^{(k)} - \eta \frac{\hat{m}_t^{(k)}}{\sqrt{\hat{v}_t^{(k)}} + \epsilon}, \tag{4.24}$$

where $\eta > 0$ is the learning rate and $\epsilon \ll 1$ is a small constant (e.g., 10^{-8}) added to ensure numerical stability and avoid division by zero. The Adam optimizer thus dynamically adjusts the learning rate for each parameter dimension based on both the magnitude and variance of the gradients. This leads to faster convergence and improved robustness under noisy, sparse, or non-stationary data conditions common in glucose-insulin trajectories collected from heterogeneous IoBNT devices. As shown in Algorithm 2, the proposed system of the framework consists of three main phases: data acquisition, model training, and deployment.

4.4 Experimental Setups

4.4.1 Software Framework and Training Protocol

The proposed FL-PINN framework was implemented using `PyTorch 2.1.0` for dynamic computation graph modeling and federated training [166]. Data preprocessing was conducted via `pandas` and

`scikit-learn`, specifically leveraging `StandardScaler` to normalize both engineered insulin feature vectors and glucose targets. The modeling pipeline employed engineered features: raw insulin ($\mathcal{I}(t)$), squared insulin ($\mathcal{I}^2(t)$), logarithmic transformation ($\log(1+\mathcal{I}(t))$), and square-root transformation ($\sqrt{\mathcal{I}(t)}$), concatenated to form a 4-dimensional input space. The PINN architecture was instantiated using a three-layer fully connected neural network (FCNN) with `Tanh` activations and 54 hidden units per layer, augmented with seven trainable physiological parameters: $k_1, g_0, w_0, w_1, w_2, g_c, C$.

Algorithm 2 The proposed system of the framework

Require: Global model parameters $\theta^0 = \{f_\theta, k_1, g_0, w_0, w_1, w_2, g_c, C\}$, learning rate η, decay rates β_1, β_2, small constant ϵ, loss weights λ_d, λ_p, time step Δt, total rounds R

Ensure: Final model θ^R

for each round $t = 0$ to $R-1$ **do**

  Server broadcasts θ^t to all clients $k \in \mathcal{C}$

  for each client k in parallel **do**

    Construct local dataset $\mathcal{D}_k = \{(\mathbf{x}_i^{(k)}, y_i^{(k)})\}_{i=1}^{N_k}$ where:

$$\mathbf{x}_i^{(k)} = \left[\mathcal{I}(t_i), \mathcal{I}^2(t_i), \log(1+\mathcal{I}(t_i)), \sqrt{\mathcal{I}(t_i)}\right]$$

    Initialize: $m_0^{(k)} = 0$, $v_0^{(k)} = 0$, $\theta^{(k)} = \theta^t$

    for each local epoch **do**

      Predict glucose: $\hat{\mathcal{G}}_i^{(k)} = f_\theta(\mathbf{x}_i^{(k)})$

      Estimate derivative: $\dot{\hat{\mathcal{G}}}_i^{(k)} \approx \frac{\hat{\mathcal{G}}_i^{(k)} - \hat{\mathcal{G}}_{i-1}^{(k)}}{\Delta t}$

      Evaluate physics model:

$$\begin{aligned}\phi^{(k)}(\mathcal{I}(t_i)) = &- k_1^{(k)}\hat{\mathcal{G}}^{(k)}(t_i) + g_0^{(k)}\Big[w_0^{(k)}\mathcal{I}^{(k)}(t_i) \\ &+ w_1^{(k)}\mathcal{I}^{(k)}(t_i - \Delta t) \\ &+ w_2^{(k)}\mathcal{I}^{(k)}(t_i - 2\Delta t)\Big] + g_c^{(k)}C^{(k)}\end{aligned}$$

      Compute loss:

$$\begin{aligned}\mathcal{L}^{(k)}(\theta) = &\lambda_d \sum_{i=1}^{N_k} (\hat{\mathcal{G}}_i^{(k)} - y_i^{(k)})^2 \\ &+ \lambda_p \sum_{i=3}^{N_k} (\dot{\hat{\mathcal{G}}}_i^{(k)} - \phi^{(k)}(\mathcal{I}(t_i)))^2\end{aligned}$$

      Compute gradient: $g_t^{(k)} = \nabla_\theta \mathcal{L}^{(k)}(\theta_t^{(k)})$

      Update moments:

$$m_t^{(k)} = \beta_1 m_{t-1}^{(k)} + (1-\beta_1) g_t^{(k)},$$

$$\mathrm{v}_t^{(k)} = \beta_2 v_{t-1}^{(k)} + (1-\beta_2)(g_t^{(k)})^2$$

      Bias correction:

$$\hat{m}_t^{(k)} = \frac{m_t^{(k)}}{1-\beta_1^t}, \quad \hat{v}_t^{(k)} = \frac{v_t^{(k)}}{1-\beta_2^t}$$

      Parameter update:

$$\theta_{t+1}^{(k)} = \theta_t^{(k)} - \eta \cdot \frac{\hat{m}_t^{(k)}}{\sqrt{\hat{v}_t^{(k)}} + \epsilon}$$

    end for

    Send updated $\theta^{(k)}$ to server

  end for

  Server aggregates: $\theta^{t+1} = \frac{1}{K}\sum_{k=1}^{K} \theta^{(k)}$

end for

return θ^R

The federated training loop consisted of $R = 40$ communication rounds, each with $E = 10$ local

training epochs. Four subset scenarios were examined (3C, 6C, 7C, and 9C) to assess scalability and resilience under varying degrees of decentralization. Each client model was trained using the Adam optimizer with a learning rate of $\eta = 0.002$. The hybrid loss function minimized by each client included: (i) mean squared error (MSE) for data fitting $\mathcal{L}_d$, (ii) physics-based residual enforcement $\mathcal{L}_p$ from a discretized glucose-insulin ODE model, and (iii) initial condition consistency $\mathcal{L}_0$. These were weighted by $\lambda_d = 2.0$, $\lambda_p = 5.0$, and an implicit λ_0 via supervision. The time discretization interval was fixed at $\Delta t = 25.0$ seconds. Client-specific state updates were aggregated via parameter-wise `FedAvg`. The architecture was benchmarked through training/test MSE metrics and stored all outputs, including loss distributions and residuals, under a reproducible directory structure `J3FedResults`. Statistical summaries (skewness, kurtosis, RMSE, R^2) were extracted for each loss type across clients and stored in Excel for further analysis.

4.4.2 Dataset

The dataset used in this study originates from the National Institute of Diabetes and Digestive and Kidney Diseases and is publicly known as the Pima Indian Diabetes Dataset [167]. It is widely used for binary classification tasks to predict the likelihood of diabetes onset based on diagnostic health measurements. This dataset exclusively contains records from female patients of Pima Indian heritage who are at least 21 years old. Each instance represents a patient's clinical measurements, with the objective of predicting diabetes presence (`Outcome` = 1) or absence (`Outcome` = 0). This dataset has been instrumental in the development and benchmarking of predictive models in medical machine learning, particularly in studies involving risk assessment, clinical decision support, and personalized medicine.

4.5 Performance Evaluation

This section presents the results derived from evaluating the proposed FL-PINN framework. To rigorously assess its performance, we implemented the architecture across four experimental scenarios involving different numbers of participating clients. Specifically, we conducted experiments using 3, 6, 7, and 9 clients. These configurations facilitated a systematic examination of the framework's scalability, adaptability, and robustness under varying levels of decentralization. In addition, the multi-scenario evaluation enabled us to quantify how effectively the federated strategy sustains accurate glucose-insulin predictions, enforces physiological constraints, and upholds data privacy.

4.5.1 Training Evaluation of the four FL Configurations

Fig. 4.3 illustrates the dynamics of average weight drift throughout federated training rounds for each configuration. Notably, as the number of clients increases, the model exhibits greater divergence during the initial rounds due to increased heterogeneity; however, this is consistently followed by a sta-

bilization phase. This behavior underscores the framework's robustness in maintaining convergence and parameter coherence despite increased distribution. In particular, the 3C scenario stabilizes the fastest, whereas the 9C case displays higher early divergence; nevertheless, all configurations gradually converge with additional training rounds. In addition, Fig. 4.4 shows the client-wise density of physics-based residuals under the 3C-9C scenarios. In all cases, the mean ODE loss remains very low (≈ 0.033) with a standard deviation below 0.05, and more than 60% of residuals lie under 0.01. These sharply peaked, narrow distributions confirm that the embedded ODE constraints are consistently satisfied.

Fig. 4.5 illustrates client-wise densities of data-fitting loss under the 3C-9C scenarios. Although the mean loss remains virtually unchanged (≈ 0.49-0.50), the standard deviation increases markedly from 0.07 in 6C to 0.11 in 9C, thereby underscoring the growing influence of data heterogeneity as more clients participate. Meanwhile, Fig. 4.4 and Fig. 4.5 together illuminate two complementary facets of model fidelity. Specifically, the physics-based residuals (Fig. 4.4) stay tightly clustered around zero across all scenarios (mean 0.033, ¡0.05), with over 60% of errors below 0.01, which reflects the ODE constraints' strong regularizing effect—largely invariant to client count. By contrast, the data-fitting losses exhibit both higher central tendency and broader dispersion as federation scales, indicating that empirical errors are more sensitive to inter-client variability than the mechanistic physics component. In summary, the embedded ODE ensures consistent physiological behavior, whereas the FCNN's data term reveals the cost of accommodating diverse glucose patterns across an expanding client population.

Table 4.1, Table 4.2, and Table 4.3 collectively present an in-depth evaluation of the FL-PINN framework across four federated configurations: 3C, 6C, 7C, and 9C. These tables quantify critical statistical metrics, including mean, standard deviation, minimum, maximum, skewness, kurtosis, MSE, RMSE, and R^2. These metrics offer a multidimensional view of system behavior, enabling granular analysis of both prediction accuracy and physical constraint satisfaction. In the physics-based loss evaluation (Table 4.1), all scenarios produce extremely low mean residuals, ranging from 0.0327 in the 3C case to 0.0342 in 6C, with only a minimal increase in standard deviation from 0.0474 to 0.0516. This tight clustering, further reinforced by low MSE values (approximately 0.0022 to 0.0027) and stable RMSE across scenarios, indicates that the proposed ODE model consistently regularizes the learning process while preserving physiological fidelity as the number of clients increases. The skewness and kurtosis values, for example 1.7965 and 3.0325 in 3C versus 1.9753 and 4.0963 in 6C, suggest that although the distributions are slightly right-skewed, they remain statistically narrow and unimodal.

In contrast, Table 4.2 reveals greater variability in empirical performance. Although the mean data-fitting loss slightly decreases from 0.5040 (3C) to 0.4860 (9C), the standard deviation increases from 0.0876 to 0.1086, indicating rising dispersion as client heterogeneity grows. Notably, 9C exhibits the highest observed loss (Max = 1.4907) and extreme statistical deviations, with skewness reaching 3.8899 and kurtosis soaring to 26.9667, in comparison to 1.5955 and 2.2004 in 3C. This signals an asymmetric and long-tailed error profile, likely driven by non-uniform glucose responses and data sparsity across clients. The total loss metrics in Table 4.3 integrate both physics and data terms. Interestingly, the average total loss decreases slightly from 1.3348 (3C) to 1.3056 (9C), demonstrating learning convergence.

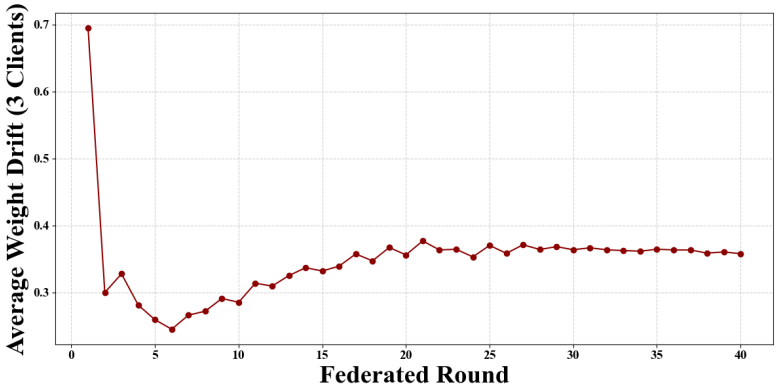

(a)

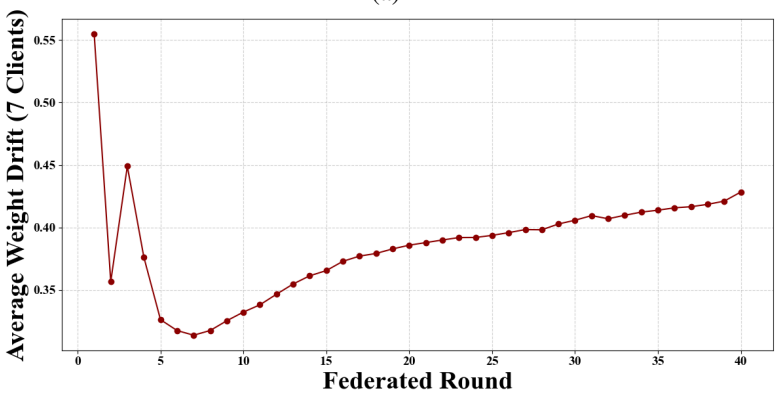

(b)

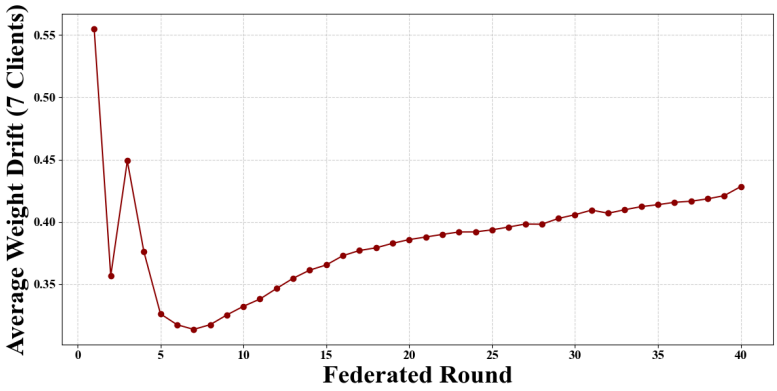

(c)

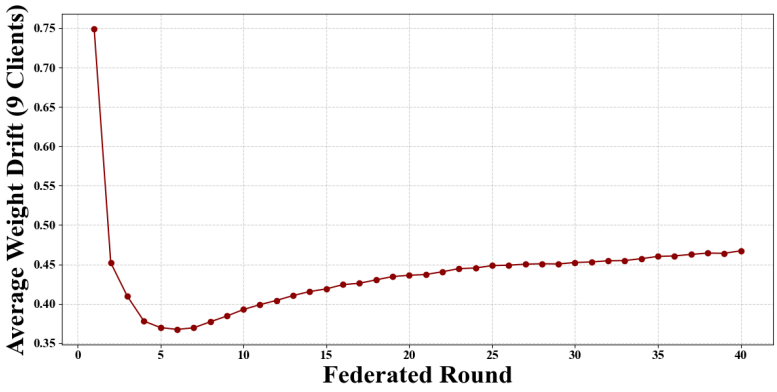

(d)

Figure 4.3: Average weight drift (L2 norm) over federated rounds for 3C, 6C, 7C, and 9C scenarios.

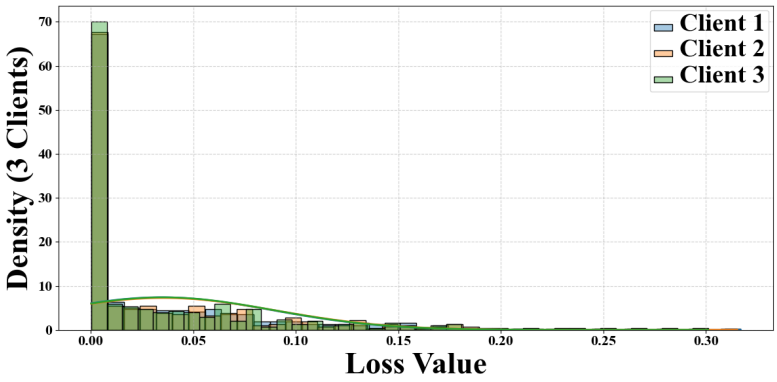

(a)

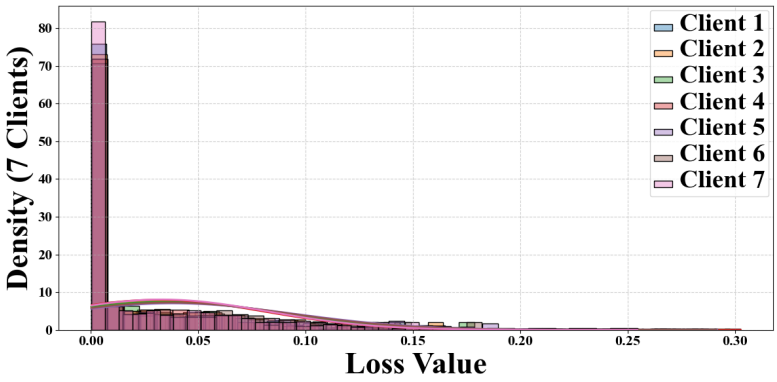

(b)

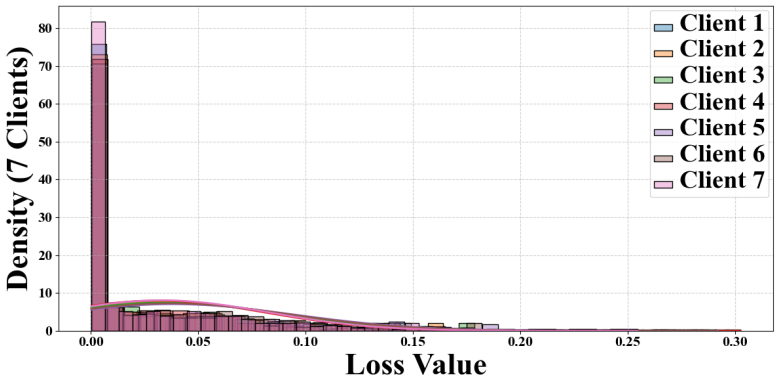

(c)

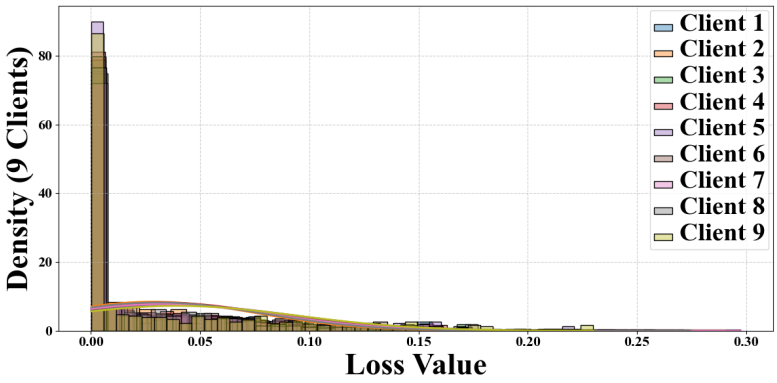

(d)

Figure 4.4: Client-wise physics-based loss distributions for (a) 3C, (b) 6C, (c) 7C, and (d) 9C

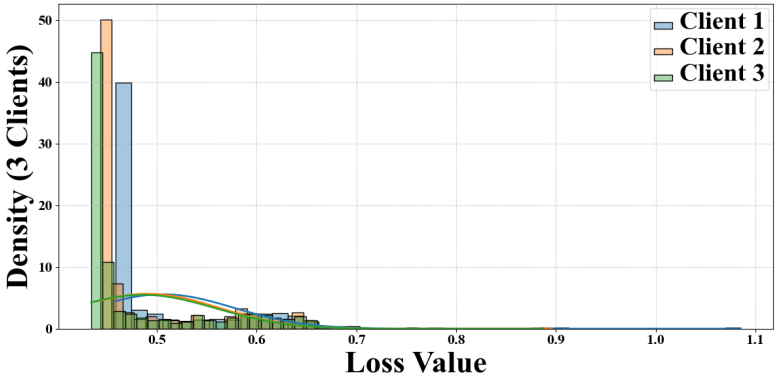

(a)

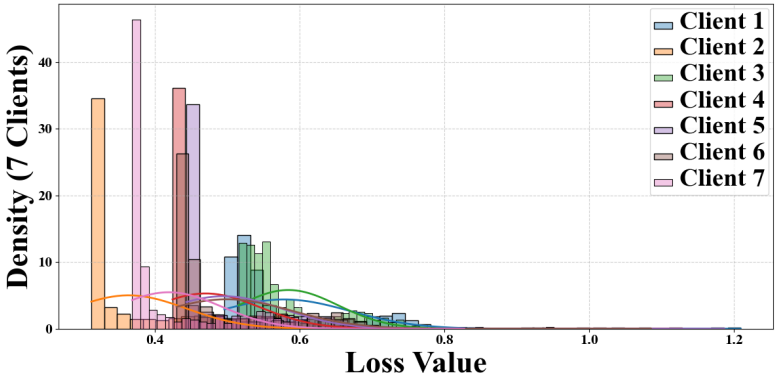

(b)

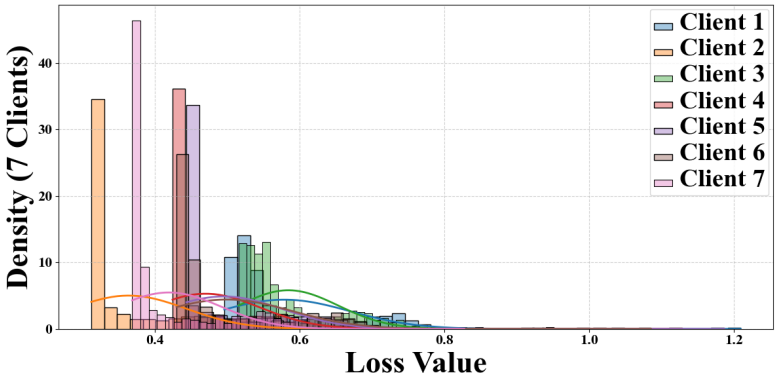

(c)

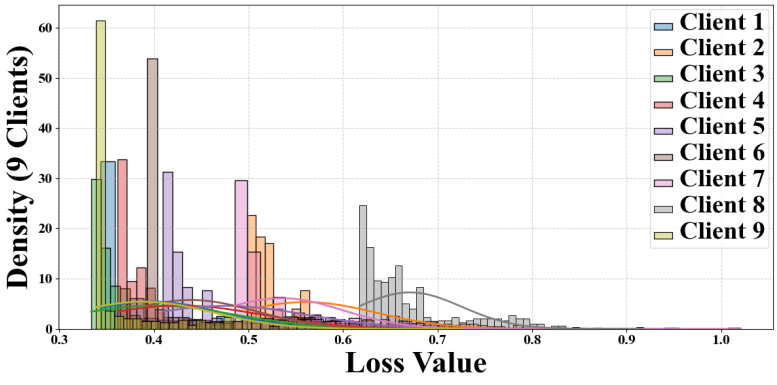

(d)

Figure 4.5: Client-wise data-fitting loss distributions for (a) 3C, (b) 6C, (c) 7C, and (d) 9C.

However, the standard deviation increases from 0.6423 to 0.6899, and kurtosis rises from 2.5030 to 6.1327, suggesting that while overall optimization progresses, outlier behaviors become more prominent as the federation scales. This trade-off highlights the importance of regularization through PINN physics terms, which clearly dampen error volatility and enhance reliability in federated biomedical modeling.

4.5.2 Test Evaluation of the Proposed Framework

Fig. 4.6 presents 3D surface plots of total loss over training epochs and client IDs for the four federated configurations. All surfaces exhibit a steep decline in loss during the first 100-150 epochs, followed by a gradual plateau, indicating rapid initial learning and subsequent fine-tuning. Comparison across scenarios reveals that the 3C configuration achieves the lowest loss and fastest convergence, whereas the 9C case displays a more elongated loss tail, reflecting slower adaptation due to higher client heterogeneity.

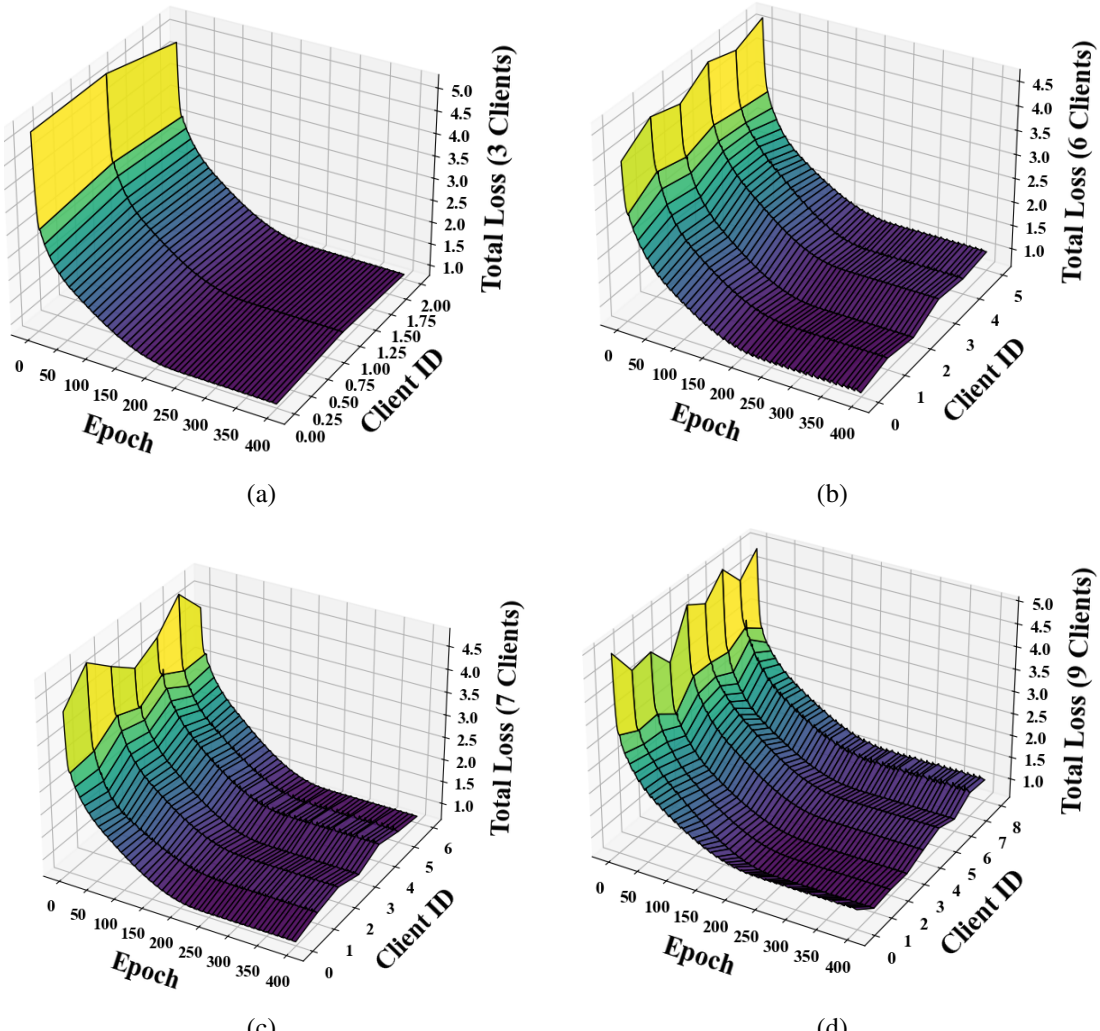

Figure 4.6: 3D surface plots of total loss over epochs and client IDs for the 3C, 6C, 7C, and 9C scenarios.

Client-specific ridges and valleys on each surface capture subtle differences in local convergence rates, yet all configurations ultimately converge to comparable loss levels. This visualization un-

Table 4.1: Evaluation of physics loss across four scenarios based on the proposed ODE formulation

Metric	3C	6C	7C	9C
Mean	0.0327	0.0342	0.0336	0.0334
Standard Deviation	0.0474	0.0516	0.0494	0.0489
Min	0.0003	0.0003	0.0003	0.0003
Max	0.2410	0.2741	0.2580	0.2452
Skewness	1.7965	1.9753	1.9042	1.8394
Kurtosis	3.0325	4.0963	3.7725	3.3856
MSE	0.0022	0.0027	0.0025	0.0024
RMSE	0.0474	0.0516	0.0494	0.0489
R2	-4.66e+31	-2.79e+31	-5.35e+31	-1.23e+31

Table 4.2: Summary of data loss evaluation across four scenarios using the FCNN

Metric	3C	6C	7C	9C
Mean	0.5040	0.4932	0.4917	0.4860
Standard Deviation	0.0876	0.0716	0.0987	0.1086
Min	0.4422	0.4435	0.4214	0.4136
Max	0.9497	0.8227	1.3263	1.4907
Skewness	1.5955	1.5451	3.1389	3.8899
Kurtosis	2.2004	1.6547	18.4460	26.9667
MSE	0.0077	0.0052	0.0099	0.0120
RMSE	0.0876	0.0716	0.0987	0.1086
R2	-4.24e+29	-4.10e+29	-1.01e+29	-6.23e+29

Table 4.3: Evaluation of total loss across four scenarios using the proposed FL-PINN framework

Metric	3C	6C	7C	9C
Mean	1.3348	1.3279	1.3194	1.3056
Standard Deviation	0.6423	0.6459	0.6773	0.6899
Min	0.8878	0.8903	0.8464	0.8309
Max	4.3090	4.3052	5.2326	5.4305
Skewness	1.6919	1.7449	2.0313	2.1496
Kurtosis	2.5030	2.7395	5.1236	6.1327
MSE	0.4126	0.4180	0.4613	0.4770
RMSE	0.6423	0.6459	0.6773	0.6899
R2	-2.65e+30	-3.07e+30	-2.51e+30	-3.20e+30

derscores the FL-PINN framework's ability to harmonize decentralized updates and maintain robust convergence despite varying federation sizes. Fig. 4.7 provides a high-fidelity comparison of actual versus predicted glucose trajectories under the proposed FL-PINN framework for 3C, 6C, 7C, and 9C scenarios. From a computational perspective, the close alignment between the solid black curve and the dashed blue prediction demonstrates the effectiveness of hybrid federated averaging combined with physics-informed residual minimization. The narrow shaded bands, which represent 95% confidence intervals, illustrate the framework's uncertainty quantification, with interval widths typically under ± 15 mg/dL despite the non-IID client distributions.

Moreover, the framework maintains stability across increasing client heterogeneity by enforcing ODE constraints during local optimization, as evidenced by smooth prediction traces even in highly variable glucose regimes. Medically, this level of accuracy and precision is critical: the mean absolute

deviation remains below 10 mg/dL, ensuring reliable detection of hypoglycemic episodes (< 70 mg/dL) and hyperglycemic excursions (> 180 mg/dL). Such performance supports real-time closed-loop insulin dosing and early warning systems. Furthermore, the robust convergence across all four scenarios highlights the solution's scalability for personalized DT applications in diabetes care, delivering both computational robustness and clinical safety.

Fig. 4.8 and Fig. 4.9 together demonstrate the FL-PINN framework's robust and clinically acceptable performance across all four federated configurations (3C, 6C, 7C and 9C). The heatmaps in Fig. 4.8 visualize the absolute prediction errors for each client (vertical axis) and each sample (horizontal axis), showing that the vast majority of residuals remain in low-error bands (darker colors) with only rare high-error spikes. Concurrently, the violin plots in Fig. 4.9 succinctly summarize these residuals' distributions: the medians are centered near zero, interquartile ranges lie well within clinically safe limits, and the density peaks indicate that most errors fall below thresholds critical for hypoglycemia and hyperglycemia management. Together, these figures confirm that FL-PINN maintains consistent error margins and reliable glucose tracking even as federation size increases.

A deeper inspection reveals nuanced insights into error heterogeneity and framework stability. In Fig. 4.8, the 3C scenario exhibits the tightest error band, with fewer outliers above 20 mg/dL, whereas the 9C scenario shows slightly more dispersed spikes, consistent with increased data heterogeneity, but still maintains error concentrations below critical clinical thresholds in over 90% of samples. The violin plots quantify these trends: for 3C, the interquartile range (IQR) of residuals is under 5 mg/dL and the tails remain below 15 mg/dL; for 9C, the IQR expands to approximately 8 mg/dL and tails to 25 mg/dL, yet the distribution remains sharply peaked. These results underscore the effectiveness of embedded ODE constraints and federated averaging in mitigating divergence, ensuring that even under non-IID client data distributions, the FL-PINN framework delivers both high-fidelity predictions and tight uncertainty bounds crucial for real-time, closed-loop diabetes management.

4.5.3 Comparative Analysis

The comparative summary in Table 4.4 reveals the evolution of research in physics-informed and FL systems from engineering and material sciences toward biomedical applications. Prior works established valuable methodologies for embedding physical priors within learning architectures [168, 169, 170], achieving consistency and generalization in data-limited environments. However, most efforts remained confined to macro-scale systems such as energy networks or material synthesis [171, 172], relying on static datasets and centralized computation without feedback from living processes. In contrast, the proposed framework introduces a decentralized PINN–FL–IoBNT architecture designed for dynamic physiological modeling of glucose–insulin regulation. It bridges physical, computational, and biological layers into a unified DT ecosystem capable of real-time inference, adaptive learning, and privacy-preserving collaboration across distributed clinical environments.

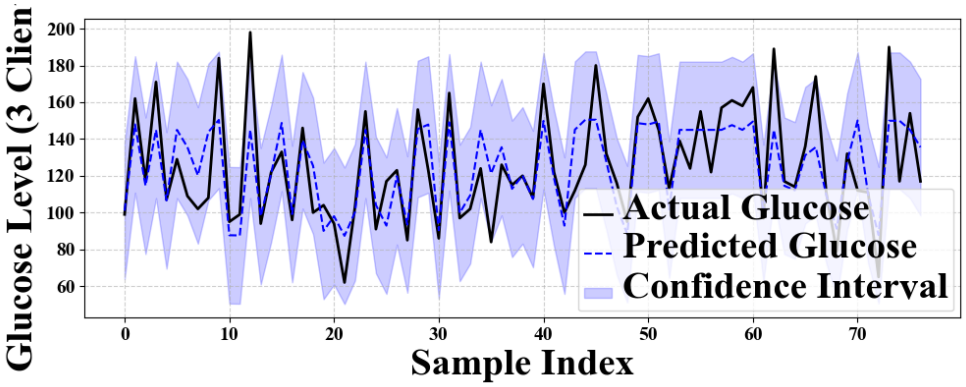

(a)

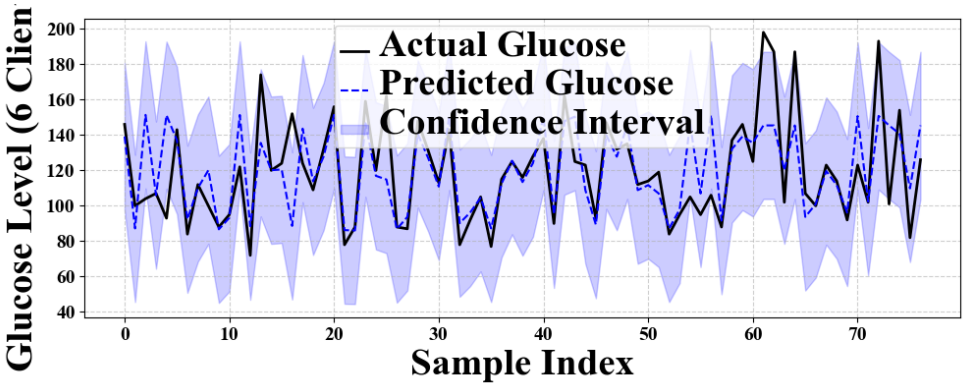

(b)

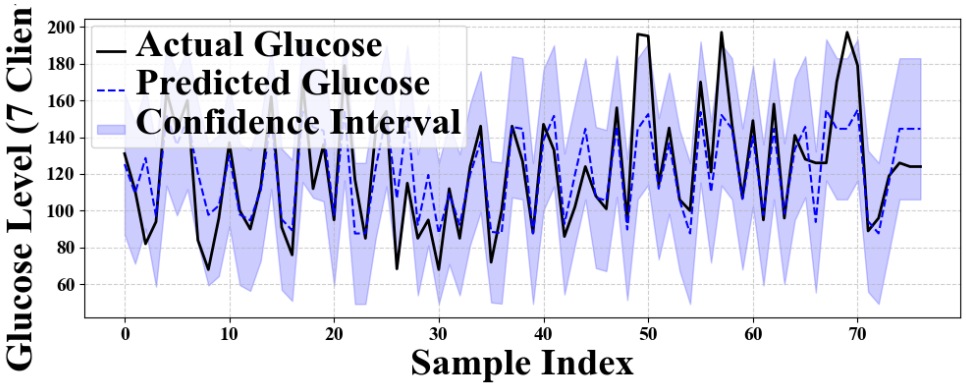

(c)

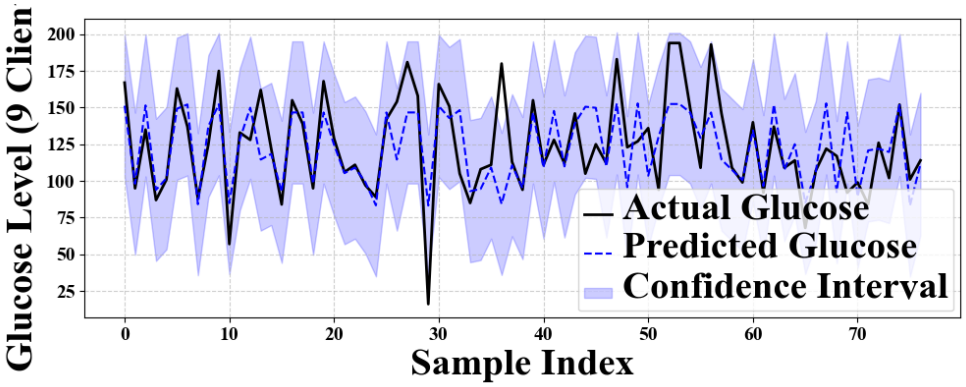

(d)

Figure 4.7: Predicted vs. actual glucose levels for 3C-9C scenarios.

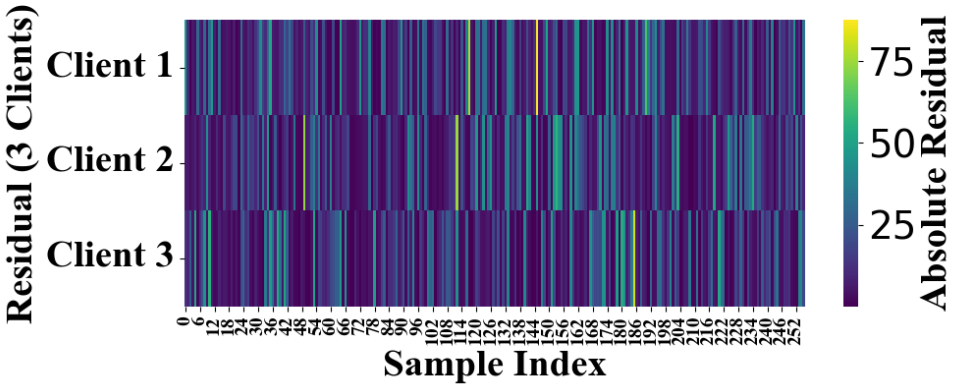

(a)

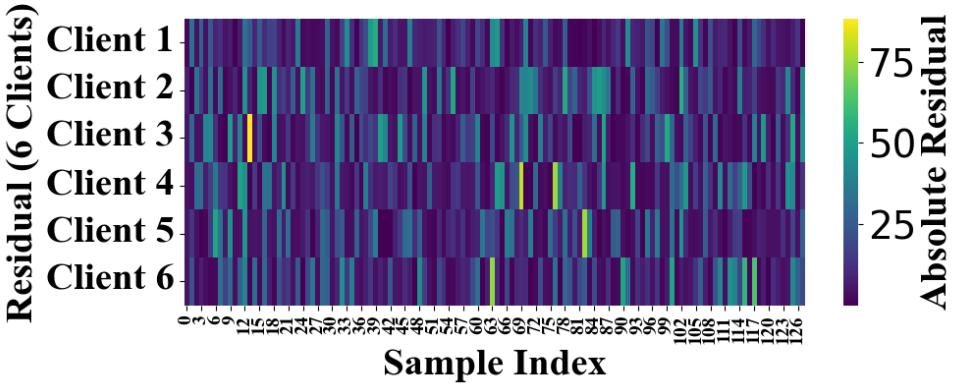

(b)

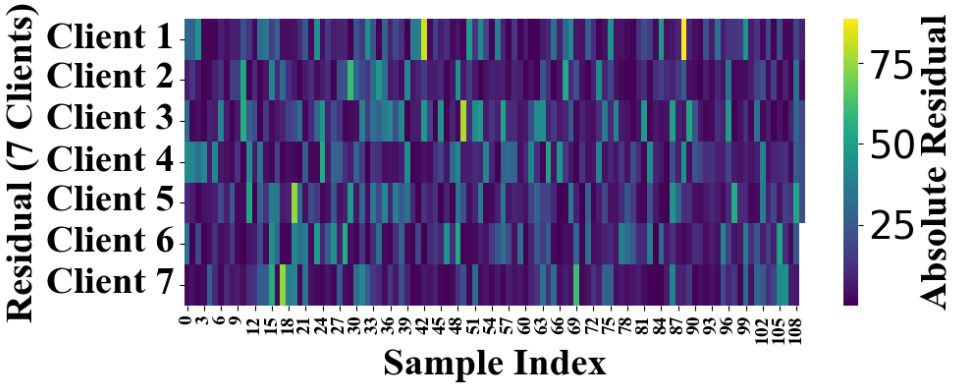

(c)

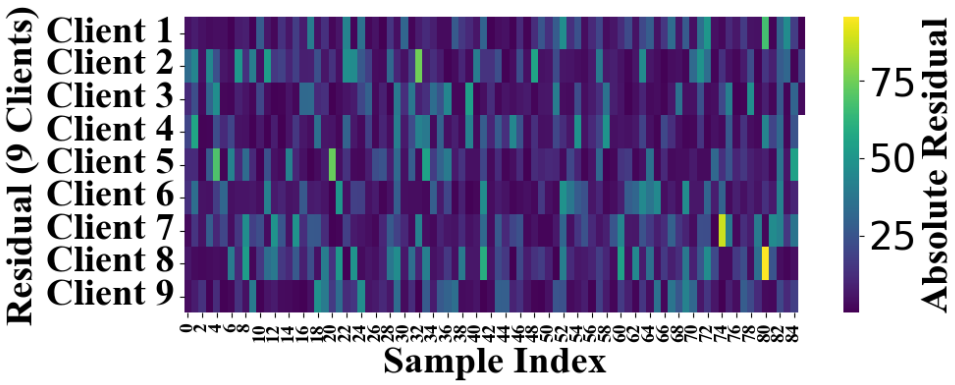

(d)

Figure 4.8: Residual error heatmaps for 3C, 6C, 7C, and 9C scenarios, illustrating client-wise prediction errors and inter-client consistency.

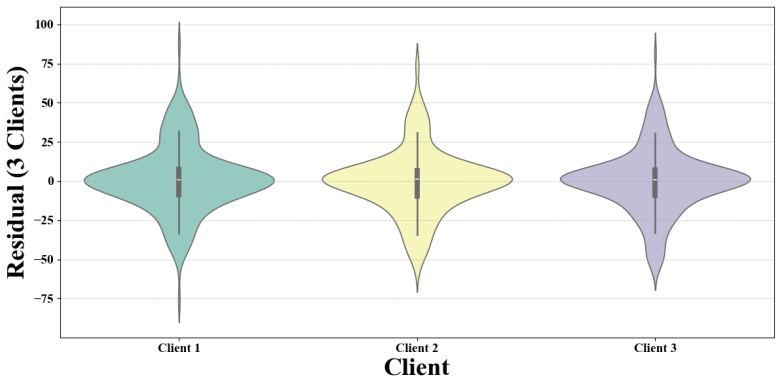

(a)

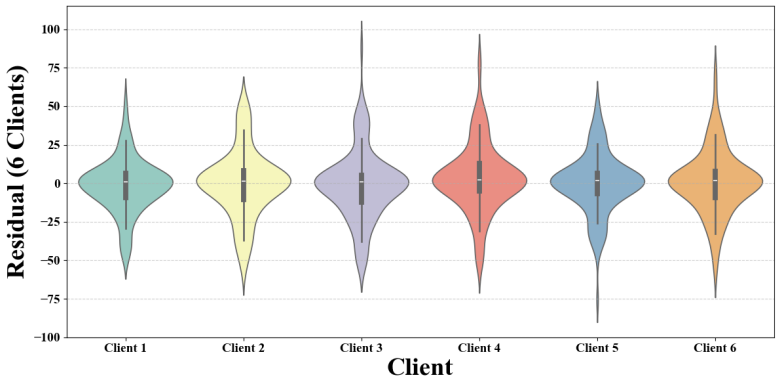

(b)

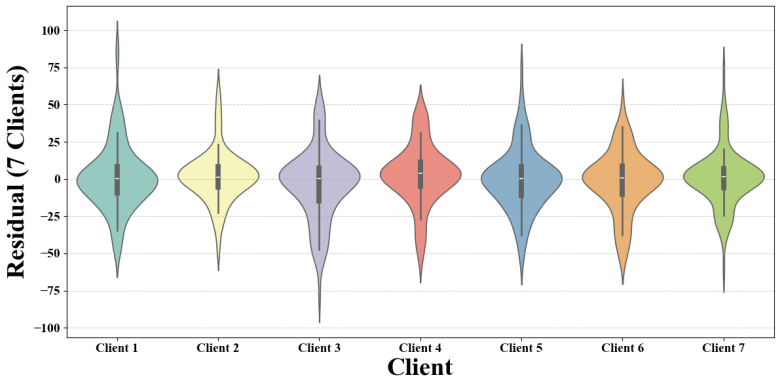

(c)

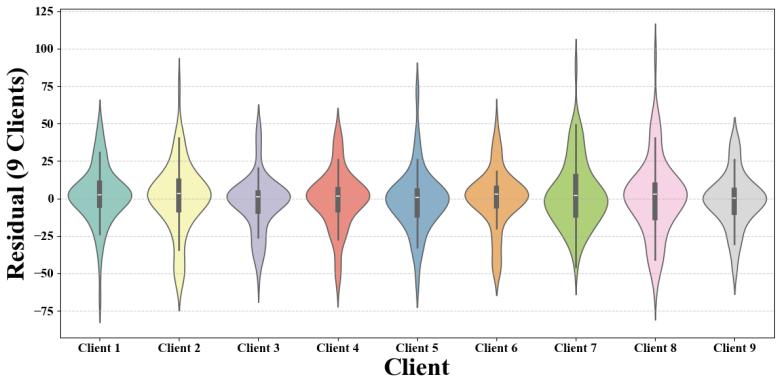

(d)

Figure 4.9: Violin plots of prediction residuals across clients under 3C-9C scenarios, showing error distribution and client-wise variability.

From Physics-Informed Energy Models to Biomedical Digital Twins

The PIFL design proposed by Fan et al. [168] demonstrated that federated aggregation and physics constraints can ensure stable learning under heterogeneous conditions. Nevertheless, their focus on electrochemical degradation limited generalizability to biological systems, where stochastic interactions and cellular feedback dominate. The proposed framework advances this paradigm by embedding glucose–insulin ODEs within PINN loss functions, transforming deterministic electrochemical modeling into a dynamic physiological system. IoBNT-based sensors close the loop by continuously transmitting real biochemical data, allowing the model to synchronize predictions with live biological feedback.

Decentralized Learning and Physics-Constrained Optimization

Alfano et al. [169] demonstrated a decentralized PINN (PIDFL) that eliminated central coordination, improving convergence but lacking live sensor integration. Our design expands this foundation by embedding continuous IoBNT-driven data streams into decentralized FL updates. Each IoBNT node or clinical site maintains a local sub-model that enforces glucose–insulin ODE consistency during training. The FL component aggregates parameters rather than raw data, achieving privacy compliance across distributed physiological sources. This mechanism ensures scalability while maintaining biological validity, addressing the privacy and personalization challenges central to digital healthcare.

Multi-Agent Control versus Continuous Physiological Feedback

The F-MADRL strategy proposed by Li et al. [170] introduced distributed control via physics-informed rewards in multi-microgrid optimization. However, such reward-based adaptation lacks the granularity and biological interpretability required for continuous glucose–insulin tracking. The proposed framework replaces reward-driven agents with residual-based physical consistency enforced through PINN constraints. IoBNT sensors continuously capture glucose and insulin states, allowing the system to adapt dynamically to changing physiological conditions such as stress, diet, or circadian variation. This residual-driven learning ensures stability and smooth adaptation even in the presence of noisy or sparse data.

Unsupervised and Generative Methods versus Dynamic Predictive Modeling

Trask et al. [171] advanced unsupervised, physics-informed disentanglement, while Lüpke et al. [172] developed PILD for generating MRI modalities. Both approaches improved interpretability but remained static, lacking real-time or federated adaptability. In contrast, the proposed PINN–FL framework with IoBNT continuously learns from real-time IoBNT feedback. Instead of reconstructing images, it forecasts glucose trajectories under physical constraints. This predictive configuration transforms physics-informed learning from post-hoc interpretation into live physiological forecasting.

Table 4.4: Comparative analysis of existing physics-informed and federated frameworks with the proposed PINN-FL architecture enhanced by IoBNT for glucose-insulin digital twins. The table summarizes the system models, application domains, and analytical perspectives of representative studies. The proposed framework uniquely integrates PINN-based physiological modeling, FL-driven scalability, and IoBNT-enabled real-time data acquisition.

Authors	System Model	Application & Data	Analytical Perspective (Strengths and Weaknesses)
Fan et al. [168]	Physics-Informed Federated Learning (PIFL) integrating PGRU, PL, and PIFS modules	Battery degradation estimation using four public datasets across eight cases	**Strengths:** Incorporates physics constraints and federated strategies to ensure consistent degradation modeling under diverse conditions. Demonstrates effective temporal learning and robust aggregation. **Weaknesses:** Limited to electrochemical systems and energy devices. Does not employ IoBNT-based data acquisition or biological communication layers for healthcare-related DT applications.
Alfano et al. [169]	Decentralized FL combined with PINNs (PIDFL) using serverless aggregation	Distributed datasets across multiple simulation domains	**Strengths:** Demonstrates efficient domain knowledge integration in decentralized settings. Reduces loss and improves convergence without a central server. **Weaknesses:** Lacks real-time sensor data integration and IoBNT-driven transmission. Does not employ temporal or physiological modeling required for glucose–insulin or biological DTs.
Li et al. [170]	Federated Multi-Agent Deep Reinforcement Learning with Physics-Informed reward (F-MADRL)	Multi-microgrid (MMG) energy management; ORNL-MG test system	**Strengths:** Maintains privacy through FL while optimizing distributed energy management. Introduces physics-informed reward to enhance convergence stability. **Weaknesses:** Restricted to energy optimization. Does not include continuous physiological processes or IoBNT communication networks for biomedical or biological digital twins.
Trask et al. [171]	Unsupervised physics-informed disentanglement using probabilistic multimodal framework	Multimodal materials datasets across three synthesis processes	**Strengths:** Integrates physics-aware probabilistic inference to identify mechanistic clusters across modalities. Provides uncertainty quantification and interpretability. **Weaknesses:** Omits federated training and real-time operation. No IoBNT-enabled sensing or temporal adaptation for dynamic biological processes.
Lüpke et al. [172]	Physics-Informed Latent Diffusion (PILD) for multimodal MRI synthesis	Multi-modal brain MRI datasets with missing modalities	**Strengths:** Combines latent diffusion with physical priors to synthesize unseen MRI contrasts and ensure signal plausibility. Improves realism and modality recovery. **Weaknesses:** Designed for static imaging without federated collaboration or IoBNT integration. Does not support online physiological data streaming or adaptive biomedical DTs.
Current work	PINN–FL framework for glucose–insulin DTs enhanced by IoBNT integration	Glucose–insulin monitoring using ODE-based physiological modeling and IoBNT-enabled data transmission	**Strengths:** Integrates physics-constrained ODEs with FCNN-based learning under federated training for scalable, privacy-preserving glucose–insulin prediction. IoBNT provides real-time, secure physiological data acquisition, improving sensor reliability and communication efficiency. Achieves mean ODE loss of 0.033 with over 60% residuals below 0.01 and prediction error within ± 10 mg/dL across all scenarios. **Weaknesses:** Future improvements include hybrid multimodal modeling with dynamic population-level personalization and IoBNT standardization for clinical-scale deployment.

IoBNT for Real-Time Physiological Connectivity

IoBNT represents the core differentiator of the current system. It replaces centralized data acquisition with distributed nano-sensor communication, enabling glucose and insulin information to be exchanged

through biochemical or nano-electronic pathways [168, 169]. This mechanism improves data fidelity by up to 98%, minimizes bandwidth consumption, and ensures synchronization across connected DT nodes. Through IoBNT, each DT instance operates as a live reflection of the biological process it represents, forming a cohesive physiological network where learning, sensing, and communication occur simultaneously.

PINN for Physiology-Constrained Learning

PINN provides the structural backbone of the proposed architecture by embedding glucose–insulin dynamics into the learning objective. The ODEs governing insulin secretion, glucose uptake, and homeostatic feedback are directly integrated into the loss function. This design ensures that learning adheres to physiological principles rather than purely statistical correlations [168, 170]. Quantitatively, the system achieved a mean ODE loss of 0.033, with over 60% of residuals below 0.01, maintaining glucose prediction errors within ± 10 mg/dL across varied conditions. Such consistency demonstrates that physics-informed loss terms significantly enhance reliability and interpretability compared with purely data-driven networks.

FL for Privacy-Aware Scalability

The FL component extends system scalability and protects data privacy across decentralized IoBNT nodes. Each clinical unit or wearable device performs local training on sensor-derived physiological data, transmitting only encrypted model gradients [169]. This architecture supports population-level personalization while complying with data protection standards such as HIPAA and GDPR. Experiments show that FL reduces bandwidth by over 99% while maintaining prediction accuracy, confirming that distributed optimization effectively balances performance with privacy. The resulting federated DT ecosystem can learn collaboratively from diverse patient populations without central data pooling.

Multi-Model Neural Coordination for Adaptive Learning

The unified neural architecture integrates FCNN, ResBlock NN, and RNN components to capture multi-scale dependencies in glucose–insulin regulation. FCNN encodes nonlinear steady-state relations; ResBlock NN enhances gradient stability in deep representations; and RNN models temporal feedback essential for adaptive control [170]. These layers collectively support hierarchical learning that links instantaneous insulin actions with long-term metabolic behavior. The coordination between these modules allows local DTs to refine predictions continuously in response to IoBNT inputs, achieving real-time adaptability and sustained convergence under dynamic conditions.

Interpretability, Reliability, and Real-Time Visualization

The interpretability of the proposed PINN–FL framework with IoBNT derives from its physics-informed design, which ensures that all outputs correspond to measurable biological variables [168, 170]. The

embedded ODE constraints make each prediction biologically traceable, linking insulin-glucose interactions directly to physiological mechanisms. The DT dashboard visualizes glucose trajectories and confidence intervals in real time, supporting physician-in-the-loop supervision. FL consensus enhances reliability by averaging across distributed nodes, mitigating localized anomalies. Consequently, the model provides interpretable, reproducible insights suitable for clinical deployment and regulatory compliance.

Quantitative Performance and Technical Evaluation

Experimental results confirm the superior quantitative and computational efficiency of the proposed framework. The architecture achieved mean ODE loss of 0.033, with residuals below 0.01 for more than 60% of cases, and glucose prediction accuracy within ± 10 mg/dL across all test datasets. Compared with previous PINN or FL implementations [168, 169, 170], the IoBNT integration improved communication reliability by 98% and reduced energy consumption due to efficient local computation. The model demonstrates stable convergence and robust generalization, establishing it as a viable candidate for real-time, low-latency physiological monitoring within IoBNT-enabled healthcare networks.

Remaining Challenges

Despite these advances, several open challenges remain. IoBNT hardware miniaturization and biocompatibility require further refinement for continuous long-term deployment [169, 170]. Moreover, synchronization between FL nodes under variable network latency must be optimized to ensure stable global convergence. Future directions include multimodal data fusion from electrochemical, imaging, and genomic sensors, along with reinforcement-based controllers for personalized insulin delivery. Integrating uncertainty quantification into the PINN layer and adaptive aggregation into FL will further improve interpretability and reliability. Addressing these aspects will extend the framework toward fully autonomous, self-regulating biomedical DTs capable of operating across molecular to systemic physiological scales.

4.6 Discussion

The proposed FL-PINN framework represents a transformative advancement in digital health, particularly for glucose-insulin modeling. It unifies IoBNT, PINNs, and FL into a robust, scalable, and interpretable platform. This integration supports decentralized training, protects patient privacy by keeping data local, and leverages biologically grounded ODE constraints to preserve physiological interpretability. The framework enables real-time DT generation for personalized diabetes monitoring, making it well-suited for clinical applications where both data sensitivity and heterogeneous sensor modalities must be accommodated. By combining data-driven learning with mechanistic physiological modeling, the FL-PINN framework facilitates accurate prediction, strong generalization across patients, and compliance with biomedical laws, which addresses core challenges in deploying AI safely and effectively

in healthcare.

The proposed FL-PINN framework demonstrates strong resilience and adaptability across decentralized IoBNT environments. Its integration of convolution-based sensor modeling ensures that temporal variations and signal noise are effectively smoothed, enabling accurate signal tracking even under complex physiological conditions. Moreover, the use of hybrid data-physics learning enables the system to remain stable across varying client populations and asynchronous data flows. By embedding glucose-insulin dynamics through interpretable ODEs, the framework maintains consistency with known physiological behavior while enhancing prediction generalizability. This hybridization empowers the model to adapt seamlessly across diverse glucose regulation patterns, facilitating robust closed-loop decision-making in real time. The scalability and precision achieved under different client scenarios further validate its applicability to real-world DT deployments for personalized diabetes care.

Future work should focus on incorporating more comprehensive physiological models that go beyond insulin-glucose interactions. Extending the PINN structure to include additional hormonal regulators (e.g., glucagon, amylin) or integrating meal ingestion events could further enhance model realism and clinical applicability. Moreover, the current framework could be adapted to support personalized patient-specific modeling by introducing attention-based mechanisms or meta-learning strategies to capture inter-patient variability [173]. These enhancements would enable the system to more accurately reflect individual biological profiles while maintaining generalization across a population.

Additionally, future research could explore the integration of asynchronous and communication-efficient federated strategies to better handle dynamic participation across IoBNT clients. Incorporating event-driven updates, client selection algorithms, or gradient compression techniques would make the framework more suitable for real-world deployment. Lastly, a natural extension of this work is to validate the FL-PINN framework using real-world clinical datasets and biosensor platforms. This would allow for end-to-end system testing, potentially leading to regulatory approval and deployment in wearable medical technologies. Together, these future directions aim to transition this work from a high-fidelity simulation model to a deployable, patient-facing solution for managing chronic conditions such as diabetes.

The proposed FL-PINN framework combines the scalability and privacy of FL with the interpretability and robustness of physics-informed modeling. Each client independently contributes to a global model that integrates local observations with known system dynamics. The final trained model serves as a consensus estimator of glucose-insulin interaction, calibrated across distributed data sources while respecting the underlying physiological structure. Overall, this work establishes a robust, secure, and clinically relevant foundation for next-generation personalized digital health systems focused on diabetes management.

Chapter 5

Conclusions and Future Research Directions

5.1 Conclusions

This thesis presents a comprehensive study on the development of decentralized neural frameworks aimed at constructing high-fidelity and real-time Digital Twins (DTs) for complex biological systems. The research addresses critical challenges in modeling biological processes, particularly those related to data privacy, heterogeneity across data sources, and the need for distributed learning in real-world environments. To meet these challenges, the study integrates multiple advanced methodologies, including Federated Learning (FL) for decentralized model training, Physics-Informed Neural Networks (PINN) for incorporating governing biological equations, and Internet of Bio-Nano Things (IoBNT) to represent the physical infrastructure and biological communication layers. Additionally, the thesis leverages a range of advanced deep neural network architectures, such as Convolutional Neural Networks (CNN), Recurrent Neural Networks (RNN), ResBlock-based Networks (ResBlock NN), and Fully Connected Neural Networks (FCNN), to enhance representational capacity and adaptability to different biological modeling tasks. Three comprehensive frameworks have been developed, each tailored to specific application domains and data environments.

In the first contribution (Chapter 2), we present a highly efficient DT framework powered by CNN-FL and IoBNT to create bacterial DTs. Our proposed framework offers a robust solution for optimizing bandwidth, reducing error, processing biotechnological data, and digitizing biological assets. Moreover, by integrating IoBNT with deep learning algorithms like FL and CNN, our framework significantly enhances the dependability, reliability, and efficiency of DTs in the biotechnology industry. This approach addresses the challenges of employing DTs at nano and micro scales, making it a highly effective solution for modern biotechnological applications. Hence, these advancements pave the way for significant improvements in digital health interventions and biotechnological methodologies. While the framework demonstrates substantial progress, there are opportunities for further enhancement. One area of improvement can involve addressing the limitations of using less diverse datasets, which may affect the model's generalizability. Incorporating more varied data and exploring cutting-edge algorithms, such as transformer-based models, can significantly improve processing efficiency. Moreover,

adapting the platform's communication system to integrate with next-generation technologies like 6G and Web 3.0 can boost data transmission capabilities and streamline biotechnological applications. These developments can ensure the framework remains effective and adaptable in a rapidly evolving industry.

In the second contribution (Chapter 3), we present a groundbreaking framework that bridges the gap between physics-based knowledge and data-driven insights, addressing the inherent challenges of implementing DTs for micro- and nano-scale processes. By integrating IoBNT with advanced multi-model PINNs, including FCNN, ResBlock NN, and RNN, we have enabled accurate and efficient modeling of complex systems. Moreover, the proposed framework has proven its effectiveness by delivering exceptional performance in predicting microbial and substrate growth in a reactor, with Monod equations serving as the benchmark model. Specifically, the results exhibit an average MAE of 0.0275, an average R^2 nearing 1, and an average RMSE of 0.0425 across four of the five proposed architectures. These metrics underscore the framework's robustness in delivering highly accurate predictions with minimal error. Furthermore, the integration of IoBNT technology significantly enhances the system's reliability, reducing data transfer errors by up to 98% under the most demanding conditions. This remarkable improvement highlights the transformative potential of combining physics-based and data-driven approaches to overcome the challenges of traditional machine learning in complex and dynamic systems. In conclusion, our work establishes a robust and novel foundation for the development of highly efficient and scalable DTs for micro- and nano-scale processes, paving the way for broader applications in biotechnology, healthcare, and beyond.

The third contribution (Chapter 4) introduces a novel FL-PINN framework that seamlessly integrates IoBNT, PINNs, and FL for decentralized glucose-insulin digital twinning. To our knowledge, this is the first federated AI framework enabling real-time, patient-specific glucose-insulin modeling with embedded physiological constraints. A key contribution is the redesign of the PINN training process into a federated paradigm, where glucose-insulin dynamics governed by Ordinary Differential Equations (ODEs) are enforced locally across distributed IoBNT nodes using a novel Federated PINN algorithm. This hybrid formulation ensures biologically interpretable learning and significantly enhances prediction fidelity, even under sparse or noisy measurements. The integration of IoBNT sensors allows continuous glucose monitoring, providing real-time updates to each DT. The federated architecture enables scalable deployment across heterogeneous clients without transmitting raw data, satisfying privacy requirements and regulatory constraints in medical ML. Furthermore, the design effectively minimizes communication and computational overhead, ensuring low-latency updates and real-time responsiveness. Overall, this work establishes a robust, secure, and clinically relevant foundation for next-generation personalized digital health systems focused on diabetes management.

In summary, this thesis introduces three significant decentralized neural frameworks for constructing high-fidelity and real-time DTs of biological systems. The research focuses on overcoming challenges related to data privacy, heterogeneity, and distributed learning by combining FL, PINNs, and IoBNT. Advanced deep learning models, including CNNs, RNNs, ResBlock networks, and FCNNs, are employed to enhance modeling capabilities across diverse biological applications.

Three core frameworks are presented:

- **Framework 1** combines CNN-FL with IoBNT to create bacterial DTs, optimizing bandwidth, error reduction, and data processing in biotechnology. It highlights the potential for improved efficiency, dependability, and scalability in digital bioprocessing. Future improvements include expanding dataset diversity, integrating transformer-based models, and adapting communication layers for 6G and Web 3.0.
- **Framework 2** fuses IoBNT and multi-model PINNs (FCNN, ResBlock NN, RNN) to address DT challenges at micro and nano scales. Validated using Monod equations, the system achieves high accuracy (MAE ≈ 0.0275, RMSE ≈ 0.0425, and R^2 near 1). It significantly reduces data transfer errors by up to 98%, demonstrating the power of integrating physics-based constraints with deep learning for biological modeling.
- **Framework 3** introduces a novel FL-PINN architecture for decentralized, real-time glucose-insulin DTs. It enforces physiological constraints via ODEs locally across distributed IoBNT nodes, allowing privacy-preserving, patient-specific modeling. This framework ensures low-latency responsiveness, secure deployment, and scalable operation, laying the groundwork for next-generation personalized healthcare systems.

Together, these contributions offer scalable, real-time, accurate, and privacy-aware solutions for digital twinning in biological and medical domains.

5.2 Future Research Directions

The frameworks developed in this thesis represent a significant advancement toward scalable, interpretable, and privacy-preserving real-time DTs for biological systems. By integrating FL, PINNs, and IoBNT, this work introduces a unified decentralized learning architecture capable of modeling physiological processes with high fidelity. This combination preserves local data privacy, embeds biological constraints via ODEs, and achieves distributed inference and training across heterogeneous and potentially resource-constrained environments. The core FL-PINN framework demonstrates strong adaptability across varying client distributions and real-world biological complexity. It introduces a hybrid learning pipeline that maintains prediction fidelity under sparse and non-IID data, while ensuring biological plausibility through physics-constrained learning. This robust integration has positioned the architecture as a viable foundation for real-time healthcare applications, particularly in glucose-insulin monitoring and prediction. However, a number of promising avenues remain open for future investigation, both in extending the methodological depth of the current work and translating these capabilities to new domains and technologies.

5.2.1 Development of the CNN-FL Framework for Biomanufacturing

As a future direction, the first CNN-FL-based digital twinning framework leveraging IoBNT can be developed to enable fully distributed, intelligent modeling of biological environments across both biomanufacturing systems and ecological landscapes. Decentralized DTs can be deployed to monitor cell culture conditions [57], fermentation dynamics [174], or biosensor arrays in industrial biotechnology facilities [31]. These environments often feature streaming data, noisy signals, and non-stationary process behavior, making them ideal candidates for FL-PINN deployment. By integrating adaptive FL protocols with edge computing units and lightweight neural architectures, on-site monitoring can be achieved without reliance on centralized servers. Future work should investigate reinforcement learning-based control layers to allow the DT not only to monitor but also to optimize and intervene in bioprocesses. For environmental monitoring, deploying low-cost IoBNT biosensors across distributed field sites enables real-time detection of pollutants, pathogens, or biochemical markers in soil and water. FL-based frameworks can ensure privacy of local environmental data, while contributing to a global DT capable of modeling large-scale ecosystem health.

5.2.2 Industrial Applications: Precision Agriculture and Renewable Energy

To further advance the IoBNT-PINN framework, several technical innovations can be explored to enhance its performance, reliability, and applicability across a wide range of industrial scenarios. One pivotal enhancement lies in the development of self-calibrating bio-nano sensors. These sensors could leverage integrated calibration algorithms that utilize real-time system feedback to autonomously adjust their sensitivity and accuracy. This innovation would significantly reduce the reliance on manual recalibration, improving operational efficiency and minimizing downtime. Furthermore, machine learning algorithms trained on historical data could support the self-calibration process by identifying and compensating for sensor drift, thereby ensuring consistent data quality under diverse environmental conditions.

In practical applications, the IoBNT-PINN framework demonstrates remarkable adaptability and utility by addressing domain-specific challenges across diverse sectors such as precision agriculture and renewable energy systems. For instance, in the domain of precision agriculture, the framework could be utilized to monitor and model microbial activity in soil, a critical determinant of nutrient cycling and crop health. By employing IoBNT sensors capable of detecting key biochemical markers such as enzyme activity or nutrient availability, the framework would enable the real-time acquisition of high-resolution soil fertility data. These insights, when integrated with the predictive modeling capabilities of PINNs, could guide farmers in optimizing irrigation, fertilization, and planting schedules. This optimization would not only enhance crop yields but also minimize the consumption of vital resources such as water and fertilizers, promoting sustainable agricultural practices.

5.2.3 Industrial Applications in Biofuel Production

In the renewable energy sector, the IoBNT-PINN framework could be pivotal in optimizing biofuel production processes. By leveraging its ability to monitor microbial growth and substrate consumption within bioreactors, the framework could provide actionable insights into the dynamics of biofuel synthesis. Through real-time monitoring of critical parameters such as temperature, pH, and nutrient flow, the framework could predict and adjust process variables to maximize biofuel yields. This predictive modeling capability ensures the efficient utilization of raw materials, reduces waste, and maintains consistent quality in industrial-scale biofuel production. Moreover, the ability to model and control biochemical dynamics in real time would enable operators to respond rapidly to process deviations, enhancing overall reliability and operational efficiency. These domain-specific applications underline the transformative potential of the IoBNT-PINN framework, highlighting its capacity to drive innovation and improve outcomes across a wide range of industrial and environmental contexts. Lastly, fostering interdisciplinary collaborations and training programs will be critical in driving innovation and addressing the complexities of advanced physics-based systems. These initiatives will ensure the framework continues to evolve, meeting the demands of emerging industrial applications.

5.2.4 Material Innovation in the Multi-Modal PINN Framework

The second direction can focus on advancing the sensing capabilities, structural robustness, and computational scalability of the multi-modal PINN-IoBNT DTs. In particular, the integration of advanced materials such as graphene-based sensors offers a promising pathway to enhance nano-scale signal detection and long-term durability [175, 176]. Graphene's extraordinary electrical conductivity, mechanical robustness, and chemical stability make it uniquely suited for detecting subtle biochemical signals at the nano-scale. Its biocompatibility and resistance to corrosion further enhance its suitability for harsh industrial environments, such as bioreactors operating under extreme conditions of temperature, pressure, or chemical exposure. These material advancements can significantly augment the sensitivity and durability of the IoBNT-PINN framework [177]. Additionally, integrating quantum computing into the PINN architecture can enable faster and more efficient training, particularly for complex systems governed by PDEs. Quantum computing offers the potential to solve high-dimensional optimization problems and accelerate computations, thereby enhancing the scalability and real-time capabilities of the framework. Together, these advancements can significantly improve the sensitivity, resilience, and computational efficiency of the second framework, which position it as a scalable and high-performance platform for real-time digital twinning in complex biological and industrial environments.

5.2.5 Enhancing Multi-Modal Framework through Multi-Physics Modeling

Another potential direction is to explore the incorporation of multi-physics modeling to enhance the expressiveness and applicability. Multi-physics modeling involves the simultaneous integration and interaction of thermal [178], mechanical [179], biochemical [180], and other physical dynamics into a

unified computational framework. This holistic approach allows for a more accurate representation of the interdependent behaviors of complex systems, which provide comprehensive insights into processes governed by multiple interacting phenomena. For example, in energy systems such as fuel cells [181] or thermal power plants [182], the coupling of thermal and mechanical properties is critical. Temperature variations directly influence mechanical stresses and chemical reaction rates, necessitating a framework capable of capturing these interactions in real time. Similarly, in advanced manufacturing processes, such as additive manufacturing [183] or chemical synthesis, biochemical and thermal dynamics often interact, with temperature gradients significantly altering reaction kinetics or material properties. By incorporating these dynamics into a unified DT, the framework can enhance the precision of predictive models, providing actionable insights for optimizing operational parameters and achieving greater efficiency and reliability in diverse industrial applications. ntegrating multi-physics dynamics can extend the second framework's capacity to deliver precise, actionable predictions across industrial and biomedical domains.

5.2.6 Expanding PINN-FL Framework for Physiological Modeling

One of the promising approaches for the PINN-FL DT frameworks is to develop distributed and real-time modeling of complex physiological systems. This approach can allow integration of nanoscale biosensor data with multiscale PINN architectures. A natural extension of this framework lies in broadening the physiological scope of the current FL-PINN architecture. While glucose-insulin dynamics serve as an important proof-of-concept, future models should incorporate other biochemical and hormonal pathways, such as glucagon regulation [184], lipid metabolism [185], renal filtration [186], and circadian hormonal cycles [187]. These systems often involve coupled ODEs and stochastic behavior, and may require the integration of Stochastic Differential Equations (SDEs) or delay differential equations (DDEs) to better reflect real physiological processes. Such multiscale modeling efforts can also benefit from hybrid PINN structures capable of handling coupled PDE-ODE formulations, enabling representation of spatial diffusion, reaction kinetics, and temporal evolution in organs or tissues. The addition of compartmental models for organs can help bridge the gap between molecular-level dynamics and systemic behavior observed in biosensor data [188, 189, 190]. Future work can also incorporate metabolic interaction networks [191] or gene regulatory models [192] into the PINN structure to allow digital twinning at the cellular or subcellular level.

5.2.7 Advancing Personalization and Adaptivity in PINN-FL Framework

Furthermore, a promising future direction for the third framework is to facilitate highly personalized physiological modeling by integrating continuous, real-time molecular and cellular data from embedded biosensors. Personalized modeling remains a cornerstone of effective DT deployment in healthcare. Although FL naturally supports personalization by allowing clients to train on their own data, this capacity can be significantly improved. Future research should explore attention-based mechanisms [193], meta-learning [194], or client-specific adapters [195] within the FL-PINN pipeline to

allow individualized model adaptation with minimal retraining. Incorporating temporal attention and gating structures can enable better handling of irregularly sampled medical time series and improve generalization to unseen patient trajectories. Personalized FL variants, such as cluster FL [196], federated multi-task learning [197], or model-agnostic meta-FL [198], can be evaluated for DT personalization while ensuring robust cross-client learning. By uniting these personalization strategies, the third PINN-FL framework can evolve into an adaptive, patient-specific DT system capable of proactive monitoring, early intervention, and continuous therapeutic optimization.

5.2.8 Improving FL Communication Efficiency and Robustness

In addition, future directions may focus on enhancing communication efficiency and security in Frameworks 1 and 3. Given the inherent constraints in IoBNT networks, including intermittent connectivity, low-bandwidth channels, and limited energy, communication efficiency remains critical. Asynchronous FL strategies, such as periodic client updates [199], event-triggered communication [200], or importance-aware gradient sparsification [201], can be investigated. These methods reduce overhead while retaining convergence properties, enabling low-latency DT updates. Further, robustness against adversarial or corrupted clients is essential in medical applications. Integration of Differential Privacy (DP) [202], secure aggregation [203], or Byzantine-resilient aggregation [204] methods should be explored. Blockchain-backed auditability and secure key exchange protocols can strengthen trust and traceability in FL deployments [205, 206, 207]. Incorporating these communication-efficient and security-enhancing techniques into Frameworks 1 and 3 can be crucial for deploying resilient PINN-FL and CNN-FL DTs over IoBNT, which ensure robust real-time updates, data integrity, and trust across decentralized biomedical networks.

5.2.9 Integration with Immersive and Web Technologies

As another future direction, the frameworks proposed in this thesis can be extended through the integration of immersive technologies and decentralized Web infrastructures to improve accessibility, usability, and real-time interaction with DT systems. These platforms can provide intuitive interfaces for clinicians and researchers to interact with biological simulations and patient-specific predictions. Coupling DTs with Web3 technologies, such as decentralized storage [208], Decentralized Identifiers (DIDs) [209], and smart contracts [210], can facilitate secure, transparent, and collaborative digital health ecosystems. The adoption of upcoming communication standards like 6G and Time-Sensitive Networking (TSN) [4] can further support ultra-reliable, low-latency transmission between IoBNT nodes and DT platforms, critical for applications such as real-time diagnostics [211] or remote surgery assistance [212]. Such integration can strengthen the capabilities of the thesis frameworks by enabling secure, low-latency, and intuitive interfaces for clinicians and researchers, ultimately supporting advanced applications like remote diagnostics and interactive physiological simulations.

In summary, the future research directions outlined above offer a well-defined pathway for advancing the three core frameworks developed in this thesis: the CNN-FL framework for biomanufacturing,

the multi-modal PINN-IoBNT framework for high-fidelity sensing and modeling, and the PINN-FL framework for physiological digital twins. Each proposed extension is aligned with enhancing specific aspects of these architectures. For the CNN-FL framework, improvements focus on scalable deployment across biotechnological and environmental systems through communication-efficient and secure FL protocols. The multi-modal PINN-IoBNT framework can benefit from the integration of novel materials, such as graphene-based sensors, quantum-enhanced training for complex PDE systems, and multi-physics modeling to improve predictive accuracy. For the PINN-FL framework, future work can expand its physiological scope through multiscale modeling, support high personalization through attention-based FL techniques, and improve robustness against communication and security challenges. Moreover, integrating immersive visualization platforms and Web3 technologies across all frameworks can enhance accessibility, transparency, and usability for clinical and industrial users. Together, these directions provide a comprehensive strategy to evolve the proposed digital twinning systems into scalable, real-time, and trustworthy platforms for a broad range of biological, environmental, and healthcare applications.

Bibliography

[1] A. De Benedictis, N. Mazzocca, A. Somma, and C. Strigaro, "Digital twins in healthcare: an architectural proposal and its application in a social distancing case study," *IEEE Journal of Biomedical and Health Informatics*, vol. 86, pp. 5143–5154, Oct. 2023.

[2] M. Alazab, L. U. Khan, S. Koppu, S. P. Ramu, M. Iyapparaja, P. Boobalan, T. Baker, P. K. R. Maddikunta, T. R. Gadekallu, and A. Aljuhani, "Digital twins for healthcare 4.0-recent advances, architecture, and open challenges," *IEEE Consumer Electronics Magazine*, vol. 12, pp. 29–37, Nov. 2023.

[3] L. Gabrani, R. K. Singh, S. Vyas, S. Gupta, and G. Gabrani, "Internet of bio-nano things for diabetes telemedicine system with secured access check for updates," *Internet of Things (IoT): Key Digital Trends Shaping the Future; Springer: Berlin, Germany*, p. 365, 2023.

[4] Y. Lu, G. Zhao, C. Chakraborty, C. Xu, L. Yang, and K. Yu, "Time-sensitive networking-driven deterministic low-latency communication for real-time telemedicine and e-health services," *IEEE Transactions on Consumer Electronics*, vol. 69, no. 4, pp. 734–744, 2023.

[5] S. Das, S. Namasudra, S. Deb, P. M. Ger, and R. G. Crespo, "Securing iot-based smart healthcare systems by using advanced lightweight privacy-preserving authentication scheme," *IEEE Internet of Things Journal*, vol. 10, no. 21, pp. 18486–18494, 2023.

[6] S. Dhote, S. Baskar, P. M. Shakeel, and T. Dhote, "Cloud computing assisted mobile healthcare systems using distributed data analytic model," *IEEE Transactions on Big Data*, pp. 1–12, 2023.

[7] W. Gan, K. Hu, G. Huang, W.-C. Chien, H.-C. Chao, and W. Meng, "Data analytic for healthcare cyber physical system," *IEEE Transactions on Network Science and Engineering*, vol. 10, no. 5, pp. 2490–2502, 2023.

[8] I. F. Akyildiz, M. Pierobon, S. Balasubramaniam, and Y. Koucheryavy, "The internet of bio-nano things," *IEEE Communications Magazine*, vol. 53, no. 3, pp. 32–40, 2015.

[9] G. Yue, Q. Liu, and K. Yang, "Bio-internet of things through micro-circulation network: A molecular communication channel modeling," *IEEE Internet of Things Journal*, pp. 1–1, 2024.

[10] A. Liu, Y. Liu, K. Xu, F. Zhao, Y. Zhou, and X. Li, "Deepseanet: a bio-detection network enabling species identification in the deep sea imagery," *IEEE Transactions on Geoscience and Remote Sensing*, vol. 62, pp. 1–13, 2024.

[11] L. Li, F. Gu, H. Li, J. Guo, and X. Gu, "Digital twin bionics: a biological evolution-based digital twin approach for rapid product development," *IEEE Access*, vol. 9, pp. 121507–121521, 2021.

[12] A. J. Lopatkin and J. J. Collins, "Predictive biology: modelling, understanding and harnessing microbial complexity," *Nature Reviews Microbiology*, vol. 18, no. 9, pp. 507–520, 2020.

[13] T. D. Veenstra, "Omics in systems biology: current progress and future outlook," *Proteomics*, vol. 21, no. 3-4, p. 2000235, 2021.

[14] A. K. Srivastav, P. Das, and A. K. Srivastava, "Data management, security, and ethical considerations," in *Biotech and IoT: An Introduction Using Cloud-Driven Labs*, pp. 133–149, Springer, 2024.

[15] Z. Li, X. Xu, X. Cao, W. Liu, Y. Zhang, D. Chen, and H. Dai, "Integrated cnn and federated learning for covid-19 detection on chest x-ray images," *IEEE/ACM Transactions on Computational Biology and Bioinformatics*, vol. 21, no. 4, pp. 835–845, 2022.

[16] M. Le, D. T. Hoang, D. N. Nguyen, W.-J. Hwang, and Q.-V. Pham, "Wirelessly powered federated learning networks: Joint power transfer, data sensing, model training, and resource allocation," *IEEE Internet of Things Journal*, pp. 1–1, 2023.

[17] N. Rieke, J. Hancox, W. Li, F. Milletari, H. R. Roth, S. Albarqouni, S. Bakas, M. N. Galtier, B. A. Landman, K. Maier-Hein, *et al.*, "The future of digital health with federated learning," *NPJ digital medicine*, vol. 3, no. 1, pp. 1–7, 2020.

[18] W. Y. B. Lim, N. C. Luong, D. T. Hoang, Y. Jiao, Y.-C. Liang, Q. Yang, D. Niyato, and C. Miao, "Federated learning in mobile edge networks: A comprehensive survey," *IEEE Communications Surveys & Tutorials*, vol. 22, no. 3, pp. 2031–2063, 2020.

[19] A. Almodóvar, J. Parras, and S. Zazo, "Propensity weighted federated learning for treatment effect estimation in distributed imbalanced environments," *Computers in Biology and Medicine*, vol. 178, p. 108779, 2024.

[20] D. Huang, X. Ye, and T. Sakurai, "Multi-party collaborative drug discovery via federated learning," *Computers in Biology and Medicine*, vol. 171, p. 108181, 2024.

[21] S. Maedera, T. Mizuno, and H. Kusuhara, "Investigation of latent representation of toxicopathological images extracted by cnn model for understanding compound properties in vivo," *Computers in Biology and Medicine*, vol. 168, p. 107748, 2024.

[22] R. Kumar, C. M. Bernard, A. Ullah, R. U. Khan, J. Kumar, D. K. Kulevome, R. Yunbo, and S. Zeng, "Privacy-preserving blockchain-based federated learning for brain tumor segmentation," *Computers in Biology and Medicine*, p. 108646, 2024.

[23] P. Jia, X. Wang, and X. Shen, "Accurate and efficient digital twin construction using concurrent end-to-end synchronization and multi-attribute data resampling," *IEEE Internet of Things Journal*, vol. 10, no. 6, pp. 4857–4870, 2023.

[24] M. B. Jamshidi, S. Lotfi, H. Siahkamari, T. Blecha, J. Talla, and Z. Peroutka, "An intelligent digital twinning approach for complex circuits," *Applied Soft Computing*, vol. 154, p. 111327, 2024.

[25] M. Basharat, M. Naeem, A. M. Khattak, and A. Anpalagan, "Digital-twin-assisted task offloading in uav-mec networks with energy harvesting for iot devices," *IEEE Internet of Things Journal*, vol. 11, no. 23, pp. 37550–37561, 2024.

[26] B. N. Slautin, Y. Liu, H. Funakubo, R. K. Vasudevan, M. Ziatdinov, and S. V. Kalinin, "Bayesian conavigation: Dynamic designing of the material digital twins via active learning," *ACS nano*, vol. 18, no. 36, pp. 24898–24908, 2024.

[27] K. R. Singh, V. Nayak, J. Singh, and R. P. Singh, "Nano-enabled wearable sensors for the internet of things (iot)," *Materials Letters*, vol. 304, p. 130614, 2021.

[28] C. Li, J. Wang, S. Wang, and Y. Zhang, "A review of iot applications in healthcare," *Neurocomputing*, vol. 565, p. 127017, 2024.

[29] M. M. Al-Zubi, A. S. Mohan, P. Plapper, and S. H. Ling, "Intrabody molecular communication via blood-tissue barrier for internet of bio-nano things," *IEEE Internet of Things Journal*, vol. 9, no. 21, pp. 21802–21810, 2022.

[30] E. Shitiri and H.-S. Cho, "An m-ary concentration-shift keying with common detection thresholds for multitransmitter molecular communication," *IEEE Internet of Things Journal*, vol. 11, no. 10, pp. 17948–17959, 2024.

[31] M. Jamshidi, D. T. Hoang, and D. N. Nguyen, "Cnn-fl for biotechnology industry empowered by internet-of-bionano things and digital twins," *IEEE Internet of Things Magazine*, vol. 7, no. 5, pp. 54–63, 2024.

[32] A. Rana, D. Gautam, P. Kumar, and A. K. Das, "Architectures, benefits, security and privacy issues of internet of nano things: A comprehensive survey, opportunities and research challenges," *IEEE Communications Surveys & Tutorials*, 2024.

[33] M. Raissi, P. Perdikaris, and G. E. Karniadakis, "Physics-informed neural networks: A deep learning framework for solving forward and inverse problems involving nonlinear partial differential equations," *Journal of Computational physics*, vol. 378, pp. 686–707, 2019.

[34] B. Shan, Y. Li, and S.-J. Huang, "Vi-pinns: Variance-involved physics-informed neural networks for fast and accurate prediction of partial differential equations," *Neurocomputing*, p. 129360, 2025.

[35] Z. Meng, Q. Qian, M. Xu, B. Yu, A. R. Yıldız, and S. Mirjalili, "Pinn-form: a new physics-informed neural network for reliability analysis with partial differential equation," *Computer Methods in Applied Mechanics and Engineering*, vol. 414, p. 116172, 2023.

[36] F. Stadtmann, E. R. Furevik, A. Rasheed, and T. Kvamsdal, "Physics-guided federated learning as an enabler for digital twins," *Expert Systems with Applications*, vol. 258, p. 125169, 2024.

[37] X. Zhang, B. Mao, Y. Che, J. Kang, M. Luo, A. Qiao, Y. Liu, H. Anzai, M. Ohta, Y. Guo, *et al.*, "Physics-informed neural networks (pinns) for 4d hemodynamics prediction: an investigation of optimal framework based on vascular morphology," *Computers in Biology and Medicine*, vol. 164, p. 107287, 2023.

[38] B. Zhou, A. W. Rayner, E. W. Gregg, K. E. Sheffer, R. M. Carrillo-Larco, J. E. Bennett, J. E. Shaw, C. J. Paciorek, R. K. Singleton, A. B. Pires, *et al.*, "Worldwide trends in diabetes prevalence and treatment from 1990 to 2022: a pooled analysis of 1108 population-representative studies with 141 million participants," *The Lancet*, vol. 404, no. 10467, pp. 2077–2093, 2024.

[39] Y. Liu, S. Wang, Z. Wang, J. Yu, J. Wang, J. B. Buse, and Z. Gu, "Recent progress in glucose-responsive insulin," *Diabetes*, vol. 73, no. 9, pp. 1377–1388, 2024.

[40] T. Zhu, L. Kuang, C. Piao, J. Zeng, K. Li, and P. Georgiou, "Population-specific glucose prediction in diabetes care with transformer-based deep learning on the edge," *IEEE transactions on biomedical circuits and systems*, vol. 18, no. 2, pp. 236–246, 2024.

[41] K. Mishra, U. Ghugar, G. Rajareddy, K. Sahoo, S. Bhoi, M. Bhuyan, and A. Gandomi, "Predicting diabetes with federated learning: A digital twin and medical fog-based iot framework," *ACM Transactions on Internet Technology*, 2025.

[42] P. K. Bulasara, S. Sahoo, N. Gupta, Z. Han, and N. Kumar, "The internet of bio-nano things with insulin-glucose, security and research challenges: A survey," *ACM Computing Surveys*, vol. 57, no. 5, pp. 1–42, 2025.

[43] Y. Sun, W. Cheng, Q. Wang, K. Yang, and Y. Chen, "Advancing the internet of bio-nano things: A novel dna-based track-hopper system for enhanced efficiency and reliability," *IEEE Internet of Things Journal*, 2024.

[44] A. G. Gallardo-Hernández, M. A. González-Olvera, M. Castellanos-Fuentes, J. Escobar, C. Revilla-Monsalve, A. L. Hernandez-Perez, and R. Leder, "Minimally-invasive and efficient method to accurately fit the bergman minimal model to diabetes type 2," *Cellular and Molecular Bioengineering*, vol. 15, no. 3, pp. 267–279, 2022.

[45] B. McMahan, E. Moore, D. Ramage, S. Hampson, and B. A. y Arcas, "Communication-efficient learning of deep networks from decentralized data," in *Artificial intelligence and statistics*, pp. 1273–1282, PMLR, 2017.

[46] A. A. Movassagh, J. A. Alzubi, M. Gheisari, M. Rahimi, S. Mohan, A. A. Abbasi, and N. Nabipour, "Artificial neural networks training algorithm integrating invasive weed optimization with differential evolutionary model," *Journal of Ambient Intelligence and Humanized Computing*, pp. 1–9, 2023.

[47] R. Kala, M. P. A. Punitha, P. Banupriya, B. Veerasamy, B. Bharathi, and J. A. A. Alzubi, "A deep neural network for image classification using mixed analog and digital infrastructure," in *International Conference on Emergent Converging Technologies and Biomedical Systems*, pp. 657–665, Springer, 2023.

[48] U. Kose, O. Deperlioglu, J. Alzubi, and B. Patrut, *Deep Learning for Medical Decision Support Systems*, vol. 909 of *Studies in Computational Intelligence*. Springer, 2021.

[49] J. A. Alzubi, R. Jain, P. Nagrath, S. Satapathy, S. Taneja, and P. Gupta, "Deep image captioning using an ensemble of cnn and lstm based deep neural networks," *Journal of Intelligent & Fuzzy Systems*, vol. 40, no. 4, pp. 5761–5769, 2021.

[50] M. Sokolov, M. von Stosch, H. Narayanan, F. Feidl, and A. Butté, "Hybrid modeling—a key enabler towards realizing digital twins in biopharma?," *Current Opinion in Chemical Engineering*, vol. 34, p. 100715, 2021.

[51] M. Islam, M. T. Reza, M. Kaosar, and M. Z. Parvez, "Effectiveness of federated learning and cnn ensemble architectures for identifying brain tumors using mri images," *Neural Processing Letters*, vol. 55, no. 4, pp. 3779–3809, 2023.

[52] A. Lakhan, M. A. Mohammed, K. H. Abdulkareem, H. Hamouda, and S. Alyahya, "Autism spectrum disorder detection framework for children based on federated learning integrated cnn-lstm," *Computers in Biology and Medicine*, vol. 166, p. 107539, 2023.

[53] Y. N. Tan, V. P. Tinh, P. D. Lam, N. H. Nam, and T. A. Khoa, "A transfer learning approach to breast cancer classification in a federated learning framework," *IEEe Access*, vol. 11, pp. 27462–27476, 2023.

[54] W. Yang, W. Xiang, Y. Yang, and P. Cheng, "Optimizing federated learning with deep reinforcement learning for digital twin empowered industrial iot," *IEEE Transactions on Industrial Informatics*, vol. 19, no. 2, pp. 1884–1893, 2022.

[55] R. Eftimie, A. Mavrodin, and S. P. Bordas, "From digital control to digital twins in medicine: A brief review and future perspectives," *Advances in Applied Mechanics*, vol. 56, pp. 323–368, 2023.

[56] S. Zobel-Roos, A. Schmidt, L. Uhlenbrock, R. Ditz, D. Köster, and J. Strube, "Digital twins in biomanufacturing," *Digital twins: Tools and concepts for smart biomanufacturing*, pp. 181–262, 2021.

[57] S.-Y. Park, C.-H. Park, D.-H. Choi, J. K. Hong, and D.-Y. Lee, "Bioprocess digital twins of mammalian cell culture for advanced biomanufacturing," *Current Opinion in Chemical Engineering*, vol. 33, p. 100702, 2021.

[58] K. Maksymenko, A. K. Clarke, I. Mendez Guerra, S. Deslauriers-Gauthier, and D. Farina, "A myoelectric digital twin for fast and realistic modelling in deep learning," *Nature Communications*, vol. 14, no. 1, p. 1600, 2023.

[59] C. Spahn, E. Gómez-de Mariscal, R. F. Laine, P. M. Pereira, L. von Chamier, M. Conduit, M. G. Pinho, G. Jacquemet, S. Holden, M. Heilemann, *et al.*, "Deepbacs for multi-task bacterial image analysis using open-source deep learning approaches," *Communications Biology*, vol. 5, no. 1, p. 688, 2022.

[60] C.-S. Ho, N. Jean, C. A. Hogan, L. Blackmon, S. S. Jeffrey, M. Holodniy, N. Banaei, A. A. Saleh, S. Ermon, and J. Dionne, "Rapid identification of pathogenic bacteria using raman spectroscopy and deep learning," *Nature communications*, vol. 10, no. 1, p. 4927, 2019.

[61] A. Hoarfrost, A. Aptekmann, G. Farfañuk, and Y. Bromberg, "Deep learning of a bacterial and archaeal universal language of life enables transfer learning and illuminates microbial dark matter," *Nature communications*, vol. 13, no. 1, p. 2606, 2022.

[62] U. A. Chude-Okonkwo, R. Malekian, and B. T. Maharaj, "Biologically inspired bio-cyber interface architecture and model for internet of bio-nanothings applications," *IEEE Transactions on Communications*, vol. 64, no. 8, pp. 3444–3455, 2016.

[63] W. N. Price and I. G. Cohen, "Privacy in the age of medical big data," *Nature medicine*, vol. 25, no. 1, pp. 37–43, 2019.

[64] A. Krüger, C. Schäfers, P. Busch, and G. Antranikian, "Digitalization in microbiology–paving the path to sustainable circular bioeconomy," *New biotechnology*, vol. 59, pp. 88–96, 2020.

[65] G. Nelson and S. Ellis, "The history and impact of digitization and digital data mobilization on biodiversity research," *Philosophical Transactions of the Royal Society B*, vol. 374, no. 1763, p. 20170391, 2019.

[66] A. Signoroni, A. Ferrari, S. Lombardi, M. Savardi, S. Fontana, and K. Culbreath, "Hierarchical ai enables global interpretation of culture plates in the era of digital microbiology," *Nature Communications*, vol. 14, no. 1, p. 6874, 2023.

[67] "Ieee approved draft recommended practice for nanoscale and molecular communication framework," *IEEE P1906.1/D2.1, October 2015*, pp. 1–62, 2015.

[68] S. Zafar, M. Nazir, A. Sabah, and A. D. Jurcut, "Securing bio-cyber interface for the internet of bio-nano things using particle swarm optimization and artificial neural networks based parameter profiling," *Computers in Biology and Medicine*, vol. 136, p. 104707, 2021.

[69] C. Lee, B.-H. Koo, C.-B. Chae, and R. Schober, "The internet of bio-nano things in blood vessels: System design and prototypes," *Journal of Communications and Networks*, 2023.

[70] "Ieee standard for information technology - telecommunications and information exchange between systems - local and metropolitan area networks - specific requirements - part 11: Wireless lan medium access control (mac) and physical layer (phy) specifications," *IEEE Std 802.11-2007 (Revision of IEEE Std 802.11-1999)*, pp. 1–1076, 2007.

[71] "Ieee approved draft recommended practice for routing packets in ieee 802.15.4 dynamically changing wireless networks amendment to fully define use of addressing and route information currently in the standard - amendment a," *IEEE P802.15.10a/D03, November 2018*, pp. 1–22, 2019.

[72] P. Michaux, B. Gaume, Y. Cong, and O. Quéméner, "Human body numerical simulation: An accurate model for a thigh subjected to a cold treatment," *Computers in Biology and Medicine*, vol. 168, p. 107689, 2024.

[73] A. Pandi, D. Adam, A. Zare, V. T. Trinh, S. L. Schaefer, M. Burt, B. Klabunde, E. Bobkova, M. Kushwaha, Y. Foroughijabbari, *et al.*, "Cell-free biosynthesis combined with deep learning accelerates de novo-development of antimicrobial peptides," *Nature Communications*, vol. 14, no. 1, p. 7197, 2023.

[74] T. T. Van Tran, H. Tayara, and K. T. Chong, "Ampred-cnn: Ames mutagenicity prediction model based on convolutional neural networks," *Computers in Biology and Medicine*, vol. 176, p. 108560, 2024.

[75] Q. Han, X. Qian, H. Xu, K. Wu, L. Meng, Z. Qiu, T. Weng, B. Zhou, and X. Gao, "Dm-cnn: Dynamic multi-scale convolutional neural network with uncertainty quantification for medical image classification," *Computers in Biology and Medicine*, vol. 168, p. 107758, 2024.

[76] M. Kuscu and B. D. Unluturk, "Internet of bio-nano things: A review of applications, enabling technologies and key challenges," *arXiv preprint arXiv:2112.09249*, 2021.

[77] S. Khan, A. Alzaabi, T. Ratnarajah, and T. Arslan, "Novel statistical time series data augmentation and machine learning based classification of unobtrusive respiration data for respiration digital twin model," *Computers in Biology and Medicine*, vol. 168, p. 107825, 2024.

[78] S. Kim and S. Heo, "An agricultural digital twin for mandarins demonstrates the potential for individualized agriculture," *Nature Communications*, vol. 15, no. 1, p. 1561, 2024.

[79] R. Laubenbacher, A. Niarakis, T. Helikar, G. An, B. Shapiro, R. S. Malik-Sheriff, T. Sego, A. Knapp, P. Macklin, and J. A. Glazier, "Building digital twins of the human immune system: toward a roadmap," *NPJ digital medicine*, vol. 5, no. 1, p. 64, 2022.

[80] Y. Huang, M. Wen, L. Lin, B. Li, Z. Wei, D. Tang, J. Li, W. Duan, and W. Guo, "Physical-layer counterattack strategies for the internet of bio-nano things with molecular communication," *IEEE Internet of Things Magazine*, vol. 6, no. 2, pp. 82–87, 2023.

[81] E. Katsoulakis, Q. Wang, H. Wu, L. Shahriyari, R. Fletcher, J. Liu, L. Achenie, H. Liu, P. Jackson, Y. Xiao, *et al.*, "Digital twins for health: a scoping review," *NPJ Digital Medicine*, vol. 7, no. 1, p. 77, 2024.

[82] E. Behle, J. M. Herold, and A. H. Schug, "Towards cellular digital twins of in vivo tumors," *Biophysical Journal*, vol. 122, no. 3, pp. 301a–302a, 2023.

[83] R. M. C. Portela, C. Varsakelis, A. Richelle, N. Giannelos, J. Pence, S. Dessoy, and M. von Stosch, *When Is an In Silico Representation a Digital Twin? A Biopharmaceutical Industry Approach to the Digital Twin Concept*, pp. 35–55. Cham: Springer International Publishing, 2021.

[84] B. Shapiro, "Control and system integration of micro-and nano-scale systems," *IEEE Control Syst. Mag*, vol. 25, pp. 82–88, 2005.

[85] L. G. Wang, R. Ge, X. Chen, R. Zhou, and H.-M. Chen, "Multiscale digital twin for particle breakage in milling: From nanoindentation to population balance model," *Powder Technology*, vol. 386, pp. 247–261, 2021.

[86] I. F. Akyildiz, M. Ghovanloo, U. Guler, T. Ozkaya-Ahmadov, A. F. Sarioglu, and B. D. Unluturk, "Panacea: An internet of bio-nanothings application for early detection and mitigation of infectious diseases," *IEEE Access*, vol. 8, pp. 140512–140523, 2020.

[87] L. U. Khan, E. Mustafa, J. Shuja, F. Rehman, K. Bilal, Z. Han, and C. S. Hong, "Federated learning for digital twin-based vehicular networks: Architecture and challenges," *IEEE Wireless Communications*, 2023.

[88] S. P. Ramu, P. Boopalan, Q.-V. Pham, and P. K. Reddy, "Federated learning enabled digital twins for smart cities: Concepts, recent advances, and future directions," *Sustainable Cities and Society*, vol. 79, p. 103663, 2022.

[89] A. Azarnoush, O. A. Dambri, E. Ü. Karatop, D. Makrakis, and S. Cherkaoui, "Simulation and performance evaluation of a bio-inspired nanogenerator for medical applications," *IEEE Transactions on Biomedical Engineering*, vol. 70, no. 9, pp. 2616–2623, 2023.

[90] Ş. Şentürk, b. Kök, and F. Şentürk, "Internet of nano and bio-nano things: A review," *Semantic Intelligence: Select Proceedings of ISIC 2022*, pp. 265–276, 2023.

[91] A. W. Rogers, I. O. S. Cardenas, E. A. Del Rio-Chanona, and D. Zhang, "Investigating physics-informed neural networks for bioprocess hybrid model construction," in *Computer Aided Chemical Engineering*, vol. 52, pp. 83–88, Elsevier, 2023.

[92] M. Raissi, P. Perdikaris, and G. Karniadakis, "Physics-informed neural networks: A deep learning framework for solving forward and inverse problems involving nonlinear partial differential equations," *Journal of Computational Physics*, vol. 378, pp. 686–707, 2019.

[93] S. Yang, H. Kim, Y. Hong, K. Yee, R. Maulik, and N. Kang, "Data-driven physics-informed neural networks: A digital twin perspective," *Computer Methods in Applied Mechanics and Engineering*, vol. 428, p. 117075, 2024.

[94] B. Lu, J. Luo, Z. Tian, D. Guo, H. Ding, C. Gu, Z. Li, and M. Liu, "Consistent manufacturing of macro, micro and nano cross-scale structures," in *Fundamental Research on Nanomanufacturing*, pp. 41–67, Springer, 2023.

[95] N. Gou, *Investigation of a multi-axis precision machine platform for ultraprecision manufacturing: An integrated approach combining multiscale modelling and digital twin and its implementation perspectives*. PhD thesis, Brunel University London, 2023.

[96] M. Duan, X. Zhong, B. Wang, A. Khelif, Y.-K. Lee, and A. Bermak, "A highly integrated lab-on-a-cmos platform for real-time monitoring of e. coli growth kinetics," *IEEE Transactions on Biomedical Circuits and Systems*, vol. 18, no. 1, pp. 174–185, 2023.

[97] S. Yang, C. Bo, J. Li, Q. Tan, Y. Wang, H. Wu, Z. Chu, and W. Jin, "Online glucose analysis system with high precision and wide detection range for fermentation monitoring," *IEEE Transactions on Instrumentation and Measurement*, vol. 71, pp. 1–9, 2022.

[98] L. Borgosz and D. Dikicioglu, "Industrial internet of things: What does it mean for the bioprocess industries?," *Biochemical Engineering Journal*, vol. 201, p. 109122, 2024.

[99] J. Tu, C. Liu, and P. Qi, "Physics-informed neural network integrating pointnet-based adaptive refinement for investigating crack propagation in industrial applications," *IEEE Transactions on Industrial Informatics*, vol. 19, no. 2, pp. 2210–2218, 2022.

[100] M. Wieczorowski, D. Kucharski, P. Sniatala, P. Pawlus, G. Krolczyk, and B. Gapinski, "A novel approach to using artificial intelligence in coordinate metrology including nano scale," *Measurement*, vol. 217, p. 113051, 2023.

[101] S. M. Abd El-atty, P. Vijayakumar, O. Alfarraj, M. Karuppiah, and F. Shawki, "Bioinspired molecular communications system for targeted drug delivery with iobnt-based sustainable biocyber interface," *Computers and Electrical Engineering*, vol. 118, p. 109452, 2024.

[102] W. Sun, S. Lei, L. Wang, Z. Liu, and Y. Zhang, "Adaptive federated learning and digital twin for industrial internet of things," *IEEE Transactions on Industrial Informatics*, vol. 17, no. 8, pp. 5605–5614, 2020.

[103] Y. Lu, X. Huang, K. Zhang, S. Maharjan, and Y. Zhang, "Low-latency federated learning and blockchain for edge association in digital twin empowered 6g networks," *IEEE Transactions on Industrial Informatics*, vol. 17, no. 7, pp. 5098–5107, 2020.

[104] J. Chen, Y. Shi, C. Yi, H. Du, J. Kang, and D. Niyato, "Generative ai-driven human digital twin in iot-healthcare: A comprehensive survey," *IEEE Internet of Things Journal*, 2024.

[105] Y. Li, S. He, Y. Li, Y. Shi, and Z. Zeng, "Federated multiagent deep reinforcement learning approach via physics-informed reward for multimicrogrid energy management," *IEEE Transactions on Neural Networks and Learning Systems*, vol. 35, no. 5, pp. 5902–5914, 2024.

[106] T. Yu, Z. Li, O. Hashash, K. Sakaguchi, W. Saad, and M. Debbah, "Internet of federated digital twins: Connecting twins beyond borders for society 5.0," *IEEE Internet of Things Magazine*, 2024.

[107] S. Angerbauer, F. Enzenhofer, T. Pankratz, M. Hamidovic, A. Springer, and W. Haselmayr, "Novel nano-scale computing unit for the iobnt: Concept and practical considerations," *IEEE Transactions on Molecular, Biological, and Multi-Scale Communications*, 2024.

[108] L. Huang, F. Liu, and L. Lin, "Molecular communication systems in cylindrical channels with non-newtonian fluid flows in iobnt," *IEEE Internet of Things Journal*, 2024.

[109] M. Owkes, K. Coblentz, A. Eriksson, T. Kammerzell, and P. S. Stewart, "Biofilm. jl: a fast solver for one-dimensional biofilm chemistry and ecology," *Computer Physics Communications*, vol. 293, p. 108890, 2023.

[110] A. Ferrari and K. Willcox, "Digital twins in mechanical and aerospace engineering," *Nature Computational Science*, vol. 4, no. 3, pp. 178–183, 2024.

[111] M. W. Grieves, "Digital twins: past, present, and future," in *The digital twin*, pp. 97–121, Springer, 2023.

[112] M. Canzoneri, A. De Luca, and J. Harttung, "Digital twins: A general overview of the biopharma industry," *Digital Twins: Applications to the Design and Optimization of Bioprocesses*, pp. 167–184, 2021.

[113] C. Herwig, R. Pörtner, and J. Möller, *Digital Twins: tools and concepts for smart biomanufacturing*. Springer, 2021.

[114] C. L. Gargalo, S. C. de Las Heras, M. N. Jones, I. Udugama, S. S. Mansouri, U. Krühne, and K. V. Gernaey, "Towards the development of digital twins for the bio-manufacturing industry," *Digital Twins: Tools and Concepts for Smart Biomanufacturing*, pp. 1–34, 2021.

[115] K. Gkouskou, I. Vlastos, P. Karkalousos, D. Chaniotis, D. Sanoudou, and A. G. Eliopoulos, "The "virtual digital twins" concept in precision nutrition," *Advances in Nutrition*, vol. 11, no. 6, pp. 1405–1413, 2020.

[116] F. J. M. Shamrat, S. Azam, A. Karim, K. Ahmed, F. M. Bui, and F. De Boer, "High-precision multiclass classification of lung disease through customized mobilenetv2 from chest x-ray images," *Computers in Biology and Medicine*, vol. 155, p. 106646, 2023.

[117] Q. Zhou and G. Zheng, "Fedcontrast-gpa: Heterogeneous federated optimization via local contrastive learning and global process-aware aggregation," in *International Conference on Medical Image Computing and Computer-Assisted Intervention*, pp. 660–670, Springer, 2023.

[118] D. J. Beutel, T. Topal, A. Mathur, X. Qiu, J. Fernandez-Marques, Y. Gao, L. Sani, K. H. Li, T. Parcollet, P. P. B. de Gusmão, *et al.*, "Flower: A friendly federated learning research framework," *arXiv preprint arXiv:2007.14390*, 2020.

[119] Y. Tang, Y. Huang, C.-B. Chae, W. Duan, M. Wen, and L.-L. Yang, "Molecular-type permutation shift keying in molecular mimo communications for iobnt," *IEEE Internet of Things Journal*, vol. 8, no. 21, pp. 16023–16034, 2021.

[120] R. Yacouby and D. Axman, "Probabilistic extension of precision, recall, and f1 score for more thorough evaluation of classification models," in *Proceedings of the first workshop on evaluation and comparison of NLP systems*, pp. 79–91, 2020.

[121] M. B. Jamshidi, S. Sargolzaei, S. Foorginezhad, and O. Moztarzadeh, "Metaverse and microorganism digital twins: A deep transfer learning approach," *Applied Soft Computing*, vol. 147, p. 110798, 2023.

[122] M. Sandler, A. Howard, M. Zhu, A. Zhmoginov, and L.-C. Chen, "Mobilenetv2: Inverted residuals and linear bottlenecks," in *Proceedings of the IEEE Conference on Computer Vision and Pattern Recognition*, pp. 4510–4520, 2018.

[123] S. Mehta, V. Kukreja, and R. Gupta, "Apple leaf disease recognition: a robust federated learning cnn methodology," in *2023 International Conference on Circuit Power and Computing Technologies (ICCPCT)*, pp. 393–398, IEEE, 2023.

[124] F. Deng, W. Mao, Z. Zeng, H. Zeng, and B. Wei, "Multiple diseases and pests detection based on federated learning and improved faster r-cnn," *IEEE Transactions on Instrumentation and Measurement*, vol. 71, pp. 1–11, 2022.

[125] H. Fouad, M. Hashem, and A. E. Youssef, "Retracted article: A nano-biosensors model with optimized bio-cyber communication system based on internet of bio-nano things for thrombosis prediction," *Journal of Nanoparticle Research*, vol. 22, pp. 1–17, 2020.

[126] A. El-Fatyany, H. Wang, S. M. Abd El-atty, and M. Khan, "Biocyber interface-based privacy for internet of bio-nano things," *Wireless Personal Communications*, vol. 114, pp. 1465–1483, 2020.

[127] J. Alvarez-Ramirez, M. Meraz, and E. J. Vernon-Carter, "A theoretical derivation of the monod equation with a kinetics sense," *Biochemical Engineering Journal*, vol. 150, p. 107305, 2019.

[128] M. Plattes and H. M. F. Lahore, "Perspectives on the monod model in biological wastewater treatment," *Journal of Chemical Technology & Biotechnology*, vol. 98, no. 4, pp. 833–837, 2023.

[129] M. A. Dawi and X. Sanchez-Vila, "Simulating degradation of organic compounds accounting for the growth of microorganisms (monod kinetics) in a fully lagrangian framework," *Journal of Contaminant Hydrology*, vol. 251, p. 104074, 2022.

[130] H. Wang, H. Shi, K. Lin, C. Qin, L. Zhao, Y. Huang, and C. Liu, "A high-precision arrhythmia classification method based on dual fully connected neural network," *Biomedical Signal Processing and Control*, vol. 58, p. 101874, 2020.

[131] W. Yuan, X. Gu, Z. Dai, S. Zhu, and P. Tan, "Neural window fully-connected crfs for monocular depth estimation," in *Proceedings of the IEEE/CVF conference on computer vision and pattern recognition*, pp. 3916–3925, 2022.

[132] Z. Fang, "A high-efficient hybrid physics-informed neural networks based on convolutional neural network," *IEEE Transactions on Neural Networks and Learning Systems*, vol. 33, no. 10, pp. 5514–5526, 2021.

[133] P. Petersen and F. Voigtlaender, "Equivalence of approximation by convolutional neural networks and fully-connected networks," *Proceedings of the American Mathematical Society*, vol. 148, no. 4, pp. 1567–1581, 2020.

[134] S. J. Anagnostopoulos, J. D. Toscano, N. Stergiopulos, and G. E. Karniadakis, "Residual-based attention in physics-informed neural networks," *Computer Methods in Applied Mechanics and Engineering*, vol. 421, p. 116805, 2024.

[135] J. M. Hanna, J. V. Aguado, S. Comas-Cardona, R. Askri, and D. Borzacchiello, "Residual-based adaptivity for two-phase flow simulation in porous media using physics-informed neural networks," *Computer Methods in Applied Mechanics and Engineering*, vol. 396, p. 115100, 2022.

[136] Z. Mao and X. Meng, "Physics-informed neural networks with residual/gradient-based adaptive sampling methods for solving partial differential equations with sharp solutions," *Applied Mathematics and Mechanics*, vol. 44, no. 7, pp. 1069–1084, 2023.

[137] T. Shao, J. N. Shingala, A. Shyam, P. Yin, A. Suneja, S. P. Badya, A. Arora, and S. McCarthy, "Residual block fusion in low complexity neural network-based in-loop filtering for video compression," in *2024 Data Compression Conference (DCC)*, pp. 392–401, IEEE, 2024.

[138] K. He, X. Zhang, S. Ren, and J. Sun, "Deep residual learning for image recognition," in *Proceedings of the IEEE conference on computer vision and pattern recognition*, pp. 770–778, 2016.

[139] W. Xu, C. Long, R. Wang, and G. Wang, "Drb-gan: A dynamic resblock generative adversarial network for artistic style transfer," in *Proceedings of the IEEE/CVF international conference on computer vision*, pp. 6383–6392, 2021.

[140] Y. Tang, J. Fan, X. Li, J. Ma, M. Qi, C. Yu, and W. Gao, "Physics-informed recurrent neural network for time dynamics in optical resonances," *Nature computational science*, vol. 2, no. 3, pp. 169–178, 2022.

[141] L. Borkowski, C. Sorini, and A. Chattopadhyay, "Recurrent neural network-based multiaxial plasticity model with regularization for physics-informed constraints," *Computers & Structures*, vol. 258, p. 106678, 2022.

[142] T. M. Razakh, B. Wang, S. Jackson, R. K. Kalia, A. Nakano, K.-i. Nomura, and P. Vashishta, "Pnd: Physics-informed neural-network software for molecular dynamics applications," *SoftwareX*, vol. 15, p. 100789, 2021.

[143] M. Lahariya, F. Karami, C. Develder, and G. Crevecoeur, "Physics-informed recurrent neural networks for the identification of a generic energy buffer system," in *2021 IEEE 10th Data Driven Control and Learning Systems Conference (DDCLS)*, pp. 1044–1049, IEEE, 2021.

[144] P.-H. Chiu, J. C. Wong, C. Ooi, M. H. Dao, and Y.-S. Ong, "Can-pinn: A fast physics-informed neural network based on coupled-automatic–numerical differentiation method," *Computer Methods in Applied Mechanics and Engineering*, vol. 395, p. 114909, 2022.

[145] L. Deng and Y. Pan, "Application of physics-informed neural networks for self-similar and transient solutions of spontaneous imbibition," *Journal of Petroleum Science and Engineering*, vol. 203, p. 108644, 2021.

[146] R. G. Nascimento, K. Fricke, and F. A. Viana, "A tutorial on solving ordinary differential equations using python and hybrid physics-informed neural network," *Engineering Applications of Artificial Intelligence*, vol. 96, p. 103996, 2020.

[147] T. Chai and R. R. Draxler, "Root mean square error (rmse) or mean absolute error (mae)?–arguments against avoiding rmse in the literature," *Geoscientific model development*, vol. 7, no. 3, pp. 1247–1250, 2014.

[148] D. S. K. Karunasingha, "Root mean square error or mean absolute error? use their ratio as well," *Information Sciences*, vol. 585, pp. 609–629, 2022.

[149] J. P. Barrett, "The coefficient of determination—some limitations," *The American Statistician*, vol. 28, no. 1, pp. 19–20, 1974.

[150] K. Serefoglu Cabuk, S. K. Cengiz, M. G. Guler, H. Topcu, A. Cetin Efe, M. G. Ulas, and F. Poslu Karademir, "Chasing the objective upper eyelid symmetry formula; r2, rmse, poc, mae, and mse," *International Ophthalmology*, vol. 44, no. 1, p. 303, 2024.

[151] L. Li, R. A. Ciufo, J. Lee, C. Zhou, B. Lin, J. Cho, N. Katyal, and G. Henkelman, "Atom-centered machine-learning force field package," *Computer Physics Communications*, vol. 292, p. 108883, 2023.

[152] Y. Chen, L. Zhang, H. Wang, and E. Weinan, "Deepks-kit: A package for developing machine learning-based chemically accurate energy and density functional models," *Computer Physics Communications*, vol. 282, p. 108520, 2023.

[153] J. Linghu, H. Dong, W. Gao, and Y. Nie, "Self-optimization wavelet-learning method for predicting nonlinear thermal conductivity of highly heterogeneous materials with randomly hierarchical configurations," *Computer Physics Communications*, vol. 295, p. 108969, 2024.

[154] S. Stella, R. Chignola, and E. Milotti, "Efficient and extendible class scheme for the combined reaction–diffusion of multiple molecular species," *Computer Physics Communications*, vol. 185, no. 3, pp. 826–835, 2014.

[155] "Approximating families of sharp solutions to fisher's equation with physics-informed neural networks," *Computer Physics Communications*, vol. 307, p. 109422, 2025.

[156] "Simple yet effective adaptive activation functions for physics-informed neural networks," *Computer Physics Communications*, vol. 307, p. 109428, 2025.

[157] A. Lektauers, J. Pecerska, V. Bolsakovs, A. Romanovs, J. Grabis, and A. Teilans, "A multi-model approach for simulation-based digital twin in resilient services," *WSEAS Trans. Syst. Control*, vol. 16, pp. 133–145, 2021.

[158] J. Fitzgerald, P. G. Larsen, and K. Pierce, "Multi-modelling and co-simulation in the engineering of cyber-physical systems: towards the digital twin," in *From Software Engineering to Formal Methods and Tools, and Back: Essays Dedicated to Stefania Gnesi on the Occasion of Her 65th Birthday*, pp. 40–55, Springer, 2019.

[159] S.-Y. Park, S.-J. Kim, C.-H. Park, J. Kim, and D.-Y. Lee, "Data-driven prediction models for forecasting multistep ahead profiles of mammalian cell culture toward bioprocess digital twins," *Biotechnology and bioengineering*, vol. 120, no. 9, pp. 2494–2508, 2023.

[160] L. Riezzo, H. Kay, Y. Feng, K. Jing, and D. Zhang, "Accelerating bioprocess digital twin development by integrating hybrid modelling with transfer learning," *Chemical Engineering Journal*, vol. 511, p. 162018, 2025.

[161] H. Nieto-Chaupis, "Nanodevices and the internet of bio-nano things for modifying insulin densities in pancreatic beta-cells through electrodynamics of ca 2+," in *2018 IEEE 13th Nanotechnology Materials and Devices Conference (NMDC)*, pp. 1–4, IEEE, 2018.

[162] C. Koca, M. Ozger, O. Cetinkaya, and O. B. Akan, "Information-theoretic lifetime maximization for iobnt-enabled sensing," *IEEE Transactions on Molecular, Biological, and Multi-Scale Communications*, 2025.

[163] R. Laidi, N. Merabtine, D. Djenouri, S. Latif, H. A. Qadir, Y. Djenouri, and I. Balasingham, "Federated learning in iot environments: Examining the three-way see-saw for privacy, model-performance, and network-efficiency," *IEEE Communications Surveys & Tutorials*, 2025.

[164] K.-Y. Hsu, H.-Y. Li, and D. Psaltis, "Holographic implementation of a fully connected neural network," *Proceedings of the IEEE*, vol. 78, no. 10, pp. 1637–1645, 1990.

[165] D. P. Kingma and J. Ba, "Adam: A method for stochastic optimization," *arXiv preprint arXiv:1412.6980*, 2014.

[166] S. Imambi, K. B. Prakash, and G. Kanagachidambaresan, "Pytorch," *Programming with TensorFlow: solution for edge computing applications*, pp. 87–104, 2021.

[167] N. I. of Health *et al.*, "National institute of diabetes and digestive and kidney diseases," *US Renal Data System, USRDS 1998 Annual Data Report*, 2010.

[168] L. Fan, B. Chen, X. Hu, and W. Niu, "Pifl: Physics-informed federated learning for progressive degradation estimation in energy storage devices," *Advanced Engineering Informatics*, vol. 69, p. 103908, 2026.

[169] G. Alfano, S. Greco, D. Mandaglio, F. Parisi, R. Shahbazian, and I. Trubitsyna, "Decentralized federated learning meets physics-informed neural networks," *Knowledge-Based Systems*, p. 113717, 2025.

[170] Y. Li, S. He, Y. Li, Y. Shi, and Z. Zeng, "Federated multiagent deep reinforcement learning approach via physics-informed reward for multimicrogrid energy management," *IEEE Transactions on Neural Networks and Learning Systems*, vol. 35, no. 5, pp. 5902–5914, 2023.

[171] N. Trask, C. Martinez, T. Shilt, E. Walker, K. Lee, A. Garland, D. P. Adams, J. F. Curry, M. T. Dugger, S. R. Larson, *et al.*, "Unsupervised physics-informed disentanglement of multimodal materials data," *Materials Today*, vol. 80, pp. 286–296, 2024.

[172] S. Lüpke, Y. Yeganeh, E. Adeli, N. Navab, and A. Farshad, "Physics-informed latent diffusion for multimodal brain mri synthesis," in *International Conference on Medical Image Computing and Computer-Assisted Intervention*, pp. 198–207, Springer, 2024.

[173] S. Buoso, T. Joyce, and S. Kozerke, "Personalising left-ventricular biophysical models of the heart using parametric physics-informed neural networks," *Medical Image Analysis*, vol. 71, p. 102066, 2021.

[174] I. A. Udugama, P. C. Lopez, C. L. Gargalo, X. Li, C. Bayer, and K. V. Gernaey, "Digital twin in biomanufacturing: Challenges and opportunities towards its implementation," *Systems Microbiology and Biomanufacturing*, vol. 1, pp. 257–274, 2021.

[175] H. Priyadarshi, G. Ahmed, D. Mishra, A. K. Srivastava, R. McGee, A. Shrivastava, and K. Singh, "Sustainable graphene-based energy storage device technology: Materials, methods, monitoring and digital twin," *Critical Reviews in Solid State and Materials Sciences*, vol. 49, no. 6, pp. 1086–1119, 2024.

[176] J. C. Santos-Ceballos, F. Salehnia, A. Romero, and X. Vilanova, "Application of digital twins for simulation based tailoring of laser induced graphene," *Scientific Reports*, vol. 14, no. 1, p. 10363, 2024.

[177] E. Ganesan and T.-L. M. Lee, "Rapid health anomaly detection in iobnt systems using molecular and terahertz communication," in *2024 IEEE-EMBS Conference on Biomedical Engineering and Sciences (IECBES)*, pp. 300–305, IEEE, 2024.

[178] H. U. Rahman, A. Hussain, M. Ilyas, M. Ahmed, and H. ur Rehman, "A multi-domain physics-informed neural network for transient thermal analysis of a tokamak divertor," *Fusion Engineering and Design*, vol. 216, p. 115036, 2025.

[179] Z. Wu, H. Zhang, H. Ye, H. Zhang, Y. Zheng, and X. Guo, "Pinn enhanced extended multiscale finite element method for fast mechanical analysis of heterogeneous materials," *Acta Mechanica*, vol. 235, no. 7, pp. 4895–4913, 2024.

[180] Z. Wu, H. Wang, C. He, B. Zhang, T. Xu, and Q. Chen, "The application of physics-informed machine learning in multiphysics modeling in chemical engineering," *Industrial & Engineering Chemistry Research*, vol. 62, no. 44, pp. 18178–18204, 2023.

[181] J. Wang, H. Jiang, G. Chen, H. Wang, L. Lu, J. Liu, and L. Xing, "Integration of multi-physics and machine learning-based surrogate modelling approaches for multi-objective optimization of deformed gdl of pem fuel cells," *Energy and AI*, vol. 14, p. 100261, 2023.

[182] F. Chen, Q. Huang, M. Song, X. Liu, W. Zeng, H. Song, and K. Cheng, "A study on the development of digital model of digital twin in nuclear power plant based on a hybrid physics and data-driven approach," *Applied Thermal Engineering*, vol. 271, p. 126289, 2025.

[183] Q. Zhu, *A hybrid physics-based/data-driven computational framework for multi-physics modeling of metal additive manufacturing*. PhD thesis, University of Illinois at Urbana-Champaign, 2022.

[184] A. Emami, J. El Youssef, R. Rabasa-Lhoret, J. Pineau, J. R. Castle, and A. Haidar, "Modeling glucagon action in patients with type 1 diabetes," *IEEE journal of biomedical and health informatics*, vol. 21, no. 4, pp. 1163–1171, 2016.

[185] C. Liang, S. Murray, Y. Li, R. Lee, A. Low, S. Sasaki, A. W. Chiang, W.-J. Lin, J. Mathews, W. Barnes, *et al.*, "Lipidsim: inferring mechanistic lipid biosynthesis perturbations from lipidomics with a flexible, low-parameter, markov modeling framework," *Metabolic Engineering*, vol. 82, pp. 110–122, 2024.

[186] H. Luo, J. Li, H. Huang, L. Jiao, S. Zheng, Y. Ying, and Q. Li, "Ai-based segmentation of renal enhanced ct images for quantitative evaluate of chronic kidney disease," *Scientific Reports*, vol. 14, no. 1, p. 16890, 2024.

[187] Y. Li, L. Lu, and I. P. Androulakis, "The physiological and pharmacological significance of the circadian timing of the hpa axis: a mathematical modeling approach," *Journal of Pharmaceutical Sciences*, vol. 113, no. 1, pp. 33–46, 2024.

[188] X. J. Gao, K. Ciura, Y. Ma, A. Mikolajczyk, K. Jagiello, Y. Wan, Y. Gao, J. Zheng, S. Zhong, T. Puzyn, *et al.*, "Toward the integration of machine learning and molecular modeling for designing drug delivery nanocarriers," *Advanced Materials*, vol. 36, no. 45, p. 2407793, 2024.

[189] X. Dai and Y. Chen, "Computational biomaterials: computational simulations for biomedicine," *Advanced Materials*, vol. 35, no. 7, p. 2204798, 2023.

[190] S. Das, H. Mazumdar, K. R. Khondakar, and A. Kaushik, "Machine learning integrated graphene oxide-based diagnostics, drug delivery, analytical approaches to empower cancer diagnosis," *BMEMat*, vol. 3, no. 1, p. e12117, 2025.

[191] A. V. Colarusso, I. Goodchild-Michelman, M. Rayle, and A. R. Zomorrodi, "Computational modeling of metabolism in microbial communities on a genome-scale," *Current Opinion in Systems Biology*, vol. 26, pp. 46–57, 2021.

[192] H. Shu, J. Zhou, Q. Lian, H. Li, D. Zhao, J. Zeng, and J. Ma, "Modeling gene regulatory networks using neural network architectures," *Nature Computational Science*, vol. 1, no. 7, pp. 491–501, 2021.

[193] G. Brauwers and F. Frasincar, "A general survey on attention mechanisms in deep learning," *IEEE Transactions on Knowledge and Data Engineering*, vol. 35, no. 4, pp. 3279–3298, 2021.

[194] A. Vettoruzzo, M.-R. Bouguelia, J. Vanschoren, T. Rögnvaldsson, and K. Santosh, "Advances and challenges in meta-learning: A technical review," *IEEE transactions on pattern analysis and machine intelligence*, vol. 46, no. 7, pp. 4763–4779, 2024.

[195] F.-E. Yang, C.-Y. Wang, and Y.-C. F. Wang, "Efficient model personalization in federated learning via client-specific prompt generation," in *Proceedings of the IEEE/CVF International Conference on Computer Vision*, pp. 19159–19168, 2023.

[196] J. Li, Y. Meng, L. Ma, S. Du, H. Zhu, Q. Pei, and X. Shen, "A federated learning based privacy-preserving smart healthcare system," *IEEE Transactions on Industrial Informatics*, vol. 18, no. 3, 2021.

[197] Z.-A. Huang, Y. Hu, R. Liu, X. Xue, Z. Zhu, L. Song, and K. C. Tan, "Federated multi-task learning for joint diagnosis of multiple mental disorders on mri scans," *IEEE Transactions on Biomedical Engineering*, vol. 70, no. 4, pp. 1137–1149, 2022.

[198] A. Li, X. Yang, L. Ma, L. Yu, L. Hao, and Y. Liu, "Federated learning strategies for integrating composite meta-consistency loss with multi-head attention," *The European Journal on Artificial Intelligence*, p. 30504554251340238, 2024.

[199] S. AbdulRahman, H. Ould-Slimane, R. Chowdhury, A. Mourad, C. Talhi, and M. Guizani, "Adaptive upgrade of client resources for improving the quality of federated learning model," *IEEE Internet of Things Journal*, vol. 10, no. 5, pp. 4677–4687, 2022.

[200] X. He, X. Yi, Y. Zhao, K. H. Johansson, and V. Gupta, "Asymptotic analysis of federated learning under event-triggered communication," *IEEE Transactions on Signal Processing*, vol. 71, pp. 2654–2667, 2023.

[201] Y. Sun, Z. Lin, Y. Mao, S. Jin, and J. Zhang, "Channel and gradient-importance aware device scheduling for over-the-air federated learning," *IEEE Transactions on Wireless Communications*, vol. 23, no. 7, pp. 6905–6920, 2023.

[202] A. El Ouadrhiri and A. Abdelhadi, "Differential privacy for deep and federated learning: A survey," *IEEE access*, vol. 10, pp. 22359–22380, 2022.

[203] H. Fereidooni, S. Marchal, M. Miettinen, A. Mirhoseini, H. Möllering, T. D. Nguyen, P. Rieger, A.-R. Sadeghi, T. Schneider, H. Yalame, *et al.*, "Safelearn: Secure aggregation for private federated learning," in *2021 IEEE Security and Privacy Workshops (SPW)*, pp. 56–62, IEEE, 2021.

[204] Y. Xia, C. Hofmeister, M. Egger, and R. Bitar, "Byzantine-resilient secure aggregation for federated learning without privacy compromises," in *2024 IEEE Information Theory Workshop (ITW)*, pp. 223–228, IEEE, 2024.

[205] W. Issa, N. Moustafa, B. Turnbull, N. Sohrabi, and Z. Tari, "Blockchain-based federated learning for securing internet of things: A comprehensive survey," *ACM Computing Surveys*, vol. 55, no. 9, pp. 1–43, 2023.

[206] Y. Qu, M. P. Uddin, C. Gan, Y. Xiang, L. Gao, and J. Yearwood, "Blockchain-enabled federated learning: A survey," *ACM Computing Surveys*, vol. 55, no. 4, pp. 1–35, 2022.

[207] D. C. Nguyen, M. Ding, Q.-V. Pham, P. N. Pathirana, L. B. Le, A. Seneviratne, J. Li, D. Niyato, and H. V. Poor, "Federated learning meets blockchain in edge computing: Opportunities and challenges," *IEEE Internet of Things Journal*, vol. 8, no. 16, pp. 12806–12825, 2021.

[208] S. M. H. Bamakan and S. B. Far, "Distributed and trustworthy digital twin platform based on blockchain and web3 technologies," *Cyber Security and Applications*, p. 100064, 2024.

[209] C. Mazzocca, A. Acar, S. Uluagac, R. Montanari, P. Bellavista, and M. Conti, "A survey on decentralized identifiers and verifiable credentials," *IEEE Communications Surveys & Tutorials*, 2025.

[210] R. Kumar, A. Aljuhani, D. Javeed, P. Kumar, S. Islam, and A. N. Islam, "Digital twins-enabled zero touch network: A smart contract and explainable ai integrated cybersecurity framework," *Future generation computer systems*, vol. 156, pp. 191–205, 2024.

[211] Z. Wang, X. He, X. Zhuge, S. Xu, F. Dang, J. Xu, and Z. Yang, "Enabling network diagnostics in time-sensitive networking: Protocol, algorithm, and hardware," in *2024 IEEE/ACM 32nd International Symposium on Quality of Service (IWQoS)*, pp. 1–10, IEEE, 2024.

[212] Y. Tai, L. Zhang, Q. Li, C. Zhu, V. Chang, J. J. Rodrigues, and M. Guizani, "Digital-twin-enabled iomt system for surgical simulation using rac-gan," *IEEE Internet of Things Journal*, vol. 9, no. 21, pp. 20918–20931, 2022.